J. Michael McCarthy *Editor*

21st Century Kinematics

The 2012 NSF Workshop

Springer

21st Century Kinematics

J. Michael McCarthy
Editor

21st Century Kinematics

The 2012 NSF Workshop

Springer

Editor
J. Michael McCarthy
Dept. of Mech. & Aerospace Engineering
Robotics and Automation Laboratory
University of California
Irvine, USA

ISBN 978-1-4471-4509-7 ISBN 978-1-4471-4510-3 (eBook)
DOI 10.1007/978-1-4471-4510-3
Springer London Heidelberg New York Dordrecht

Library of Congress Control Number: 2012945173

Printed on acid-free paper

Springer is part of Springer Science+Business Media (www.springer.com)

This book is dedicated to our Mechanisms and Robotics research community.
With the strong foundation prepared by those before us, we look to advance our field into the 21st century.

Preface

This book was developed by the contributors to the Workshop on 21st Century Kinematics to provide supplementary material for their presentations. This book was made possible by an award (CMMI-1068497) from the National Science Foundation.[1]

I would like to express my sincere gratitude to James Schmeideler, Michael Stanisic, Phil Vogelwede and Erin Dolan for their assistance with coordinating the Workshop as part of the 2012 ASME Design Engineering Technical Conference, as well as to colleagues at Springer who prepared this volume.

Finally, I would like to gratefully acknowledge each of our contributors, Vincenzo Parenti-Castelli, Manfred Husty, Charles Wampler, Vijay Kumar, Larry Howell, and Kazem Kazerounian for their hard work in preparing this volume and their presentations at the Workshop, as well as for their ongoing commitment to the success of our Mechanisms and Robotics community, and for their friendship and inspiration over many years.

Irvine, CA J. Michael McCarthy

[1] Any opinions, findings, and conclusions or recommendations expressed in this material are those of the authors and do not necessarily reflect the views of the National Science Foundation.

Acknowledgements

Just a final word, the contributions that are described in this book are the result of collaborations with many students and colleagues over the years. Though I cannot name all of those who deserve recognition, let me acknowledge Horea Ilieş, Nicola Sancisi, Qimi Jiang, and Holly Greenberg, who helped complete this book. Finally, without the support of Christina Bloebaum this book would not have been possible. Many thanks to all of you.

Contents

Contributors

Larry L. Howell Brigham Young University, Provo, UT, USA

Manfred L. Husty Institute of Basic Sciences in Engineering, Unit Geometry and CAD, University Innsbruck, Innsbruck, Austria

Horea T. Ilieş Departments of Computer Science and Mechanical Engineering, The University of Connecticut, Storrs, CT, USA

Qimi Jiang Automation Specialist, Mining Technologies International Inc., Greater Sudbury, Ontario, Canada

Kazem Kazerounian Department of Mechanical Engineering, The University of Connecticut, Storrs, CT, USA

Vijay Kumar Department of Mechanical Engineering, University of Pennsylvania, Philadelphia, PA, USA

J. Michael McCarthy Robotics and Automation Laboratory, University of California, Irvine, USA

Vincenzo Parenti-Castelli DIEM—Department of Mechanical Engineering, HST-ICIR—Health Sciences and Technologies, University of Bologna, Bologna, Italy

Nicola Sancisi DIEM—Department of Mechanical Engineering, University of Bologna, Bologna, Italy

Hans-Peter Schröcker Institute of Basic Sciences in Engineering, Unit Geometry and CAD, University Innsbruck, Innsbruck, Austria

Andrew J. Sommese Applied and Computational Mathematics and Statistics, University of Notre Dame, Notre Dame, IN, USA

Charles W. Wampler Manufacturing Systems Laboratory, General Motors Global R&D Center, Warren, MI, USA

Chapter 1
Polynomials, Computers, and Kinematics for the 21st Century

J. Michael McCarthy

1.1 Introduction

It is a regular practice to organize a session to discuss research directions in the theory and practice, and such a panel was organized at the 2010 ASME Mechanisms and Robotics Conference of the International Design Engineering Technical Conferences. Unlike the usual format which has senior researchers advise their younger colleagues of recent successes and current challenges, the session in 2010 included our younger colleagues who took the opportunity to make their views known.

What our young colleagues had to say opened the eyes of many of us and motivated the organization of an National Science Foundation Workshop on 21st Century Kinematics held in conjunction with the 2012 Mechanisms and Robotics Conference. Our younger colleagues conveyed their excitement regarding many new and different opportunities for research built on theoretical and applied kinematics. However they expressed a clear frustration that the foundational material that was readily available to an earlier generation has not been taught for decades, and therefore seems lost to our younger colleagues and their students.

It took two years to organize, but the 2012 NSF Workshop is our response to this concern. However, rather than revive the lessons and notes from the past, we have sought to place that theory in a context that serves research goals in this new century.

1.2 The Recent Past

In order to consider the needs for the 21st century, it seems reasonable to consider the historical relationship between kinematics, mathematics and machine design.

J.M. McCarthy (✉)
Robotics and Automation Laboratory, University of California, Irvine, USA
e-mail: jmmccart@uci.edu

J.M. McCarthy (ed.), *21st Century Kinematics*,
DOI 10.1007/978-1-4471-4510-3_1,

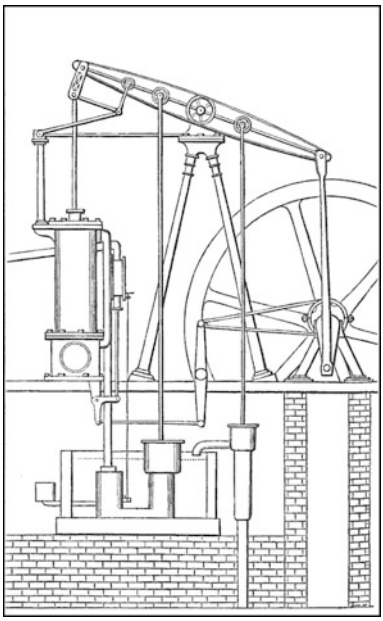

Fig. 1.1 An engraving of Watt's steam engine (R. Stuart 1824)

The following is taken from Editorials published in the February 2011 and May 2011 issues of the ASME Journal of Mechanisms and Robotics.

1.2.1 Polynomials and Kinematics

Mechanisms have been characterized by the curves that they trace since the time of Archimedes [1]. In the 1800's, F. Reuleaux, A.B.W. Kennedy and L. Burmester formalized this by applying the descriptive geometry of Gaspard Monge to the analysis and synthesis of machines [2].

James Watt's invention of a straight-line linkage to convert the linear expansion of steam into the rotation of the great beam making the steam engine practical (Fig. 1.1) captured the imagination of the mathematician P.L. Chebyshev, who introduced the mathematical analysis and synthesis of linkages.

About the same time, J.J. Sylvester, who introduced the Sylvester resultant for the solution of polynomial equations, went on to lecture about the importance of the Peaucellier linkage which generates a pure linear movement from a rotating link [3]. Influenced by Sylvester, A.B. Kempe developed a method for designing a linkage that traces a given algebraic curve [4] that even now inspires research at the intersection of geometry [5, 6] and computation.

In the mid 1950's, J. Denavit and R.S. Hartenberg introduced a matrix formulation of the loop equations of a mechanism to obtain polynomials that define- its movement [7]. During a speech in 1972, F. Freudenstein famously used the phrase

"Mount Everest of kinematics" to describe the solution of these polynomials for the 7R spatial linkage [8]. In this context "solution" is not a single root but an algorithm that yields all of the roots of the polynomial system, which in turn defines all of the configurations of the linkage for a given input.

It was immediately recognized that the 7R analysis problem was equivalent to solving the inverse kinematics for a general robot manipulator to obtain the configurations that are available to pick up an object. By the end of the 1970's, J. Duffy [9] had formulated an efficient set of equations for this problem, but it was not until the late 1980's when the degree 16 polynomial that yields the 16 robot configurations was obtained by Q. Liao, H.Y. Lee and C.G. Liang [10].

By the mid-1990's, computer algebra and sparse resultant techniques were the most advanced tools for formulating and solving increasingly complex arrays of polynomials obtained in the study of mechanisms and robotics systems [11, 12]. In 1996, M. Husty used computer algebra to reduce eight quadratic equations in eight soma coordinates that locate the end-effector of a general six-legged Stewart platform to a degree 40 polynomial [13], which allowed the calculation of the 40 configurations of the system.

1.2.2 Computers and Kinematics

In 1959 F. Freudenstein and G.N. Sandor [14] used the newly developed digital computer and the loop equations of a linkage to determine its dimensions, initiating the computer-aided design of mechanisms. Within two decades the computer solution of the equations introduced by Denavit and Hartenberg was integral to the analysis of complex machine systems [15, 16] and the control of robot manipulators [17].

R.E. Kaufman [18, 19] combined the computer's ability to rapidly compute the roots of polynomial equations with a graphical display to unite Freudenstein's techniques with the geometrical methods of Reuleaux and Burmester to form *KINSYN*, an interactive computer graphics system for mechanism design (Fig. 1.2). This was followed by A.G. Erdman's *LINCAGES* system [20, 21] and K.J. Waldron's *RECSYN* system [22], which combined sophisticated computer graphics and polynomial solvers to implement Burmester's strategy for linkage synthesis. Computerized linkage synthesis was extended to spherical linkages [23, 24] and spatial linkages [25] by the turn of the 21st century.

The pursuit of solutions to the design equations for the particularly challenging problem of finding a four-bar linkage that traces a curve through nine specified points lead Freudenstein and B. Roth [26, 27] to develop a unique solution strategy, now called numerical continuation. They started with a set of polynomials with a known solution, which was then deformed slightly and the solution updated numerically. Iterating this "parameter-perturbation procedure," they obtained a sequence of polynomials and solutions that converged to the target polynomials and the desired solution. While this yielded the first solutions to the nine-point problem, their heuristic deformation procedure could not find all of the solutions.

Fig. 1.2 Roger Kaufman using interactive computer graphics for linkage synthesis at MIT in 1970

By the 1980's theoretical advances in numerical continuation yielded algorithms that could reliably and efficiently find all solutions to small sets of polynomial equations [28, 29]. L.W. Tsai and A.P. Morgan [30] applied the polynomial continuation routine *SYMPOL* to the eight quadratic polynomials of the inverse kinematics problem for a general manipulator and obtained the 16 roots in four minutes. In the early 1990's, C.W. Wampler and A.P. Morgan [31] revisited Freudenstein and Roth's nine-point synthesis problem to obtain 1442 solutions, demonstrating that polynomial continuation algorithms had come of age.

A few years later M. Raghavan and Roth [32, 33] included polynomial continuation with resultant elimination among the strategies to obtain complete solutions to kinematics problems. In fact, Raghavan [34] used polynomial continuation to obtain 40 configurations for the general Stewart platform anticipating Husty's degree 40 polynomial.

1.3 Recent Results

The past century shows that our ability to analyze and design mechanisms and robotic systems of increasing complexity has depended on our ability to derive and solve the associated increasingly complex polynomial systems. From this, we can expect that advances in computer algebra and numerical continuation for the derivation and solution of the even more complex polynomial systems will advance research in mechanisms and robotics.

Now examining recent research, we can identify three research trends that we can expect to persist into the future. They are the analysis and synthesis of (i) spatial mechanisms and robotic systems, (ii) compliant linkage systems, and (iii) tensegrity and cable-driven systems. In each case, we find that researchers are formulating and solving polynomial systems of total degrees that dwarf those associated with major kinematics problems of the previous century.

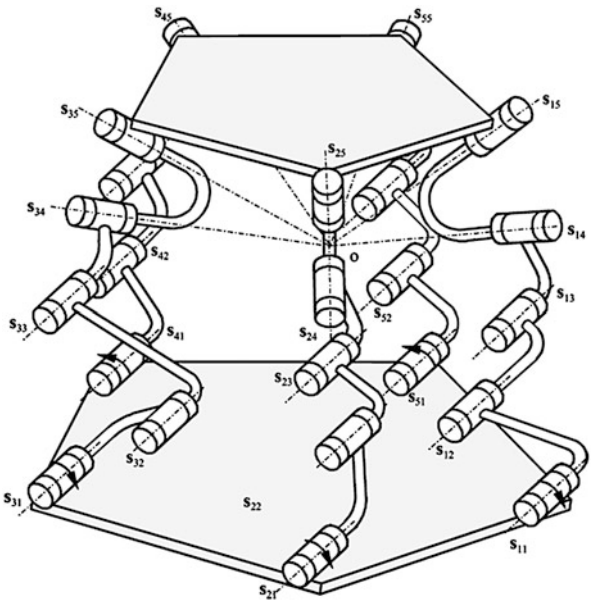

Fig. 1.3 A spatial one degree-of-freedom linkage formed from 5-5R chains

1.3.1 Analysis and Synthesis of Machine Systems

Early in the 2000's, E. Lee and D. Mavroidis [35] formulated the synthesis of a spatial serial chain as a generalized inverse kinematics problem, where in order to position a serial chain in a required set of task positions one computes the dimensions of the chain as well as its joint angles. About the same time general polynomial continuation algorithms such as PHCpack [36, 37] and POLSYS [38] became available. Lee and Mavroidis used PHCpack to solve 13 polynomials in 13 unknowns and obtained 36 sets of dimensions for spatial 3R chains that reach four required task positions. This system of polynomials had a total degree of 1,417,174 and took 33 days to solve on a computer workstation [39].

In 2004, H. Su and colleagues reported that a parallel version of the POLSYS code [40, 41] obtained 42,625 solutions to the RRS design problem consisting of 11 polynomials in 11 unknowns for a total degree of 4,194,304. The computation time was 42 minutes on 128 nodes of the San Diego Supercomputer Center's Blue Horizon system.

A. Perez used dual quaternion coordinates to formulate the design equations for general spatial serial chains and obtained 126 synthesis equations in 126 unknowns for a spatial 5R chain that reaches a set of 21 task positions [42, 43] (Fig. 1.3). This set of equations has been solved numerically to verify that they are correct, but so far a complete solution has not been achieved.

A.J. Sommese and C.W. Wampler published their text [44] on the mathematical theory of polynomial continuation and its applications to systems that arise in engineering and science, which they term "numerical algebraic geometry." This includes

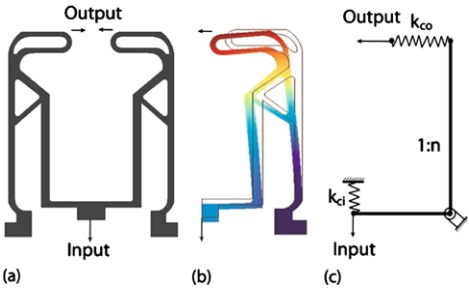

Fig. 1.4 A compliant mechanism designed for use as a gripper

the polynomial continuation algorithm HomLab, which has recently been upgraded and renamed Bertini [45].

By 2008, Lee [46] found that the performance of polynomial continuation algorithms had advanced to the point that on a Dell PC they averaged 15 continuation paths per second for PHCpack and Bertini, and reached 150 paths per second for some problems using their HOM4PS package. At computation speeds of 1500 paths per second Su's RRS synthesis problem could be achieved on a PC in 5 minutes.

Continued improvements in processing speed, parallel processing architectures, and algorithm efficiency have the potential to yield such rapid solution of very large polynomial systems that numerical analysis and synthesis of complex spatial linkage systems can become practical and routine.

1.3.2 Compliant Mechanisms

In his speech of 1972, F. Freudenstein identified "a theory of kinematics of mechanisms with elasticity" as one of nine areas for future research. Initial work in this area was limited to flexibility effects in the analysis of linkage movement [47], but this evolved in the late 1980's to yield a design theory for compliant linkages [48, 49]. In the 1990's, compliant mechanisms found a wide range of applications including micro-mechanisms [50, 51], and by 2001, L. Howell presented a complete design theory [52].

As the study of compliant mechanisms matured, it was shown that the flexibility in the links can be modeled by spring-loaded joints. This allowed kinematic loop equations to be combined with static equilibrium for the analysis and synthesis of these systems [53]. The result was the ability to design a linkage system with compliance that resists displacement from specific configurations [54]. H.J. Su formulated a system of polynomials for the synthesis of a four-bar compliant linkage with three specified equilibrium positions [55, 56]. He obtained a 12 polynomials with a total degree of 16,384, which was solved using polynomial continuation.

Current research directions in compliant linkage design include increasing the ease of the design process and extending it to spatial linkages. As an example, S. Ananthasuresh describes the sophistication of compliant mechanism synthesis methods and proposes a simplified approach for planar linkages [57] (Fig. 1.4).

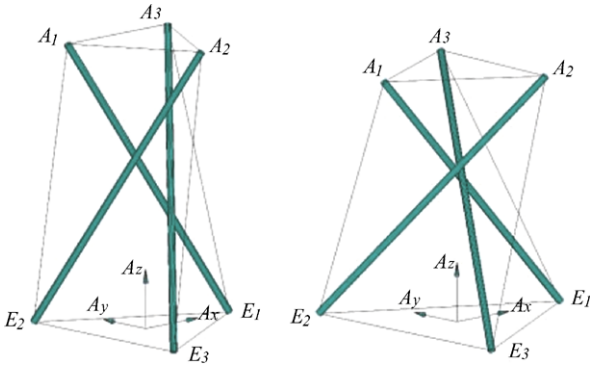

Fig. 1.5 A three-strut tensegrity system in its unloaded and loaded configurations

Similarly, C.P. Lusk [58, 59] describes the need for compliant linkages that are constructed in the plane by layered manufacturing but have the ability to move out of the plane for operation.

It is clear that computer algebra and polynomial continuation that serve the needs of design and analysis of mechanisms and robotics will also serve to advance the analysis and design of compliant linkage systems.

1.3.3 Cable Robots and Tensegrity Systems

In the early 1990's J. Duffy analyzed the stiffness of a Stewart platform supported by compliant legs [60], and by 2000 he had formalized this into a theory of deployable tensegrity structures with elastic ties [61]. A tensegrity structure [62, 63] is an assembly of compression elements, or struts, and extension elements, called ties, that form a stable structure.

C.D. Crane [64] considered the equilibrium configurations of a set of struts and cable ties of a tensegrity system. His formulation yields 12 equations for a system of three struts and nine cables (Fig. 1.5). This formulation also applies to cable systems ranging from deployable structures [65] to cable manipulators [66]. In fact, Moon et al. [67] construct spring-loaded actuators for a parallel mechanism to combine tensegrity and compliant mechanism design.

Recently, V. Kumar formulated the problem of determining the equilibrium positions of objects supported by cables [68, 69] which yielded nine polynomials in nine unknowns (Fig. 1.6). He reports that the complexity of the polynomials and associated resultants overwhelmed his computer algebra software.

The lightweight mechanical structures that become possible with a combination of actuators, cables, springs and struts motivate the integration of spatial robots and compliant mechanisms into a new theory for the analysis and synthesis of tensegrity systems.

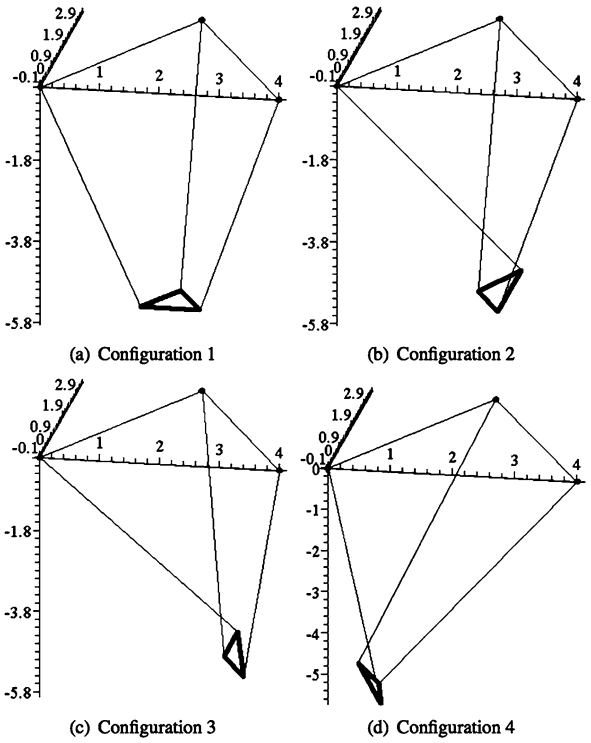

Fig. 1.6 Direct kinematic analysis of a cable robotic systems

1.4 Workshop on 21st Century Kinematics

Solutions to the inverse kinematics of a general serial chain robot and to the direct kinematics of the general Stewart-Gough platform, which yielded polynomials of degree 16 and degree 40, respectively, were major advances in the last century. Less than ten years later, researchers are deriving and solving polynomial systems for the analysis and design of robotic systems, compliant mechanisms and tensegrity systems that have total degrees in the millions. Advances in computational speed and effective algorithms to process these solutions promise new technologies and products well into the 21st Century.

The analysis and design of innovative mechanical systems yield increasingly complex systems of polynomials that characterize these devices. At the same time increasingly sophisticated computational tools are being developed for numerical algebraic geometry that can assist derivation and solution of these polynomial systems. It is now routine for kinematics researchers to derive polynomial systems that dwarf landmark problems of the recent past.

Discussions at the 2010 and 2011 ASME Mechanisms and Robotics Conference resulted in a proposal for NSF workshop to advance the analysis and design of innovative machine systems. This workshop echoes the NSF supported 1963 Yale Mechanisms Teachers Conference that taught a generation of university educators the fundamental principles of kinematic theory.

Our Workshop on 21st Century Kinematics focuses on algebraic problems in the analysis and synthesis of mechanisms and robots, compliant mechanisms and tensegrity and cable-driven systems. The presentations are:

1. Computer-aided invention of mechanisms and robots, J. Michael McCarthy (Professor, University of California, Irvine)
2. Mechanism synthesis for modeling human movement, Vincenzo Parenti-Castelli (Professor, University of Bologna)
3. Algebraic Geometry and Kinematic Synthesis, Manfred Husty (Professor, University of Innsbruck)
4. Numerical Algebraic Geometry and Kinematics, Charles Wampler (Technical Fellow, General Motors Research and Development)
5. Kinematic analysis of cable robotic systems, Vijay Kumar (Professor, University of Pennsylvania)
6. Kinematic synthesis of compliant mechanisms, Larry Howell (Professor, Brigham Young University)
7. Protein Kinematics, Kazem Kazerounian (Professor, University of Connecticut)

The workshop presentations will be made available on-line. This book has been prepared to provide the background materials for each of these presentations.

Acknowledgements The author gratefully acknowledges National Science Foundation grant CMMI 1068497 which provided support for materials in this book as part of the Workshop on 21st Century Kinematics. In addition, the leadership of Michael Stanisic and James Schmiedeler and Phil Vogelwede, organizers of the 2012 ASME Design Engineering Technical Conferences, the support of Jian Dai, Stephen Cranfield, and Carl Nelson, who are responsible for the ASME Mechanisms and Robotics Conference, and attention to detail by Erin Dolan, who managed the execution of the Workshop are gratefully acknowledged.

References

1. Koetsier, T.: From kinematically generated curves to instantaneous invariants: episodes in the history of instantaneous planar kinematics. Mech. Mach. Theory **21**(6), 489–498 (1986)
2. Moon, F.C.: History of the dynamics of machines and mechanisms from Leonardo to Timoshenko. In: Yan, H.S., Ceccarelli, M. (eds.) International Symposium on History of Machines and Mechanisms (2009). doi:10.1007/978-1-4020-9485-9-1
3. Koetsier, T.: A contribution to the history of kinematics—II. Mech. Mach. Theory **18**(1), 43–48 (1983)
4. Kempe, A.B.: On a general method of describing plane curves of the nth degree by linkwork. Proc. Lond. Math. Soc. **VII**, 213–216 (1976)
5. Jordan, D., Steiner, M.: Configuration spaces of mechanical linkages. Discrete Comput. Geom. **22**, 297–315 (1999)
6. Connelly, R., Demaine, E.D.: Geometry and topology of polygonal linkages. In: Goodman, J.E., O'Rourke, J. (eds.) Handbook of Discrete and Computational Geometry. CRC Press, Boca Raton (2004), Chap. 9
7. Denavit, J., Hartenberg, R.S.: A kinematic notation for lower-pair mechanisms based on matrices. ASME J. Appl. Mech. **22**, 215–221 (1955)
8. Freudenstein, F.: Kinematics: past, present and future. Mech. Mach. Theory **8**, 151–160 (1973)

9. Duffy, J.: The Analysis of Mechanisms and Robot Manipulators. Wiley, New York (1980), 419 pp.
10. Lee, H.Y., Liang, C.G.: Displacement analysis of the general spatial 7-link 7R mechanisms. Mech. Mach. Theory **23**(2), 219–226 (1988)
11. Canny, J., Emiris, I.: An efficient algorithm for the sparse matrix resultant. Applied algebra, algebraic algorithms and error correcting codes. Lect. Notes Comput. Sci. **673**, 89–104 (1993). doi:10.1007/3-540-56686-4-36
12. Neilsen, J., Roth, B.: Elimination methods for spatial synthesis. In: Merlet, J.P., Ravani, B. (eds.) Computational Kinematics. Solid Mechanics and Its Applications, vol. 40, pp. 51–62 (1995)
13. Husty, M.L.: An algorithm for solving the direct kinematics of general Stewart-Gough platforms. Mech. Mach. Theory **31**(4), 365–380 (1996)
14. Freudenstein, F., Sandor, G.N.: Synthesis of path generating mechanisms by means of a programmed digital computer. ASME J. Eng. Ind. **81**, 159–168 (1959)
15. Sheth, P.N., Uicker, J.J.: IMP (Integrated Mechanisms Program), a computer-aided design analysis system for mechanisms and linkages. ASME J. Eng. Ind. **94**, 454–464 (1972)
16. Suh, C.H., Radcliffe, C.W.: Kinematics and Mechanism Design. Wiley, New York (1978), p. 458
17. Paul, R.P.: Robot Manipulators: Mathematics, Programming and Control. MIT Press, Cambridge (1981)
18. Kaufman, R.E., Maurer, W.G.: Interactive linkage synthesis on a small computer. In: ACM National Conference, Aug. 3–5 (1971)
19. Rubel, A.J., Kaufman, R.E.: KINSYN III: a new human-engineered system for interactive computer-aided design of planar linkages. ASME Trans. J. Eng. Ind., May (1977)
20. Erdman, A.G., Gustafson, J.: LINCAGES—a linkage interactive computer analysis and graphically enhanced synthesis package. ASME Paper No. 77-DTC-5, Chicago, Illinois (1977)
21. Hunt, L., Erdman, A.G., Riley, D.R.: MicroLINCAGES: microcomputer synthesis and analysis of planar linkages. In: Proceedings of the Seventh OSU Applied Mechanisms Conference, Dec. (1981)
22. Chuang, J.C., Strong, R.T., Waldron, K.J.: Implementation of solution rectification techniques in an interactive linkage synthesis program. ASME J. Mech. Des. **103**, 657–664 (1981)
23. Ruth, D.A., McCarthy, J.M.: SphinxPC: an implementation of four position synthesis for planar and spherical linkages. In: Proceedings of the ASME Design Engineering Technical Conferences, Sacramento, CA, Sept. 14–17 (1997)
24. Furlong, T.J., Vance, J.M., Larochelle, P.M.: Spherical mechanism synthesis in virtual reality. ASME J. Mech. Des. **121**, 515 (1999)
25. Liao, Q., McCarthy, J.M.: On the seven position synthesis of a 5-SS platform linkage. ASME J. Mech. Des. **123**, 74–79 (2001)
26. Roth, B., Freudenstein, F.: Synthesis of path-generating mechanisms by numerical methods. ASME J. Eng. Ind. **85B-3**, 298–306 (1963)
27. Freudenstein, F., Roth, B.: Numerical solution of systems of nonlinear equations. J. ACM **10**(4), 550–556 (1963)
28. Watson, L.T.: A globally convergent algorithm for computing fixed points of C^2 maps. J. Appl. Math. Comput. **18**, 87–92 (1986)
29. Morgan, A.P.: A homotopy for solving polynomial systems. J. Appl. Math. Comput. **5**, 297–311 (1979)
30. Tsai, L.W., Morgan, A.P.: Solving the kinematics of the most general six- and five-degree-of-freedom manipulators by continuation methods. J. Mech. Transm. Autom. Des. **107**, 189–200 (1985)
31. Wampler, C.W., Morgan, A.P.: Complete solution for the nine-point path synthesis problem for four-bar linkages. J. Mech. Des. **114**(1), 153–159 (1992). doi:10.1115/1.2916909
32. Raghavan, M., Roth, B.: Inverse kinematics of the general 6R manipulator and related linkages. J. Mech. Des. **115**(3), 502–508 (1993). doi:10.1115/1.2919218

33. Raghavan, M., Roth, B.: Solving polynomial systems for kinematic analysis and synthesis of mechanisms and robot manipulators. J. Mech. Des. **117**(B), 71–79 (1995). doi:10.1115/1.2836473
34. Raghavan, M.: The Stewart platform of general geometry has 40 configurations. J. Mech. Des. **115**(2), 277–282 (1993). doi:10.1115/1.2919188
35. Lee, E., Mavroidis, C.: Solving the geometric design problem of spatial 3R robot manipulators using polynomial homotopy continuation. ASME J. Mech. Des. **124**(4), 652–661 (2002)
36. Verschelde, J., Haegemans, A.: The GBQ algorithm for constructing start systems of homotopies for polynomial systems. SIAM J. Numer. Anal. **30**(2), 583–594 (1993)
37. Verschelde, J.: Algorithm 795: PHCpack: a general-purpose solver for polynomial systems by homotopy continuation. ACM Trans. Math. Softw. **25**(2), 251–276 (1999)
38. Wise, S.M., Sommese, A.J., Watson, L.T.: Algorithm 801: POLSYS PLP: a partitioned linear product homotopy code for solving polynomial systems of equations. ACM Trans. Math. Softw. **26**, 176–200 (2000)
39. Lee, E., Mavroidis, C.: Geometric design of 3R robot manipulators for reaching four end-effector spatial poses. Int. J. Robot. Res. **23**(3), 247–254 (2004)
40. Su, H., McCarthy, J.M., Sosonkina, M., Watson, L.T.: POLSYS GLP: a parallel general linear product homotopy code. ACM Trans. Math. Softw. **32**(4), 561–579 (2006)
41. Su, H., McCarthy, J.M., Watson, L.T.: Generalized linear product homotopy algorithms and the computation of reachable surfaces. ASME J. Comput. Inf. Sci. Eng. **4**(3), 226–234 (2004)
42. Perez, A., McCarthy, J.M.: Dual quaternion synthesis of constrained robotic systems. ASME J. Mech. Des. **126**(3), 425–435 (2004)
43. Perez-Gracia, A., McCarthy, J.M.: Kinematic synthesis of spatial serial chains using Clifford algebra exponentials. Proc. Inst. Mech. Eng. Part C, J. Mech. Eng. Sci. **220**(C7), 951–966 (2006)
44. Sommese, A.J., Wampler, C.W.: The Numerical Solution of Systems of Polynomials Arising in Engineering and Science. World Scientific Publishing Co., New Jersey (2005)
45. Bates, D.J., Hauenstein, J.D., Sommese, A.J., Wampler, C.W.: Bertini: Software for Numerical Algebraic Geometry. http://www.nd.edu/sommese/bertini
46. Lee, T.L., Li, T.Y., Tsai, C.H.: HOM4PS-2.0: a software package for solving polynomial systems by the polyhedral homotopy continuation method. Computing **83**, 109–133 (2008)
47. Midha, A., Erdman, A.G., Frohrib, D.A.: An approximate method for the dynamic analysis of elastic linkages. ASME J. Eng. Ind. **99**, 449 (1977)
48. Her, I., Midha, A.: A compliance number concept for compliant mechanisms and type synthesis. ASME J. Mech. Transm. Autom. Des. **109**, 348 (1987)
49. Hill, T.C., Midha, A.: A graphical, user-driven Newton-Raphson technique for use in the analysis and design of compliant mechanisms. ASME J. Mech. Des. **112**, 123 (1990)
50. Kota, S., Ananthasuresh, G.K., Crary, S.B., Wise, K.D.: Design and fabrication of microelectromechanical systems. ASME J. Mech. Des. **116**, 1081 (1994)
51. Frecker, M.I., Ananthasuresh, G.K., Nishiwaki, S., Kikuchi, N., Kota, S.: Topological synthesis of compliant mechanisms using multi-criteria optimization. ASME J. Mech. Des. **119**, 238 (1997)
52. Howell, L.: Compliant Mechanisms. Wiley, New York (2001)
53. Kimball, C., Tsai, L.W.: Modeling of flexural beams subjected to arbitrary end loads. ASME J. Mech. Des. **124**, 223 (2002)
54. Jensen, B.D., Howell, L.L.: Bistable configurations of compliant mechanisms modeled using four links and translational joints. ASME J. Mech. Des. **126**, 657 (2004)
55. Su, H.J., McCarthy, J.M.: A polynomial homotopy formulation of the inverse static analysis for planar compliant mechanisms. ASME J. Mech. Des. **128**, 776 (2006)
56. Su, H.J., McCarthy, J.M.: Synthesis of bistable compliant four-bar mechanisms using polynomial homotopy. ASME J. Mech. Des. **129**, 1094 (2007)
57. Hegde, S., Ananthasuresh, G.K.: Design of single-input-single-output compliant mechanisms for practical applications using selection maps. ASME J. Mech. Des. **132**, 081007 (2010)

58. Lusk, C.P., Howell, L.L.: A micro helico-kinematic platform via spherical crank-sliders. ASME Journal of Mechanical Design **130** (2008)
59. Espinosa, D.A., Lusk, C.P.: Part 1: moment-dependent pseudo-rigid-body models for straight beams. In: Proc. ASME 2010 Design Engineering Technical Conferences. Paper No. DETC2010-29230 (2010)
60. Griffis, M., Duffy, J.: Kinestatic control: a novel theory for simultaneously regulating force and displacement. ASME J. Mech. Des. **113**, 508–515 (1991)
61. Wang, B.B.: Cable-strut systems: part I—Tensegrity. J. Constr. Steel Res. **45**(3), 281–289 (1998)
62. Motro, R.: Tensegrity: Structural Systems for the Future. Kogan Page Ltd., London (2003)
63. Duffy, J., Rooney, J., Knight, B., Crane, C.D. III: A review of a family of self-deploying tensegrity structures with elastic ties. Shock Vib. Dig. **32**(2), 100–106 (2000)
64. Crane, C.D. III, Duffy, J., Correa, J.C.: Static analysis of tensegrity structure. ASME J. Mech. Des. **127**, 257–268 (2005)
65. Tibert, A.G., Pellegrino, S.: Deployable tensegrity masts. In: 44th Structures, Structural Dynamics, and Materials Conference. Paper No. AIAA2003, 1978 (2003)
66. Barrette, G., Gosselin, C.M.: Determination of the dynamic workspace of cable-driven planar parallel mechanisms. ASME J. Mech. Des. **127**, 242–248 (2005)
67. Moon, Y., Crane, C.D. III, Roberts, R.G.: Analysis of a planar tensegrity-based compliant mechanism. In: Proc. ASME 2010 Design Engineering Technical Conferences. Paper No. DETC2010-28 (2010)
68. Stump, E., Kumar, V.: Workspaces of cable-actuated parallel manipulators. ASME J. Mech. Des. **128**(1), 159–167 (2006)
69. Jiang, Q., Kumar, V.: The direct kinematics of objects suspended from cables. In: Proc. ASME 2010 Design Engineering Technical Conferences. Paper No. DETC2010-280 (2010)

Chapter 2
Kinematic Synthesis

J. Michael McCarthy

2.1 Kinematics Equations of a Serial Chain

To study the relative movement at each joint of a spatial linkage,[1] we introduce three 4×4 matrices that we call *coordinate screw displacements*. Each of these matrices defines a translation along one coordinate axis combined with a rotation about that axis. This is the movement allowed by an RP open chain that has the axis of the revolute joint parallel to the guide of the slider. This assembly is called a cylindric joint, or C-joint, because trajectories traced by points in the moving body lie on cylinders about the joint axis.

Let S_1 be the axis of a cylindric joint that connects a link $\mathsf{S}_1\mathsf{S}_2$ to ground. Locate the fixed frame F so that its z-axis is along S_1 and its origin is the point $\mathbf{p}$. Attach the link frame B so that its z-axis is along S_1 and its x-axis is along the common normal N from S_1 and S_2. The displacement of B relative to F consists of a slide d and rotation θ along and around the z-axis of F. Combine the rotation matrix and translation vector for this displacement to form the 4×4 *homogeneous transform*, given by

$$\begin{Bmatrix} X \\ Y \\ Z \\ 1 \end{Bmatrix} = \begin{bmatrix} \cos\theta & -\sin\theta & 0 & 0 \\ \sin\theta & \cos\theta & 0 & 0 \\ 0 & 0 & 1 & d \\ 0 & 0 & 0 & 1 \end{bmatrix} \begin{Bmatrix} x \\ y \\ z \\ 1 \end{Bmatrix}, \tag{2.1}$$

or

$$\mathbf{X} = \big[Z(\theta, d)\big]\mathbf{x}. \tag{2.2}$$

[1] This chapter combines excerpts from J.M. McCarthy and G.S. Soh, *Geometric Design of Linkages*, Springer, 2010, and is based on the Ph.D. research by Alba Perez and Haijun Su. Reproduced by kind permission of Springer © 2012.

J.M. McCarthy (✉)
Robotics and Automation Laboratory, University of California, Irvine, USA
e-mail: jmmccart@uci.edu

J.M. McCarthy (ed.), *21st Century Kinematics*,
DOI 10.1007/978-1-4471-4510-3_2, © Springer-Verlag London 2013

This defines the transformation of coordinates $\mathbf{x}$ in B to $\mathbf{X}$ in F that represents the movement allowed by a cylindric joint. Notice that we do not distinguish between point coordinate vectors with and without the fourth component of 1. In what follows the difference should be clear from the context of our calculations.

The transform $[Z(\theta, d)]$ is the *coordinate screw displacement* about the z-axis. We can define similar screw displacements $[X(\cdot, \cdot)]$ and $[Y(\cdot, \cdot)]$ about the x- and y-axes,

$$\begin{aligned}
\big[X(\theta, d)\big] &= \begin{bmatrix} 1 & 0 & 0 & d \\ 0 & \cos\theta & -\sin\theta & 0 \\ 0 & \sin\theta & \cos\theta & 0 \\ 0 & 0 & 0 & 1 \end{bmatrix}, \\
\big[Y(\theta, d)\big] &= \begin{bmatrix} \cos\theta & 0 & \sin\theta & 0 \\ 0 & 1 & 0 & d \\ -\sin\theta & 0 & \cos\theta & 0 \\ 0 & 0 & 0 & 1 \end{bmatrix}.
\end{aligned} \tag{2.3}$$

We use these coordinate screw displacements to formulate the kinematics equations for spatial linkages.

It is useful to note that the inverse of a coordinate screw displacement can be obtained by negating its parameters. For example,

$$\big[Z(\theta, d)^{-1}\big] = \big[Z(-\theta, -d)\big] = \begin{bmatrix} \cos\theta & \sin\theta & 0 & 0 \\ -\sin\theta & \cos\theta & 0 & 0 \\ 0 & 0 & 1 & -d \\ 0 & 0 & 0 & 1 \end{bmatrix}. \tag{2.4}$$

Notice that $[Z(\theta, d)^{-1}]$ is not the transpose of $[Z(\theta, d)]$.

2.1.1 The Denavit-Hartenberg Convention

A spatial open chain can be viewed as a sequence of joint axes S_i connected by common normal lines, Fig. 2.1. Let A_{ij} be the common normal from joint axis S_i to S_j. The Denavit-Hartenberg convention attaches the link frame B_i such that its z-axis is directed along the axis S_i and its x-axis is directed along the common normal A_{ij}. This convention leaves undefined the initial and final coordinate frames F and M. These frames usually have their z-axes aligned with the first and last axes of the chain. However, their x-axes can be assigned any convenient direction.

This assignment of standard frames B_i allows us to define the 4×4 transformation $[D]$ that locates the end-link of a spatial open chain as the sequence of transformations

$$[D] = \big[Z(\theta_1, d_1)\big]\big[X(\alpha_{12}, a_{12})\big]\big[Z(\theta_2, d_2)\big] \cdots \big[X(\alpha_{n-1,n}, a_{n-1,n})\big]\big[Z(\theta_n, d_n)\big], \tag{2.5}$$

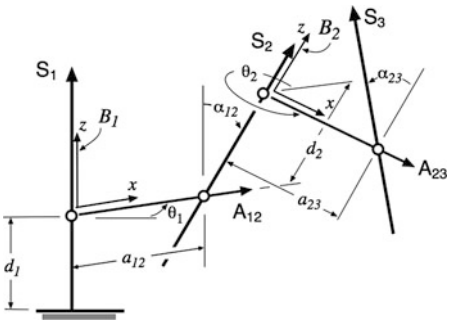

Fig. 2.1 Joint axes S_1, S_2, and S_3 and the link frames B_1 and B_2

where α_{ij} and a_{ij} are the *twist angle* and *offset* between the axes S_i and S_j. This matrix equation defines the *kinematics equations* of the open chain.

The 4×4 transform $[T_j] = [X(\alpha_{ij}, a_{ij})][Z(\theta_j, d_j)]$ is the transformation from frame B_i to B_j. Equation (2.5) is often written as

$$[D] = [T_1][T_2] \cdots [T_n]. \tag{2.6}$$

Notice that $[T_1] = [Z(\theta_1, d_1)]$.

2.2 The Product of Exponentials Form of the Kinematics Equations

The synthesis equations for a spatial serial chain are obtained from the matrix exponential form of its kinematics equations. This form of the kinematics equations replaces the Denavit-Hartenberg parameters with the coordinates of the n joint axes, $\mathsf{S}_i, i = 1, \ldots n$. It is the coordinates of these axes that are the unknowns of the design problem.

Consider a displacement defined such that the moving body rotates the angle ϕ and slides the distance k around and along the screw axis $\mathsf{S} = (\mathbf{S}, \mathbf{C} \times \mathbf{S})$. Let $\mu = k/\phi$, then we can introduce the screw $\mathsf{J} = (\mathbf{S}, \mathbf{V}) = (\mathbf{S}, \mathbf{C} \times \mathbf{S} + \mu\mathbf{S})$, where μ is called the *pitch* of the screw. The components of J define the 4×4 twist matrix,

$$J = \begin{bmatrix} 0 & -s_z & s_y & v_x \\ s_z & 0 & -s_x & v_y \\ -s_y & s_x & 0 & v_z \\ 0 & 0 & 0 & 0 \end{bmatrix}, \tag{2.7}$$

and we find that the 4×4 homogeneous transform representing a rotation ϕ and a translation k about and along an axis S, $[T(\phi, k, \mathsf{S})]$, is defined as the matrix exponential

$$\left[T(\phi, k, \mathsf{S})\right] = e^{\phi J}. \tag{2.8}$$

The matrix exponential takes a simple form for the matrices $[Z(\theta_i, d_i)]$ and $[X(\alpha_{i,i+1}, a_{i,i+1})]$. The screws defined for these two transformations are $\mathsf{K} = (\mathbf{k}, \nu\mathbf{k})$ and $\mathsf{I} = (\boldsymbol{\imath}, \lambda\boldsymbol{\imath})$, where $\nu = d_i/\theta_i$ and $\lambda = a_{i,i+1}/\alpha_{i,i+1}$ are their respective pitches. Thus, we have

$$\big[Z(\theta_i, d_i)\big] = e^{\theta_i K} \quad \text{and} \quad \big[X(\alpha_{i,i+1}, a_{i,i+1})\big] = e^{\alpha_{i,i+1} I}, \tag{2.9}$$

and the kinematics equations become

$$[D] = [G]e^{\theta_1 K} e^{\alpha_{12} I} e^{\theta_2 K} \dots e^{\alpha_{n-1,n} I} e^{\theta_n K} [H]. \tag{2.10}$$

This is one way to write the product of exponentials form of the kinematics equations. In the next section, we modify this slightly for use as our design equations.

2.2.1 Relative Displacements

If we choose a reference position for the end-effector, denoted by $[D_0]$, then the associated joint angle vector $\boldsymbol{\theta}_0$ can be determined, as well as the world frame coordinates of each of the joint axes. The transformation $[D_0]$ is often selected to be the configuration in which the joint parameters are zero and is called the *zero reference position* by Gupta (1986) [1].

The displacement of the serial chain relative to this reference configuration is defined by $[D(\Delta\boldsymbol{\theta})] = [D(\boldsymbol{\theta})][D(\boldsymbol{\theta}_0)]^{-1}$ and yields a convenient formulation for the kinematics equations. Assume that $[D_0]$ is a general position of the end-effector defined by joint parameters $\boldsymbol{\theta}_0$, so $\Delta\boldsymbol{\theta} = \boldsymbol{\theta} - \boldsymbol{\theta}_0$. Then, using the usual kinematics equations, we have

$$\begin{aligned}\big[D(\Delta\boldsymbol{\theta})\big] = &\big([G]\big[Z(\theta_1, d_1)\big] \dots \big[Z(\theta_n, d_n)\big][H]\big) \\ &\big([G]\big[Z(\theta_{10}, d_{10})\big] \dots \big[Z(\theta_{n0}, d_{n0})\big][H]\big)^{-1}.\end{aligned} \tag{2.11}$$

In order to expand this equation, we introduce the partial displacements

$$[A_{i0}] = [G]\big[Z(\theta_{10}, d_{10})\big]\big[X(\alpha_{12}, a_{12})\big] \dots \big[X(\alpha_{i-1,i}, a_{i-1,i})\big], \tag{2.12}$$

where, for example,

$$[A_{10}] = [G], \quad \text{and} \quad [A_{20}] = [G]\big[Z(\theta_{10}, d_{10})\big]\big[X(\alpha_{12}, a_{12})\big].$$

Now, insert the identity $[Z(\theta_{i,0})]^{-1}[A_{i0}]^{-1}[A_{i0}][Z(\theta_{i0})] = [I]$ after the first $n-1$ joint transforms $[Z(\theta_i, d_i)]$ in (2.11), in order to obtain the sequence of terms

$$\big[T(\Delta\theta_i, \mathsf{S}_i)\big] = [A_{i0}]\big[Z(\theta_i, d_i)\big]\big[Z(\theta_{i,0})\big]^{-1}[A_{i0}]^{-1} = [A_{i0}]\big[Z(\Delta\theta_i, \Delta d_i)\big][A_{i0}]^{-1}. \tag{2.13}$$

The result is the relative transformation that takes the form

$$\big[D(\Delta\boldsymbol{\theta})\big] = \big[T(\Delta\theta_1, \mathsf{S}_1)\big]\big[T(\Delta\theta_2, \mathsf{S}_2)\big]\ldots\big[T(\Delta\theta_n, \mathsf{S}_n)\big], \tag{2.14}$$

where S_i are the Plucker coordinates of each joint axis obtained by transforming the joint screw K to the world frame by the coordinate transformations defined in (2.13).

Using the exponential form the transformations $[T(\Delta\theta_i, \mathsf{S}_i)]$, we write the relative kinematics equations (2.14) as

$$\big[D(\Delta\boldsymbol{\theta})\big] = e^{\Delta\theta_1 S_1} e^{\Delta\theta_2 S_2} \ldots e^{\Delta\theta_n S_n}, \tag{2.15}$$

where the matrices S_i are defined as

$$S_i = A_{i0} K A_{i0}^{-1}. \tag{2.16}$$

The product of exponentials form of the kinematics equations (2.10) is now obtained as

$$[D] = \big[D(\Delta\boldsymbol{\theta})\big][D_0] = e^{\Delta\theta_1 S_1} e^{\Delta\theta_2 S_2} \ldots e^{\Delta\theta_n S_n}[D_0]. \tag{2.17}$$

The difference between this equation and (2.10) is that here the coordinates of the joint axes of the serial chain are defined in the world frame.

2.3 The Even Clifford Algebra $C^+(P^3)$

The Clifford algebra of the projective three space P^3 is a sixteen-dimensional vector space with a product operation that is defined in terms of a scalar product, see McCarthy (1990) [2]. The elements of even rank form an eight-dimensional subalgebra $C^+(P^3)$ that can be identified with the set of 4×4 homogeneous transforms.

The typical element of $C^+(P^3)$ can be written as the eight dimensional vector given by

$$\hat{A} = a_0 + a_1 i + a_2 j + a_3 k + a_4 \varepsilon + a_5 i\varepsilon + a_6 j\varepsilon + a_7 k\varepsilon, \tag{2.18}$$

where the basis elements i, j, and k are the well-known quaternion units, and ε is called the dual unit. The quaternion units satisfy the multiplication relations

$$i^2 = j^2 = k^2 = -1, \qquad ij = k,\ jk = i,\ ki = j, \quad \text{and} \quad ijk = -1. \tag{2.19}$$

The dual number ε commutes with i, j, and k, and multiplies by the rule $\varepsilon^2 = 0$.

In our calculations, it is convenient to consider the linear combination of quaternion units to be a vector in three dimensions, so we use the notation $\mathbf{A} = a_1 i + a_2 j + a_3 k$ and $\mathbf{A}^\circ = a_5 i + a_6 j + a_7 k$—the small circle superscript is often used to distinguish coefficients of the dual unit. This allows us to write the Clifford algebra element (2.18) as

$$\hat{A} = a_0 + \mathbf{A} + a_4\varepsilon + \mathbf{A}^\circ\varepsilon. \tag{2.20}$$

Now, collect the scalar and vector terms so this element takes the form

$$\hat{A} = (a_0 + a_4\varepsilon) + \left(\mathbf{A} + \mathbf{A}^\circ\varepsilon\right) = \hat{a} + \mathsf{A}. \tag{2.21}$$

The dual vector $\mathsf{A} = \mathbf{A} + \mathbf{A}^\circ\varepsilon$ can be identified with the pairs of vectors that define lines and screws.

Using this notation the Clifford algebra product of elements $\hat{A} = \hat{a} + \mathsf{A}$ and $\hat{B} = \hat{b} + \mathsf{B}$ takes the form

$$\hat{C} = (\hat{b} + \mathsf{B})(\hat{a} + \mathsf{A}) = (\hat{b}\hat{a} - \mathsf{B}\cdot\mathsf{A}) + (\hat{a}\mathsf{B} + \hat{b}\mathsf{A} + \mathsf{B}\times\mathsf{A}), \tag{2.22}$$

where the usual vector dot and cross products are extended linearly to dual vectors.

2.3.1 Exponential of a Vector

The product operation in the Clifford algebra allows us to compute the exponential of a vector $\theta\mathbf{S}$, where $|\mathbf{S}| = 1$, as

$$e^{\theta\mathbf{S}} = 1 + \theta\mathbf{S} + \frac{\theta^2}{2}\mathbf{S}^2 + \frac{\theta^3}{3!}\mathbf{S}^3 + \cdots. \tag{2.23}$$

Using (2.22) we can write $\mathbf{S} = 0 + \mathbf{S}$ and compute

$$\mathbf{S}^2 = (0+\mathbf{S})(0+\mathbf{S}) = -1, \qquad \mathbf{S}^3 = -\mathbf{S}, \qquad \mathbf{S}^4 = 1, \quad \text{and} \quad \mathbf{S}^5 = \mathbf{S}, \tag{2.24}$$

which means we have

$$\begin{aligned} e^{\theta\mathbf{S}} &= \left(1 - \frac{\theta^2}{2} + \frac{\theta^4}{4!} + \cdots\right) + \left(\theta - \frac{\theta^3}{3!} + \frac{\theta^5}{5!} + \cdots\right)\mathbf{S} \\ &= \cos\theta + \sin\theta\mathbf{S}. \end{aligned} \tag{2.25}$$

This is the well-known *unit quaternion* that represents a rotation around the axis $\mathbf{S}$ by the angle $\phi = 2\theta$. The rotation angle ϕ is double that given in the quaternion, because the Clifford algebra form of a rotation requires multiplication by both $Q = \cos\theta + \sin\theta\mathbf{S}$ and its conjugate $Q^* = \cos\theta - \sin\theta\mathbf{S}$. In particular, if $\mathbf{x}$ and $\mathbf{X}$ are the coordinates of a point before and after the rotation, then we have the quaternion coordinate transformation equation

$$\mathbf{X} = Q\mathbf{x}Q^*. \tag{2.26}$$

For this reason the quaternion is often written in terms of one-half the rotation angle, that is $Q = \cos\frac{\phi}{2} + \sin\frac{\phi}{2}\mathbf{S}$.

2.3.2 Exponential of a Screw

The Plücker coordinates $\mathsf{S} = (\mathbf{S}, \mathbf{C} \times \mathbf{S})$ of a line can be identified with the Clifford algebra element $\mathsf{S} = \mathbf{S} + \varepsilon \mathbf{C} \times \mathbf{S}$. Similarly, the screw $\mathsf{J} = (\mathbf{S}, \mathbf{V}) = (\mathbf{S}, \mathbf{C} \times \mathbf{S} + \mu \mathbf{S})$ becomes the element $\mathsf{J} = \mathbf{S} + \varepsilon \mathbf{V} = (1 + \mu\varepsilon)\mathsf{S}$. Using the Clifford product we can compute the exponential of the screw $\theta\mathsf{J}$,

$$e^{\theta \mathsf{J}} = 1 + \mathsf{J} + \frac{\theta^2}{2}\mathsf{J}^2 + \frac{\theta^3}{3!}\mathsf{J}^3 + \cdots . \tag{2.27}$$

Notice that $\mathsf{S}^2 = -1$, therefore

$$\begin{aligned} &\mathsf{J}^2 = -(1 + \mu\varepsilon)^2 = -(1 + 2\mu\varepsilon), \qquad \mathsf{J}^3 = -(1 + 3\mu\varepsilon)\mathsf{S}, \\ &\mathsf{J}^4 = 1 + 4\mu\varepsilon, \quad \text{and} \quad \mathsf{J}^5 = (1 + 5\mu\varepsilon)\mathsf{S}, \end{aligned} \tag{2.28}$$

and, we obtain

$$\begin{aligned} e^{\theta \mathsf{J}} &= \left(1 - \frac{\theta^2}{2} + \frac{\theta^4}{4!} + \cdots\right) + \left(\theta - \frac{\theta^3}{3!} + \frac{\theta^5}{5!} + \cdots\right)\mathsf{S} \\ &\quad - \theta\mu\varepsilon\left(\theta - \frac{\theta^3}{3!} + \cdots\right) + \theta\mu\varepsilon\left(1 - \frac{\theta^2}{2} + \cdots\right)\mathsf{S} \\ &= (\cos\theta - d\sin\theta\varepsilon) + (\sin\theta + d\cos\theta\varepsilon)\mathsf{S}. \end{aligned} \tag{2.29}$$

Let $d = \theta\mu$ be the slide along the screw axis associated with the angle θ. At this point it is convenient to introduce the dual angle $\hat{\theta} = \theta + d\varepsilon$, so we have the identities

$$\sin\hat{\theta} = \sin\theta + d\cos\theta\varepsilon, \quad \text{and} \quad \cos\hat{\theta} = \cos\theta - d\sin\theta\varepsilon, \tag{2.30}$$

which are derived using the series expansions of sine and cosine.

Equation (2.29) introduces the *unit dual quaternion* which is identified with spatial displacements. To see the relationship we factor out the rotation term to obtain

$$\hat{Q} = \cos\hat{\theta} + \sin\hat{\theta}\mathsf{S} = (1 + \mathbf{t}\varepsilon)(\cos\theta + \sin\theta\mathbf{S}), \tag{2.31}$$

where

$$\mathbf{t} = d\mathbf{S} + \sin\theta\cos\theta\mathbf{C} \times \mathbf{S} - \sin^2\theta(\mathbf{C} \times \mathbf{S}) \times \mathbf{S}. \tag{2.32}$$

This vector is one-half the translation $\mathbf{d} = 2\mathbf{t}$ of the spatial displacement associated with this dual quaternion in the same way that we saw that the rotation angle is $\phi = 2\theta$. This is because the Clifford algebra form of the transformation of line coordinates x to X by the rotation ϕ around an axis S with the translation $\mathbf{d}$ involves multiplication by both the Clifford algebra element $\hat{Q} = \cos\hat{\theta} + \sin\hat{\theta}\mathsf{S}$ and its conjugate $\hat{Q}^* = \cos\hat{\theta} - \sin\hat{\theta}\mathsf{S}$, given by

$$\mathsf{X} = \hat{Q}\mathsf{x}\hat{Q}^*. \tag{2.33}$$

For this reason the unit dual quaternion is usually written in terms of the half rotation angle and half displacement vector,

$$\hat{Q} = \cos\frac{\hat{\phi}}{2} + \sin\frac{\hat{\phi}}{2}\mathsf{S} = \left(1 + \frac{1}{2}\mathbf{d}\varepsilon\right)\left(\cos\frac{\phi}{2} + \sin\frac{\phi}{2}\mathbf{S}\right), \tag{2.34}$$

where

$$\mathbf{d} = 2\left(\frac{k}{2}\mathbf{S} + \sin\frac{\phi}{2}\cos\frac{\phi}{2}\mathbf{C}\times\mathbf{S} - \sin^2\frac{\phi}{2}(\mathbf{C}\times\mathbf{S})\times\mathbf{S}\right). \tag{2.35}$$

Notice that we introduced the slide along S given by $k = \phi\mu$, so we have the dual angle $\hat{\phi} = \phi + k\varepsilon$.

2.3.3 Clifford Algebra Kinematics Equations

The exponential of a screw defines a relative displacement from an initial position to a final position in terms of a rotation around and slide along an axis. This means the composition of Clifford algebra elements defines the relative kinematics equations for a serial chain that are equivalent to (2.15) [21].

Consider the nC serial chain in which each joint can rotate an angle θ_i around, and slide the distance d_i along, the axis S_i, for $i = 1, \ldots, n$. Let $\boldsymbol{\theta}_0$ and $\mathbf{d}_0$ be the joint parameters of this chain when in the reference configuration, so we have

$$\Delta\hat{\boldsymbol{\theta}} = (\boldsymbol{\theta} + \mathbf{d}\varepsilon) - (\boldsymbol{\theta}_0 + \mathbf{d}_0\varepsilon) = (\Delta\hat{\theta}_1, \Delta\hat{\theta}_2, \ldots, \Delta\hat{\theta}_n). \tag{2.36}$$

Then, the movement from this reference configuration is defined by the kinematics equation,

$$\begin{aligned}\hat{D}(\Delta\hat{\boldsymbol{\theta}}) &= e^{\frac{\Delta\hat{\theta}_1}{2}\mathsf{S}_1} e^{\frac{\Delta\hat{\theta}_2}{2}\mathsf{S}_2}\cdots e^{\frac{\Delta\hat{\theta}_n}{2}\mathsf{S}_n} \\ &= \left(\mathrm{c}\frac{\Delta\hat{\theta}_1}{2} + \mathrm{s}\frac{\Delta\hat{\theta}_1}{2}\mathsf{S}_1\right)\left(\mathrm{c}\frac{\Delta\hat{\theta}_2}{2} + \mathrm{s}\frac{\Delta\hat{\theta}_2}{2}\mathsf{S}_2\right)\cdots\left(\mathrm{c}\frac{\Delta\hat{\theta}_n}{2} + \mathrm{s}\frac{\Delta\hat{\theta}_n}{2}\mathsf{S}_n\right).\end{aligned} \tag{2.37}$$

Note that s and c denote the sine and cosine functions, respectively.

2.4 Design Equations for a Serial Chain

The goal of our design problem is to determine the dimensions of a spatial serial chain that can position a tool held by its end-effector in a given set of task positions. The location of the base of the robot, the position of the tool frame, as well as the link dimensions and joint angles are considered to be design variables.

2.4.1 Specified Task Positions

Identify a set of task positions $[P_j]$, $j = 1, \ldots, m$. Then, the physical dimensions of the chain are defined by the requirement that for each position $[P_j]$ there is a joint parameter vector $\boldsymbol{\theta}_j$ such that the kinematics equations of the chain satisfy the relations

$$[P_j] = \left[D(\boldsymbol{\theta}_j)\right], \quad i = 1, \ldots, m. \tag{2.38}$$

Now, choose $[P_1]$ as the reference position and compute the relative displacements $[P_j][P_1^{-1}] = [P_{1j}]$, $j = 2, \ldots, m$.

For each of these relative displacements $[P_{1j}]$ we can determine the dual unit quaternion $\hat{P}_{1j} = \cos\frac{\Delta\hat{\phi}_{1j}}{2} + \sin\frac{\Delta\hat{\phi}_{1j}}{2}\mathsf{P}_{1j}$, $j = 2, \ldots, m$. The dual angle $\Delta\hat{\phi}_{1j}$ defines the rotation about and slide along the axis P_{1j} that defines the displacement from the first to the jth position. Now writing (2.37) for the $m-1$ relative displacements, we obtain

$$\hat{P}_{1j} = e^{\frac{\Delta\hat{\theta}_{1j}}{2}\mathsf{S}_1} e^{\frac{\Delta\hat{\theta}_{2j}}{2}\mathsf{S}_2} \cdots e^{\frac{\Delta\hat{\theta}_{nj}}{2}\mathsf{S}_n}, \quad j = 2, \ldots, m. \tag{2.39}$$

The result is $8(m-1)$ design equations. The unknowns are the n joint axes S_i, $i = 1, \ldots, n$, and the $n(m-1)$ pairs of joint parameters $\Delta\hat{\theta}_{ij} = \Delta\theta_{ij} + \Delta d_{ij}\varepsilon$.

2.4.2 The Independent Synthesis Equations

The eight components of the unit Clifford algebra kinematics equations (2.39) are not independent. It is easy to see that a dual unit quaternion satisfies the identity,

$$\hat{Q}\hat{Q}^* = e^{\frac{\Delta\hat{\phi}}{2}\mathsf{S}} e^{-\frac{\Delta\hat{\phi}}{2}\mathsf{S}} = 1, \tag{2.40}$$

which imposes a two constraints. Thus, only six of the eight synthesis equations obtained for each relative task position are independent, which means there are only $6(n-1)$ independent synthesis equations for an n position task. Furthermore, the axis S has unit magnitude with means that only four of its six components are independent.

In order to count the number of independent equations and unknowns in the Clifford algebra synthesis equations, it is useful to identify the relationship between the constraints on a dual unit quaternion and the constraints on the dual unit vector that generates it. Therefore, we take a moment as verify

Remark 2.1 (Normality Condition) The dual quaternion arising from the product of dual quaternions has unit magnitude if and only if each factor is the exponential of dual unit vector.

Proof For the screw displacement $\hat{Q} = e^{\frac{\Delta\hat{\phi}}{2}\mathsf{S}}$ the unit condition yields,

$$\hat{Q}\hat{Q}^* = \left(\mathrm{c}\frac{\Delta\hat{\phi}}{2} + \mathrm{s}\frac{\Delta\hat{\phi}}{2}\mathsf{S}\right)\left(\mathrm{c}\frac{\Delta\hat{\phi}}{2} - \mathrm{s}\frac{\Delta\hat{\phi}}{2}\mathsf{S}\right) = \mathrm{c}\frac{\Delta\hat{\phi}}{2}\mathrm{c}\frac{\Delta\hat{\phi}}{2} + \mathrm{s}\frac{\Delta\hat{\phi}}{2}\mathrm{s}\frac{\Delta\hat{\phi}}{2}\mathsf{S}\cdot\mathsf{S}. \quad (2.41)$$

Notice that, if $\mathsf{S}\cdot\mathsf{S} = 1$, then

$$\hat{Q}\hat{Q}^* = \mathrm{c}\frac{\Delta\hat{\phi}}{2}\mathrm{c}\frac{\Delta\hat{\phi}}{2} + \mathrm{s}\frac{\Delta\hat{\phi}}{2}\mathrm{s}\frac{\Delta\hat{\phi}}{2} = \mathrm{c}\frac{\Delta\phi}{2}^2 + \mathrm{s}\frac{\Delta\phi}{2}^2 = 1. \quad (2.42)$$

Now, for a dual quaternion obtained as the composition of transformations about n joint axes, we have

$$\hat{Q}\hat{Q}^* = \left(e^{\frac{\Delta\hat{\phi}_1}{2}\mathsf{S}_1}\ldots e^{\frac{\Delta\hat{\phi}_n}{2}\mathsf{S}_n}\right)\left(e^{\frac{\Delta\hat{\phi}_1}{2}\mathsf{S}_1}\ldots e^{\frac{\Delta\hat{\phi}_n}{2}\mathsf{S}_n}\right)^*. \quad (2.43)$$

Expand this product and use the associative property of the Clifford algebra to obtain

$$\hat{Q}\hat{Q}^* = e^{\frac{\Delta\hat{\phi}_1}{2}\mathsf{S}_1}\ldots\left(e^{\frac{\Delta\hat{\phi}_n}{2}\mathsf{S}_n}e^{\frac{-\Delta\hat{\phi}_n}{2}\mathsf{S}_n}\right)\ldots e^{\frac{-\Delta\hat{\phi}_1}{2}\mathsf{S}_1}, \quad (2.44)$$

such that the terms $e^{\frac{\Delta\hat{\phi}_n}{2}\mathsf{S}_n}e^{\frac{-\Delta\hat{\phi}_n}{2}\mathsf{S}_n} = 1$ when $\mathsf{S}_n\cdot\mathsf{S}_n = 1$. The result is

$$\hat{Q}\hat{Q}^* = 1 \quad \Longleftrightarrow \quad \mathsf{S}_i\cdot\mathsf{S}_i = 1, \quad i = 1\ldots,n. \quad (2.45)$$

□

This condition shows that six of the eight components of the dual quaternion kinematics equations combine with the normal conditions on the Plücker coordinates of the joint axes to define the minimum set of independent synthesis equations for the serial chain problem.

2.4.3 Counting the Equations and Unknowns

Consider a spatial serial chain that consists of r revolute joints and p prismatic joints. A purely prismatic joint is defined by the unit vector $\mathbf{S}$ that defines the slide direction, so it has two independent parameters. The revolute joint axis is defined by Plücker coordinate vectors, $\mathsf{S}_i = \mathbf{S} + \mathbf{C}\times\mathbf{S}\varepsilon$, that have four independent components due to the normal conditions

$$|\mathbf{S}| = 1 \quad \text{and} \quad \mathbf{S}\cdot(\mathbf{C}\times\mathbf{S}) = 0. \quad (2.46)$$

Thus, the joint axes that define this chain have $K = 6r + 3p$ components, minus $2r + p$ Plücker constraints, which yields $4r + 2p$ independent unknowns.

Revolute and prismatic joints each have a single joint parameter, either a rotation angle or slide distance, which means that our chain has $(r + p)(m - 1)$ unknown joint parameters that define the m relative positions.

Table 2.1 The number of task positions that determine the structural parameters for five degree-of-freedom serial chains

Chain	K	Task positions	Total equations
PRPRP	21	15	91
RPRPR	24	17	104
RRRRP	27	19	117
RRRRR	30	21	130

Subtracting the number of equations from the number of unknowns, we obtain

$$\begin{aligned} E &= 4r + 2p + (r + p)(m - 1) - 6(m - 1) \\ &= (3r + p + 6) + (r + p - 6)m, \end{aligned} \tag{2.47}$$

where E excess of unknowns over equations. This excess can be made to equal zero for chains with degree of freedom dof $= r + p \leq 5$, in which case we specify

$$m = \frac{3r + p + 6 - c}{6 - (r + p)}, \tag{2.48}$$

task positions. If fewer than this number of task positions are defined, or if the chain has six or more degrees of freedom, then we are free to select values for the excess design parameters. In (2.48) we have added c to denote any extra constraint that may be imposed on the axes. Table 2.1 presents the maximum number of positions that can be defined for some chains with 5 degrees of freedom.

It is interesting to notice that, because the composition of displacements has structure of semi-direct product, the rotations are obtained by operating rotations only. A specific counting scheme can be generated for the rotations by considering the first quaternion of the dual quaternion only. We obtain that the maximum number of task rotations is

$$m_R = \frac{3 + r}{3 - r}. \tag{2.49}$$

In some cases with $r = 1$ or 2, the rotation part of the design equations can be used to determine the directions of these axes independently. Perez and McCarthy [3] call these chains "orientation limited."

2.5 Assembling the Design Equations

The structure of the Clifford algebra design equations provides a systematic approach to assembling the design equations for a broad range of serial chains. The basic approach is to formulate the design equations for the nC serial chain, and then (i) restrict the joint variables to form prismatic or sliding joints, and (ii) impose geometric conditions on the axes to form universal or spherical joints or to account for specific geometry. The result is a systematic way of defining the design equations

for a broad range of chains. Here we present the procedure for the 3C serial chain, but it has been implemented in our numerical solver for the 2C, 4C and 5C cases, as well.

2.5.1 The 3C Chain

The Clifford algebra form of the relative kinematics equations for the 3C chain can be written as

$$\hat{D}(\Delta\hat{\boldsymbol{\theta}}) = \left(\mathrm{c}\frac{\Delta\hat{\theta}_1}{2} + \mathrm{s}\frac{\Delta\hat{\theta}_1}{2}\mathsf{S}_1\right)\left(\mathrm{c}\frac{\Delta\hat{\theta}_2}{2} + \mathrm{s}\frac{\Delta\hat{\theta}_2}{2}\mathsf{S}_2\right)\left(\mathrm{c}\frac{\Delta\hat{\theta}_3}{2} + \mathrm{s}\frac{\Delta\hat{\theta}_3}{2}\mathsf{S}_3\right), \quad (2.50)$$

where $\mathsf{S}_i = \mathbf{S}_i + \mathbf{S}_i^\circ\varepsilon$ define the joint axes in the reference position, and $\Delta\hat{\theta}_i = \Delta\theta_i + \Delta d_i$ define the rotation and slide of the cylindric joint around the ith axis.

Expand the right side of (2.50) using the Clifford product to obtain

$$\begin{aligned}\hat{D}(\Delta\hat{\boldsymbol{\theta}}) &= (\hat{\mathrm{c}}_1\hat{\mathrm{c}}_2 - \hat{\mathrm{s}}_1\hat{\mathrm{s}}_2\mathsf{S}_1\cdot\mathsf{S}_2 + \hat{\mathrm{s}}_1\hat{\mathrm{c}}_2\mathsf{S}_1 + \hat{\mathrm{c}}_1\hat{\mathrm{s}}_2\mathsf{S}_2 + \hat{\mathrm{s}}_1\hat{\mathrm{s}}_2\mathsf{S}_1\times\mathsf{S}_2)(\hat{\mathrm{c}}_3 + \hat{\mathrm{s}}_3\mathsf{S}_3)\\ &= \hat{\mathrm{c}}_1\hat{\mathrm{c}}_2\hat{\mathrm{c}}_3 - \hat{\mathrm{s}}_1\hat{\mathrm{s}}_2\hat{\mathrm{c}}_3\mathsf{S}_1\cdot\mathsf{S}_2 - \hat{\mathrm{s}}_1\hat{\mathrm{c}}_2\hat{\mathrm{s}}_3\mathsf{S}_1\cdot\mathsf{S}_3 - \hat{\mathrm{c}}_1\hat{\mathrm{s}}_2\hat{\mathrm{s}}_3\mathsf{S}_2\cdot\mathsf{S}_3\\ &\quad - \hat{\mathrm{s}}_1\hat{\mathrm{s}}_2\hat{\mathrm{s}}_3\mathsf{S}_1\times\mathsf{S}_2\cdot\mathsf{S}_3 + \hat{\mathrm{s}}_1\hat{\mathrm{c}}_2\hat{\mathrm{c}}_3\mathsf{S}_1 + \hat{\mathrm{c}}_1\hat{\mathrm{s}}_2\hat{\mathrm{c}}_3\mathsf{S}_2 + \hat{\mathrm{c}}_1\hat{\mathrm{c}}_2\hat{\mathrm{s}}_3\mathsf{S}_3\\ &\quad + \hat{\mathrm{s}}_1\hat{\mathrm{s}}_2\hat{\mathrm{c}}_3\mathsf{S}_1\times\mathsf{S}_2 + \hat{\mathrm{s}}_1\hat{\mathrm{c}}_2\hat{\mathrm{s}}_3\mathsf{S}_1\times\mathsf{S}_3 + \hat{\mathrm{c}}_1\hat{\mathrm{s}}_2\hat{\mathrm{s}}_3\mathsf{S}_2\times\mathsf{S}_3\\ &\quad + \hat{\mathrm{s}}_1\hat{\mathrm{s}}_2\hat{\mathrm{s}}_3\big((\mathsf{S}_1\times\mathsf{S}_2)\times\mathsf{S}_3 - (\mathsf{S}_1\cdot\mathsf{S}_2)\,\mathsf{S}_3\big). \end{aligned} \quad (2.51)$$

For convenience, we have introduced the notation $\hat{\mathrm{c}}_i = \cos\frac{\Delta\hat{\theta}_i}{2}$ and $\hat{\mathrm{s}}_i = \sin\frac{\Delta\hat{\theta}_i}{2}$.

Equation (2.51) can be written in matrix form to emphasize that it is the linear combination of the eight monomials formed as products of the joint angles, which we assemble into an array in reversed lexicographic order obtained by reading right to left,

$$\hat{\mathbf{V}} = (\hat{\mathrm{c}}_1\hat{\mathrm{c}}_2\hat{\mathrm{c}}_3, \hat{\mathrm{s}}_1\hat{\mathrm{c}}_2\hat{\mathrm{c}}_3, \hat{\mathrm{c}}_1\hat{\mathrm{s}}_2\hat{\mathrm{c}}_3, \hat{\mathrm{c}}_1\hat{\mathrm{c}}_2\hat{\mathrm{s}}_3, \hat{\mathrm{s}}_1\hat{\mathrm{s}}_2\hat{\mathrm{c}}_3, \hat{\mathrm{s}}_1\hat{\mathrm{c}}_2\hat{\mathrm{s}}_3, \hat{\mathrm{c}}_1\hat{\mathrm{s}}_2\hat{\mathrm{s}}_3, \hat{\mathrm{s}}_1\hat{\mathrm{s}}_2\hat{\mathrm{s}}_3)^T. \quad (2.52)$$

To do this, we must introduce the vector form of the dual unit quaternion $\hat{Q} = \cos\frac{\Delta\hat{\theta}}{2} + \sin\frac{\Delta\hat{\theta}}{2}\mathsf{S}$ given by

$$\hat{\mathbf{Q}} = \begin{Bmatrix} \sin\frac{\Delta\hat{\theta}}{2}(S_x + S_x^\circ\varepsilon)\\ \sin\frac{\Delta\hat{\theta}}{2}(S_y + S_y^\circ\varepsilon)\\ \sin\frac{\Delta\hat{\theta}}{2}(S_z + S_z^\circ\varepsilon)\\ \cos\frac{\Delta\hat{\theta}}{2}\end{Bmatrix} = \begin{Bmatrix}\sin\frac{\Delta\hat{\theta}}{2}\mathsf{S}\\ \cos\frac{\Delta\hat{\theta}}{2}\end{Bmatrix}. \quad (2.53)$$

Collecting terms in (2.51), we obtain the matrix equation

$$\hat{\mathbf{D}}(\Delta\hat{\boldsymbol{\theta}}) = \begin{bmatrix} 0 & \mathsf{S}_1 & \mathsf{S}_2 & \mathsf{S}_3 & \mathsf{S}_1 \times \mathsf{S}_1 & \mathsf{S}_1 \times \mathsf{S}_3 & \mathsf{S}_2 \times \mathsf{S}_3 & -(\mathsf{S}_1 \cdot \mathsf{S}_2)\,\mathsf{S}_3 + (\mathsf{S}_1 \times \mathsf{S}_2) \times \mathsf{S}_3 \\ 1 & 0 & 0 & 0 & -\mathsf{S}_1 \cdot \mathsf{S}_2 & -\mathsf{S}_1 \cdot \mathsf{S}_3 & -\mathsf{S}_2 \cdot \mathsf{S}_3 & -\mathsf{S}_1 \times \mathsf{S}_2 \cdot \mathsf{S}_3 \end{bmatrix} \hat{\mathbf{V}}. \tag{2.54}$$

The Clifford algebra notation is compact in that each column of this matrix actually forms a column of four dual coefficients, or eight real coefficients if we write the dual components of the dual quaternion after the real components, forming an eight-dimensional vector. Similarly, each of the monomials in $\hat{\mathbf{V}}$ expands into four real terms, which we can list as

$$\mathbf{N} = \left(\mathbf{V}, \frac{\Delta d_1}{2}\mathbf{V}, \frac{\Delta d_2}{2}\mathbf{V}, \frac{\Delta d_3}{2}\mathbf{V} \right), \tag{2.55}$$

where $\mathbf{V}$ is the array of real parts of $\hat{\mathbf{V}}$. Thus, (2.54) expands to an 8×32 matrix equation. The number k of joint variable monomials in an nC serial chain is given by

$$k = (n+1)2^n. \tag{2.56}$$

Thus, these equations become 8×12 for 2C, 8×80 for 4C and 8×192 for 5C chains.

The kinematics equations (2.54) can be used directly for the design of a 3C chain. In what follows, we specialize these equations to obtain design equations for a variety of special serial chains.

2.5.2 RCC, RRC and RRR Chains

The ith cylindric joint in the 3C chain is converted to a revolute joint simply by setting $\Delta d_i = 0$. This can be done in seven different ways to define three permutations of the RRC chain, three permutations of the RRC chain and the RRR chain [23–25].

For example, the monomials in (2.54) that define the RCC, CRC or CCR chains are given by

$$\begin{aligned} \text{RCC:} \quad & \mathbf{N} = \left(\mathbf{V}, \frac{\Delta d_2}{2}\mathbf{V}, \frac{\Delta d_3}{2}\mathbf{V} \right), \\ \text{CRC:} \quad & \mathbf{N} = \left(\mathbf{V}, \frac{\Delta d_1}{2}\mathbf{V}, \frac{\Delta d_3}{2}\mathbf{V} \right), \\ \text{CCR:} \quad & \mathbf{N} = \left(\mathbf{V}, \frac{\Delta d_1}{2}\mathbf{V}, \frac{\Delta d_2}{2}\mathbf{V} \right). \end{aligned} \tag{2.57}$$

Similarly, the RRC, RCR and CRR chains have the monomials

$$\begin{aligned} \text{RRC:} \quad & \mathbf{N} = \left(\mathbf{V}, \frac{\Delta d_3}{2}\mathbf{V} \right), \\ \text{RCR:} \quad & \mathbf{N} = \left(\mathbf{V}, \frac{\Delta d_2}{2}\mathbf{V} \right), \\ \text{CRR:} \quad & \mathbf{N} = \left(\mathbf{V}, \frac{\Delta d_1}{2}\mathbf{V} \right). \end{aligned} \tag{2.58}$$

Finally, the RRR chain is defined by the monomial list

$$\text{RRR:} \quad \mathbf{N} = \mathbf{V}. \tag{2.59}$$

Notice that if an nC chain is specialized to have r revolute joints, then the number of monomials is given by

$$k = (n - r + 1)2^n. \tag{2.60}$$

2.5.3 PCC, PPC and PPP Chains

A two-step process is required to convert the ith cylindric joint to a prismatic joint. The first step is to set $\Delta\theta_i = 0$. The second step consists of specializing the joint axis $\mathsf{S}_i = \mathbf{S}_i$, so that its dual part is zero. This latter constraint arises because the pure translation defined by a prismatic joint depends only on the direction, not the location in space, of its axis.

In order to define the monomials for the three permutations of the PCC chain, we introduce $\mathbf{W}_1 = (\mathrm{c}_1\mathrm{c}_2\mathrm{c}_3, \mathrm{c}_1\mathrm{s}_2\mathrm{c}_3, \mathrm{c}_1\mathrm{c}_2\mathrm{s}_3, \mathrm{c}_1\mathrm{s}_2\mathrm{s}_3)$, and similarly define $\mathbf{W}_2$ and $\mathbf{W}_3$, where the subscript i indicates that we make $s_i = 0$. This allows us to define the arrays of monomials,

$$\begin{aligned} \text{PCC:} \quad & \mathbf{N} = \left(\mathbf{W}_1, \frac{\Delta d_1}{2}\mathbf{W}_1, \frac{\Delta d_2}{2}\mathbf{W}_1, \frac{\Delta d_3}{2}\mathbf{W}_1 \right), \\ \text{CPC:} \quad & \mathbf{N} = \left(\mathbf{W}_2, \frac{\Delta d_1}{2}\mathbf{W}_2, \frac{\Delta d_2}{2}\mathbf{W}_2, \frac{\Delta d_3}{2}\mathbf{W}_2 \right), \\ \text{CCP:} \quad & \mathbf{N} = \left(\mathbf{W}_3, \frac{\Delta d_1}{2}\mathbf{W}_3, \frac{\Delta d_2}{2}\mathbf{W}_3, \frac{\Delta d_3}{2}\mathbf{W}_3 \right). \end{aligned} \tag{2.61}$$

The monomials for the three permutations of the PPC chain are easily determined by introducing the set of monomials $\mathbf{W}_{12} = (\mathrm{c}_1\mathrm{c}_2\mathrm{c}_3, \mathrm{c}_1\mathrm{c}_2\mathrm{s}_3)$, and similarly $\mathbf{W}_{13}$

Table 2.2 Constraints that specialize C-joints to R, P, T and S joints

Joint	Axes	Constraints
R	S_i	$\Delta d_i = 0$
P	S_i	$\Delta\theta_i = 0$
C	S_i	None
T	$\mathsf{S}_i, \mathsf{S}_{i+1}$	$\Delta d_i = 0$, $\Delta d_{i+1} = 0$, $\mathsf{S}_i \cdot \mathsf{S}_{i+1} = 0$
S	$\mathsf{S}_i, \mathsf{S}_{i+1}, \mathsf{S}_{i+2}$	$\Delta d_i = 0$, $\Delta d_{i+1} = 0$, $\Delta d_{i+2} = 0$ $\mathsf{S}_i \cdot \mathsf{S}_{i+1} = 0$, $\mathsf{S}_{i+1} \cdot \mathsf{S}_{i+2} = 0$, $\mathsf{S}_i \cdot \mathsf{S}_{i+2} = 0$

and $\mathbf{W}_{23}$,

$$\begin{aligned}
\text{PPC:} \quad & \mathbf{N} = \left(\mathbf{W}_{12}, \frac{\Delta d_1}{2}\mathbf{W}_{12}, \frac{\Delta d_2}{2}\mathbf{W}_{12}, \frac{\Delta d_3}{2}\mathbf{W}_{12} \right), \\
\text{PCP:} \quad & \mathbf{N} = \left(\mathbf{W}_{13}, \frac{\Delta d_1}{2}\mathbf{W}_{13}, \frac{\Delta d_2}{2}\mathbf{W}_{13}, \frac{\Delta d_3}{2}\mathbf{W}_{13} \right), \\
\text{CPP:} \quad & \mathbf{N} = \left(\mathbf{W}_{23}, \frac{\Delta d_1}{2}\mathbf{W}_{23}, \frac{\Delta d_2}{2}\mathbf{W}_{23}, \frac{\Delta d_3}{2}\mathbf{W}_{23} \right).
\end{aligned} \tag{2.62}$$

Finally, the PPP chain is defined by the monomial list

$$\text{PPP:} \quad \mathbf{N} = \left((\mathrm{c}_1\mathrm{c}_2\mathrm{c}_3), \frac{\Delta d_1}{2}(\mathrm{c}_1\mathrm{c}_2\mathrm{c}_3), \frac{\Delta d_2}{2}(\mathrm{c}_1\mathrm{c}_2\mathrm{c}_3), \frac{\Delta d_3}{2}(\mathrm{c}_1\mathrm{c}_2\mathrm{c}_3) \right). \tag{2.63}$$

The number of monomials in an nC chain with p of the joints restricted to be prismatic is seen to be

$$k = (n+1)2^{n-p}. \tag{2.64}$$

Table 2.2 summarizes the constraints needed to transform the C joint into the most common types of joints. Notice that, for the spherical joint and other special cases, we use the approach of adding constraints between consecutive joint axes. This will not yield the minimum set of joint parameters, but it gives satisfactory results with the numerical solver.

This approach to the formulation of the design equations for special cases of the CCC chain can be extended to any nC chain [22].

2.6 The Synthesis of 5C and Related Chains

In this section, we present a numerical synthesis algorithm which uses the Clifford algebra exponential design equations for the 5C serial chain, see Fig. 2.2. The special cases of this chain include robots with up to five joints and up to ten degrees of freedom.

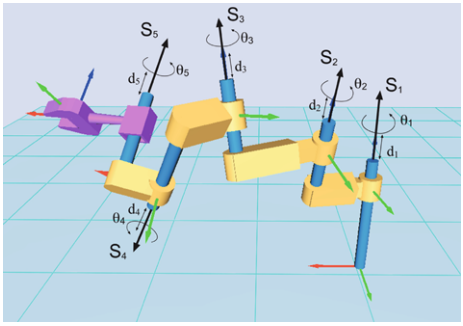

Fig. 2.2 The 5C serial robot

The design equations for a specific serial robot are be obtained from the 5C robot equations by imposing conditions on some of the axes or joint variables. The kinematics equations for the 5C robot are given by

$$\hat{Q}_{5C} = e^{\frac{\Delta\hat{\theta}_1}{2}\mathsf{S}_1} e^{\frac{\Delta\hat{\theta}_2}{2}\mathsf{S}_2} e^{\frac{\Delta\hat{\theta}_3}{2}\mathsf{S}_3} e^{\frac{\Delta\hat{\theta}_4}{2}\mathsf{S}_4} e^{\frac{\Delta\hat{\theta}_5}{2}\mathsf{S}_5}, \tag{2.65}$$

or

$$\hat{Q}_{5C} = \left(\cos\frac{\Delta\hat{\theta}_1}{2} + \sin\frac{\Delta\hat{\theta}_1}{2}\mathsf{S}_1\right)\left(\cos\frac{\Delta\hat{\theta}_2}{2} + \sin\frac{\Delta\hat{\theta}_2}{2}\mathsf{S}_2\right)\cdots$$
$$\left(\cos\frac{\Delta\hat{\theta}_5}{2} + \sin\frac{\Delta\hat{\theta}_5}{2}\mathsf{S}_5\right). \tag{2.66}$$

The kinematics equations for a serial chain consisting of revolute R, prismatic P, universal T, cylindrical C or spherical S joints can be obtained from the 5C robot using the approach presented in the previous section. For example, the kinematics equation of the TPR serial chain are obtained by requiring the axes S_1 and S_2 to be perpendicular and coincident, which is obtained by setting the joint variables d_1, d_2, θ_3 and d_4 to zero. The extra joint is eliminated by setting θ_5 and d_5 to zero. Other joints, like the helical H or planar E joints can also be modeled by imposing constraints on the axes and joint parameters.

In order to facilitate the specialization of the general 5C robot to a specific serial chain topology,the kinematics equations are organized as a linear combination of the products of joint angles and slides, which form the *monomials* of these equations with coefficients that are given by the structural parameters of the chain. In this way, the kinematics equations of the 5C serial chain is a linear combination of 192 monomials, which can be organized into six sets of 32 products of sines and cosines of the $\Delta\theta_i$ joint angles, given by,

$$\mathbf{V} = \big(s_1s_2s_3s_4s_5, (s_1s_2s_3s_4c_5)_5, (s_1s_2s_3c_4c_5)_{10}, (s_1s_2c_3c_4c_5)_{10},$$
$$(s_1c_2c_3c_4c_5)_5, c_1c_2c_3c_4c_5\big), \tag{2.67}$$

where $c_i = \cos\frac{\Delta\theta_i}{2}$, $s_i = \sin\frac{\Delta\theta_i}{2}$. The notation $()_j$ denotes j permutations of each set of sines and cosines. The remaining five sets of monomials are obtained by

multiplying $\mathbf{V}$ by the joint slides $\frac{\Delta d_i}{2}$, so we have a total set of monomials $\mathbf{N}$, where

$$\mathbf{N} = \left(\mathbf{V}, \frac{\Delta d_1}{2}\mathbf{V}, \frac{\Delta d_2}{2}\mathbf{V}, \frac{\Delta d_3}{2}\mathbf{V}, \frac{\Delta d_4}{2}\mathbf{V}, \frac{\Delta d_5}{2}\mathbf{V} \right). \tag{2.68}$$

The kinematics equations of the 5C robot can now be written as the linear combination,

$$\hat{Q}_{5C} = \sum_{i=1}^{192} \mathbf{K}_i m_i, \quad m_i \in \mathbf{N}. \tag{2.69}$$

The coefficients $\mathbf{K}_i$ are 8-dimensional vectors containing the structural variables defining the joint axes.

This equation is adjusted to accommodate a revolute or prismatic joints inserted as the jth joint axis by selecting the non-zero components of the vector $\mathbf{N}$. Notice if the jth C joint is restricted to be a revolute joint, then the slide Δd_j is zero, which eliminates 32 components in $\mathbf{N}$. Similarly, if this joint is replaced by a prismatic joint the angle becomes $\Delta\theta_j = 0$, which eliminates 16 terms from the vector $\mathbf{V}$.

In order to construct these equations start with the array $L_{5C} = \{1, 2, \ldots, 192\}$ of indices that denote the components of $\mathbf{N}$ for the general 5C chain, sorted as shown above. Next define the arrays L_{R_j}, L_{P_j} and L_{C_j} that denote the non-zero components of $\mathbf{N}$ for the cases when joint j is either a revolute, prismatic or cylindrical joint, given by

$$\begin{aligned}
L_{R_j} &= \left\{ i : \left(\cos\frac{\Delta\theta_j}{2} \wedge \sin\frac{\Delta\theta_j}{2} \right) \in m_i \vee \frac{\Delta d_j}{2} \notin m_i \right\}, \\
L_{P_j} &= \left\{ i : \left(\frac{\Delta d_j}{2} \wedge \cos\frac{\Delta\theta_j}{2} \right) \in m_i \vee \sin\frac{\Delta\theta_j}{2} \notin m_i \right\}, \\
L_{C_j} &= \left\{ i : \left(\frac{\Delta d_j}{2} \wedge \cos\frac{\Delta\theta_j}{2} \wedge \sin\frac{\Delta\theta_j}{2} \right) \in m_i \right\},
\end{aligned} \tag{2.70}$$

where $\wedge$ and $\vee$ are the logical or, and operations, respectively. Finally, compute the array of indices L for a specific serial chain topology by intersecting the arrays obtained for all of the joints, that is,

$$L = \bigcap_{j=1}^{5} (L_{R_j} \cup L_{P_j} \cup L_{C_j}), \tag{2.71}$$

where $L_{P_j} = \emptyset$ and $L_{C_j} = \emptyset$ if j is a revolute joint, for example.

The kinematics equations for the specific serial chain is now given by

$$\hat{Q} = \sum_{i \in L} \mathbf{K}_i m_i. \tag{2.72}$$

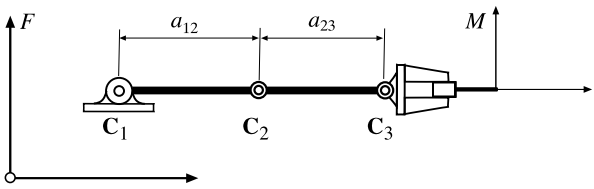

Fig. 2.3 A planar 3R chain in the reference configuration

The synthesis equations for the chain are obtained by equating the kinematics equations in (2.72) to the set of task positions $\hat{P}_{1i}$, that is

$$\hat{Q} = \hat{P}_{1i}, \quad i = 2, \ldots, m, \tag{2.73}$$

where the maximum number of task positions, m, is obtained for the chosen topology using (2.48) and (2.49). Additional constraint equations may be added to account for the specialized geometry of T and S joints or for any other geometric constraint present in the robot.

These synthesis equations are solved to determine the joint axes S_i in the reference configuration, as well as for values for the joint variables that ensure that the serial chain reaches each of the task positions.

2.6.1 The Synthesis Process

It is possible to automate the generation of the synthesis equations as cases of the four classes of 2C, 3C, 4C and 5C related serial chains. The synthesis equations can then be solved numerically given a random start value. The input data consists of a set of task positions and topology of the serial chain. The topology of the chains is used to construct its kinematics equations $\hat{Q}$. These equations are set equal to the task positions $\hat{P}_{1i}$ to yield the synthesis equations as the difference $\hat{Q} - \hat{P}_{1i}$, $i = 2, \ldots, m$. The numerical solver finds values for the components of the joint axes and joint variables that minimize this difference.

It is not necessary that the numerical solver use the minimum set of design equations as defined by (2.48). In fact, it is convenient to use all $8(m-1)+c$ synthesis equations. For the cases of 3R, 4R and 5R serial chains this approach introduces two, eight and 30 redundant equations, respectively. Experience shows that the additional equations enhance the convergence of the numerical algorithm.

2.7 Planar Serial Chains

We now specialize the kinematics equations defined above to the case of planar serial chains. It is convenient for our purposes to focus on chains consisting only of revolute joints, the nR chain [22].

The Plucker coordinates of the axis of a typical revolute joint in a planar chain are given by $\mathsf{J} = (\mathbf{k}, \mathbf{C} \times \mathbf{k})$, where $\mathbf{k} = (0, 0, 1)$ is directed along the z-axis of the base frame, and $\mathbf{C} = (c_x, c_y, 0)$ is the point of intersection of this axis with the x-y plane. The associated twist matrix $\hat{J}$ is

$$\hat{J} = \begin{bmatrix} 0 & -1 & 0 & -c_y \\ 1 & 0 & 0 & c_x \\ 0 & 0 & 0 & 0 \\ 0 & 0 & 0 & 0 \end{bmatrix}. \tag{2.74}$$

Let the transformation to the base of the chain be a translation by the vector $\mathbf{G} = (g_x, g_y, 0)$, then he zero configuration of the nR planar chain has the points $\mathbf{C}_i$, $i = 1, \ldots, n$ on the joint axes J_i distributed along a line parallel to x-axis (see Fig. 2.3), such that

$$\begin{aligned} \mathbf{C}_1 &= \begin{Bmatrix} g_x \\ g_y \\ 0 \end{Bmatrix}, \qquad \mathbf{C}_2 = \begin{Bmatrix} g_z + a_{12} \\ g_y \\ 0 \end{Bmatrix}, \quad \ldots, \\ \mathbf{C}_n &= \begin{Bmatrix} g_x + a_{12} + a_{23} + \cdots + a_{n-1,n} \\ g_y \\ 0 \end{Bmatrix}. \end{aligned} \tag{2.75}$$

Substituting these points into (2.74) we obtain a twist matrix $\hat{J}_i$ for each revolute joint, and the product of exponentials kinematics equations

$$\big[D(\boldsymbol{\theta})\big] = e^{\Delta\theta_1 \hat{J}_1} e^{\Delta\theta_2 \hat{J}_2} \ldots e^{\Delta\theta_n \hat{J}_n} [D_0]. \tag{2.76}$$

The zero frame transformation $[D_0]$ can be define by introducing $[C]$ which is the translation by the vector $\mathbf{c} = (a_{12} + a_{23} + \cdots + a_{n-1,n})\boldsymbol{\imath}$ along the chain in the zero configuration, so we have

$$[D_0] = [G][C][H]. \tag{2.77}$$

The matrix exponential defining the rotation about J by the angle $\Delta\theta$ can be computed using formulas in Murray et al. (1994) [4] to yield,

$$e^{\Delta\theta \hat{J}} = \begin{bmatrix} \cos\Delta\theta & -\sin\Delta\theta & 0 & (1-\cos\Delta\theta)c_x + \sin\Delta\theta c_y \\ \sin\Delta\theta & \cos\Delta\theta & 0 & -\sin\Delta\theta c_x + (1-\cos\Delta\theta)c_y \\ 0 & 0 & 1 & 0 \\ 0 & 0 & 0 & 1 \end{bmatrix}. \tag{2.78}$$

This matrix defines a displacement consisting of a planar rotation about the point $\mathbf{C}$, called the *pole of the displacement*.

2.7.1 Complex Number Kinematics Equations

It is convenient at this point to introduce the complex numbers $e^{i\Delta\theta} = \cos\Delta\theta + i\sin\Delta\theta$ and $\mathbf{C} = c_x + ic_y$ to simplify the representation of the displacement (2.78).

Let $\mathbf{X}_1 = x + iy$ be the coordinates of a point in the world frame in the first position and $\mathbf{X}_2 = X + iY$ be its coordinates in the second position, then this transformation becomes

$$\mathbf{X}_2 = e^{i\Delta\theta}\mathbf{X}_1 + \big(1 - e^{i\Delta\theta}\big)\mathbf{C}. \tag{2.79}$$

The complex numbers $[e^{i\Delta\theta}, (1 - e^{i\Delta\theta})\mathbf{C}]$ define the rotation and translation, that form the planar displacement $e^{\Delta\theta\hat{J}}$. The point $\mathbf{C}$ is the pole of the displacement, and the translation vector $\mathbf{D}$ associated with this displacement is given by

$$\mathbf{D} = \big(1 - e^{i\Delta\theta}\big)\mathbf{C}. \tag{2.80}$$

The composition of the exponentials $e^{\theta_1\hat{C}_1}$ and $e^{\theta_2\hat{C}_2}$ that define rotations about the points $\mathbf{C}_1$ and $\mathbf{C}_2$, respectively, yields

$$\begin{aligned} e^{\phi\hat{P}} &= e^{\theta_1\hat{C}_1}e^{\theta_2\hat{C}_2}, \quad \text{or} \\ \big[e^{i\phi}, \big(1 - e^{i\phi}\big)\mathbf{P}\big] &= \big[e^{i\theta_1}, \big(1 - e^{i\theta_1}\big)\mathbf{C}_1\big]\big[e^{i\theta_2}, \big(1 - e^{i\theta_2}\big)\mathbf{C}_2\big] \\ &= \big[e^{i(\theta_1+\theta_2)}, \big(1 - e^{i\theta_1}\big)\mathbf{C}_1 + e^{i\theta_1}\big(1 - e^{i\theta_2}\big)\mathbf{C}_2\big]. \end{aligned} \tag{2.81}$$

Here $\mathbf{P}$ denotes the pole of the composite displacement.

The complex form of the relative kinematics equations (2.15) is seen to be

$$\big[D(\Delta\boldsymbol{\theta})\big] = \big[e^{i\Delta\theta_1}, \big(1 - e^{i\Delta\theta_1}\big)\mathbf{C}_1\big]\big[e^{i\Delta\theta_2}, \big(1 - e^{i\Delta\theta_2}\big)\mathbf{C}_2\big]\ldots\big[e^{i\Delta\theta_n}, \big(1 - e^{i\Delta\theta_n}\big)\mathbf{C}_n\big]. \tag{2.82}$$

If we define the relative displacement of the end-effector to be $[D] = [e^{i\Delta\phi}, (1 - e^{i\Delta\phi})\mathbf{P}]$, then we can expand this equation and equate the rotation and translation components to obtain,

$$\begin{aligned} e^{i\Delta\phi} &= e^{i\Delta\theta_1}e^{i\Delta\theta_2}\ldots e^{i\Delta\theta_n} = e^{i(\Delta\theta_1+\Delta\theta_2+\cdots+\Delta\theta_n)}, \\ \big(1 - e^{i\Delta\phi}\big)\mathbf{P} &= \big(1 - e^{i\Delta\theta_1}\big)\mathbf{C}_1 + e^{i\Delta\theta_1}\big(1 - e^{i\Delta\theta_2}\big)\mathbf{C}_2 + \cdots \\ &\quad + e^{i(\Delta\theta_1+\Delta\theta_2+\cdots+\Delta\theta_{n-1})}\big(1 - e^{i\Delta\theta_n}\big)\mathbf{C}_n. \end{aligned} \tag{2.83}$$

These complex vector equations can be used to design planar nR serial chains. We will see shortly that they are exactly Sandor and Erdman's standard form equations. However, in the next section we introduce an equivalent set of design equations using the Clifford algebra form of the kinematics equations.

2.8 The Even Clifford Algebra $C^+(P^2)$

The even Clifford algebra of the projective plane P^2 is a generalization of complex numbers. It is a vector space with a product operation that is linked to a scalar product. The elements of this Clifford algebra can be identified with the complex vectors that define points in the plane, and with rotations and translations of these coordinates. Our goal is a structure for the design equations that facilitates treating the relative joint angles as design parameters and can be generalized to the design of spatial serial chains [3].

Using homogeneous coordinates of points in the projective plane as the vectors and a degenerate scalar product, we obtain an eight dimensional Clifford algebra, $C(P^2)$. See McCarthy (1990) [2]. This Clifford algebra has an even sub-algebra, $C^+(P^2)$, which is a set of four dimensional elements of the form

$$A = a_1 i\varepsilon + a_2 j\varepsilon + a_3 k + a_4. \tag{2.84}$$

The basis elements $i\varepsilon$, $j\varepsilon$, k and 1 satisfy the following multiplication table,

	$i\varepsilon$	$j\varepsilon$	k	1
$i\varepsilon$	0	0	$-j\varepsilon$	$i\varepsilon$
$j\varepsilon$	0	0	$i\varepsilon$	$j\varepsilon$
k	$j\varepsilon$	$-i\varepsilon$	-1	k
1	$i\varepsilon$	$j\varepsilon$	k	1

(2.85)

Notice that the set of Clifford algebra elements $\mathbf{z} = x + ky$ formed using the basis element k ($k^2 = -1$) is isomorphic to the usual set of complex numbers. This means that we have $e^{k\theta} = \cos\theta + k\sin\theta$.

Translation by the vector $\mathbf{d} = d_x + kd_y$ and rotation by the angle ϕ are represented by the Clifford algebra elements

$$T(\mathbf{d}) = 1 + \frac{1}{2}\mathbf{d}i\varepsilon \quad \text{and} \quad R(\phi) = e^{k\phi/2}, \tag{2.86}$$

and a general planar displacement $D = T(\mathbf{d})R(\phi)$ is given by

$$D = \left(1 + \frac{1}{2}\mathbf{d}i\varepsilon\right)e^{k\phi/2}. \tag{2.87}$$

McCarthy (1993) [12] shows that a displacement defined to be a rotation by $\Delta\theta$ about a point $\mathbf{C}$ has the associated Clifford algebra element

$$D = \left(1 + \frac{1}{2}\left(1 - e^{k\Delta\theta}\right)\mathbf{C}i\varepsilon\right)e^{k\Delta\theta/2}, \tag{2.88}$$

which is the Clifford algebra version of the matrix exponential (2.78). Expand this equation to obtain the four dimensional vector

$$D = \frac{1}{2}\left(e^{-k\Delta\theta/2} - e^{k\Delta\theta/2}\right)\mathbf{C}i\varepsilon + e^{k\Delta\theta/2}$$

$$= -\sin\frac{\Delta\theta}{2}\mathbf{C}j\varepsilon + e^{k\Delta\theta/2}$$
$$= c_y \sin\frac{\Delta\theta}{2}i\varepsilon - c_x \sin\frac{\Delta\theta}{2}j\varepsilon + \sin\frac{\Delta\theta}{2}k + \cos\frac{\Delta\theta}{2}. \tag{2.89}$$

The components of this vector form the kinematic mapping used by Bottema and Roth (1979) [26] to study planar displacements. Also see DeSa and Roth (1981) [5] and Ravani and Roth (1983) [6].

2.8.1 Clifford Algebra Kinematics Equations

The relative kinematics equations of an nR planar chain (2.82) can be written in terms of the Clifford algebra elements (2.89) to define,

$$\begin{aligned} -\sin\frac{\Delta\phi}{2}\mathbf{P}j\varepsilon + e^{k\Delta\phi/2} = &\left(-\sin\frac{\Delta\theta_{1j}}{2}\mathbf{C}_1 j\varepsilon + e^{k\Delta\theta_1/2}\right) \\ &\times\left(-\sin\frac{\Delta\theta_2}{2}\mathbf{C}_2 j\varepsilon + e^{k\Delta\theta_2/2}\right) \\ &\cdots\left(-\sin\frac{\Delta\theta_n}{2}\mathbf{C}_n j\varepsilon + e^{k\Delta\theta_n/2}\right). \end{aligned} \tag{2.90}$$

Expand this equations and equate coefficients of the basis elements to obtain

$$\begin{aligned} e^{k\Delta\phi/2} &= e^{k(\Delta\theta_1+\Delta\theta_2+\cdots+\Delta\theta_n)/2}, \\ \sin\frac{\Delta\phi}{2}\mathbf{P} &= \sin\frac{\Delta\theta_1}{2}\mathbf{C}_1 e^{-k(\Delta\theta_2+\cdots+\Delta\theta_n)/2} + e^{k\Delta\theta_1/2}\sin\frac{\Delta\theta_2}{2}\mathbf{C}_2 e^{-k(\Delta\theta_3+\cdots+\Delta\theta_n)/2} \\ &\quad + \cdots + e^{k(\Delta\theta_1+\Delta\theta_2+\cdots+\Delta\theta_{n-1})/2}\sin\frac{\Delta\theta_n}{2}\mathbf{C}_n. \end{aligned} \tag{2.91}$$

These equations are equivalent to the complex vector equations presented above. In fact, multiplication of (2.91) by $e^{k\Delta\phi/2}$ directly yields (2.83), note we must replace k by in the usual complex number i.

2.9 Design Equations for the Planar nR Chain

The goal of our design problem is to determine the dimensions of the planar nR chain that can position a tool held by its end-effector in a given set of task positions. The location of the base of the robot, the position of the tool frame, as well as the link dimensions and joint angles are considered to be design variables [22].

2.9.1 Relative Kinematics Equations for Specified Task Positions

Identify a set of planar task positions $[P_j]$, $j = 1, \ldots, m$. Then, the physical dimensions of the chain are defined by the requirement that for each position $[P_j]$ there is a joint parameter vector $\boldsymbol{\theta}_j$ such that the kinematics equations of the chain yield

$$[P_j] = \big[D(\boldsymbol{\theta}_j)\big], \quad i = 1, \ldots, m. \tag{2.92}$$

Now, choose $[P_1]$ as the reference position and compute the relative displacements $[P_j][P_1^{-1}] = [P_{1j}]$, $j = 2, \ldots, m$. This formulation of the linkage design equations can be found in Suh and Racliffe (1978) [7]. The result is the relative kinematics equations

$$[P_{1j}] = e^{\Delta\theta_{1j}\hat{J}_1} e^{\Delta\theta_{2j}\hat{J}_2} \ldots e^{\Delta\theta_{nj}\hat{J}_n}, \quad j = 2, \ldots, m, \tag{2.93}$$

where

$$\Delta\boldsymbol{\theta}_j = \boldsymbol{\theta}_j - \boldsymbol{\theta}_1 = (\Delta\theta_{1j}, \ldots, \Delta\theta_{nj}).$$

The complex number form of (2.93) yields the equations

$$\begin{aligned} e^{i\Delta\phi_j} &= e^{i(\Delta\theta_{1j}+\Delta\theta_{2j}+\cdots+\Delta\theta_{nj})}, \\ \big(1 - e^{i\Delta\phi_j}\big)\mathbf{P}_{1j} &= \big(1 - e^{i\Delta\theta_{1j}}\big)\mathbf{C}_1 + e^{i\Delta\theta_{1j}}\big(1 - e^{i\Delta\theta_{2j}}\big)\mathbf{C}_2 + \cdots \\ &\quad + e^{i(\Delta\theta_{1j}+\Delta\theta_{2j}+\cdots+\Delta\theta_{n-1,j})}\big(1 - e^{i\Delta\theta_{nj}}\big)\mathbf{C}_n, \quad j = 2, \ldots, m, \end{aligned} \tag{2.94}$$

where $\Delta\phi_j = \phi_j - \phi_1$ and $\mathbf{P}_{1j}$ is the pole of the relative displacement $[P_{1j}]$. These are the equations we use to design the planar nR chain.

In terms of elements of the Clifford algebra we obtain the equivalent set of design equations,

$$\begin{aligned} e^{k\Delta\phi_j/2} &= e^{k(\Delta\theta_{1j}+\Delta\theta_{2j}+\cdots+\Delta\theta_{nj})/2}, \\ \sin\frac{\Delta\phi_j}{2}\mathbf{P}_{1j} &= \sin\frac{\Delta\theta_{1j}}{2}\mathbf{C}_1 e^{-k(\Delta\theta_{2j}+\cdots+\Delta\theta_{nj})/2} \\ &\quad + e^{k\Delta\theta_{1j}/2}\sin\frac{\Delta\theta_{2j}}{2}\mathbf{C}_2 e^{-k(\Delta\theta_{3j}+\cdots+\Delta\theta_{nj})/2} \\ &\quad + \cdots + e^{k(\Delta\theta_{1j}+\Delta\theta_{2j}+\cdots+\Delta\theta_{n-1,j})/2}\sin\frac{\Delta\theta_{nj}}{2}\mathbf{C}_n, \quad j = 2, \ldots, m. \end{aligned} \tag{2.95}$$

Equations (2.95) allow the introduction of $\sin\frac{\Delta\theta_{ij}}{2}$ and $\cos\frac{\Delta\theta_{ij}}{2}$ as algebraic unknowns so these equations can be solved for the various joint angles as well as the coordinates of the joints. This is demonstrated below in our algebraic solution of the five position synthesis of a 2R chain.

2.9.2 The Number of Design Positions and Free Parameters

If we specify m task positions, then (2.94) provide $m-1$ rotation and $2(m-1)$ translation equations. The unknowns consist of the $n(m-1)$ relative joint angles, and the $2n$ coordinates $\mathbf{C}_i$, $i = 1, \ldots, n$.

It is useful to notice that the rotation equations are solved independently, which means that they determine $m-1$ of the relative joint angles. Thus, we have $2(m-1)$ translation equations to solve for $(n-1)(m-1)$ joint variables and $2n$ coordinates $\mathbf{C}_i$, that is

$$E = 2n + (n-1)(m-1) - 2(m-1) = m(n-3) + n + 3, \tag{2.96}$$

where E excess of unknowns over equations.

Notice that except for $n = 1$ and $n = 2$ the excess of variables over equations is greater than zero. For $n = 1$, we see that $m = 2$ yields an exact formula for what is equivalent to the pole of a relative displacement. For $n = 2$, we find that an exact solution is possible for $m = 5$, which is Burmester's result that a 2R chain can be designed to reach five specified positions (Burmester 1886 [8], Hartenberg and Denavit 1964 [9]).

Now consider the case $n = 3$, which has six unknown coordinates $\mathbf{C}_i$, $i = 1, 2, 3$, and $2(m-1)$ joint variables that are determined by $2(m-1)$ equations. The excess is $E = 6$ no matter how many positions are specified. In order to formulate this design problem, we specify the $m-1$ relative joint angles around $\mathbf{C}_1$. This is equivalent to adding $m-1$ design equations, which means that (2.47) takes the form $E = 6-(m-1)$. The result is that given seven positions, $m = 7$, we obtain a set of equations that determine the six coordinates $\mathbf{C}_i$, $i = 1, 2, 3$.

2.9.3 The Standard Form Equations

The synthesis of planar 2R chains is the primary step in the design of four-bar linkages, which are constructed by joining the end links of two 2R chains to form the floating link, or coupler. Specializing the relative kinematics equations (2.94) to this case, we obtain

$$\begin{aligned} e^{i\Delta\phi_j} &= e^{i(\Delta\theta_{1j}+\Delta\theta_{2j})}, \\ \left(1-e^{i\Delta\phi_j}\right)\mathbf{P}_{1j} &= \left(1-e^{i\Delta\theta_{1j}}\right)\mathbf{C}_1 + e^{i\Delta\theta_{1j}}\left(1-e^{i\Delta\theta_{2j}}\right)\mathbf{C}_2, \quad j = 2, \ldots, m. \end{aligned} \tag{2.97}$$

We now show that this is the standard form equation used by Sandor and Erdman for planar mechanism synthesis.

The standard form equation is obtained by equating the relative displacement vector between two positions to the difference of vectors along the chain in the two

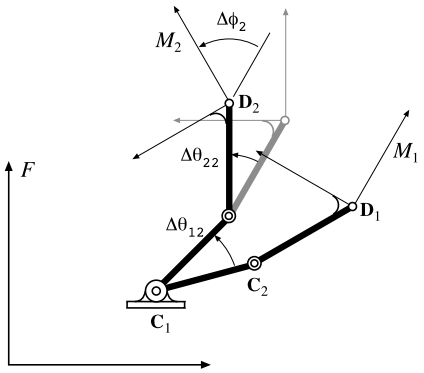

Fig. 2.4 Two positions of a planar 2R chain

positions. See Fig. 2.4. Let $\mathbf{C}_1$ be the fixed pivot and $\mathbf{C}_2$ the moving pivot when the tool frame of 2R chain is aligned with the first position.

Introduce the relative vectors $\mathbf{W} = \mathbf{C}_2 - \mathbf{C}_1$ and $\mathbf{Z} = \mathbf{D}_1 - \mathbf{C}_2$, where $\mathbf{D}_1$ is the translation vector to the first task position. We can now form the vector equations

$$\begin{aligned} \mathbf{D}_1 &= \mathbf{C}_1 + \mathbf{W} + \mathbf{Z}, \\ \mathbf{D}_2 &= \mathbf{C}_1 + \mathbf{W}e^{i\,\Delta\theta_{12}} + \mathbf{Z}e^{i(\Delta\theta_{12}+\Delta\theta_{22})}, \\ &\cdots \\ \mathbf{D}_m &= \mathbf{C}_1 + \mathbf{W}e^{i\,\Delta\theta_{1m}} + \mathbf{Z}e^{i(\Delta\theta_{1m}+\Delta\theta_{2m})}. \end{aligned} \tag{2.98}$$

Recall that multiplication by the complex exponential rotates a vector by an angle measured relative to the x-axis of the fixed frame.

Subtract the first equation from the remaining m to obtain

$$\delta_{1j} = \mathbf{W}\big(e^{i\,\Delta\theta_{1j}} - 1\big) + \mathbf{Z}\big(e^{i(\Delta\theta_{1j}+\Delta\theta_{2j})} - 1\big), \quad j = 2, \ldots, m, \tag{2.99}$$

where $\delta_{1j} = \mathbf{D}_j - \mathbf{D}_1$. Notice that the rotation of the jth task frame relative to the first position is

$$\Delta\phi_j = \Delta\theta_{1j} + \Delta\theta_{2j}. \tag{2.100}$$

Sandor and Erdman (1984) [11] call (2.99) the *standard form equation* and they use it to formulate a range of linkage synthesis problems based on the planar 2R chain.

Now substitute the definition of the relative vectors $\mathbf{W}$, $\mathbf{Z}$ and δ_{ij} back into the standard form equation to obtain

$$\mathbf{D}_j - \mathbf{D}_1 = (\mathbf{C}_2 - \mathbf{C}_1)\big(e^{i\,\Delta\theta_{1j}} - 1\big) + (\mathbf{D}_1 - \mathbf{C}_2)\big(e^{i(\Delta\theta_{1j}+\Delta\theta_{2j})} - 1\big),$$

and simplify to obtain

$$\mathbf{D}_j - \mathbf{D}_1 e^{i\,\Delta\phi_j} = \big(1 - e^{i\,\Delta\theta_{1j}}\big)\mathbf{C}_1 + e^{i\,\Delta\theta_{1j}}\big(1 - e^{i\,\Delta\theta_{2j}}\big)\mathbf{C}_2, \quad j = 1, \ldots, m. \tag{2.101}$$

In order to show that this equation is identical to (2.97) we compute the pole $\mathbf{P}_{1j}$ in terms of the translation vectors $\mathbf{D}_j$ and $\mathbf{D}_1$.

Let $[D_j] = [e^{i\phi_j}, \mathbf{D}_j]$, $j = 1, \ldots, m$, and compute

$$[D_{1j}] = [D_j][D_1]^{-1} = \left[e^{i(\phi_j - \phi_1)}, \mathbf{D}_j - \mathbf{D}_1 e^{i(\phi_j - \phi_1)}\right]. \tag{2.102}$$

Now the pole $\mathbf{P}_{1j}$ of this relative displacement is defined as the point that has the same coordinates before and after the displacement, which means it satisfies the condition

$$\mathbf{P}_{1j} = e^{i(\phi_j - \phi_1)}\mathbf{P}_{1j} + \mathbf{D}_j - \mathbf{D}_1 e^{i(\phi_j - \phi_1)}. \tag{2.103}$$

Thus, we obtain

$$\left(1 - e^{i\Delta\phi_j}\right)\mathbf{P}_{1j} = \mathbf{D}_j - \mathbf{D}_1 e^{\Delta\phi_j}, \tag{2.104}$$

and substituting this into (2.101), we find that the relative kinematics equations (2.97) are exactly Sandor and Erdman's standard form equations.

2.9.4 Synthesis of 3R Serial Chains

The planar 3R robot has three degrees of freedom and can reach any set of positions within its workspace boundary. The design equations for m task positions take the form

$$\begin{aligned} e^{i\Delta\phi_j} &= e^{i(\Delta\theta_{1j} + \Delta\theta_{2j} + \Delta\theta_{3j})}, \\ \left(1 - e^{i\Delta\phi_j}\right)\mathbf{P}_{1j} &= \left(1 - e^{i\Delta\theta_{1j}}\right)\mathbf{C}_1 + e^{i\Delta\theta_{1j}}\left(1 - e^{i\Delta\theta_{2j}}\right)\mathbf{C}_2 \\ &\quad + e^{i(\Delta\theta_{1j} + \Delta\theta_{2j})}\left(1 - e^{i\Delta\theta_{3j}}\right)\mathbf{C}_3, \quad j = 2, \ldots, m. \end{aligned} \tag{2.105}$$

We consider the design of this chain for three, five and seven task positions with the condition that the relative joint angles around $\mathbf{C}_1$ are specified by the designer.

Three Task Positions If we specify three task positions, the result is four translation design equations, or two complex equations, which determine the six coordinates of $\mathbf{C}_i$ and the $2(3-1) = 4$ relative joint angles around $\mathbf{C}_1$ and $\mathbf{C}_2$. The joint angles around $\mathbf{C}_3$ are determined by the rotation design equations.

If we specify the four unknown relative joint angles and $\mathbf{C}_1$, then these four design equations are linear in the coordinates of $\mathbf{C}_2$ and $\mathbf{C}_3$. The result is two complex linear equations in two complex unknowns,

$$\begin{aligned} \kappa_{12} &= e^{i\Delta\theta_{12}}\left(1 - e^{i\Delta\theta_{22}}\right)\mathbf{C}_2 + e^{i(\Delta\theta_{12} + \Delta\theta_{22})}\left(1 - e^{i\Delta\theta_{32}}\right)\mathbf{C}_3, \\ \kappa_{13} &= e^{i\Delta\theta_{13}}\left(1 - e^{i\Delta\theta_{23}}\right)\mathbf{C}_2 + e^{i(\Delta\theta_{13} + \Delta\theta_{23})}\left(1 - e^{i\Delta\theta_{33}}\right)\mathbf{C}_3, \end{aligned} \tag{2.106}$$

where κ_{1j} are the known complex numbers,

$$\kappa_{1j} = \left(1 - e^{i\Delta\phi_j}\right)\mathbf{P}_{1j} - \left(1 - e^{i\Delta\theta_{1j}}\right)\mathbf{C}_1. \tag{2.107}$$

Five Task Positions If five task positions are specified, then we have eight translation design equations in fourteen unknowns, the six coordinate $\mathbf{C}_i$ and eight relative joint angles. Now specify the coordinates of $\mathbf{C}_1$ and the four relative angles around it to define six parameters. The result is the four complex equations

$$\begin{aligned}
\kappa_{12} &= e^{i\Delta\theta_{12}}\left(1 - e^{i\Delta\theta_{22}}\right)\mathbf{C}_2 + e^{i(\Delta\theta_{12}+\Delta\theta_{22})}\left(1 - e^{i\Delta\theta_{32}}\right)\mathbf{C}_3, \\
&\cdots \\
\kappa_{15} &= e^{i\Delta\theta_{15}}\left(1 - e^{i\Delta\theta_{25}}\right)\mathbf{C}_2 + e^{i(\Delta\theta_{15}+\Delta\theta_{25})}\left(1 - e^{i\Delta\theta_{35}}\right)\mathbf{C}_3,
\end{aligned} \tag{2.108}$$

where κ_{1j} are known complex number defined by (2.107). These equations have exactly the same structure as Sandor and Erdman's standard form (2.101) for five position synthesis and are solved in the same way.

Seven Task Positions If seven task positions are specified as well as the six relative joint angles around $\mathbf{C}_1$, then we obtain 12 translation design equations in the twelve unknowns consisting of the six joint coordinates $\mathbf{C}_i$ and six relative joint angles around $\mathbf{C}_2$. The result is six complex equations

$$\begin{aligned}
\left(1 - e^{i\Delta\phi_2}\right)\mathbf{P}_{12} &= \left(1 - e^{i\Delta\theta_{12}}\right)\mathbf{C}_1 + e^{i\Delta\theta_{12}}\left(1 - e^{i\Delta\theta_{22}}\right)\mathbf{C}_2 \\
&\quad + e^{i(\Delta\theta_{12}+\Delta\theta_{22})}\left(1 - e^{i\Delta\theta_{32}}\right)\mathbf{C}_3, \\
&\cdots \\
\left(1 - e^{i\Delta\phi_7}\right)\mathbf{P}_{17} &= \left(1 - e^{i\Delta\theta_{17}}\right)\mathbf{C}_1 + e^{i\Delta\theta_{17}}\left(1 - e^{i\Delta\theta_{27}}\right)\mathbf{C}_2 \\
&\quad + e^{i(\Delta\theta_{17}+\Delta\theta_{27})}\left(1 - e^{i\Delta\theta_{37}}\right)\mathbf{C}_3.
\end{aligned} \tag{2.109}$$

This problem has been solved using matrix resultants by Lin and Erdman (1987) [13] and using homotopy continuation by Subbian and Flugrad (1994) [14].

2.9.5 Single DOF Coupled Serial Chains

Krovi et al. (2002) [15] expand the standard form equations to nR chains in which the joints are coupled by cable transmissions so the system has one degree of freedom. They call the chain a *single degree-of-freedom coupled serial chain*, or SDCSC. We formulate an equivalent form of their design equations using the relative kinematics equations (2.94).

Consider a planar nR serial chain in which each joint is connected to ground through a series of cables and pulleys located at each joint. Let each pulley have the same diameter and the cables routed through the links so they form parallelogram linkages. The result is n drive pulleys at the base of the chain that control the angle α_i of the ith link relative to the x-axis of the world frame, which means each joint angle is given by

$$\theta_i = \alpha_i - \alpha_{i-1}. \tag{2.110}$$

We now introduce a single drive angle β such that each joint angle is given by relation $\theta_i = R_i\beta$, where R_i denotes a constant speed ratio. The relations (2.110) yield the transmission matrix $[C]$ to the base drive angles are given by

$$\begin{Bmatrix} \alpha_1 \\ \alpha_2 \\ \vdots \\ \alpha_n \end{Bmatrix} = \begin{bmatrix} 1 & 0 & \cdots & 0 \\ 1 & 1 & \cdots & 0 \\ \vdots & & \cdots & \vdots \\ 1 & 1 & \cdots & 1 \end{bmatrix} \begin{bmatrix} R_1 \\ R_2 \\ \vdots \\ R_n \end{bmatrix} \beta, \tag{2.111}$$

or

$$\boldsymbol{\alpha} = [C][R]\beta, \tag{2.112}$$

where $[R]$ is the column matrix formed by the speed ratios. Our formulation differs slightly from Krovi et al. (2002) [15] in that we have added the drive variable β and therefore an additional speed ratio R_1.

Consider the design of an nR chain in which the speed ratios $R_i, i = 1, \ldots, n$, are specified. Substitute these speed ratios into the rotation term of the design equations (2.94) to obtain

$$e^{i\Delta\phi_j} = e^{i(R_1+R_2+\cdots+R_m)\Delta\beta_j}, \quad j = 2, \ldots, m, \tag{2.113}$$

where $\Delta\beta_j = \beta_j - \beta_1$ is the relative rotation of the drive angle. We find for each relative task position that

$$\Delta\beta_j = \frac{\Delta\phi_j}{R_1 + R_2 + \cdots + R_n}. \tag{2.114}$$

Substitute this into the translation terms of (2.94) to define a linear equation in the coordinates $\mathbf{C}_i, i = 1, \ldots, n$ for each relative task position,

$$\begin{aligned}\left(1 - e^{i\Delta\phi_j}\right)\mathbf{P}_{1j} = {} & \left(1 - e^{iR_1\Delta\beta j}\right)\mathbf{C}_1 + e^{iR_1\Delta\beta j}\left(1 - e^{iR_2\Delta\beta j}\right)\mathbf{C}_2 + \cdots \\ & + e^{i(R_1+R_2+\cdots+R_{n-1})\Delta\beta j}\left(1 - e^{iR_n\Delta\beta_j}\right)\mathbf{C}_n, \quad j = 2, \ldots, m.\end{aligned} \tag{2.115}$$

Given $m = n + 1$ task positions, we can solve these equations for the n complex unknowns $\mathbf{C}_i$. The result is a coupled serial nR chain designed to reach $n + 1$ arbitrarily specified task positions.

2.10 Reachable Surfaces

In this section, we consider the design of spatial serial chains that guide a body such that a point in the body moves on a specific algebraic surface. The problem originates with Schoenflies [16], who sought points that remained in a given configuration for a given set of spatial displacements. Burmester [8] applied this idea to

planar mechanism design by seeking the points in a planar moving body that remain on a circle. Chen and Roth [10] generalized this problem to find points and lines in a moving body that take positions on surfaces associated with the articulated chains used to build robot manipulators.

2.11 Spatial Serial Chains

For our purposes, we consider five degree-of-freedom spatial serial chains that include a spherical wrist. Thus, the reachable surface is traced by the point, **P**, at the wrist center of this chain under the movement of two remaining joints. Considering only, revolute and prismatic joints, we can enumerate the seven possibilities:

1. The PPS chain, for which the wrist center, **P**, lies on a plane—notice that the angle between the slide can be any angle α except zero, similarly the distance ρ between the slides can be any value because a prismatic joint guides all points in the body in the same direction;
2. The TS chain that has **P** on a sphere—recall the T joint is constructed from two perpendicular intersecting revolute joints, that is with link angle $\alpha = \pi/2$ and length $\rho = 0$;
3. The CS chain for which **P** lies on a cylinder—the C joint is constructed from a PR chain for which direction of the prismatic slide is parallel to the axis of the revolute joint, that is $\alpha = 0$, note ρ can be any value;
4. The RPS chain that guides **P** on the surface of a right circular hyperboloid—the link angle α can be any value except zero;
5. The PRS chain in which the angle between of the prismatic slide and the axis of the revolute is not zero guides **P** on an elliptic cylinder—the link angle α can be any value except zero;
6. The "right" RRS chain in which the revolute joints are perpendicular but do not intersect traces has **P** trace a right circular torus—the linkage angle $\alpha = \phi/2$; and
7. The general RRS chain in which the revolute joint axes are not perpendicular nor intersecting guides the wrist center on a general circular torus—the linkage angle cannot be $\alpha = 0, \pi/2$.

The result is seven articulated chains and the associated algebraic surfaces that are reachable by their wrist centers, Table 2.3. These algebraic equations of these surfaces can be used to formulate the synthesis equations for these seven spatial serial chains. In what follows, we determine the number of free parameters for each chain, the associated number of task positions that define these parameters, and assemble the synthesis equations. These equations can be solved using numerical homotopy.

Table 2.3 The basic serial chains and their associated reachable surfaces

Case	Chain	Angle	Length	Surface
1	PPS	$\alpha \neq 0$	ρ	Plane
2	TS	$\alpha = \pi/2$	$\rho = 0$	Sphere
3	CS	$\alpha = 0$	ρ	Circular cylinder
4	RPS	$\alpha \neq 0$	ρ	Circular hyperboloid
5	PRS	$\alpha \neq 0$	ρ	Elliptic cylinder
6	Right RRS	$\alpha = \pi/2$	ρ	Circular torus
7	RRS	α	ρ	General torus

2.11.1 Linear Product Decomposition

The synthesis equations for the seven spatial serial chains describe above result in polynomial systems of very high degree. Bezout's theorem states that the number of solutions to a polynomial system is less than or equal to the degree of the polynomial system, which is obtained by multiplying the degrees of each of the polynomials in the system. In what follows, we find that the synthesis equations of these serial chains have so much internal structure that the total degree over-estimates the number of solutions by two orders of magnitude.

In order to efficiently use numerical homotopy techniques to find all of the solutions to our synthesis equations, it is useful to have a better estimate for the number of solutions than the total degree. Here we present the linear product decomposition of a polynomial system and then use it to determine a bound on the number of solutions for each of our systems of synthesis equations. The linear product decomposition also serves as a convenient start system for numerical homotopy algorithms.

Morgan et al. [17] show that a "generic" system of polynomials that includes every monomial of a specified system of polynomials will have as many or more solutions as the specified polynomial system. The *linear product decomposition* of a specified system of polynomials is a way of constructing this generic polynomial system that includes all of the monomials of the specified system, so that it allows convenient computation of the number of roots. Each polynomial in the linear product decomposition consists of polynomials formed by the products of linear combinations of the variables and all of the monomials of the corresponding original polynomial.

Let $\langle x, y, 1\rangle$ represent the set of linear combinations of parameters x, y and 1, which means a typical term is $\alpha x + \beta y + \gamma \in \langle x, y, 1\rangle$, where α, β and γ are arbitrary constants. Using this notation, we define the product of $\langle x, y, 1\rangle\langle u, v, 1\rangle$ as the set of linear combinations of the product of the elements of the two sets, that is

$$\langle x, y, 1\rangle\langle u, v, 1\rangle = \langle xu, xv, yu, yv, x, y, u, v, 1\rangle. \tag{2.116}$$

This product commutes, which means $\langle x\rangle\langle y\rangle = \langle y\rangle\langle x\rangle$, and it distributes over unions, such that $\langle x\rangle\langle y\rangle \cup \langle x\rangle\langle z\rangle = \langle x\rangle(\langle y\rangle \cup \langle z\rangle) = \langle x\rangle\langle y, z\rangle$. Furthermore, we represent repeated factors using exponents, so $\langle x, y, 1\rangle\langle x, y, 1\rangle = \langle x, y, 1\rangle^2$.

In order to illustrate the construction of the linear product decomposition consider the synthesis equations of the TS chain presented in the previous chapter, given by

$$\left(\mathbf{P}^i - \mathbf{B}\right) \cdot \left(\mathbf{P}^i - \mathbf{B}\right) = R^2, \quad i = 1, \ldots, 7, \tag{2.117}$$

where the dot denotes the vector dot product. Now subtract the first equation from the rest in order to eliminate R^2. This reduces the problem to six equations in the unknowns $\mathbf{z} = (x, y, z, u, v, w)$, given by

$$\mathscr{S}_j(\mathbf{z}) = \left(\mathbf{P}^{j+1} \cdot \mathbf{P}^{j+1} - \mathbf{P}^1 \cdot \mathbf{P}^1\right) - 2\mathbf{B} \cdot \left(\mathbf{P}^{j+1} - \mathbf{P}^1\right) = 0, \quad j = 1, \ldots, 6. \tag{2.118}$$

We now focus attention on the monomials formed by the unknowns.

Recall that $\mathbf{P}^i = [A_i]\mathbf{p} + \mathbf{d}_i$ where $[A_i]$ and $\mathbf{d}_i$ are known, so it is easy to see that

$$2\mathbf{B} \cdot \left(\mathbf{P}^{j+1} - \mathbf{P}^1\right) \in \langle u, v, w\rangle\langle x, y, z, 1\rangle. \tag{2.119}$$

It is also possible to compute

$$\begin{aligned}\mathbf{P}^{j+1} \cdot \mathbf{P}^{j+1} - \mathbf{P}^1 \cdot \mathbf{P}^1 &= 2\mathbf{d}_{j+1} \cdot [A_{j+1}]\mathbf{p} - 2\mathbf{d}_1 \cdot [A_1]\mathbf{p} + \mathbf{d}_{j+1}^2 - \mathbf{d}_1^2 \\ &\in \langle x, y, z, 1\rangle. \end{aligned} \tag{2.120}$$

Thus, we find that each of the equations in (2.118) has the monomial structure given by

$$\langle x, y, z, 1\rangle \cup \langle u, v, w\rangle\langle x, y, z, 1\rangle \subset \langle x, y, z, 1\rangle\langle u, v, w, 1\rangle. \tag{2.121}$$

This allows us to construct a generic set of polynomials as a product of linear factors that contains our synthesis equations as a special case, that is

$$Q(\mathbf{z}) = \left\{ \begin{array}{c} (a_1x + b_1y + c_1z + d_1)(e_1u + f_1v + g_1w + h_1) \\ \vdots \\ (a_6x + b_6y + c_6z + d_6)(e_6u + f_6v + g_6w + h_6) \end{array} \right\} = 0, \tag{2.122}$$

where the coefficients are known constants. This is the *linear product decomposition* of the synthesis equations for the TS chain.

This linear product decomposition provides a convenient way to determine a bound on the number of solutions for the original polynomial system. This is done by assembling all combinations of the linear factors, one from each equation, that can be set to zero and solved for the unknown parameters. The number of combinations that yield solutions is the LPD bound for the original polynomial system.

In the example above, select three factors $a_ix + b_iy + c_iz + d_i = 0$ from the six equations, and combine this with the three factors $e_iu + f_iv + g_iw + h_i = 0$ in the remaining equations. A solution of this set of six linear equations is a root of (2.122). Thus, we find that this system has $\binom{6}{3} = 20$ solutions, which matches the known result for (2.118).

In the following sections, we determine the synthesis equations for each of the seven spatial serial chains with a reachable surface. We evaluate its total degree,

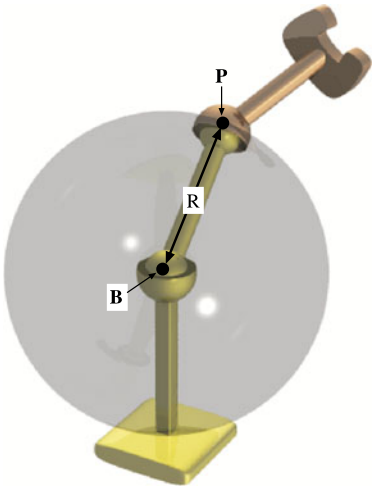

Fig. 2.5 A sphere traced by a point at the wrist center of a TS serial chain

compute its linear product decomposition bound, and then numerically solve a generic problem to find the number of articulated chains that reach a specified set of displacements.

2.11.2 The Sphere

We now return to our opening example in which a point $\mathbf{P} = (X, Y, Z)$ constrained to lie on a sphere of radius R around the point $\mathbf{B} = (u, v, w)$, Fig. 2.5. This means its coordinates satisfy the equation

$$(X-u)^2 + (Y-v)^2 + (Z-w)^2 - R^2 = (\mathbf{P}-\mathbf{B})^2 - R^2 = 0. \tag{2.123}$$

We now consider $\mathbf{P}^i$ to be the image of a point $\mathbf{p} = (x, y, z)$ in a moving frame M that takes positions in space defined by the displacements $\hat{\mathbf{Q}}_i$, $i = 1, \ldots, n$.

This problem has seven parameters, therefore we can evaluate (2.123) on $n = 7$ displacements. We reduced these equations to the set of six quadratic polynomials,

$$\mathscr{S}_j : \left(\mathbf{P}^{j+1\,2} - \mathbf{P}^{1\,2}\right) - 2\mathbf{B} \cdot \left(\mathbf{P}^{j+1} - \mathbf{P}^1\right) = 0, \quad j = 1, \ldots, 6. \tag{2.124}$$

This system has total degree of $2^6 = 64$.

We have already seen that the system (2.124) has the linear product decomposition

$$\mathscr{S}_j \in \langle x, y, z, 1\rangle \langle u, v, w, 1\rangle|_j = 0, \quad j = 1, \ldots, 6. \tag{2.125}$$

From this we can compute the LPD bound $\binom{6}{3} = 20$. Parameter elimination yields a univariate polynomial of degree 20, so we see that this bound is exact. Innocenti

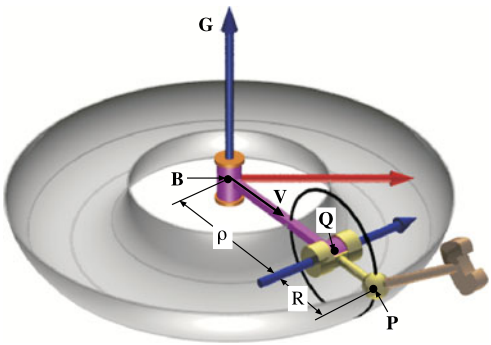

Fig. 2.6 The circular torus traced by the wrist center of a right RRS serial chain

[18] presents an example that results in 20 real roots. Also see Liao and McCarthy [19] and Raghavan [20].

The conclusion is that given seven arbitrary spatial positions there can be as many as 20 points in the moving body that have positions lying on a sphere. For each real point, it is possible to determine an associated TS chain.

2.11.3 The Circular Torus

A circular torus is generated by sweeping a circle around an axis so its center traces a second circle. Let the axis be $L(t) = \mathbf{B} + t\mathbf{G}$, with Plucker coordinates $\mathsf{G} = (\mathbf{G}, \mathbf{B} \times \mathbf{G})$. See Fig. 2.6. Introduce a unit vector $\mathbf{v}$ perpendicular to this axis so the center of the generating circle is given by $\mathbf{Q} - \mathbf{B} = \rho\mathbf{v}$. Now define $\mathbf{u}$ to be the unit vector in the direction $\mathbf{G}$, then a point $\mathbf{P}$ on the torus is defined by the vector equation,

$$\mathbf{P} - \mathbf{B} = \rho\mathbf{v} + R(\cos\phi\mathbf{v} + \sin\phi\mathbf{u}), \tag{2.126}$$

where ϕ is the angle measured from $\mathbf{v}$ to the radius vector of the generating circle.

An algebraic equation of the torus is obtained from (2.126) by first computing the magnitude

$$(\mathbf{P} - \mathbf{B})^2 = \rho^2 + R^2 + 2\rho R\cos\phi. \tag{2.127}$$

Next compute the dot product with $\mathbf{u}$, to obtain

$$(\mathbf{P} - \mathbf{B}) \cdot \mathbf{u} = R\sin\phi. \tag{2.128}$$

Finally, eliminate $\cos\phi$ and $\sin\phi$ from these equations, and the result is

$$\mathbf{G}^2\big((\mathbf{P} - \mathbf{B})^2 - \rho^2 - R^2\big)^2 + 4\rho^2\big((\mathbf{P} - \mathbf{B}) \cdot \mathbf{G}\big)^2 = 4\rho^2\mathbf{G}^2R^2. \tag{2.129}$$

This is the equation of a circular torus. It has 11 parameters, the scalars ρ and R, and the three vectors $\mathbf{G}$, $\mathbf{P}$ and $\mathbf{B}$.

In contrast to what we have done previously, here we set the magnitude of $\mathbf{G}$ to a constant, in order to simplify the polynomial (2.129),

$$\mathscr{G} : \mathbf{G} \cdot \mathbf{G} = 1. \tag{2.130}$$

Unfortunately, this doubles the number of solutions since $-\mathbf{G}$ and $\mathbf{G}$ define the same torus, however, it reduces this polynomial from degree sixth to degree four.

Let $[T_i] = [A_i, \mathbf{d}_i]$ be a specified set of displacements, so we have the 10 positions $\mathbf{P}^i = [T_i]\mathbf{p}$ of a point $\mathbf{p} = (x, y, z)$ that is fixed in the moving frame M. Evaluating (2.129) on these points, we obtain the polynomial system

$$\begin{aligned} &\mathscr{T}_i\colon \left(\left(\mathbf{P}^i - \mathbf{B}\right)^2 - \rho^2 - R^2\right)^2 + 4\rho^2\left(\left(\mathbf{P}^i - \mathbf{B}\right)\cdot \mathbf{G}\right)^2 - 4\rho^2 R^2 = 0, \quad i = 1, \ldots, 10, \\ &\mathscr{G}\colon \mathbf{G}\cdot\mathbf{G} - 1 = 0. \end{aligned} \tag{2.131}$$

The total degree of this system is $2(4^{10}) = 2{,}097{,}152$.

In order to simplify the polynomials $\mathscr{T}_i$ we introduce the parameters

$$\mathbf{H} = 2\rho\mathbf{G} \quad \text{and} \quad k_1 = \mathbf{B}^2 - \rho^2 - R^2, \tag{2.132}$$

which yields the identity

$$4\rho^2 R^2 = \mathbf{H}^2\left(\mathbf{B}^2 - \frac{\mathbf{H}^2}{4} - k_1\right). \tag{2.133}$$

Substitute these relations into $\mathscr{T}_i$ to obtain

$$\begin{aligned} &\mathscr{T}_i'\colon \left(\left(\mathbf{P}^i\right)^2 - 2\mathbf{P}^i\cdot\mathbf{B} + k_1\right)^2 + \left(\left(\mathbf{P}^i - \mathbf{B}\right)\cdot\mathbf{H}\right)^2 - \mathbf{H}^2\left(\mathbf{B}^2 - \frac{\mathbf{H}^2}{4} - k_1\right) = 0, \\ &\quad i = 1, \ldots, 10. \end{aligned} \tag{2.134}$$

It is difficult to find a simplified formulation for these equations, even if we subtract the first equation from the remaining in order to cancel terms.

Expanding the polynomial $\mathscr{T}_i'$ and examining each of the terms, we can identify the linear product decomposition

$$\mathscr{T}_i' \in \langle x, y, z, h_1, h_2, h_3, 1\rangle^2 \langle x, y, z, h_1, h_2, h_3, u, v, w, k_1, 1\rangle^2. \tag{2.135}$$

This allows us to compute the LPD bound on the number of roots as

$$\text{LPD} = 2^{10}\sum_{j=0}^{6}\binom{10}{j} = 868{,}352. \tag{2.136}$$

Our POLSYS_GLP algorithm obtained 94,622 real and complex solutions for a random set of specified displacements. However, this problem needs further study to provide an efficient way to evaluate and sort the large number of right RRS chains.

2.12 Summary

The exponential form of the kinematics equations of the chain are reformulated using Clifford algebra exponentials to obtain an efficient and systematic set of design equations. These design equations can be obtained as special cases of those for 2C, 3C, 4C and 5C serial chains. The solution process is demonstrated by determining the structural parameters of a CCS serial chain so that it reaches an arbitrarily specified 12 position task trajectory. While individual solutions can be obtained numerically, these synthesis equations have not yet been formulated for complete solution by numerical homotopy. The complexity of this problem is illustrated by 5R chain synthesis to reach 21 task positions, which requires the solution of 130 equations in 130 unknowns.

We have also formulated the synthesis equations the special cases of serial chains that can position a spherical wrist center on an algebraic surface. A linear product decomposition provides a bound for the number of solutions to these equations. We focus on the SS and RRS which show the challenges of solving the synthesis equations. While algebraic techniques yield 20 solutions for the SS chain, numerical homotopy was needed to compute the over 90,000 solutions for the RRS chain.

This chapter shows that we can derive the synthesis equations for spatial serial chains, however, they are complex and difficult to solve.

References

1. Gupta, K.C.: Kinematic analysis of manipulators using the zero reference position description. Int. J. Robot. Res. **5**(2), 5–13 (1986)
2. McCarthy, J.M.: An Introduction to Theoretical Kinematics. MIT Press, Cambridge (1990)
3. Perez, A., McCarthy, J.M.: Dual quaternion synthesis of constrained robotic systems. ASME J. Mech. Des. **126**(3), 425–435 (2004)
4. Murray, R.M., Li, X., Sastry, S.: A Mathematical Introduction to Robotic Manipulation. CRC Press, Boca Raton (1995)
5. De Sa, S., Roth, B.: Kinematic mappings. Part 2: rational algebraic motions in the plane. ASME J. Mech. Des. **103**, 712–717 (1981)
6. Ravani, B., Roth, B.: Motion synthesis using kinematic mapping. ASME J. Mech. Transm. Autom. Des. **105**(3), 460–467 (1983)
7. Suh, C.H., Radcliffe, C.W.: Kinematics and Mechanisms Design. Wiley, New York (1978)
8. Burmester, L.: Lehrbuch der Kinematik. Verlag Von Arthur Felix, Leipzig (1886)
9. Hartenberg, R.S., Denavit, J.: Kinematic Synthesis of Linkages. McGraw-Hill, New York (1964)
10. Chen, P., Roth, B.: Design equations for the finitely and infinitesimally separated position synthesis of binary links and combined link chains. ASME J. Eng. Ind. **91**, 209–219 (1969)
11. Sandor, G.N., Erdman, A.G.: Advanced Mechanism Design: Analysis and Synthesis, Vol. 2. Prentice-Hall, Englewood Cliffs (1984)
12. McCarthy, J.M.: 4.6: dual quaternions and the pole triangle. In: Erdman, A.G. (ed.) Forty Years of Modern Kinematics: A Tribute to Ferdinand Freudenstein. Wiley, New York (1993)
13. Lin, C.S., Erdman, A.G.: Dimensional synthesis of planar triads: motion generation with prescribed timing for six precision positions. Mech. Mach. Theory **22**(5), 411–419 (1987)
14. Subbian, T., Flugrad, D.R.: 6 and 7 position triad synthesis using continuation methods. J. Mech. Des. **116**(2), 660–665 (1994)

15. Krovi, V., Ananthasuresh, G.K., Kumar, V.: Kinematic and kinetostatic synthesis of planar coupled serial chain mechanisms. ASME J. Mech. Des. **124**(2), 301–312 (2002)
16. Schoenflies, A.: Geometrie der Bewegung in Synthetischer Darstellung, Leipzig (1886). (See also the French translation: La Géométrie du Mouvement, Paris, 1983)
17. Morgan, A.P., Sommese, A.J., Wampler, C.W.: A product-decomposition bound for Bezout numbers. SIAM J. Numer. Anal. **32**(4), 1308–1325 (1995)
18. Innocenti, C.: Polynomial solution of the spatial Burmester problem. Mechanism Synthesis and Analysis, ASME DE-Vol. 7 (1994)
19. Liao, Q., McCarthy, J.M.: On the seven position synthesis of a 5-SS platform linkage. ASME J. Mech. Des. **123**(1), 74–79 (2001)
20. Raghavan, M.: Suspension mechanism synthesis for linear toe curves. In: Proceedings for the Design Engineering Technical Conferences. Paper No. DETC2002/MECH-34305, Sept. 29–Oct. 2, Montreal, Canada (2002)
21. Perez-Gracia, A., McCarthy, J.M.: The kinematic synthesis of spatial serial chains using Clifford algebra exponentials. Proc. Inst. Mech. Eng., C J. Mech. Eng. Sci. **220**(7), 953–968 (2006). doi:10.1243/09544062JMES166
22. Perez, A., McCarthy, J.M.: Clifford algebra exponentials and planar linkage synthesis equations. ASME J. Mech. Des. **127**(5), 931–940 (2005). doi:10.1115/1.1904047
23. Lee, E., Mavroidis, C.: Solving the geometric design problem of spatial 3R robot manipulators using polynomial homotopy continuation. ASME J. Mech. Des. **124**(4), 652–661 (2002)
24. Lee, E., Mavroidis, C.: Geometric design of 3R manipulators for reaching four end-effector spatial poses. Int. J. Robot. Res. **23**(3), 247–254 (2004)
25. Perez, A., McCarthy, J.M.: Geometric design of RRP, RPR and PRR serial chains. Mech. Mach. Theory **40**(11), 1294–1311 (2005). doi:10.1016/j.mechmachtheory.2004.12.023
26. Bottema, O., Roth, B.: Theoretical Kinematics. Dover Publications, New York (1979)

Chapter 3
Synthesis of Spatial Mechanisms to Model Human Joints

Vincenzo Parenti-Castelli and Nicola Sancisi

3.1 Introduction

The study of human diarthrodial joints has involved efforts of an impressive number of researchers. Basic studies focused on experimental measurements of the relative motion of the main bones of the joint under investigation. The measurements performed in vitro (cadaver specimens) or in vivo (patients and volunteers) have the following various purposes:

- to test and validate measurement techniques [1, 6] as well as define standardization of diagnosis and rehabilitation procedures;
- to obtain a deeper knowledge on the behaviour of these joints which exhibit a quite complicated anatomical structure [28, 30];
- to validate and improve mathematical models of the articulations [29, 58].

Mathematical models are among the most powerful tools for the functional analysis of such a complicated biological structures and represent helpful tools for the solution of important issues such as, for instance:

- definition of surgical and diagnostic procedures for joint disorders caused by injuries or diseases;
- designing prosthesis devices [12, 19];
- assessment of the role of the joint biological structures in the joint characteristics in normal and pathological conditions [6].

V. Parenti-Castelli (✉)
DIEM—Department of Mechanical Engineering, HST-ICIR—Health Sciences and Technologies, University of Bologna, Viale del Risorgimento 2, 40136, Bologna, Italy
e-mail: vincenzo.parenti@unibo.it

N. Sancisi
DIEM—Department of Mechanical Engineering, University of Bologna, Viale del Risorgimento 2, 40136, Bologna, Italy
e-mail: nicola.sancisi@unibo.it

J.M. McCarthy (ed.), *21st Century Kinematics*,
DOI 10.1007/978-1-4471-4510-3_3,

Plane and spatial mathematical models of joints have been presented in the literature [23, 29, 58]. Plane models proved to be of great usefulness. However, for many joints they cannot take into account some complicated and subtle phenomena involved in the joint motion since most of them intrinsically have a three-dimensional motion.

The models presented in the literature are based on two different approaches. The first one models the biological structures of the joint connections such as ligaments, muscles, and articular surfaces by means of linear and non-linear elastic and dumping elements, lumped or distributed parameters, and finds the relative motion of the main bones by solving the equations of motion of the resulting model [1, 44, 56, 59]. The main bones are allowed to have up to six degrees of freedom (DOF) in their relative motion which finally depends on the external forces applied to the joint and on the elastic and dumping characteristics of the joint connecting structures. These models are computationally demanding but are also suitable to simulate the dynamic behaviour of the joint in addition to its kinematic and static behaviour.

The second approach, instead, models the joint as a linkage or an equivalent mechanism [29, 36, 58] whose geometry is based, as much as possible, on the joint anatomical structures. The motion of the mechanism predicts the relative motion of the joint main anatomical structures. These mechanisms are suitable to analyse the passive motion of the joint, that is, the motion of the joint under virtually unloaded conditions (no external loads), which is believed to have a great relevance for a deeper understanding of the joint kinematics [19]. Indeed, with regard to the knee joint, as reported in [6], the actual motion patterns of the human knee joint depend on a combination of its passive motion characteristics and the external loads. Examples of equivalent mechanisms with one or more DOFs have been proposed in the literature to account for the joint passive motion. Most of them are plane mechanisms and only a few are spatial. For example, one of the first spatial equivalent mechanism (with one DOF) for the study of the knee passive motion was presented in [58]. This model combined a relative simplicity with the ability to take the tibia-femur spatial motion into good account.

This chapter summarizes the work done in the last decade by the first author and his co-workers at DIEM (Department of Mechanical Engineering of the University of Bologna) in collaboration with Istituto Ortopedico Rizzoli, which provided the facilities for the experimental tests and measurements. The research work started by adopting the second approach [58]. Since then much work was done, mainly on the modelling of passive motion of the human knee and ankle joints. Remarkable results were obtained and presented in [10, 14, 15, 37, 41, 45, 46, 48–50].

Passive motion involves only some anatomical structures, i.e. the main passive structures of the joint. Instead, the modelling of kinetostatic and dynamic behaviour of the joints involves all the anatomical structures, that comprise both passive (ligaments, tendons, and bones) and active (muscles) structures. In this case, ligament elasticity is necessarily involved, thus making the models mathematically more complicated since model elements would have a subtle relation with the anatomical structures. This would make the outcomes of the models difficult to interpret and the model itself less useful to surgeons and to prosthesis designers.

In this context, a new approach has been devised for the kinematic, kinetostatic and dynamic modelling of diarthrodial joints [17, 47, 52]. The approach makes it possible to consider all the anatomical structures of a joint, both the passive and the active ones, making their role in the kinematic and kinetostatic-dynamic behaviour of the joint evident. The approach relies upon some basic hypotheses and is based on three main steps from which, in order, three joint models of increasing complexity can be obtained. More precisely, the first step models the joint passive motion, the second step takes into account the kinetostatic behaviour of the joint under external loads, and the third step considers the (dynamic) influence of the active elements such as the muscles.

Among the three steps, the first one is perhaps the most challenging. It deals indeed with the synthesis of a spatial parallel mechanism: this operation involves the determination of a number of geometrical parameters that are coefficients of non-linear closure equations. These parameters must be synthesized by an optimization procedure which minimizes the errors between the relative pose of the relevant links in the equivalent mechanism and the measured pose of the corresponding anatomical elements in the natural joint. The final mechanism geometry has to be congruent with the joint anatomy.

The chapter focuses in particular on this first model and reports its synthesis for the knee, the ankle and the lower leg, showing the efficiency of these models. Additional information are then reported regarding: (a) the kinematic modelling of the joint when prosthetic design is the main target; (b) the second step of the procedure, namely the kinetostatic model for the knee and ankle joints; (c) two patents for the knee prosthesis design which are related to the proposed procedure. Finally, some comments close the chapter.

3.2 New Sequential Approach

The new sequential approach relies upon experimental measurements and mechanical models of the articulations [17, 47, 52]. Three different steps are involved in the whole process. Each step refers to a model: each model is an evolution of the model obtained at the previous step. A process of optimization makes it possible to define the main geometric and structural parameters of the model at each step. The three steps therefore provide three different models, which for convenience are called M1, M2 and M3 respectively.

All models rely upon two basic rules:

- once a parameter has been identified at a particular step, it is not modified at the next steps;
- parameters identified at each step must be chosen in a way that they do not alter the results obtained at the previous steps.

These two rules guarantee that the results obtained at each step do not worsen those already obtained at previous steps and, most importantly, they make it possible to

choose new parameters without violating possible anatomical constraints satisfied at previous steps.

In this sense, the proposed sequential approach is substantially an inductive procedure that starts from the definition of a simple model that can replicate the behaviour of the articulation under very strict conditions (with only some basic anatomical structures considered). This preliminary model is then enriched, at each step, by adding further anatomical structures which make the model progressively more complex, i.e. more sophisticated, in order to obtain a more generalized model which can replicate the behaviour of the joint under less restrictive conditions. The three models identified at each step are the following:

STEP 1 (M1 model) This is the model of the passive motion of the articulation. It refers to the joint's main anatomical structures which are involved during the motion of the joint under virtually unloaded conditions. In practice they are the passive structures that guide the motion of the joint: in most cases they are represented by bones which are in mutual contact during the motion and ligaments that interconnect the bones. Since no external force and moment are considered, the passive structures involved do not normally provide forces. This allows the assumption that all structures behave as rigid bodies. Thus, the M1 model can be represented by an equivalent plane or spatial mechanism having rigid bodies. The geometric parameters of the models are identified by an optimization process based on in vivo measurements of the joint passive motion.

STEP 2 (M2 model) The M2 model comprises the M1 model with the addition of the remaining passive structures, the ones that are not considered in the previous step. External forces and moments are considered and all the passive structures involved (both those of the M1 model and those added at this step) are now considered as elastic or viscoelastic structures. The physical model no longer has the feature of a rigid body equivalent mechanism, but it incorporates elastic/viscoelastic elements. Once again, the model's geometric and structural parameters are identified by mean of an optimization procedure based on experimental data collected by in vivo experiments. The identification procedure is performed by satisfying the rules of the sequential approach.

STEP 3 (M3 model) The M3 model comprises the M2 model with the addition of all the active joint structures, i.e. mainly all muscles involved in the motion of the joint. The physical model has similar rigid-elastic/viscoelastic features to the M2 model but incorporates dynamic loads (inertia). Once again, an optimization procedure makes it possible to identify the remaining geometrical and structural parameters of the model.

At each step it is therefore possible to identify the role of the added structures.

In conclusion, the M1 model allows the study of the joint passive motion which mainly comprises kinematic concepts; in fact, no forces are involved. The role of the main passive structures, such as ligaments and bones, which guide the motion of the joint under no external load is highlighted. The M2 model studies the motion and the stiffness of the joint under external loads. It allows considerations on the joint stability, to understand the role that both the main and the secondary passive structures play on it. The model, in practice, is represented by a mechanical

system with both rigid and elastic/viscoelastic links which allow kinematic, static and kinetostatic analyses to be performed. The M3 model is the most complete and complex model: it incorporates all the structures of the joint and allows kinematic, static and dynamic analyses to be performed. The role of the active structures such as the muscles is highlighted by this model.

Each model has its own advantages and disadvantages: M1 is simple and computationally not too much expensive but provides a limited amount of information, whilst M3 is computationally demanding but provides all the information related to the behaviour of the joint.

Within this frame, for a joint different models M1 and its corresponding evolutions M2 and M3 could be devised according to the purpose the model has to pursue. Indeed, a deep investigation of the role of the main anatomical structures of the joint would lead to a rather complex equivalent mechanism [10, 14, 37, 41, 46, 49], while for prosthesis design purposes more simple equivalent mechanisms could suffice [15, 45, 48, 50].

3.3 M1 Anatomical Models of the Passive Motion

In this section, models M1 for the detailed description of both the joint anatomical structures and the joint passive motion are reported for three joints, namely the knee, the ankle and the lower leg. The stage of M1 modelling comprises the following basic steps: (a) to devise a mechanism topology whose links and constraints have a one-to-one correspondence with the main anatomical structures; (b) to synthesize the mechanism geometrical dimensions in order to obtain a mechanism which can replicate the natural passive joint motion with a proper accuracy. The complexity of the model to be devised at step (a) depends on the purpose the model has to have, and its complexity, for a given accuracy of the mechanism to replicate the joint passive motion, will greatly increase the difficulty of the dimensional synthesis of the equivalent mechanism.

3.3.1 Anatomical Knee Model

The knee is a complex joint that exhibits a three-dimensional motion. It features two main bones, the femur and tibia, interconnected by a number of ligaments, tendons, and muscles that provide both mobility and stability.

3.3.1.1 Physical Foundations of the Model

The topology of the mechanism, its geometry and, as a consequence, its geometrical parameters are devised from experimental observations on the clinical and kinematic

Fig. 3.1 The knee joint [42]

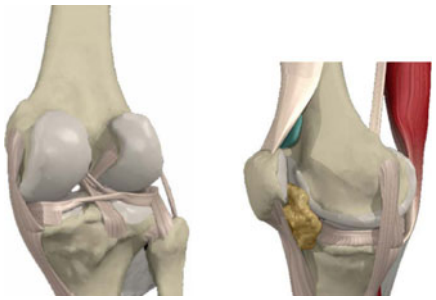

(a) Posterior view (b) Medial view

characteristics of the joint. This aspect is important to relate the mathematical results to the experimental ones, since physical significance is fundamental when the model is used for the study of the joint, for surgical purposes or for prosthetic design. This is an indirect way also to obtain a confirmation of the correctness of the model assumptions.

The knee is a joint which allows the relative motion between three bones of the legs, i.e. the femur, tibia and patella (Fig. 3.1). Two sub-joints can be recognized according to the bones that enter into contact with each other during knee flexion: the tibio-femoral joint (TF) allows the relative motion between the femur and tibia and the patello-femoral joint (PF) allows the relative motion between the patella and femur. These motions are guided in general by articular surfaces (the femur and tibia condyles, the trochlea and the back surface of the patella), by passive structures (such as the ligaments) and by active structures (such as the muscles).

The passive motion of the knee is thus the relative motion of the tibia, femur and patella when no loads are applied to the joint. Several studies [19, 58] prove that the motion of the TF during passive flexion is a one-DOF motion: once the flexion angle is imposed on the joint, the corresponding pose (position and orientation) of the tibia with respect to the femur is defined, both univocally and experimentally replicable. The same result holds also for the relative motion of the patella and femur [4]: although the PF is slightly more slack during passive flexion if compared to the TF, experimental results prove that for a given flexion angle of the knee the relative pose of the patella with respect to the femur is replicable. As a consequence, the patella also has one DOF of unresisted motion with respect to the femur.

Moreover, since no forces are exerted on the joint, no forces can be exerted by the passive structures of the knee to satisfy the equilibrium of the system composed by the tibia, femur and patella. The internal forces due to the passive structures could be internally autobalanced, thus invalidating the concept of totally unloaded condition, but these circumstances would be extremely complex to achieve on the full flexion range, even considering friction between articular components. As a consequence, the ligaments cannot be tight during passive flexion: they can reach the limit length between laxity and tension at the most (unloaded length). In particular, actually there exist some articular components which persist in this last status during the complete passive flexion: these structures are those which guide and affect the passive motion.

All these observations involve important anatomical constraints which must be considered and satisfied by the passive knee model: when no forces are applied to the model of the knee, the relative motion of the tibia, femur and patella must be a one-DOF motion, guided by passive structures that do not change their shape/length during motion. The fundamental conclusion is that the passive motion of the knee can be modelled by means of a rigid link mechanism, featuring elements that represent the passive structures that actually guide this motion; the relative motion of the tibia, femur and patella can thus be obtained from the kinematic analysis of this equivalent mechanism.

As a consequence, the problem of the knee model definition is reduced to the synthesis of a particular equivalent mechanism, whose links correspond to the anatomical structures that guide the passive motion of the knee. A further experimental evidence makes it possible to simplify the definition of this equivalent mechanism. If the tibia flexion angle is imposed, the TF pose is not influenced by the PF during passive motion: a TF mechanism can be synthesized at first, that excludes the patella; the PF mechanism can be defined subsequently [46, 49, 50].

In the last few years, a family of models was presented which can accurately replicate the passive motion of the TF by means of three-dimensional rigid link mechanisms [10, 37, 40, 41, 58]. The geometric and kinematic observations that support these mechanisms are all similar. Experimental studies show that a bundle of fibres of the anterior cruciate (ACL), one of the posterior cruciate (PCL) and another one of the medial collateral (MCL) ligaments remain almost isometric during passive flexion. These bundles are called isometric fibres (IFs). Articular contact is preserved on two points (one for the medial and the other for the lateral condyles) during passive motion. All the other components of the TF do not constrain the passive motion further. As a consequence, the three IFs and the two pairs of condyles are the anatomical structures which guide and affect the passive motion of the TF [57]. Thus, a TF equivalent mechanism can be defined featuring two rigid bodies (representing the tibia and femur), interconnected by three rigid binary links (representing the three IFs) and by two pairs of surfaces in reciprocal contact at one point (representing the articular surfaces). Mobility and a synthesis procedure of this type of mechanisms have been investigated in [33].

Different mechanisms can be defined by improving the description of articular surfaces [10, 37, 40, 41]. Accuracy does not increase with complexity all the time. Numerical instabilities may arise indeed from the kinematic analysis of a too complex mechanism and the number of parameters of the model makes the identification from experimental results very difficult and time-expensive. The limitations of higher order models were shown in [37]: the substitution of lower-order surfaces with more complex ones did not produce particular benefits; on the contrary, the use of b-splines brought computational and optimization instabilities that, paradoxically, gave worse results than those of simpler models. The approximation of the articular surfaces with spheres [41] proved very efficient for the modelling of the TF passive motion, providing a good balance between complexity of the model and accuracy of the synthesized motion.

In this case, the two pairs of spherical surfaces can be substituted each by one kinematically equivalent rigid link connecting two by two the centres of the spheres.

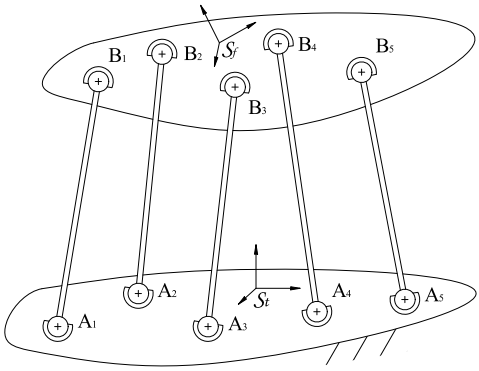

Fig. 3.2 The 5-5 parallel mechanism

The resulting mechanism is thus a 5-5 parallel mechanism (Fig. 3.2), featuring two rigid bodies (i.e. the femur and tibia), interconnected by five rigid links (i.e. the IFs and the articular contacts) through spherical pairs centred at the points $\mathbf{A}_i$ on the tibia and $\mathbf{B}_i$ on the femur ($i = 1, \ldots, 5$) [41].

The equivalent mechanism of the PF (Fig. 3.3) stems from similar considerations with respect to the TF one [46, 49]. The contact between the patella and femur occurs on a wide portion of their rigid articular surfaces for each flexion angle: this observation suggests that this contact can be modelled by means of a lower pair. In particular, the trochlea and the anterior portions of femoral condyles which are involved in the contact can be approximated by a cylinder. Thus, the relative motion of the patella and femur is almost cylindrical and occurs about an axis $\mathbf{n}_1$ fixed on the femur, i.e. the axis of the approximating cylinder. Moreover, the particular shape of the articular surfaces limits the mobility of the patella along the rotation axis: the back surface of the patella fits—in a certain sense—the trochlea, the femoral condyles and the intercondylar space, which serve as a sort of rail for the patella. These considerations all lead to the conclusion that the contact between the patella and femur can be modelled by a hinge joint which mutually connects the two bones. A more accurate description of articular surfaces could improve the accuracy of the mechanism also in this case. For instance, the patella-femur contact was modelled also by a screw joint [50], in order to account for the orientation of the anatomical rail which guides the patella motion, that is on a plane which is not perfectly orthogonal to the axis $\mathbf{n}_1$. However, the hinge joint model revealed accurate all the same, and thus it is used here. As for the other passive structures, experimental results from these and other authors [4] show that a bundle of fibres of the patellar ligament remains almost isometric in passive flexion. Thus, it is possible to substitute this bundle with a rigid link $\mathbf{C}_1\mathbf{D}_1$: this link is connected to the tibia and patella by spherical pairs respectively centred in $\mathbf{C}_1$ and $\mathbf{D}_1$.

Finally, in order to obtain a complete kinematic model of the knee, it is necessary to set the parameter of the motion whose value determines the configuration of the joint. The flexion motion—when imposed by the muscles—can be seen as the result of the action (lengthening or shortening) of the quadriceps on the patella. In other words, the length of quadriceps fixes the configuration of the joint. This can be ac-

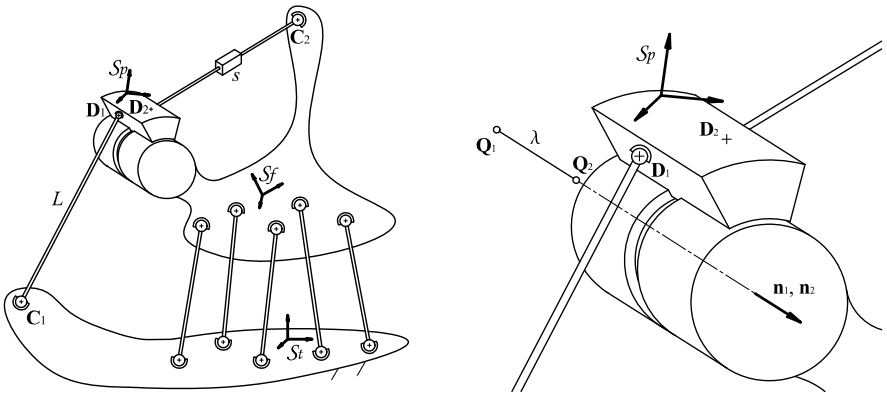

(a) The complete knee model (b) The patello–femoral joint

Fig. 3.3 The kinematic model of the knee joint (**a**) and a detail of the patello-femoral joint (**b**). The geometrical parameters of the patello-femoral joint are also represented

complished in the model, by substituting the quadriceps with a spherical-prismatic-spherical group $\mathbf{C}_2\mathbf{D}_2$: this group is composed by two rigid members interconnected by a prismatic pair, and it is connected to the femur and patella by spherical pairs respectively centred in $\mathbf{C}_2$ and $\mathbf{D}_2$. It is worth noting that the quadriceps is actually connected to both the femur and ilium; since the relative motion between the femur and ilium is not considered in this study, these two bones can be seen as a single rigid body.

The complete kinematic model of the knee in passive flexion is represented in Fig. 3.3. It can be obtained by joining the TF and the PF equivalent mechanisms. The linear displacement s of the prismatic joint defines the configuration of the knee when the flexion angle is imposed by the quadriceps: it can be easily proved that the complete mechanism has one DOF (ignoring idle inessential DOFs). In particular, the motion that is obtained by leaving the prismatic pair idle reproduces the passive motion of the knee. Moreover, it can be easily verified that the PF subchain, namely the kinematic chain constituted by the link $\mathbf{C}_1\mathbf{D}_1$, the group $\mathbf{C}_2\mathbf{D}_2$ and the patella, has zero DOFs with respect to the TF complex if the prismatic joints is idle. As a consequence, the PF motion depends on the configuration of the TF, while the TF motion is not influenced by the patella if tibia flexion is imposed: this is compatible with the previous anatomical observations.

3.3.1.2 Mathematical Formulation

The mathematical model can be deduced from the closure equations of the equivalent mechanism and the passive motion can be obtained by solving these equations. Since the PF and the TF subchains are partially independent, their closure equations are partially decoupled: the TF closure equations can be solved without considering

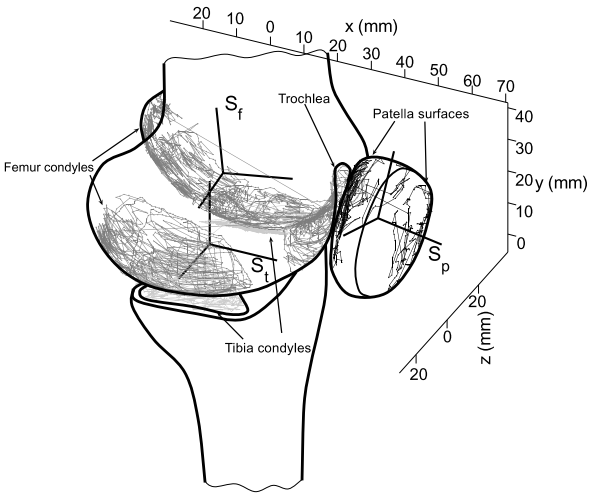

Fig. 3.4 The three anatomical frames $\mathscr{S}_t$, $\mathscr{S}_f$ and $\mathscr{S}_p$ represented together with the tibial (*light-grey*), femoral (*dark-grey*) and patellar (*black*) articular surfaces

the PF if tibia flexion is imposed; the PF closure equations are then solved sequentially, after the TF motion has been obtained.

Three anatomical frames are defined and attached to the tibia, femur and patella respectively (Fig. 3.4), to obtain the relative poses of the tibia, femur and patella as a result of the model. The tibia anatomical frame ($\mathscr{S}_t$) is defined with origin coincident with the tibia centre, i.e. the deepest point in the sulcus between the medial and lateral tibial intercondylar tubercles; x-axis orthogonal to the plane defined by the two malleoli and the tibia centre, anteriorly directed; y-axis directed from the mid-point between the malleoli to the tibia centre; z-axis as a consequence, according to the right hand rule. The femur anatomical frame ($\mathscr{S}_f$) is defined with origin coincident with the mid-point between the lateral and medial epicondyles; x-axis orthogonal to the plane defined by the two epicondyles and the head of femur, i.e. the hip joint centre, anteriorly directed; y-axis directed from the origin to the head of femur; z-axis as a consequence, according to the right hand rule. Likewise, the patella anatomical frame ($\mathscr{S}_p$) is defined with origin coincident with the mid-point between the lateral and medial apices; x-axis orthogonal to the plane defined by the lateral, medial and distal apices, anteriorly directed; y-axis directed from the distal apex to the origin; z-axis as a consequence, according to the right hand rule.

A relative pose of the femur with respect to the tibia can be expressed by means of the 3×3 rotation matrix R_{tf} for the transformation of vector components from $\mathscr{S}_f$ to $\mathscr{S}_t$, and the position $\mathbf{P}_{tf}$ of the origin of $\mathscr{S}_f$ in $\mathscr{S}_t$. Matrix R_{tf} can be expressed as a function of three angles α, β and γ:

$$R_{tf} = \begin{bmatrix} c_\alpha c_\gamma + s_\alpha s_\beta s_\gamma & -s_\alpha c_\gamma + c_\alpha s_\beta s_\gamma & -c_\beta s_\gamma \\ s_\alpha c_\beta & c_\alpha c_\beta & s_\beta \\ c_\alpha s_\gamma - s_\alpha s_\beta c_\gamma & -s_\alpha s_\gamma - c_\alpha s_\beta c_\gamma & c_\beta c_\gamma \end{bmatrix}, \tag{3.1}$$

where $c_{(\cdot)}$ and $s_{(\cdot)}$ indicate the cosine and sine of the angle $(\cdot)$ and α, β, γ represent the flexion, ab/adduction and in/external rotation angles of the femur and tibia,

using a convention deduced by the Grood and Suntay joint coordinate system [20]. Equation (3.1) can be applied for right legs. Likewise, the matrix R_{fp} and the vector $\mathbf{P}_{fp}$ express a relative pose of the patella with respect to the femur; the matrix R_{fp} can be represented by an expression similar to (3.1). Even though the Grood and Suntay convention was originally defined for the TF, its application on different joints (the PF included) is becoming an ordinary praxis in the scientific literature.

The geometrical parameters of the TF mechanism (Fig. 3.2) are the coordinates of the points $\mathbf{A}_i$ and $\mathbf{B}_i$ $(i = 1, \ldots, 5)$ expressed respectively in $\mathscr{S}_t$ and $\mathscr{S}_f$, and the lengths L_i $(i = 1, \ldots, 5)$ of links $\mathbf{A}_i\mathbf{B}_i$. Thus, the TF model is defined by 35 independent geometrical parameters. The relative poses of the femur and tibia can be obtained by solving the closure equations of the TF mechanism. As previously written, these equations can be solved independently from those of the PF model since the relative motion of the TF is not influenced by that of the PF in passive flexion, if tibia flexion is imposed. The closure equations of the TF model are:

$$\|\mathbf{A}_i - R_{tf}\mathbf{B}_i - \mathbf{P}_{tf}\| = L_i \quad (i = 1, \ldots, 5) \tag{3.2}$$

that impose a constant distance L_i between $\mathbf{A}_i$ and $\mathbf{B}_i$. If the flexion angle α is assigned (3.2) is a system of five equations in the five unknowns β, γ and $\mathbf{P}_{tf}$ components. These parameters define the relative pose of the femur and tibia.

The geometrical parameters involved in the PF model (Fig. 3.3) are the components of the unit vectors $\mathbf{n}_1$ and $\mathbf{n}_2$ of the hinge rotation axis expressed respectively in $\mathscr{S}_f$ and $\mathscr{S}_p$, the coordinates of the position vectors $\mathbf{Q}_1$ and $\mathbf{Q}_2$ of the intersections of the same axis with the x-y reference planes expressed respectively in $\mathscr{S}_f$ and $\mathscr{S}_p$, the coordinates of the insertion points $\mathbf{C}_1$ and $\mathbf{D}_1$ expressed respectively in $\mathscr{S}_t$ and $\mathscr{S}_p$, the fixed distance L between $\mathbf{C}_1$ and $\mathbf{D}_1$ and the fixed distance λ between $\mathbf{Q}_1$ and $\mathbf{Q}_2$. Since the norm of the hinge unit vector is unitary, the components of the unit vectors $\mathbf{n}_1$ and $\mathbf{n}_2$ can be expressed as a function of two independent coordinates only, for instance the azimuth δ and the altitude η, y-z being the horizontal plane and z-axis the azimuth origin:

$$\mathbf{n}_1 = \begin{pmatrix} \sin\eta_1 \\ \cos\eta_1 \sin\delta_1 \\ \cos\eta_1 \cos\delta_1 \end{pmatrix}, \qquad \mathbf{n}_2 = \begin{pmatrix} \sin\eta_2 \\ \cos\eta_2 \sin\delta_2 \\ \cos\eta_2 \cos\delta_2 \end{pmatrix}. \tag{3.3}$$

Furthermore, the coordinates of the position vectors $\mathbf{Q}_1$ and $\mathbf{Q}_2$ admit the following representation:

$$\mathbf{Q}_1 = \begin{pmatrix} Q_{1x} \\ Q_{1y} \\ 0 \end{pmatrix}, \qquad \mathbf{Q}_2 = \begin{pmatrix} Q_{2x} \\ Q_{2y} \\ 0 \end{pmatrix}. \tag{3.4}$$

From (3.3) and (3.4) and from the previous considerations, it follows that the PF model is described by means of 16 independent geometrical parameters. It is worth noting that the parameters which define the position of points $\mathbf{C}_2$ and $\mathbf{D}_2$ are not taken into account since they are not necessary for the solution of the position analysis problem of the mechanism in passive flexion, if tibia flexion is imposed.

The connection between the geometric parameters of the model and the kinematic parameters of the relative pose of the patella and femur is described by the following expressions, which represent the closure equations of the PF model:

$$\begin{aligned} &R_{fp}\mathbf{n}_2 = \mathbf{n}_1, \\ &R_{fp}\mathbf{Q}_2 + \mathbf{P}_{fp} = \lambda\mathbf{n}_1 + \mathbf{Q}_1, \\ &\left\| R_{tf}(R_{fp}\mathbf{D}_1 + \mathbf{P}_{fp}) + \mathbf{P}_{tf} - \mathbf{C}_1 \right\| = L. \end{aligned} \tag{3.5}$$

The first two vectorial equations constrain the axis identified by $\mathbf{n}_1$ and $\mathbf{Q}_1$ to be coincident with that identified by $\mathbf{n}_2$ and $\mathbf{Q}_2$. Moreover, the second vectorial equation imposes a constant distance between $\mathbf{Q}_1$ and $\mathbf{Q}_2$. The last scalar equation ensures that the distance between $\mathbf{C}_1$ and $\mathbf{D}_1$ remains constant. If the relative motion of the femur and tibia is given, i.e. if R_{tf} and $\mathbf{P}_{tf}$ are known from (3.2), (3.5) is a system of seven equations in six unknowns, namely the three components of $\mathbf{P}_{fp}$ and the angles α, β, γ which define R_{fp}, as in (3.1). However, in the first vectorial expression of (3.5) only two out of three equations are independent, since $\mathbf{n}_1$ and $\mathbf{n}_2$ both have unitary norms. Thus, given R_{tf} and $\mathbf{P}_{tf}$, (3.5) makes it possible to find the relative poses of the patella and femur at each assigned flexion angle.

Equations (3.2) and (3.5) are the closure equations of the knee joint in passive motion. By assigning the flexion angle α, they make it possible to find the relative poses of the patella, femur and tibia. As previously anticipated, points $\mathbf{C}_2$ and $\mathbf{D}_2$ have no influence on the closure equations of the mechanism in passive flexion. If the prismatic joint displacement s is required, it is sufficient to solve the position analysis problem and then to evaluate the distance between the points $\mathbf{C}_2$ and $\mathbf{D}_2$.

3.3.1.3 Experimental Sessions

Experimental sessions were carried out, in order to evaluate the accuracy of the passive knee model. Geometrical data were measured on several specimens to obtain a first approximation of the geometrical parameters of the mechanism; the experimental motion of the patella, femur and tibia during passive flexion was also recorded. In particular, an opto-electronic system was used to collect the articular surfaces of the patella, femur and tibia as clouds of points (Fig. 3.4); the ligament attachment areas and the anatomical landmarks were recorded in the same way. The same opto-electronic system was used to obtain the relative poses between the patella, femur and tibia in passive flexion.

The anatomical landmarks were used to define the reference frames $\mathscr{S}_t$, $\mathscr{S}_f$ and $\mathscr{S}_p$. Straightforward algebraic manipulations then made it possible to obtain the experimental values of the components of vectors $\mathbf{P}_{fp}$ and $\mathbf{P}_{tf}$, of the angles α, β, γ which define the matrix R_{fp}, and of the analogous angles which define the matrix R_{tf}, as in (3.1). These kinematic parameters are used to compare the synthesized motion with the experimental one during the optimization procedure and, as a final objective, to verify the accuracy of the proposed model.

The experimental data were processed to obtain a preliminary estimate of the geometrical parameters of the knee model. As for the TF mechanism, by analysing the passive motion and knowing the ligament attachment areas, it was possible to determine the attachments of ligament isometric fibres, i.e. the points $\mathbf{A}_i$ and $\mathbf{B}_i$ ($i = 1, 2, 3$) which showed the minimum distance variation during the entire motion. The tibia and femoral articular surfaces of the TF were approximated by spheres by the least-square method: the centres of these spheres were used to obtain a first estimate of the remaining points $\mathbf{A}_i$ and $\mathbf{B}_i$ ($i = 4, 5$). The link length L_i ($i = 1, \ldots, 5$) were obtained as the distance between $\mathbf{A}_i$ and $\mathbf{B}_i$ at full extension.

Similarly, an estimate of the PF parameters was deduced from the experimental data by considering the physical foundations of the model, described in Sect. 3.3.1.1. The femoral articular surfaces of the PF were approximated by a best-fitting cylinder in $\mathscr{S}_f$: the axis of the cylinder made it possible to obtain $\mathbf{n}_1$ and $\mathbf{Q}_1$. The transformation of vector components in $\mathscr{S}_p$ (an intermediate relative pose between the patella and femur was chosen along the flexion arc) allowed $\mathbf{n}_2$ and $\mathbf{Q}_2$ to be defined; the distance between $\mathbf{Q}_1$ and $\mathbf{Q}_2$ set the λ parameter. Finally, the attachment areas of the patellar ligament was analysed: the attachment points of the ligament isometric fibre $\mathbf{C}_1$ and $\mathbf{D}_1$ were the points which showed the minimum distance variation during the full flexion range. Their mean distance during passive flexion defined L.

3.3.1.4 Parameter Optimization

The preliminary estimate of the geometrical parameters is only a rough approximation of the final model: these parameters have to be optimized in order to best-fit the experimental results [45]. In particular, the TF mechanism was optimized at first; the PF model was then sequentially optimized, starting from the obtained TF model [46, 49]. The optimization procedure could also be extended to the whole mechanism, slightly improving the result accuracy: the sequential optimization was preferred just to simplify the procedure, since the final results would be very similar to the presented ones; moreover, a sequential optimization is more congruent with the independence between the TF and PF.

The optimization technique applied to the TF and PF mechanisms are substantially similar (Fig. 3.5). The preliminary estimate of the geometrical parameters $\mathbf{q}_0$ is passed to an objective function. The model is defined within the function, by means of $\mathbf{q}_0$ and other parameters (vector $\mathbf{p}$ in Fig. 3.5) which are not optimized. The passive motion of the joint is obtained by solving the closure equations at the experimental flexion angles; the simulated motion $\mathbf{x}$ is then compared with the experimental one $\mathbf{x}^\star$ and the differences are quantified by an index F. The value of this index leads the optimization algorithm to define a second guess $\mathbf{q}_1$ inside the search domain, that is passed again to the objective function. This iteration is repeated until the minimum value of F is reached. The final set of parameters $\mathbf{q}_f$ is the solution of the optimization problem. To keep the physical consistency of the knee model, the optimization search domain is bounded, having the preliminary estimate $\mathbf{q}_0$ as the central value: every parameter q_n has to fall within the interval $[q_{0n} - \delta_n,\ q_{0n} + \delta_n]$.

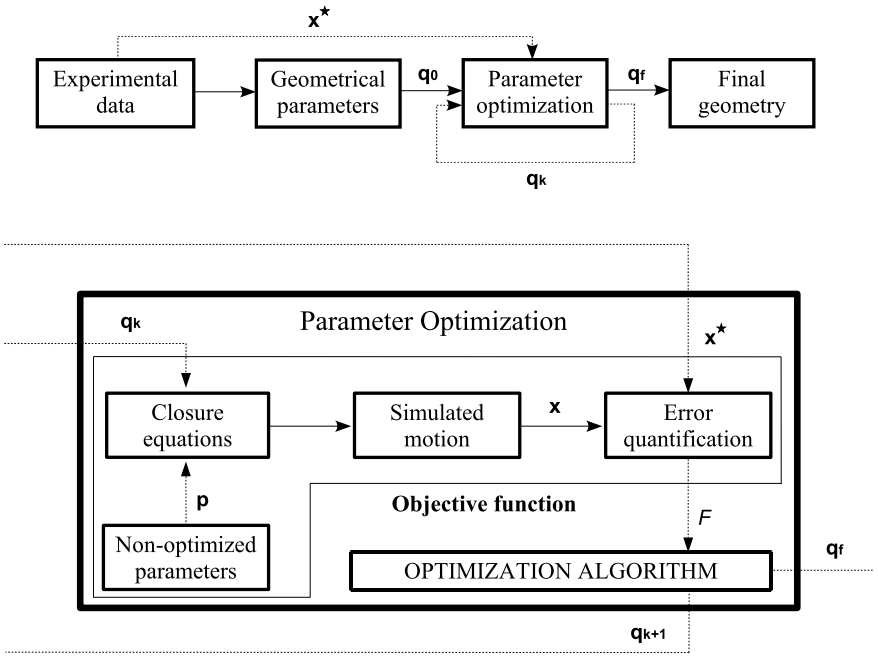

Fig. 3.5 The optimization procedure for the identification of the TF and PF mechanisms

The bounds δ_n are set in such a way that the final geometrical parameters of the model are not too far from their preliminary estimate.

As regards the TF mechanism, for each optimization iteration, the closure equations (3.2) are solved at all experimental flexion angles. The relative poses of the femur and tibia computed from the model are iteratively compared with the experimental ones: the sum of the weighted squared errors between the poses represents the error index F which has to be minimized. In particular, if x_{jk} is the computed value of the jth unknown ($j = 1, \ldots, 5$) of the system (3.2), obtained at the kth flexion angle ($k = 1, \ldots, m$), the contribution of x_{jk} to the value of F is:

$$\varepsilon_{jk} = \frac{(x_{jk} - x^{\star}_{jk})^2}{x^2_{jd}}, \tag{3.6}$$

where $x^{\star}_{jk}$ is the corresponding experimental value of the unknown. The weights x_{jd} are necessary, in order to account for the different sizes and dimensions of the unknowns. The weights are chosen as:

$$x_{jd} = \max\{x_{jk},\ k = 1, \ldots, m\} - \min\{x_{jk},\ k = 1, \ldots, m\}. \tag{3.7}$$

Thus, the error ε_{jk} is a sort of per cent error, with respect to the maximum range x_{jd} of the j^{th} pose parameter. The mechanism closure is not guaranteed for all sets

of geometrical parameters: if the model closure equations cannot be solved at all flexion angles, an arbitrary high value is assigned to the index F. Thus, the complete algorithm for the computation of F is:

$$\begin{aligned} F &= \sum_{j=1}^{5} \sum_{k=1}^{m} \varepsilon_{jk} \quad \text{if closure succeeds,} \\ F &= X \quad \text{otherwise,} \end{aligned} \tag{3.8}$$

where X is an arbitrary high value.

The objective function is highly non-linear and, because of the bifurcation of (3.8), it has many discontinuities. Quasi-Newton methods are powerful optimization algorithms which can efficiently find the minimum value of non-linear functions; unfortunately—like all deterministic algorithms which make use of derivatives of the objective function—they show numerical instabilities when solving discontinuous problems. Thus, a first approximation of the optimum solution is found by means of a genetic algorithm, which does not make use of derivatives. The bounded genetic algorithm makes it possible to find a feasible solution within the bounds, namely a geometry of the TF mechanism whose closure equations are satisfied at all flexion angles. The preliminary solution is then iteratively refined by means of a quasi-Newton algorithm: the search for the optimum solution is carried out by finding the minimum within bigger and bigger domains inside the bounds, and by keeping the algorithm on continuous zones of the objective function.

The optimization technique applied to the PF mechanism is substantially the same as the TF. The poses of the optimized TF model at the experimental flexion angles are used to solve (3.5). An error index F similar to (3.8), that compares the computed and the experimental motion of the patella, is then reduced to a minimum.

3.3.1.5 Results

The results of the optimization procedure are reported in Table 3.1 for a representative specimen [49]. A few geometrical parameters lie on the bounds of the domain, but in general all of them remain close to the preliminary estimate. These geometrical parameters are reported as an example and are strictly related to the anatomy of the considered specimen. A similar procedure could be used to define a sort of generic mechanism of an average knee; however, since the model strongly relies on anatomy, an average knee geometry should be determined.

The values of the five pose parameters of $\mathscr{S}_f$ in $\mathscr{S}_t$ during knee passive motion are reported in Figs. 3.6(a) and 3.7(a): the dotted lines are the experimental data, while the solid ones are the results of the model. The corresponding values of the six pose parameters of $\mathscr{S}_p$ in $\mathscr{S}_f$ are presented in Figs. 3.6(b) and 3.7(b).

Table 3.1 Geometrical parameters of the knee model after optimization: $\mathbf{A}_i$, $\mathbf{C}_1$ refer to $\mathscr{S}_t$, $\mathbf{B}_i$, $\mathbf{n}_1$, $\mathbf{Q}_1$ to $\mathscr{S}_f$, and $\mathbf{n}_2$, $\mathbf{Q}_2$, $\mathbf{D}_1$ to $\mathscr{S}_p$

	x [mm]	y [mm]	z [mm]	Length [mm]	δ [rad]	η [rad]
$\mathbf{A}_1$	13.30	0.68	−3.80	–	–	–
$\mathbf{A}_2$	−19.92	−10.83	−3.38	–	–	–
$\mathbf{A}_3$	14.65	−97.29	−9.88	–	–	–
$\mathbf{A}_4$	8.31	−47.21	20.55	–	–	–
$\mathbf{A}_5$	−3.61	28.79	−32.49	–	–	–
$\mathbf{B}_1$	−8.06	0.51	10.50	–	–	–
$\mathbf{B}_2$	−2.66	−1.16	−4.23	–	–	–
$\mathbf{B}_3$	1.15	4.21	−46.77	–	–	–
$\mathbf{B}_4$	−4.23	2.12	23.12	–	–	–
$\mathbf{B}_5$	2.28	6.37	−18.28	–	–	–
L_1	–	–	–	29.28	–	–
L_2	–	–	–	35.47	–	–
L_3	–	–	–	128.88	–	–
L_4	–	–	–	70.35	–	–
L_5	–	–	–	11.55	–	–
$\mathbf{Q}_1$	6.46	15.47	0	–	–	–
$\mathbf{Q}_2$	−44.10	10.40	0	–	–	–
$\mathbf{C}_1$	19.88	−25.00	10.00	–	–	–
$\mathbf{D}_1$	2.41	−26.00	−5.00	–	–	–
L	–	–	–	40.02	–	–
λ	–	–	–	−1.76	–	–
$\mathbf{n}_1$	–	–	–	–	−0.13	0.06
$\mathbf{n}_2$	–	–	–	–	−0.30	0.29

These results show that the kinematic model of the knee joint can accurately reproduce the relative motion of the patella, femur and tibia in passive flexion. The accuracy of the model and the closeness between the preliminary estimate of the geometrical parameters and their optimized values is an indirect confirmation of the correctness of the model physical foundations. In particular, the considered structures seem to be those most responsible for the knee passive motion: this aspect shows the important role these structures have to stabilize and to restrain the human knee.

Finally, it is worth noting that the proposed knee mechanism is a purely kinematic model which can replicate the joint passive motion. The model could be used to predict the behaviour of the joint under different loading conditions, but in general the model accuracy could be reduced: the considered articular structures cannot be considered rigid (as supposed in the model) when relatively high loads are applied to the real knee. In this case, indeed, the natural motion of the joint deviates from the

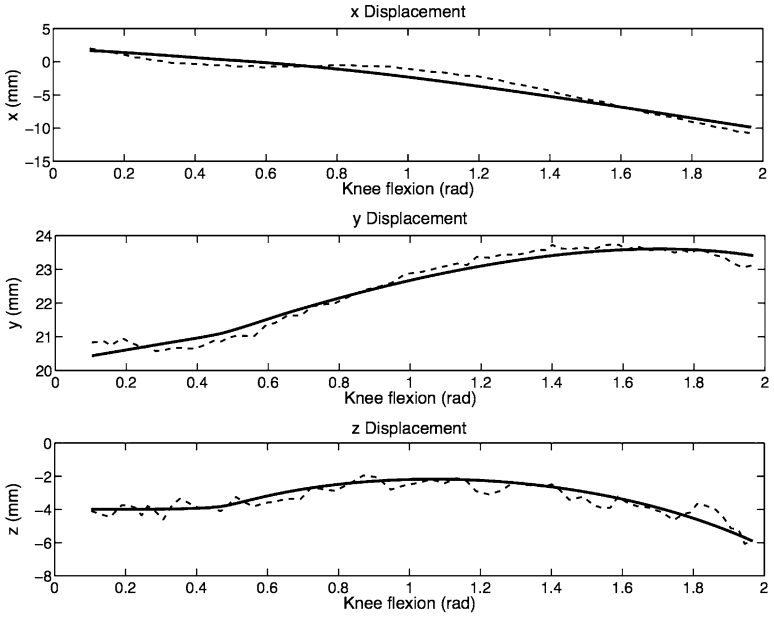

(a) Position of $\mathscr{S}_f$ in $\mathscr{S}_t$.

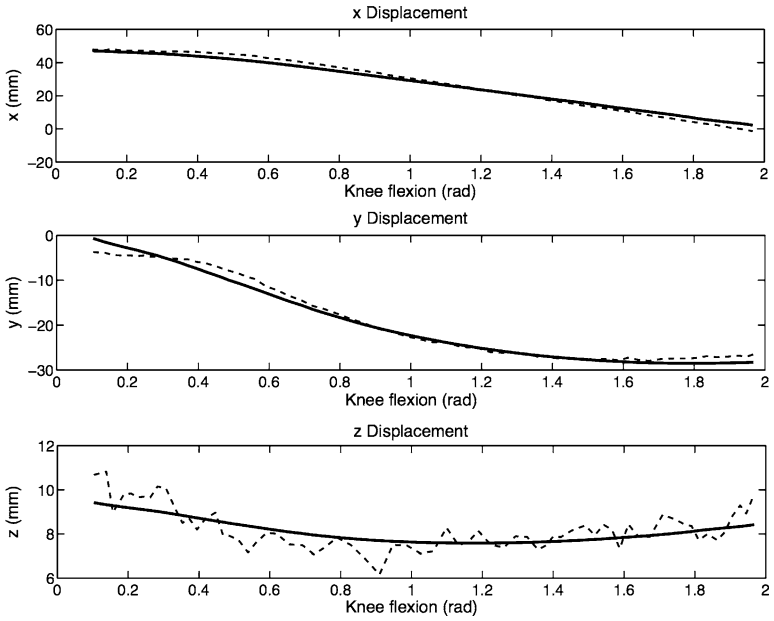

(b) Position of $\mathscr{S}_p$ in $\mathscr{S}_f$.

Fig. 3.6 Comparison of the positions of parameters of the femur, tibia and patella in relative motion. Dot = experimental data; solid = synthesized motion

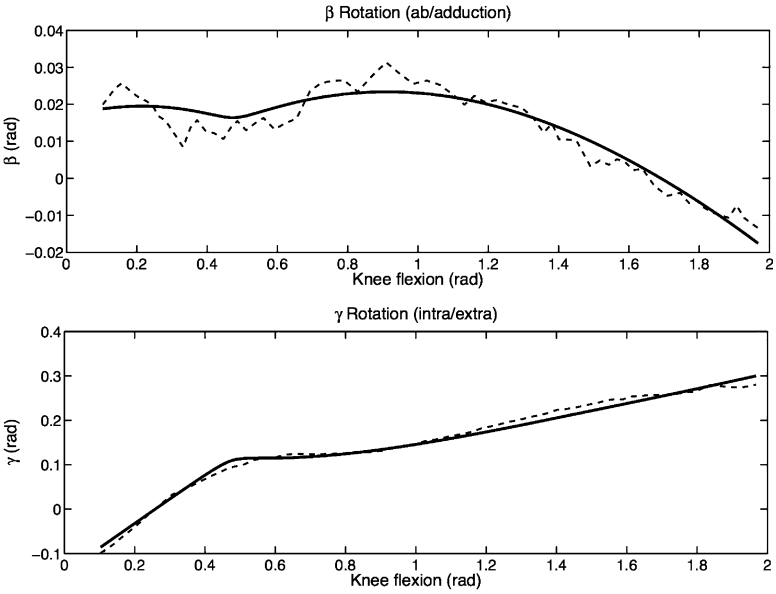

(a) Orientation of $\mathscr{S}_f$ in $\mathscr{S}_t$.

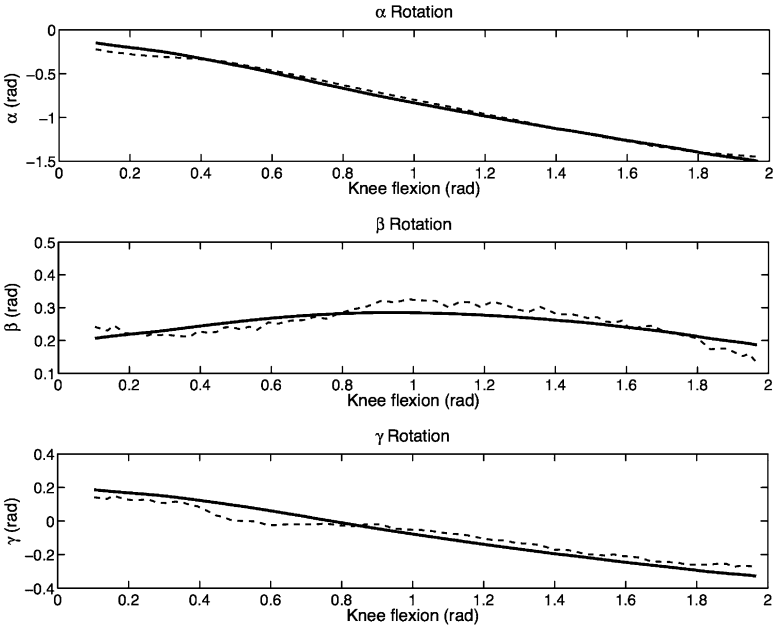

(b) Orientation of $\mathscr{S}_p$ in $\mathscr{S}_f$.

Fig. 3.7 Comparison of the orientation of the femur, tibia and patella in relative motion. Dot = experimental data; solid = synthesized motion

passive one, and other ligaments and bundles could be recruited together with the ones considered in the model. However, as reported in the introduction, the proposed rigid-link mechanism can be generalized to other loading conditions by means of the sequential procedure described in Sect. 3.2 [17, 47, 52]. In this sense, this model M1 is the foundation or the first step to obtain more generic models that can replicate the knee behaviour even when loads are applied to the joint.

3.3.2 Anatomical Ankle Model

The ankle joint complex is an anatomical structure that comprises two joints, namely the tibiotalar joint, connecting the tibia above, the fibula laterally and the talus below, and the subtalar joint, connecting the talus above and the calcaneus below. This human joint has been an important subject of study for many decades, for its fundamental role in human locomotion. Great interest has been devoted, in particular, to the mechanical behaviour of this joint. Kinematic, static and dynamic analyses of the ankle have been the main focus of a large amount of work, thanks also to the modern instrumentation that has made it possible to collect and evaluate many data. The effective advance in laboratory techniques, both in vivo and in vitro experiments, has allowed the development of relevant models that describe the ankle motion under virtually unloaded condition (passive motion) or in response to external loads.

Not many studies up to now have developed a kinematic, static or dynamic model of the ankle joint involving all the main anatomical structures (such as bones, ligaments, tendons, cartilage, ...) that play an important role in the ankle's mechanical behaviour [7, 9, 11, 14, 15, 22, 25, 31, 43, 54, 55]. Following a similar approach as that adopted for the knee in the previous sections, a one-DOF equivalent spatial mechanism is presented which overcomes the limitations of the previous models [11, 29, 30] and makes it possible to replicate very well the passive motion of the joint [14, 16].

3.3.2.1 Physical Foundations of the Model

Based on a careful inspection of the tibiocalcaneal interface, the talus and the tibio/fibula bones (modelled as rigid bodies) have been considered in mutual contact at three points. The portion of each contact surface has been approximated by a spherical surface. More precisely, the areas of the surfaces of the mating bones which come into contact during the passive motion were digitized. Three contact points were selected and the corresponding contact areas (a cloud of digitized points for each area) approximated by best fit spherical surfaces. The three contact areas were identified at the lateral malleolus (a pyramidal process on the lateral surface of the lower extremity of fibula), at the internal region of the inferior surface of the

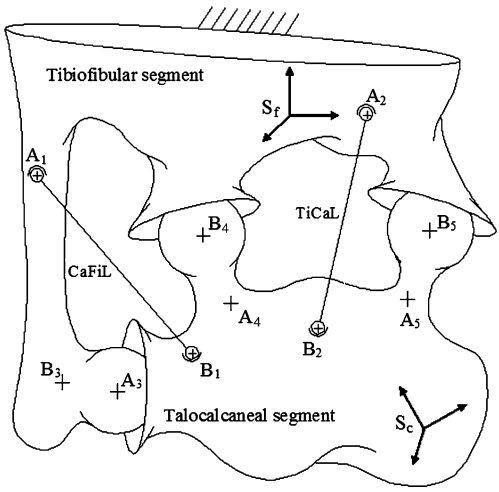

Fig. 3.8 Schematic of the ankle complex joint

distal tibia articulate with the talus surface, and at the medial malleolus (a pyramidal process on the medial surface of the lower extremity of tibia).

Moreover, experimental data showed that some fibres of the calcaneofibular ligament (CaFiL) and the tibiocalcaneal ligament (TiCaL) are nearly isometric during the ankle passive motion.

Based on these observations and assumptions a schematic of the ankle joint is shown in Fig. 3.8. Here the two talocalcaneal and tibiofibular segments feature three sphere-to-sphere contact points where points $\mathbf{A}_i$, and $\mathbf{B}_i$, $i = 3, 4, 5$, represent the centres of the mating spherical surfaces fixed to the talus/calcaneus and tibia/fibula respectively, while points $\mathbf{A}_i$, and $\mathbf{B}_i$, $i = 1, 2$, represent the insertion points on the two segments of two isometric fibres of the two ligaments CaFiL and TiCaL respectively.

Inspection of Fig. 3.8, when considering, for instance, the tibio/fibula segment as a fixed body, and the isometric fibres as connected to the bones by spherical pairs centred at points $\mathbf{A}_i$ and $\mathbf{B}_i$, $i = 1, 2$, reveals that the schematic represents a spatial mechanism with one-DOF. Indeed, Kutzbach's formula [27] provides one-DOF considering that the rotations of the two ligaments about the respective axes $\mathbf{A}_1\mathbf{B}_1$ and $\mathbf{A}_2\mathbf{B}_2$ are inessential to the relative position of the two segments. In particular the talocalcaneal segment has a one-DOF motion with respect to the tibiofibular segment.

During the relative motion of the two ankle segments each pair of mating spherical surfaces maintains the contact, therefore the distance $\mathbf{A}_i\mathbf{B}_i$, $i = 3, 4, 5$, is constant. Moreover the distance $\mathbf{A}_i\mathbf{B}_i$, $i = 1, 2$ is also constant during the passive motion since it represents the length of the ligament isometric fibre. As a consequence, each pair of points $(\mathbf{A}_i, \mathbf{B}_i)$, with $\mathbf{A}_i$ and $\mathbf{B}_i$, $i = 1, 2, \ldots, 5$, respectively fixed to the tibiofibular and talocalcaneal segments, maintains a constant mutual distance during motion.

Based on this consideration, the equivalent mechanism of Fig. 3.8 can be more synthetically represented again, likewise the knee, by a 5-5 mechanism (Fig. 3.2).

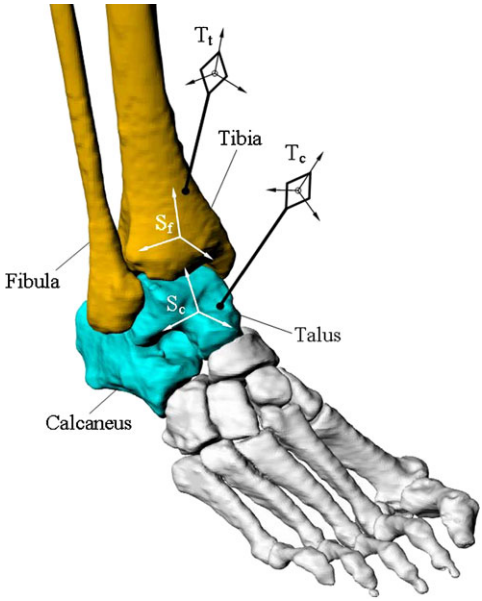

Fig. 3.9 Stereophotogrammetric system for the ankle complex joint

3.3.2.2 Mathematical Formulation

The 5-5 mechanism is then taken as the equivalent mechanism of the ankle joint. Therefore, its mathematical model is the same as that of the knee joint reported in the previous section. The mechanism closure equations are the analogous of (3.2).

3.3.2.3 Experimental Session

Similarly to the procedure adopted for the knee, experimental measurements were conducted with a number of specimens in order to obtain the physical data necessary to synthesize the equivalent mechanism. In particular, the tibia was fixed to a workbench table while the foot was free to move with respect to the tibia. A pin drilled along the calcaneus longitudinal axis and protruding from the posterior surface came into contact with a rigid link, connected to the workbench by a revolute pair, which supported and drove the pin to move, thus producing the desired passive motion of the calcaneus with respect to the tibia/fibula.

Likewise the knee, a standard stereophotogrammetric system was used as the acquisition system for both recording the relative position of the talocalcaneal segment with respect to the tibiofibular segment and digitizing points of interest (Fig. 3.9). The equipment comprises a camera system, two trackers fixed to the tibia and the talus respectively and a pointer to digitize points. The system can recognize the pose of the two trackers and pointer in a definite workspace.

Details on the chosen anatomical reference system (S_f for the tibia and S_c for the talus) are reported in [14]. In order to define the orientation of the talus with respect

Table 3.2 Geometrical data of the 5-5 mechanism obtained by the optimization procedure

	x [mm]	y [mm]	z [mm]	Length [mm]
$\mathbf{A}_1$	−2.535	−7.566	23.137	–
$\mathbf{A}_2$	1.854	1.523	−32.627	–
$\mathbf{A}_3$	9.764	0.824	39.475	–
$\mathbf{A}_4$	−4.378	3.931	−15.235	–
$\mathbf{A}_5$	3.234	−5.489	−11.928	–
${}^c\mathbf{B}_1$	−46.464	−24.569	24.599	–
${}^c\mathbf{B}_2$	−25.048	−27.721	−32.399	–
${}^c\mathbf{B}_3$	−31.147	−11.216	49.764	–
${}^c\mathbf{B}_4$	−38.116	3.455	−20.625	–
${}^c\mathbf{B}_5$	−21.908	1.048	−8.352	–
L_1	–	–	–	19.229
L_2	–	–	–	22.705
L_3	–	–	–	13.176
L_4	–	–	–	15.228
L_5	–	–	–	13.430

to the tibia, a sequence-independent joint coordinate system [20] was chosen. The three rotation axes that define the system were chosen as follows: the y_f axis of S_f fixed to the tibia as the first one, the z_c axis of S_c fixed to the talus as the second one, finally an axis coincident with the shortest distance straight line of the other two axes as the third one.

Three angles about these axes are defined: the ankle dorsiflexion(+)/plantarflexion(−) angle γ about the z-axis of S_c, the ankle internal(+)/external(−) rotation angle α about the y-axis of S_f, and the ankle pronation(+)/supination(−) angle β about a floating axis defined by the cross vector product of the unit vectors of the z-axis of S_f and the unit vector of the y-axis of S_c.

3.3.2.4 Parameter Optimization

The synthesis of the ankle 5-5 mechanism model can be performed by the same procedure adopted for the knee (Sect. 3.3.1.4).

3.3.2.5 Results

The geometry of the equivalent 5-5 mechanism obtained by the optimization procedure is reported in Table 3.2. Vectors with a left hand superscript ${}^c(\cdot)$ are measured in S_c, the remaining vectors are measured in S_f. The results of the ankle passive motion simulation obtained by the 5-5 mechanism are compared with those obtained by measurements. In particular, Figs. 3.10 and 3.11 show the positions x, y, and z of the origin of the reference system S_c with respect to S_f, and the angles α and β

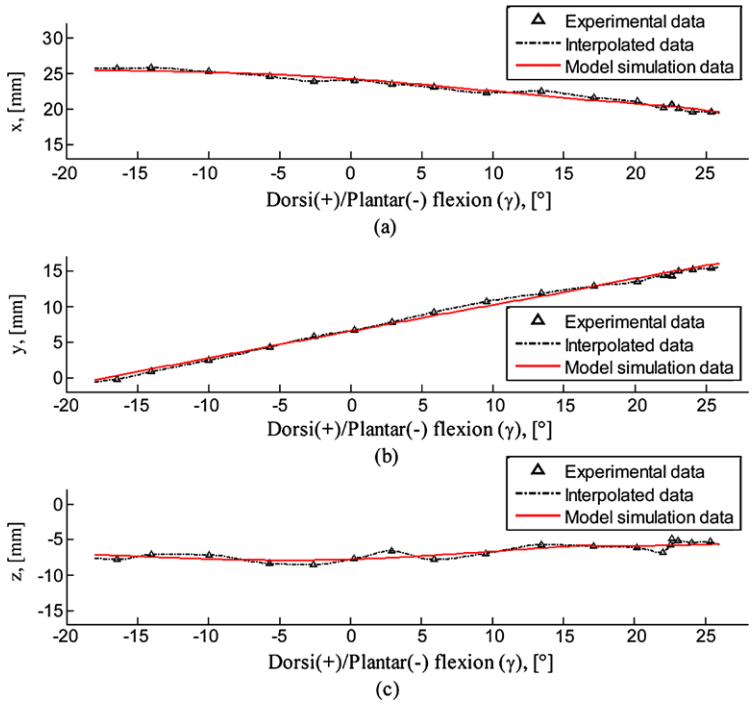

Fig. 3.10 Passive motion simulation: x, (**a**), y, (**b**), and z, (**c**) versus ankle's flexion angle γ

respectively versus the ankle flexion angle γ. All figures show both the simulation and the experimental results. In particular the experimental results are identified by the symbol Δ and interpolated by a dotted line. The interpolation makes it possible to use a higher number of (interpolated) experimental data, which may be useful for the optimal synthesis of the equivalent 5-5 geometry.

Inspection of the figures shows that the equivalent spatial mechanism replicates the passive motion of the human ankle very well. In particular the discrepancy on the position is contained within about 2.5 mm, specifically within 1 mm for the displacement x, within 1 mm for the displacement y, and within 2 mm for the displacement z; while the discrepancy on the rotation is lower than 1 degree for the intra/extra rotation α, and lower than 0.5 degrees for the prono/supination β.

3.3.3 Anatomical Lower Leg Model

For a better understanding of the ankle complex behaviour and role in human locomotion, it is necessary to study the interaction of the anatomical elements of the joint with the others that constitute the whole leg. One example is a new computational model of the lower limb presented in [32] and developed to study the

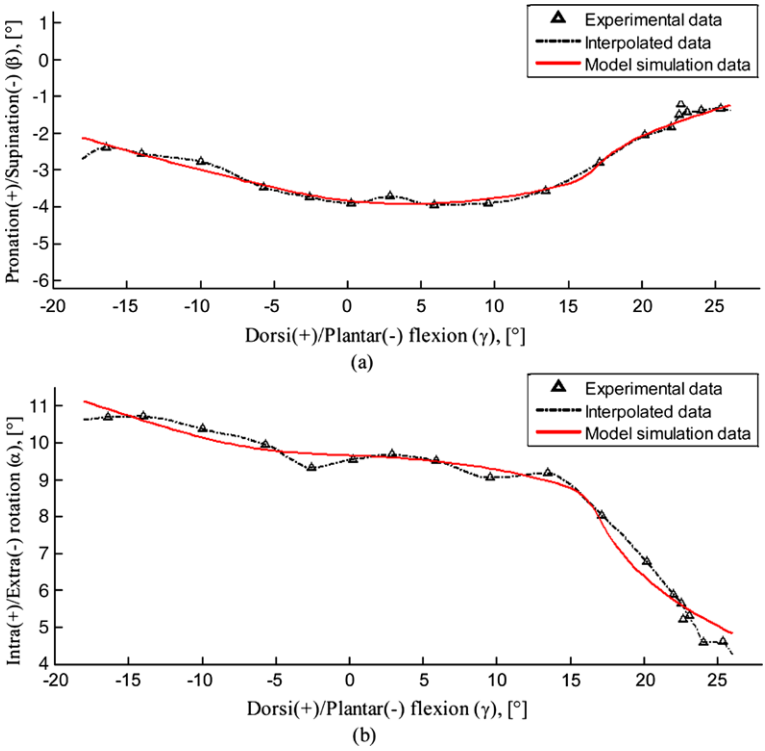

Fig. 3.11 Passive motion simulation: angles β, (**a**), and α, (**b**), versus ankle's flexion angle γ

effects of a syndesmotic injury on the relative motion between tibia and fibula, and the ankle inversion stability. The anatomical elements modelled are several bones (the whole tibia and fibula, talus and calcaneus, navicular, cuneiform and metatarsal bones), several ligaments and the interosseus membrane. In particular, bones are represented with rigid bodies in mutual contact—ignoring articular cartilage deformation—and ligaments and the interosseus membrane by linear springs. This new computational model seems to be almost an exception, because the great majority of kinematic or dynamic models of the human lower limb that can be found in the literature represent the ankle joint as an ideal hinge joint or a spherical joint that links together two rigid segments corresponding to the foot and the lower limb [5, 8, 18, 21, 24, 26, 34, 35, 53].

In this section the ankle joint complex kinematic behaviour is modelled by a spatial mechanism that takes into account several anatomical structures of the lower leg: the main ligaments and the articular contacts. The proposed approach will be shown to represent a valid procedure for future developments of complete models of the whole human lower limb.

More specifically, this section will focus on the kinematic modelling of the articulation that involves four bones: tibia, fibula, talus and calcaneus (see Fig. 3.12). In this anatomical complex (defined as TFC for brevity), the ankle joint plays a

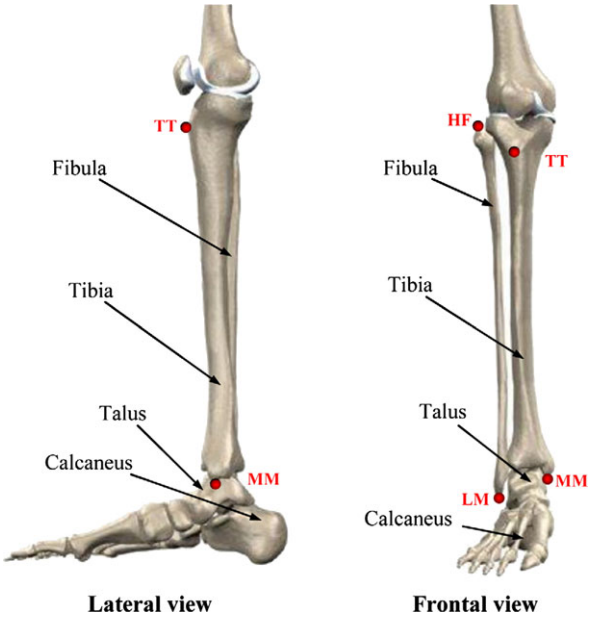

Fig. 3.12 The four bones of the TFC complex. TT, HF, LM and MM are the anatomical points for the definition of the tibia anatomical frame

fundamental role. In particular, the aim is the development of a model for the TFC complex passive motion simulation. Thus, a one-DOF spatial equivalent mechanism of the TFC complex is presented [3], following an approach similar to that adopted for the knee and the ankle joints. The geometry of the devised mechanism relies upon the anatomical structures of the TFC complex: namely, on the talus, tibia and fibula articular surfaces on one hand and on the main ligaments of the articulation on the other hand. The optimal geometry of the mechanism is found, likewise the knee and ankle models, by an iterative refinement process that relies upon the comparison of simulation results with experimental data of the talus, tibia and fibula bones passive motion.

3.3.3.1 Physical Foundations of the Model

Starting from experimental observations and previous studies, the TFC is modelled by a one-DOF equivalent spatial mechanism to simulate the passive motion of the complex.

In particular, the talus and calcaneus are considered as a single body, likewise in the ankle kinematic model, and all the bones are modelled as rigid bodies. The contacts between the bone articular surfaces are modelled in the same way as done in the previous sections for the model of the ankle complex passive motion. Specifically, the talus and the tibia bones are considered in mutual contact at two points (at the medial malleolus and at the internal region of the inferior surface of the distal tibia articulated with the talus surface), while the talus and the fibula bones are considered in mutual contact at one point (at the lateral malleolus). The portion of each

contact surface is approximated by a spherical surface. Moreover, based on a careful inspection of the proximal part of the tibia and the fibula, only one point of contact is considered between the two bones. Thus, the connection between tibia and fibula bones surfaces at the proximal end is modelled as a plane-to-sphere contact higher pair. For the generation of these kinematic pairs, the approach used is the following: the areas of the surfaces of the mating bones which come into contact during the passive motion were digitized and approximated by best fit spherical or plane surfaces.

Furthermore, experimental data [30] showed that some fibres of the calcaneofibular ligament (CaFiL) and the tibiocalcaneal ligament (TiCaL) are almost isometric during the ankle passive motion. This means that these two ligaments can be represented as two rigid rods. For the other main four ligaments of the talocrural joint (i.e. the anterior tibiotalar ligament ant-TaTiL, posterior tibiotalar ligament post-TaTiL, anterior talofibular ligament ant-TaFiL, posterior talofibular ligament post-TaFiL), there are as yet no experimental data that prove the existence of isometric fibres during passive motion; however good results of previous studies that modelled the isometric fibres of TiCaL and CaFiL ligaments as rigid rods suggest that the other ligaments could also be represented by rigid rods. Finally, the interosseus membrane between the tibia and fibula is simply represented as a single isometric constraining fibre, and modelled as a single rigid rod.

Based on these observations and assumptions, a schematic representation of the TFC complex is shown in Fig. 3.13, where every rigid link represents a specific anatomical element. Here the three talo/calcaneal, fibular and tibia segments feature three sphere-to-sphere contact points and one plane-to-sphere contact point, where points A_i and B_i, $i = 4, 5$, represent the centres of the mating spherical surfaces fixed to the tibia and talus/calcaneus respectively. Points C_9 and D_9 represent the centres of the mating spherical surfaces fixed to the fibula and talus/calcaneus respectively, and point C represents the centre of the mating spherical surface fixed to the tibia. Moreover, points A_i and B_i, $i = 1, 2, 3$, represent the insertion points on the tibia and talus/calcaneus segments of the isometric fibre of the TiCaL ligament and of the ant-TaTiL and post-TaTiL ligaments, points C_j and D_j, $j = 6, 7, 8$, represent the insertion points on the fibula and talus/calcaneus segments of the isometric fibre of the CaFiL ligament and of the ant-TaFiL and post-TaFiL ligaments. Points C_{10} and A_{10} represent the insertion points on the fibula and tibia segments of the interosseus membrane fibre.

Inspection of Fig. 3.13, when considering, for instance, the tibia segment as a fixed body, and the ligament fibres as connected to the bones by spherical pairs centred at points A_i and B_i, $i = 1, 2, 3$, C_j and D_j, $j = 6, 7, 8$, and C_{10} and A_{10}, reveals that the schematic represents a spatial mechanism with one DOF, as can be shown by Kutzbach's formula [27] here reported:

$$l = \lambda(n - 1) - \sum_{k=1}^{m} (\lambda - l_k), \tag{3.9}$$

where l is the degree of freedom of the mechanism, λ is the dimension of the space of motion, n is the number of mechanism members, l_k is the degree of freedom of

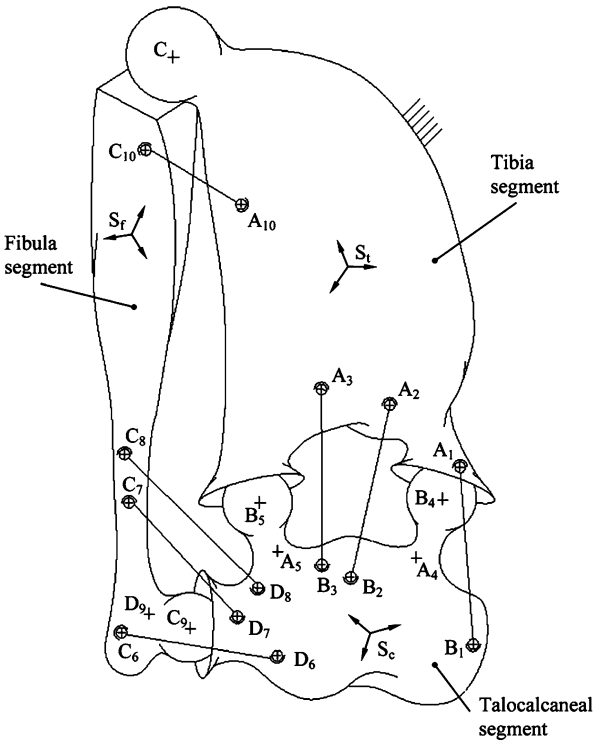

Fig. 3.13 Schematic of the TFC complex

the kth kinematic pair, $k = 1, 2, \ldots, m$, and m is the number of kinematic pairs of the mechanism. Indeed, because in this case λ is 6 and the mechanism (Fig. 3.13) is composed of 9 members ($n = 9$) and 18 kinematic pairs ($m = 18$), that are 14 spherical pairs with 3 DOFs and 4 higher pairs with 1 DOF, Kutzbach's formula provides 8 DOFs ($l = 8$). But noting that the rotations of the ligaments about the respective axes A_iB_i, $i = 1, 2, 3$, C_jD_j, $j = 6, 7, 8$, and $C_{10}A_{10}$ are inessential to the relative position of the segments, 7 DOFs have to be not considered and therefore $l = 1$ is the result of the computation. In particular, the talo/calcaneal segment has a one-DOF motion with respect to the tibia segment because the two segments are constrained by two sphere-on-sphere high pairs and three rigid rods linked to the bone segments by spherical pairs: this means that the fibula segment is dragged by the relative motion between tibia and talus/calcaneus segments during the ankle passive flexion.

During the relative motion of the three TFC segments each pair of mating spherical surfaces remains in contact; therefore the distances A_iB_i, $i = 4, 5$, C_9D_9 are constant. Moreover, the distances A_iB_i, $i = 1, 2, 3$, C_jD_j, $j = 6, 7, 8$, and $C_{10}A_{10}$ are also constant during the passive motion, since they represent the lengths of the rigid rods modelling the isometric ligament fibres. As a consequence, each pair of points (A_i, B_i), (C_j, D_j), and (C_{10}, A_{10}), with A_i, $i = 1, 2, \ldots, 5$, and A_{10} fixed to the tibia segment, C_j, $j = 6, 7, 8, 9$, and C_{10} fixed to the fibula segment, and fi-

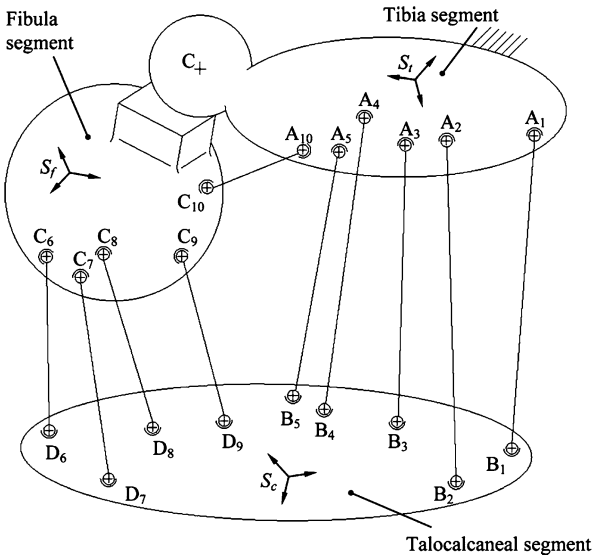

Fig. 3.14 The equivalent mechanism of the TFC complex

nally B_i, $i = 1, 2, \ldots, 5$, and D_j, $j = 6, 7, 8, 9$, fixed to the talo/calcaneal segment, respectively maintains a constant mutual distance during motion.

Based on this consideration, the equivalent mechanism of Fig. 3.13 can be more synthetically represented by the mechanism shown in Fig. 3.14. Here, the meaning of the points A_i, $i = 1, 2, \ldots, 5$, A_{10}, C_j, $j = 6, 7, 8, 9$, C_{10}, B_i, $i = 1, 2, \ldots, 5$, D_j, $j = 6, 7, 8, 9$, and C is the same as in Fig. 3.13. The elements $L_i = A_i B_i$, $i = 1, 2, \ldots, 5$, $L_j = C_j D_j$, $j = 6, 7, 8, 9$ and $L_{10} = A_{10} C_{10}$ can be regarded as constant length rigid links connected to two bone segments by spherical pairs centred at points A_i and B_i, $i = 1, 2, \ldots, 5$, C_j and D_j, $j = 6, 7, 8, 9$, and A_{10} and C_{10}, respectively. As a result, the mechanism has one DOF and in particular it provides the movable talo/calcaneal segment with one DOF with respect to the tibia base (rotation of links about the axes defined by their ending points (A_i, B_i), (C_j, D_j) and (A_{10}, C_{10}) respectively is irrelevant to the relative mobility of the three main segments). In the following considerations, for the sake of simplicity, this latter mechanism will be considered as the equivalent mechanism of the TFC complex.

3.3.3.2 Mathematical Formulation

The mathematical model of the one-DOF equivalent mechanism shown in Fig. 3.14, i.e. the model that provides the relationship between the independent variable of motion and the dependent ones, which define the configuration of the mechanism, is provided by the closure equations of the mechanism. The equations make it possible to find the relative position of the three bones (tibia, fibula and talus/calcaneus) during the ankle passive flexion. It is important to note that, with the relative po-

sition of the considered bones, the position of the other anatomical elements (such as for example the ligament insertion points) can also be easily found. In particular, in the equivalent mechanism shown in Fig. 3.14, each rigid rod constrains the distance between the two rod ending points to not change during motion; moreover, the plane-to-sphere contact higher pair causes a specific constrained relative motion between the two segments in contact, namely the tibia and fibula (as will be shown below).

In fact, with reference to Fig. 3.14, it can be noted that each pair of points $(A_i,\ B_i)$, $i = 1, 2, \ldots, 5$, $(C_j,\ D_j)$, $j = 6, 7, 8, 9$, and $(A_{10},\ C_{10})$ is constrained to maintain a constant mutual distance L_i, L_j and L_{10} respectively during motion. This makes it possible to write:

$$\begin{aligned} &\|\mathbf{A}_i - R_{tc} \cdot \mathbf{B}_i - \mathbf{p}_{tc}\|^2 = L_i^2 \quad (i = 1, \ldots, 5), \\ &\|\mathbf{D}_j - R_{cf} \cdot \mathbf{C}_j - \mathbf{p}_{cf}\|^2 = L_j^2 \quad (j = 6, \ldots, 9), \\ &\|\mathbf{A}_{10} - R_{tf} \cdot \mathbf{C}_{10} - \mathbf{p}_{tf}\|^2 = L_{10}^2, \end{aligned} \tag{3.10}$$

where $\mathbf{A}_i$ is the position vector of the point A_i measured in the reference system S_t, $\mathbf{B}_i$ and $\mathbf{D}_j$ are respective the position vectors of the points B_i and D_j measured in the reference system S_c, and $\mathbf{C}_j$ is the position vector of the point C_j measured in the reference system S_f. The Cartesian reference systems S_t, S_c and S_f are embedded in the tibia, talus/calcaneus and fibula segments respectively (see Figs. 3.13 and 3.14). The generic vector $\mathbf{p}_{ij}$ represents the position of the origin O_j of the generic reference system S_j with respect to the generic reference system S_i; the generic matrix R_{ij} is the orthogonal rotation matrix 3×3 that transforms the components of a vector measured in the generic reference frame S_j into the components of the same vector measured in the generic reference frame S_i (the indices c, t and f refer to S_c, S_t and S_f reference systems respectively). The matrix R_{ij} can be expressed as a function of three parameters that represent the orientation of the reference system S_j with respect to S_i.

The plane-to-sphere articular contact between tibia and fibula in the proximal end can be represented by constraining the centre of the sphere to move on a plane parallel to the articulating plane that approximates the fibula surface in the proximal end. Hereafter, $\mathbf{n}$ denotes the unit vector perpendicular to the plane in contact with the sphere, C the centre of the sphere, H a point of the plane the point C belongs to. Therefore, the plane-to-sphere contact constrains the vector $\mathbf{n}$ to be perpendicular to the segment CH, as it is expressed by (3.11):

$$^t\mathbf{n} \cdot \left(\mathbf{C} - ^t\mathbf{H}\right) = 0 \tag{3.11}$$

with

$$\begin{aligned} ^t\mathbf{n} &= R_{tf} \cdot \mathbf{n}, \\ ^t\mathbf{H} &= R_{tf} \cdot \mathbf{H} + \mathbf{p}_{tf}, \end{aligned} \tag{3.12}$$

where the vector $\mathbf{n}$ is measured in the reference system S_f, $\mathbf{H}$ is the position vector of the point H measured in the reference system S_f, $\mathbf{C}$ is the position vector of the point C measured in the reference system S_t, and the matrix R_{tf} and the vector $\mathbf{p}_{tf}$ have the same meaning as explained above.

The system of (3.10) and (3.11) represents the closure equations of the mechanism. When considering the tibia as a fixed body, for a given geometry, this system can be regarded as a system of eleven nonlinear equations in twelve variables, that are the three components of vector $\mathbf{p}_{tf}$, the three orientation parameters that define the rotation matrix R_{tf}, the three components of vector $\mathbf{p}_{tc}$ and the three orientation parameters that define the rotation matrix R_{tc}. By simple matrix operations, $\mathbf{p}_{cf}$ and R_{cf} can be easy calculated using the vectors $\mathbf{p}_{tf}$ and $\mathbf{p}_{tc}$, and the matrices R_{tf} and R_{tc}. Given the angle that measures the ankle flexion—i.e. the rotation between talus and tibia in the sagittal plane—, the remaining eleven variables can be found by solving the system of (3.10) and (3.11).

3.3.3.3 Experimental Session

In order to obtain the physical data necessary to synthesize the equivalent mechanism of the TFC complex, data from previous experimental sessions were used. With the experimental procedure shown in [14], the talocrural joint articular surfaces and the insertion areas of the CaFiL and TiCaL ligaments were obtained; the desired passive motion of the talus and the fibula with respect to the tibia were also measured.

The tibia anatomical frame (S_t) and the talus anatomical frame (S_c) were defined as described in [3]. The absence of many experimental anatomical data of the fibula bone made it impossible to define an anatomical frame embedded in the fibula; the reference frame of the tracker fixed to the fibula bone was thus considered as the reference frame S_f.

A sequence-independent joint coordinate system [20] was adopted in order to describe the orientation of the talus with respect to the tibia. The three following rotation axes were chosen: the z_t axis of S_t fixed to the tibia as the first one, the y_c axis of S_c fixed to the talus as the second one, finally an axis coincident with the shortest distance straight line of the other two axes as the third one. Three angles about these axes were defined: the ankle dorsiflexion(+)/plantarflexion(−) angle γ about the z-axis of S_t, the ankle internal(+)/external(−) rotation angle α about the y-axis of S_c, and the ankle pronation(+)/supination(−) angle β about a floating axis defined by the cross vector product of the unit vectors of the z-axis of S_t and the unit vector of the y-axis of S_c. Based on these conventions, the rotation matrix R_{ct} defined above was obtained.

The joint coordinate system that defines the orientation of the fibula with respect to the tibia was chosen in the same way as the one of the talus with respect to the tibia.

Table 3.3 Geometrical data of the mechanism obtained by the optimization procedure

	x [mm]	y [mm]	z [mm]	length [mm]
$\mathbf{A}_1$	1.229	13.886	36.510	–
$\mathbf{A}_2$	1.595	21.155	28.081	–
$\mathbf{A}_3$	3.949	15.083	33.483	–
$\mathbf{A}_4$	4.182	7.767	11.833	–
$\mathbf{A}_5$	12.559	−4.194	−3.713	–
$\mathbf{A}_{10}$	13.012	103.576	−18.510	–
$\mathbf{B}_1$	−14.209	−21.473	29.893	–
$\mathbf{B}_2$	−7.881	−21.839	10.398	–
$\mathbf{B}_3$	−26.293	−23.727	30.431	–
$\mathbf{B}_4$	−14.086	−14.815	9.891	–
$\mathbf{B}_5$	−11.713	−14.214	−3.319	–
$\mathbf{D}_6$	−47.171	−38.379	−7.023	–
$\mathbf{D}_7$	−7.715	−15.388	−14.858	–
$\mathbf{D}_8$	−87.580	19.809	30.818	–
$\mathbf{D}_9$	−22.168	−17.236	−47.668	–
$\mathbf{C}_6$	−30.924	159.337	−9.505	–
$\mathbf{C}_7$	−16.073	138.232	1.342	–
$\mathbf{C}_8$	−24.561	148.129	−21.234	–
$\mathbf{C}_9$	−51.610	129.629	−0.988	–
$\mathbf{C}_{10}$	−11.765	40.672	−16.166	–
$\mathbf{H}$	8.719	−187.044	−11.502	–
$\mathbf{n}$	−0.261	0.041	–	–
$\mathbf{C}$	16.276	341.897	−49.550	–
L_1	–	–	–	25.980
L_2	–	–	–	32.667
L_3	–	–	–	35.141
L_4	–	–	–	8.927
L_5	–	–	–	10.591
L_6	–	–	–	35.372
L_7	–	–	–	14.489
L_8	–	–	–	87.383
L_9	–	–	–	15.162
L_{10}	–	–	–	15.112

3.3.3.4 Parameter Optimization

Based on the topology of the TFC equivalent mechanism, its dimensional synthesis has been performed by the same procedure adopted for the knee and ankle mechanisms, as reported in Sect. 3.3.1.4.

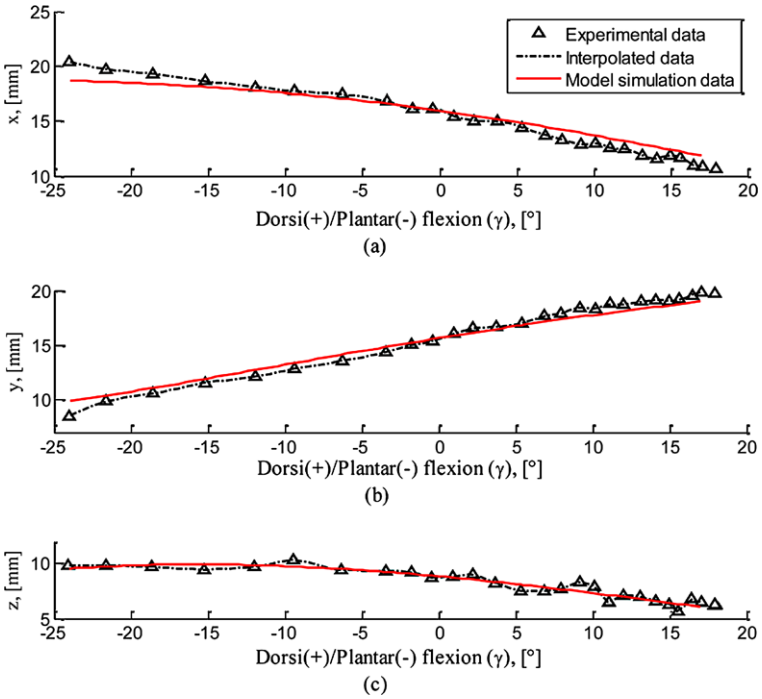

Fig. 3.15 Passive motion simulation of the talus/calcaneus respect to the tibia: x, (**a**), y, (**b**), and z, (**c**) versus ankle's flexion angle γ

3.3.3.5 Results

The geometry of the equivalent mechanism obtained by the optimization procedure is reported in Table 3.3. The distance between corresponding points in the initial mechanism and in the final mechanism is generally low, about 1–9 mm for the ligament insertions, and about 2–11 mm for the centres of the sphere.

The results of the ankle passive motion simulation (the relative passive motion between talo/calcaneal and tibia segments) obtained by the model (equivalent mechanism) were compared with those obtained by measurements. In particular, Figs. 3.15 and 3.16 show the positions x, y, and z of the origin of the reference system S_c with respect to S_t, and the angles α and β, respectively versus the ankle flexion angle γ. All figures show both the simulation and the experimental results. In particular, the experimental results are identified by the symbol Δ and interpolated by a dotted line. The interpolation makes it possible to use a higher number of (interpolated) experimental data, which may be useful for the optimal synthesis of the equivalent mechanism geometry. Inspection of the figures shows that the new equivalent spatial mechanism replicates the passive motion of the human ankle quite well.

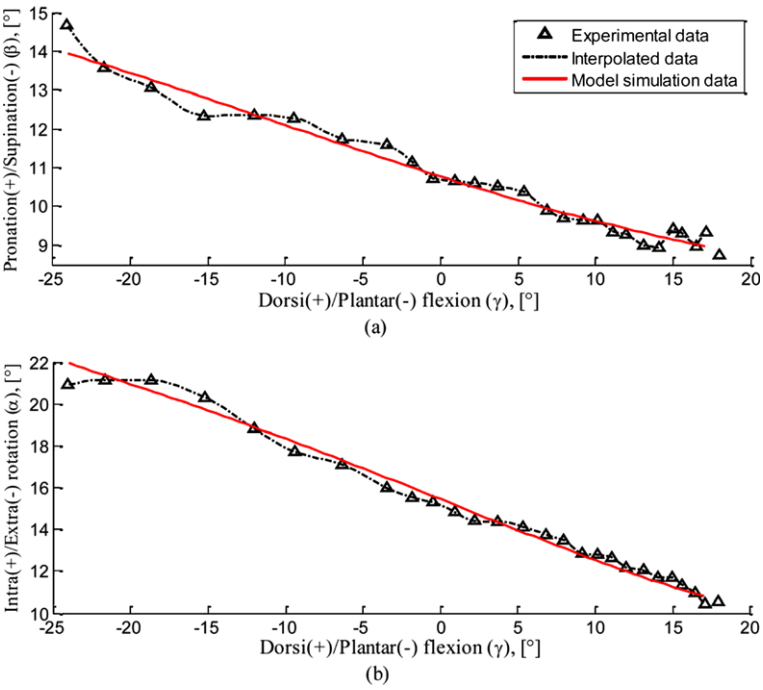

Fig. 3.16 Passive motion simulation of the talus/calcaneus respect to the tibia: angles β, (**a**), and α, (**b**), versus ankle's flexion angle γ

3.4 M1 Models for Prosthetic Design

When the aim of the modelling is to get a useful tool for prosthesis design, there is no longer the need to have a one-to-one correspondence between the joint anatomical structures and the corresponding mechanism links, but the mechanism has to be still capable to replicate the passive motion of the main bones of the joints. In this case the equivalent mechanisms can be simpler from a mechanical point of view than those presented in the previous sections and prove to be more efficient for the prosthesis design.

Within this frame, new simplified M1 mechanisms have been synthesized both for the knee and the ankle joint [15, 45, 48], which showed to be very efficient for the prosthesis design. Indeed, based on this idea, two patents were also devised [38, 39] which respectively provide some basic concepts [38] and a few solutions of innovative knee prosthesis [39].

Further papers [13, 47, 52] presented the model M2 for the knee and the ankle, making it possible to identify the joint stiffness and enlightening the role the different anatomical structures play for the joint stability. Moreover, recent papers shed light on the inherent overcontrained nature of the human joint [2, 51].

3.5 Conclusions

The chapter reported an overview of an efficient three step procedure for the definition of the kinematic, kinetostatic, and dynamic models of diarthrodial joints. Mainly focused on the kinematic model, which is the most difficult step that involves the synthesis of spatial mechanisms, the chapter reports the models of the knee, ankle and lower leg. Few additional information and comments are reported on the kinematic models and on the design of knee prosthesis.

Acknowledgements The financial support of Aer-Tech Lab, Bravo project and Lima Corporate is gratefully acknowledged. The authors also wish to thank the staff at Istituto Ortopedico Rizzoli for the collection of experimental data.

References

1. Andriacchi, T.P., Mikosz, R.P., Hampton, S.J., Galante, J.O.: Model studies of the stiffness characteristics of the human knee joint. J. Biomech. **16**(1), 23–29 (1983)
2. Baldisserri, B., Parenti-Castelli, V.: Passive motion modeling of the human ankle complex joint. In: Proceedings of 13th World Congress in Mechanism and Machine Science, pp. 1–7 (2011)
3. Baldisserri, B., Parenti-Castelli, V.: A new 3d mechanism for modeling the passive motion of the tibia-fibula-ankle complex. J. Mech. Robot. **4**, 021004 (2012)
4. Belvedere, C., Catani, F., Ensini, A., Moctezuma de la Barrera, J.L., Leardini, A.: Patellar tracking during total knee arthroplasty: an in vitro feasibility study. Knee surgery, sports traumatology. Arthroscopy **15**(8), 985–993 (2007)
5. Blajer, W., Dziewiecki, K., Mazur, Z.: Multibody modeling of human body for the inverse dynamics analysis of sagittal plane movements. Multibody Syst. Dyn. **18**(2), 217–232 (2007)
6. Blankevoort, L., Huiskes, R., Lange, A.D.: The envelope of passive knee joint motion. J. Biomech. **21**(9), 705–720 (1988)
7. Cheung, J.T.M., Zhang, M., Leung, A.K.L., Fan, Y.B.: Three-dimensional finite element analysis of the foot during standing—a material sensitivity study. J. Biomech. **38**, 1045–1054 (2005)
8. Colobert, B., Allard, A.C.P., Delamarche, P.: Force-plate based computation of ankle and hip strategies from double-inverted pendulum model. Clin. Biomech. **21**(4), 427–434 (2006)
9. Corazza, F., O'Connor, J.J., Leardini, A., Parenti-Castelli, V.: Ligament fibre recruitment and forces for the anterior drawer test at the human ankle joint. J. Biomech. **36**, 363–372 (2003)
10. Di Gregorio, R., Parenti-Castelli, V.: A spatial mechanism with higher pairs for modelling the human knee joint. J. Biomech. Eng. **125**(2), 232–237 (2003)
11. Di Gregorio, R., Parenti-Castelli, V., O'Connor, J.J., Leardini, A.: Equivalent spatial parallel mechanisms for the modelling of the ankle passive motion. In: Proceedings of ASME DETC 2004, 28th Biennial Mechanisms and Robotics Conference (2004)
12. Essinger, J.R., Leyvraz, P.F., Heegard, J.H., Robertson, D.D.: A mathematical model for the evaluation of the behaviour during flexion of condilar-type knee prosthesis. J. Biomech. **22**(11), 1229–1241 (1989)
13. Forlani, M., Baldisserri, B., Sancisi, N., Parenti-Castelli, V.: On the modelling of the ankle motion under static loads by a sequential procedure: model definition and preliminary results. In: Atti del XX CONGRESSO dell'Associazione Italiana di Meccanica Teorica e Applicata, pp. 1–10 (2011)
14. Franci, R., Parenti-Castelli, V.: A 5-5 one degree of freedom fully-parallel mechanism for the modelling of passive motion at the human ankle joint. In: Proceedings of ASME-IDETC/CIE 2007, Las Vegas, USA, pp. 1–8 (2007)

15. Franci, R., Parenti-Castelli, V.: A one-degree-of-freedom spherical wrist for the modelling of passive motion of the human ankle joint. In: Proceedings of IAK 2008, Lima, Peru, January 09–11, pp. 1–13 (2008)
16. Franci, R., Parenti-Castelli, V., Belevedere, C., Leardini, A.: A new one-dof fully parallel mechanism for modelling passive motion at the human tibiotalar joint. J. Biomech. **42**, 1403–1408 (2009)
17. Franci, R., Parenti-Castelli, V., Sancisi, N.: A three-step procedure for the modelling of human diarthrodial joints. Int. J. Mech. Control **10**(1), 3–12 (2009)
18. Glitsch, U., Baumann, W.S.: Three-dimensional determination of internal loads in the lower extremity. J. Biomech. **30**(11–12), 1123–1131 (1997)
19. Goodfellow, J.W., O'Connor, J.J.: The mechanics of the knee and prosthesis design. J. Bone Jt. Surg. **60-B**, 358–369 (1978)
20. Grood, E.S., Suntay, W.J.: A joint coordinate system for the clinical description of three-dimensional motions: application to the knee. J. Biomech. Eng. **105**, 136–144 (1983)
21. Gunther, M., Blickhan, R.: Joint stiffness of the ankle and the knee in running. J. Biomech. **35**(11), 1459–1474 (2002)
22. Hansen, A.H., Childress, D.S., Miff, S.C., Gard, S.A., Mesplay, K.P.: The human ankle during walking: implications for design of biomimetic ankle prostheses. J. Biomech. **37**, 1467–1474 (2004)
23. Hefzy, M.S., Cooke, T.D.V.: Review of knee models: 1996 update. Appl. Mech. Rev. **49**(10–2), 187–193 (1996)
24. Iida, F., Rummel, J., Seyfarth, A.: Bipedal walking and running with spring-like biarticular muscles. J. Biomech. **41**(3), 656–667 (2008)
25. Ji, Z., Findley, T., Chaudhry, H., Bruce, B.: Computational method to evaluate ankle postural stiffness with ground reaction forces. J. Rehabil. Res. Dev. **41**, 207–214 (2004)
26. Koopman, B., Grootenboer, H.J., de Jongh, H.J.: Inverse dynamics model for the analysis, reconstruction and prediction of bipedal walking. J. Biomech. **28**(11), 1369–1376 (1995)
27. Kutzbach, K.: Mechanische leitungsverzweigung; ihre gesetze und anwendungen. Maschinbau der Betrieb **8**(21), 710–716 (1929)
28. La Fortune, M.A., Cavanagh, P.R., Sommer, H.J. III, Kalenak, A.: Three-dimensional kinematics of the human knee during walking. J. Biomech. **25**(4), 347–357 (1992)
29. Leardini, A., O'Connor, J.J., Catani, F., Giannini, S.: A geometric model of the human ankle joint. J. Biomech. **32**(6), 585–591 (1999)
30. Leardini, A., O'Connor, J.J., Catani, F., Giannini, S.: Kinematics of the human ankle complex in passive flexion: a single degree of freedom system. J. Biomech. **32**(2), 111–118 (1999)
31. Ledoux, W., Camacho, D., Ching, R., Sangeorzan, B.: The development and validation of a computational foot and ankle model. In: Proceedings of Annual International Conference of the IEEE Engineering in Medicine and Biology, pp. 2899–2902 (2000)
32. Liacouras, P.C., Wayne, J.S.: Computational modeling to predict mechanical function of joints: application to the lower leg with simulation of two cadaver studies. J. Biomech. Eng. **129**, 811–817 (2007)
33. Merlet, J.P.: Kinematics and synthesis of cams-coupled parallel robots. In: Proceedings of CK2005, Cassino, Italy, May 4–6, pp. 1–12 (2005)
34. Meyer, A.R., Wang, M., Smith, P.A., Harris, G.F.: Modeling initial contact dynamics during ambulation with dynamic simulation. Med. Biol. Eng. Comput. **45**(4), 387–394 (2007)
35. Neptune, R., Kautz, S., Zajac, F.: Contributions of the individual ankle plantar flexors to support, forward progression and swing initiation during walking. J. Biomech. **34**(11), 1387–1398 (2001)
36. O'Connor, J.J., Shercliff, T.L., Biden, E., Goodfellow, J.W.: The geometry of the knee in the sagittal plane. Proc. Inst. Mech. Eng., H J. Eng. Med. **203**(4), 223–233 (1989)
37. Ottoboni, A., Parenti-Castelli, V., Sancisi, N., Belvedere, C., Leardini, A.: Articular surface approximation in equivalent spatial parallel mechanism models of the human knee joint. Proc. Inst. Mech. Eng., H J. Eng. Med. **224**(9), 1121–1132 (2010)

38. Parenti-Castelli, V.: Orthopaedic device and procedure to realize such a device (2007). Patent WO2007/074387
39. Parenti-Castelli, V., Catani, F., Sancisi, N., Leardini, A.: Improved orthopaedic device (2010). Patent WO2010/128485
40. Parenti-Castelli, V., Leardini, A., Di Gregorio, R., O'Connor, J.J.: On the modeling of passive motion of the human knee joint by means of equivalent planar and spatial parallel mechanisms. Auton. Robots **16**(2), 219–232 (2004)
41. Parenti-Castelli, V., Di Gregorio, R.: Parallel mechanisms applied to the human knee passive motion simulation. In: Lenarcic, J., Stanisic, M. (eds.) Advances in Robot Kinematics. Kluwer Academic, Dordrecht (2000)
42. Pictures, P.: Primal 3D Interactive Series: Knee. Primal Pictures Ltd., London (2003)
43. Pilkar, R.B., Moosbrugger, J.C., Bhatkar, V.V., Schilling, R.J., Storey, C.M., Robinson, C.J.: A biomechanical model of human ankle angle changes arising from short peri-threshold anterior translations of platform on which a subject stands. In: Proceedings of 29th Annual International Conference of IEEE-EMBS, pp. 4308–4311 (2007)
44. Rahman, E.A., Hefzy, M.S.: A two-dimensional dynamic anatomical model of the human knee joint. J. Biomech. Eng. **115**, 357–365 (1993)
45. Sancisi, N., Parenti-Castelli, V.: A 1-dof parallel spherical wrist for the modelling of the knee passive motion. In: Proceedings of IFToMM 2007, Besançon, France, June 17–21, pp. 1–6 (2007)
46. Sancisi, N., Parenti-Castelli, V.: A new 3d kinematic model of the patello-femoral joint during knee passive motion. In: Proceedings of AIMeTA 2007, Brescia, Italy, September 11–14, pp. 1–12 (2007)
47. Sancisi, N., Parenti-Castelli, V.: A sequential approach for modelling knee joint stiffness. In: Proceedings of Romansy 2008, Tokyo, Japan, July 05–09, pp. 1–8 (2008)
48. Sancisi, N., Parenti-Castelli, V.: A 1-dof parallel spherical wrist for the modelling of the knee passive motion. Mech. Mach. Theory **45**, 658–665 (2010)
49. Sancisi, N., Parenti-Castelli, V.: A new kinematic model of the passive motion of the knee inclusive of the patella. J. Mech. Robot. **3**(4), 041003 (2011)
50. Sancisi, N., Parenti-Castelli, V.: A novel 3d parallel mechanism for the passive motion simulation of the patella-femur-tibia complex. Meccanica **46**(1), 207–220 (2011)
51. Sancisi, N., Parenti-Castelli, V.: On the role of ligaments in the guidance of the human knee passive motion. In: Proceedings of Euromech Colloquium 511, Ponta Delgada, Azores, Portugal, March 09–12, pp. 1–9 (2011)
52. Sancisi, N., Parenti-Castelli, V.: A sequentially-defined stiffness model of the knee. Mech. Mach. Theory **46**, 1920–1928 (2011)
53. Sasimontonkul, S., Bay, B.K., Pavol, M.J.: Bone contact forces on the distal tibia during the stance phase of running. J. Biomech. **40**(15), 3503–3509 (2007)
54. Schepers, H.M., Veltink, P.H.: Estimation of ankle moment using ambulatory measurement of ground reaction force and movement of foot and ankle. In: Proceedings of First IEEE/RAS-EMBS International Conference on Biomedical Robotics and Biomechatronics, pp. 399–401 (2006)
55. Schepers, H.M., Koopman, H., Veltink, P.H.: Ambulatory assessment of ankle and foot dynamics. In: Proceedings of IEEE Transactions on Biomedical Engineering, pp. 895–900 (2006)
56. Tumer, T.S., Engin, A.E.: Three-body segment dynamic model of the human knee. J. Biomech. Eng. **115**, 350–356 (1993)
57. Wilson, D.R., Feikes, J.D., O'Connor, J.J.: Ligaments and articular contact guide passive knee flexion. J. Biomech. **31**(12), 1127–1136 (1998)
58. Wilson, D.R., O'Connor, J.J.: A three-dimensional geometric model of the knee for the study of joint forces in gait. Gait Posture **5**, 108–115 (1997)
59. Wismans, J., Velpaus, F., Janssen, J., Huson, A., Struben, P.: A three-dimensional mathematical model of the knee-joint. J. Biomech. **13**, 677–685 (1980)

Chapter 4
Kinematics and Algebraic Geometry

Manfred L. Husty and Hans-Peter Schröcker

4.1 Kinematic Mapping

A fundamental concept of relating mechanical structures with algebraic varieties is Study's representation of Euclidean displacements sometimes called kinematic mapping [30, 31]. It associates to every Euclidean displacement γ a point $\mathbf{c}$ in real projective space P^7 of dimension seven or, more precisely, a point on the Study quadric $S \subset P^7$. Sometimes it will be necessary to use also the complex extension $P^7(\mathbb{C})$ of the seven dimensional projective space. There exist other kinematic mappings besides Study's [3, 11, 25, 37] but these topics are beyond the scope of the present text.

Within the kinematics community more often four by four matrices incorporating translational and rotational part of the motion are used (4.2). Matrix elements are the design parameters of the mechanism (often called Denavit-Hartenberg parameters) and sines and cosines of the motion parameters. To move to algebra one either uses tangent half substitution transforming sines and cosines to algebraic values or one adds the identity $\sin^2 + \cos^2 = 1$.

A formal definition of Study's kinematic mapping is given below in Sect. 4.1.1. Our description is based on the original works of Study [30, 31] and Blaschke [4]. These are comprehensive and deep but not always easily readable texts and, unfor-

M.L. Husty (✉) · H.-P. Schröcker
Institute of Basic Sciences in Engineering, Unit Geometry and CAD, University Innsbruck, Technikerstraße 13, 6020 Innsbruck, Austria
e-mail: manfred.husty@uibk.ac.at
url: http://geometrie.uibk.ac.at

H.-P. Schröcker
e-mail: hans-peter.schroecker@uibk.ac.at

J.M. McCarthy (ed.), *21st Century Kinematics*,
DOI 10.1007/978-1-4471-4510-3_4,

tunately, only available in German.[1] Modern references on the same topic include [18] or [27].

4.1.1 Study's Kinematic Mapping

Euclidean three space is the three dimensional real vector space $\mathbb{R}^3$ together with the usual scalar product $\mathbf{x}^T\mathbf{y} = \sum_{i=1}^{3} x_i y_i$. A Euclidean displacement is a mapping

$$\gamma : \mathbb{R}^3 \to \mathbb{R}^3, \quad \mathbf{x} \mapsto \mathbf{A}\mathbf{x} + \mathbf{a} \tag{4.1}$$

where $\mathbf{A} \in \mathrm{SO}(3)$ is a proper orthogonal three by three matrix and $\mathbf{a} \in \mathbb{R}^3$ is a vector. The entries of $\mathbf{A}$ fulfill the well-known orthogonality condition $\mathbf{A}^T \cdot \mathbf{A} = \mathbf{I}_3$, where $\mathbf{I}_3$ is the three by three identity matrix.

The group of all Euclidean displacements is denoted by SE(3). It is a convenient convention to write (4.1) as product of a four by four matrix and a four dimensional vector according to[2]

$$\begin{bmatrix} 1 \\ \mathbf{x} \end{bmatrix} \mapsto \begin{bmatrix} 1 & \mathbf{o}^T \\ \mathbf{a} & \mathbf{A} \end{bmatrix} \cdot \begin{bmatrix} 1 \\ \mathbf{x} \end{bmatrix}. \tag{4.2}$$

Study's kinematic mapping $\varkappa$ maps an element α of SE(3) to a point $\mathbf{x} \in P^7$. If the homogeneous coordinate vector of $\mathbf{x}$ is $[x_0 : x_1 : x_2 : x_3 : y_0 : y_1 : y_2 : y_3]^T$, the kinematic pre-image of $\mathbf{x}$ is the displacement α described by the transformation matrix

$$\frac{1}{\Delta}\begin{bmatrix} \Delta & 0 & 0 & 0 \\ p & x_0^2+x_1^2-x_2^2-x_3^2 & 2(x_1x_2-x_0x_3) & 2(x_1x_3+x_0x_2) \\ q & 2(x_1x_2+x_0x_3) & x_0^2-x_1^2+x_2^2-x_3^2 & 2(x_2x_3-x_0x_1) \\ r & 2(x_1x_3-x_0x_2) & 2(x_2x_3+x_0x_1) & x_0^2-x_1^2-x_2^2+x_3^2 \end{bmatrix} \tag{4.3}$$

where

$$\begin{aligned} p &= 2(-x_0y_1 + x_1y_0 - x_2y_3 + x_3y_2), \\ q &= 2(-x_0y_2 + x_1y_3 + x_2y_0 - x_3y_1), \\ r &= 2(-x_0y_3 - x_1y_2 + x_2y_1 + x_3y_0), \end{aligned} \tag{4.4}$$

and $\Delta = x_0^2 + x_1^2 + x_2^2 + x_3^2$. The lower three by three sub-matrix is a proper orthogonal matrix if and only if

$$x_0y_0 + x_1y_1 + x_2y_2 + x_3y_3 = 0 \tag{4.5}$$

[1] An English translation of Blaschke's work is in preparation: W. Blaschke, Kinematics and Quaternions, translated by M. Husty and P. Zsombor-Murray, Springer 2013.

[2] Note that homogeneous coordinates in this chapter are written in the European notation, with homogenizing coordinate on first place.

and not all x_i are zero. When these conditions are fulfilled we call $[x_0 : \cdots : y_3]^T$ the *Study parameters* of the displacement α.

The important relation (4.5) defines a quadric $S \subset P^7$ and the range of $\varkappa$ is this quadric minus the three dimensional subspace defined by

$$E : x_0 = x_1 = x_2 = x_3 = 0. \tag{4.6}$$

We call S the *Study quadric* and E the *exceptional* or *absolute generator*.

The parameterization (4.3) of SE(3) may look rather artificial and complicated but it has an important feature: *The composition of displacements in Study parameters is bilinear* (see Sect. 4.1.2). In [30] Study shows that

- this requirement cannot be fulfilled with a smaller number of parameters and
- the representation of Euclidean displacements is unique, up to linear parameter transformations and transformations via identically fulfilled relations between the parameters.

Moreover, the Study parameters are closely related to the ring of *biquaternions* or *dual quaternions* as we shall rather say. The relation between Study parameters and dual quaternions will be discussed in Sect. 4.1.4.

For the description of a mechanical device in P^7 we usually need the inverse of the map given by (4.3) and (4.4), that is, we need to know how to compute the Study parameters from the entries of the matrix $\mathbf{A} = [a_{ij}]_{i,j=1,\ldots,3}$ and the vector $\mathbf{a} = [a_1, a_2, a_3]^T$. Mostly in kinematics literature a rather complicated and not singularity-free procedure, based on the Cayley transform of a skew symmetric matrix into an orthogonal matrix (see [10] or [2], p. 81), is used. The best way of doing this was, however, already known to Study himself. He showed that the homogeneous quadruple $x_0 : x_1 : x_2 : x_3$ can be obtained from at least one of the following proportions:

$$\begin{aligned} x_0 : x_1 : x_2 : x_3 &= 1 + a_{11} + a_{22} + a_{33} : a_{32} - a_{23} : a_{13} - a_{31} : a_{21} - a_{12} \\ &= a_{32} - a_{23} : 1 + a_{11} - a_{22} - a_{33} : a_{12} + a_{21} : a_{31} + a_{13} \\ &= a_{13} - a_{31} : a_{12} + a_{21} : 1 - a_{11} + a_{22} - a_{33} : a_{23} + a_{32} \\ &= a_{21} - a_{12} : a_{31} + a_{13} : a_{23} - a_{32} : 1 - a_{11} - a_{22} + a_{33}. \end{aligned} \tag{4.7}$$

In general, all four proportions of (4.7) yield the same result. If, however, $1 + a_{11} + a_{22} + a_{33} = 0$ the first proportion yields $0 : 0 : 0 : 0$ and is invalid. We can use the second proportion instead as long as $a_{22} + a_{33}$ is different from zero. If this happens we can use the third proportion unless $a_{11} + a_{33} = 0$. In this last case we resort to the last proportion which yields $0 : 0 : 0 : 1$. Having computed the first four Study

parameters the remaining four parameters $y_0 : y_1 : y_2 : y_3$ can be computed from

$$\begin{aligned} 2y_0 &= a_1x_1 + a_2x_2 + a_3x_3, \\ 2y_1 &= -a_1x_0 + a_3x_2 - a_2x_3, \\ 2y_2 &= -a_2x_0 - a_3x_1 + a_1x_3, \\ 2y_3 &= -a_3x_0 + a_2x_1 - a_1x_2. \end{aligned} \tag{4.8}$$

Example 4.1 A rotation about the z-axis through the angle φ is described by the matrix

$$\begin{bmatrix} 1 & 0 & 0 & 0 \\ 0 & \cos\varphi & -\sin\varphi & 0 \\ 0 & \sin\varphi & \cos\varphi & 0 \\ 0 & 0 & 0 & 1 \end{bmatrix}. \tag{4.9}$$

Its kinematic image, computed via (4.7) and (4.8) is

$$\mathbf{r} = [1 + \cos\varphi : 0 : 0 : \sin\varphi : 0 : 0 : 0 : 0]. \tag{4.10}$$

As φ varies in $[0, 2\pi)$, $\mathbf{r}$ describes a straight line on the Study quadric which reads after algebraization

$$\mathbf{r} = [1 : 0 : 0 : u : 0 : 0 : 0 : 0]. \tag{4.11}$$

Example 4.2 A special one parameter motion is defined by the matrix

$$\begin{bmatrix} 1 & 0 & 0 & 0 \\ 0 & \cos t & -\sin t & 0 \\ 0 & \sin t & \cos t & 0 \\ \sin\frac{t}{2} & 0 & 0 & 1 \end{bmatrix}. \tag{4.12}$$

Its kinematic image, computed via (4.7) and (4.8) reads

$$\mathbf{r} = \left[2 + 2\cos t : 0 : 0 : 2\sin t : \sin\frac{t}{2}\sin t : 0 : 0 : -\frac{1}{2}\sin\frac{t}{2}(2 + 2\cos t)\right]. \tag{4.13}$$

After algebraization and some manipulation we obtain

$$\mathbf{r} = \left[-1 + u^4 : 0 : 0 : -2u\left(1 + u^2\right) : 2u^2 : 0 : 0 : u\left(1 - u^2\right)\right], \tag{4.14}$$

which represents a rational curve of degree four on the Study quadric. The motion corresponding to this curve is a special case of the well known Bricard motions where all point-paths are spherical curves (see [5, p. 324]).

4.1.2 Fixed and Moving Frame

Suppose that $\alpha\colon \mathbf{x} \mapsto \mathbf{y} = \mathbf{A}\mathbf{x} + \mathbf{a}$ is a Euclidean displacement. The vectors $\mathbf{x}$ and $\mathbf{y}$ are elements of $\mathbb{R}^3$ but in kinematics it is advantageous to consider them as elements of two distinct copies of $\mathbb{R}^3$, called the *moving space* and the *fixed space*. The description of α in Study parameters depends on the choice of coordinate frames—*moving frame* and *fixed* or *base frame*—in both spaces. In kinematics, the moving frame is the space attached to a mechanism's output link, and the fixed space is the space where the mechanism itself is located (see Sect. 4.3). It is crucial for the following to know how changes of the fixed and moving frame act on the Study coordinates. Both types of transformations induce transformations of the Study quadric and thus impose a geometric structure on P^7. Kinematic mapping is constructed such that these transformations act linearly on the Study parameters (that is, they are projective transformations in P^7). We are going to compute their coordinate representations.

Consider a Euclidean displacement described by a four by four transformation matrix $\mathbf{X}$, as in (4.3). It maps a point $(1, \mathbf{a})^T$ to $(1, \mathbf{a}') = \mathbf{X} \cdot (1, \mathbf{a})^T$. Now we change coordinate frames in fixed and moving space and compute the matrix $\mathbf{Y}$ such that $(1, \mathbf{b}')^T = \mathbf{Y} \cdot (1, \mathbf{b})^T$ is the representation of the displacement in the new fixed coordinate frame and the *old* moving coordinate frame. This is slightly different from the typical change of coordinates known from linear algebra where one describes the new transformation in terms of new coordinates in *both* spaces but more suitable for application in kinematics, in particular for describing the position of the end effector tool or for concatenation of simple mechanisms. If the changes of coordinates in fixed and moving frame are described by

$$(1, \mathbf{a})^T = \mathbf{M} \cdot (1, \mathbf{b})^T, \qquad \left(1, \mathbf{b}'\right)^T = \mathbf{F} \cdot \left(1, \mathbf{a}'\right)^T, \tag{4.15}$$

we have $\mathbf{Y} = \mathbf{F} \cdot \mathbf{X} \cdot \mathbf{M}$. Denote now by $\mathbf{y}$, $\mathbf{x}$, $\mathbf{f} = [f_0, \ldots, f_7]^T$ and $\mathbf{m} = [m_0, \ldots, m_7]^T$ the corresponding Study vectors. Straightforward computation (or skillful use of dual quaternions, see Sect. 4.1.4) yields

$$\mathbf{y} = \mathbf{T}_f \mathbf{T}_m \mathbf{x}, \quad \mathbf{T}_m = \begin{bmatrix} \mathbf{A} & \mathbf{O} \\ \mathbf{B} & \mathbf{A} \end{bmatrix}, \ \mathbf{T}_f = \begin{bmatrix} \mathbf{C} & \mathbf{O} \\ \mathbf{D} & \mathbf{C} \end{bmatrix}, \tag{4.16}$$

where

$$\begin{aligned} \mathbf{A} &= \begin{bmatrix} m_0 & -m_1 & -m_2 & -m_3 \\ m_1 & m_0 & m_3 & -m_2 \\ m_2 & -m_3 & m_0 & m_1 \\ m_3 & m_2 & -m_1 & m_0 \end{bmatrix}, \qquad \mathbf{B} = \begin{bmatrix} m_4 & -m_5 & -m_6 & -m_7 \\ m_5 & m_4 & m_7 & -m_6 \\ m_6 & -m_7 & m_4 & m_5 \\ m_7 & m_6 & -m_5 & m_4 \end{bmatrix}, \\ \mathbf{C} &= \begin{bmatrix} f_0 & -f_1 & -f_2 & -f_3 \\ f_1 & f_0 & -f_3 & f_2 \\ f_2 & f_3 & f_0 & -f_1 \\ f_3 & -f_2 & f_1 & f_0 \end{bmatrix}, \qquad \mathbf{D} = \begin{bmatrix} f_4 & -f_5 & -f_6 & -f_7 \\ f_5 & f_4 & -f_7 & f_6 \\ f_6 & f_7 & f_4 & -f_5 \\ f_7 & -f_6 & f_5 & f_4 \end{bmatrix}, \end{aligned} \tag{4.17}$$

and $\mathbf{O}$ is the four by four zero matrix.

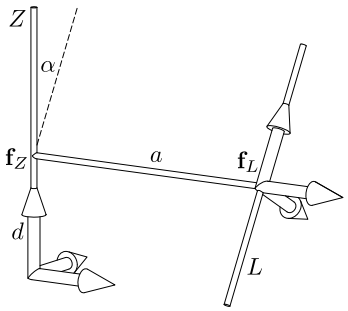

Fig. 4.1 Relative position of two lines Z and L (courtesy Martin Pfurner)

The matrices $\mathbf{T}_m$ and $\mathbf{T}_f$ commute (this means it does not matter which coordinate transformation is performed first) and they induce transformations of P^7 that fix the Study quadric S, the exceptional generator E, and the *exceptional* or *absolute quadric* $F \subset E$, defined by the equations

$$F : x_0 = x_1 = x_2 = x_3 = 0, \quad y_0^2 + y_1^2 + y_2^2 + y_3^2 = 0. \tag{4.18}$$

The quadrics S and F and the three space E are special objects in the geometry of the kinematic image space. Later we will describe a mechanism by its constraint equation(s) which will correspond to a subvariety V of P^7. A non-generic position of V with respect to these objects distinguishes its kinematic properties from a projectively equivalent subvariety W.

Example 4.3 In Example 4.1 we saw that the kinematic image of a continuous rotation about the z-axis is a straight line on the Study quadric. From the considerations in this section it follows immediately that the kinematic image of a continuous rotation about an arbitrary axis is a straight line.

Consider now a straight line $L \subset \mathbb{R}^3$ and denote the foot points of the common perpendicular to L and the z-axis Z by $\mathbf{f}_L$ and $\mathbf{f}_Z$. Assuming the common perpendicular of Z and L points in direction of the x-axis, the relative position of L with respect to Z can be specified by the z-coordinate d of $\mathbf{f}_Z$, the distance a between $\mathbf{f}_Z$ and $\mathbf{f}_L$ and the angle α between Z and L (Fig. 4.1). The numbers d, a and α are called the Denavit-Hartenberg parameters of the relative position of the line L with respect to the z-axis (see [32, Sect. 2.3]).

The displacement that transforms the standard coordinate frame to the coordinate frame with origin $\mathbf{f}_L$, x-axis in direction of the common perpendicular, and z-axis in direction of L in matrix form reads

$$\mathbf{G} = \begin{bmatrix} 1 & 0 & 0 & 0 \\ a & 1 & 0 & 0 \\ 0 & 0 & \cos\alpha & -\sin\alpha \\ d & 0 & \sin\alpha & \cos\alpha \end{bmatrix}. \tag{4.19}$$

Its Study vector is

$$\mathbf{g} = [2\gamma, 2\sin\alpha, 0, 0, a\sin\alpha, -a\gamma, -d\sin\alpha, -d\gamma]^T \tag{4.20}$$

where $\gamma = 1 + \cos\alpha$. The kinematic image of the rotation about L is $\mathbf{T}_f \cdot \mathbf{r}$ where $\mathbf{T}_f$ is obtained by substituting the components of $\mathbf{g}$ into (4.16). The result is

$$\begin{aligned}\mathbf{r}' = [&2\gamma,\ 2\sin\alpha,\ -2\sin\alpha u,\ 2\gamma u,\ a\sin\alpha + d\gamma u,\ -a\gamma - d\sin\alpha u,\\ &-d\sin\alpha + a\gamma u,\ -d\gamma + a\sin\alpha u],\end{aligned} \tag{4.21}$$

which is again linear in the motion parameter u.

4.1.3 Planar and Spherical Kinematic Mapping

The restriction of Study's kinematic mapping to certain three-spaces on the Study quadric yields elements of two important subgroups of SE(3), the group of planar Euclidean displacements SE(2) and the special orthogonal group SO(3) whose elements are pure rotations without any translational component. Both groups are of relevance in kinematics. Their kinematic mappings will be introduced in this subsection.

The planar Euclidean motion group SE(2) can be embedded into SE(3) by substituting $x_1 = x_2 = y_0 = y_3 = 0$ into (4.3). This yields the matrix parameterization

$$\frac{1}{x_0^2 + x_3^2}\begin{bmatrix} x_0^2 + x_3^2 & 0 & 0 \\ -2(x_0y_1 - x_3y_2) & x_0^2 - x_3^2 & -2x_0x_3 \\ -2(x_0y_2 + x_3y_1) & 2x_0x_3 & x_0^2 - x_3^2 \end{bmatrix} \tag{4.22}$$

of SE(2) (we omit the last row and the last column). The group SE(2) can be considered as kinematic pre-image of the three space $x_1 = x_2 = y_0 = y_3 = 0$, minus its intersection with the exceptional generator E, and we identify this three space with P^3. We describe its points by homogeneous coordinates $[x_0 : x_3 : y_1 : y_2]^T$.

The geometry of P^3 as range of planar kinematic mapping is governed by a change of coordinates in the moving or fixed frame or, equivalently, by its absolute figure consisting of the line $x_0 = x_3 = 0$ (the intersection of P^3 with the exceptional generator E) and the absolute points $[0 : 0 : 1 : \pm\mathrm{i}]^T$ (the intersection of P^3 with the absolute quadric F). This geometry is called *quasielliptic* (see for example [6, p. 399]).

The spherical motion group SO(3) can be embedded into SE(3) via

$$\frac{1}{\Delta}\begin{bmatrix} x_0^2 + x_1^2 - x_2^2 - x_3^2 & 2(x_1x_2 - x_0x_3) & 2(x_1x_3 + x_0x_2) \\ 2(x_1x_2 + x_0x_3) & x_0^2 - x_1^2 + x_2^2 - x_3^2 & 2(x_2x_3 - x_0x_1) \\ 2(x_1x_3 - x_0x_2) & 2(x_2x_3 + x_0x_1) & x_0^2 - x_1^2 - x_2^2 + x_3^2 \end{bmatrix} \tag{4.23}$$

where $\Delta = x_0^2 + x_1^2 + x_2^2 + x_3^2$. It is the kinematic pre-image of the three space $y_0 = y_1 = y_2 = y_3 = 0$. The absolute figure is the exceptional quadric $x_0^2 + x_1^2 + x_2^2 + x_3^2 = 0$ and the corresponding geometry is *elliptic* (see for example [9, Chap. VII]).

4.1.4 Euclidean Displacements and Dual Quaternions

Kinematic mapping is closely related to quaternion algebra. This relation shall be illustrated in this section. The set of quaternions $\mathbb{H}$ is the vector space $\mathbb{R}^4$ together with the quaternion multiplication

$$\begin{aligned}(a_0,a_1,a_2,a_3)\star(b_0,b_1,b_2,b_3) = (&a_0b_0 - a_1b_1 - a_2b_2 - a_3b_3,\\ &a_0b_1 + a_1b_0 + a_2b_3 - a_3b_2,\\ &a_0b_2 - a_1b_3 + a_2b_0 - a_3b_1,\\ &a_0b_3 - a_1b_2 - a_2b_1 + a_3b_0).\end{aligned} \tag{4.24}$$

The triple $(\mathbb{H},+,\star)$ (with component wise addition) forms a skew field. The real numbers can be embedded into this field via $x \mapsto (x,0,0,0)$, and vectors $\mathbf{x}\in\mathbb{R}^3$ are identified with quaternions of the shape $(0,\mathbf{x})$.

Every quaternion is a unique linear combination of the four basis quaternions $\mathbf{1} = (1,0,0,0)$, $\mathbf{i} = (0,1,0,0)$, $\mathbf{j} = (0,0,1,0)$, and $\mathbf{k} = (0,0,0,1)$. Their multiplication table is

$\star$	**1**	**i**	**j**	**k**
1	**1**	**i**	**j**	**k**
i	**i**	$-\mathbf{1}$	**k**	$-\mathbf{j}$
j	**j**	$-\mathbf{k}$	$-\mathbf{1}$	**i**
k	**k**	**j**	$-\mathbf{i}$	$-\mathbf{1}$

Conjugate quaternion and *norm* are defined as

$$\overline{A} = (a_0,-a_1,-a_2,-a_3), \qquad \|A\| = \sqrt{A\star\overline{A}} = \sqrt{a_0^2+a_1^2+a_2^2+a_3^2}. \tag{4.25}$$

Quaternions are closely related to spherical kinematic mapping.[3] Consider a vector $\mathbf{a} = [a_1,a_2,a_3]^T$ and a matrix $\mathbf{X}$ of the shape (4.23). Then the product $\mathbf{b} = \mathbf{X}\cdot\mathbf{a}$ can also be written as

$$B = X\star A\star\overline{X} \tag{4.26}$$

where $X = (x_0,x_1,x_2,x_3)$, $\|X\| = 1$ and $A = (0,\mathbf{a})$, $B = (0,\mathbf{b})$. In other words, spherical displacements can also be described by unit quaternions and spherical kinematic mapping maps a spherical displacement to the corresponding unit quaternion.

In order to describe general Euclidean displacements we have to extend the concept of quaternions. A *dual quaternion* Q is a quaternion over the ring of dual numbers, that is, it can be written as

$$Q = Q_0 + \varepsilon Q_1, \tag{4.27}$$

[3] For more detailed explanations see [4] or [27].

where $\varepsilon^2 = 0$. The algebra of dual quaternions has eight basis elements $\mathbf{1}$, $\mathbf{i}$, $\mathbf{j}$, $\mathbf{k}$, ε, $\varepsilon\mathbf{i}$, $\varepsilon\mathbf{j}$, and $\varepsilon\mathbf{k}$ and the multiplication table

$\star$	$\mathbf{1}$	$\mathbf{i}$	$\mathbf{j}$	$\mathbf{k}$	ε	$\varepsilon\mathbf{i}$	$\varepsilon\mathbf{j}$	$\varepsilon\mathbf{k}$
$\mathbf{1}$	$\mathbf{1}$	$\mathbf{i}$	$\mathbf{j}$	$\mathbf{k}$	ε	$\varepsilon\mathbf{i}$	$\varepsilon\mathbf{j}$	$\varepsilon\mathbf{k}$
$\mathbf{i}$	$\mathbf{i}$	$-\mathbf{1}$	$\mathbf{k}$	$-\mathbf{j}$	$\varepsilon\mathbf{i}$	$-\varepsilon\mathbf{1}$	$\varepsilon\mathbf{k}$	$-\varepsilon\mathbf{j}$
$\mathbf{j}$	$\mathbf{j}$	$-\mathbf{k}$	$-\mathbf{1}$	$\mathbf{i}$	$\varepsilon\mathbf{j}$	$-\varepsilon\mathbf{k}$	$-\varepsilon\mathbf{1}$	$\varepsilon\mathbf{i}$
$\mathbf{k}$	$\mathbf{k}$	$\mathbf{j}$	$-\mathbf{i}$	$-\mathbf{1}$	$\varepsilon\mathbf{k}$	$\varepsilon\mathbf{j}$	$-\varepsilon\mathbf{i}$	$-\varepsilon\mathbf{1}$
$\varepsilon\mathbf{1}$	ε	$\varepsilon\mathbf{i}$	$\varepsilon\mathbf{j}$	$\varepsilon\mathbf{k}$	0	0	0	0
$\varepsilon\mathbf{i}$	$\varepsilon\mathbf{i}$	$-\varepsilon\mathbf{1}$	$\varepsilon\mathbf{k}$	$-\varepsilon\mathbf{j}$	0	0	0	0
$\varepsilon\mathbf{j}$	$\varepsilon\mathbf{j}$	$-\varepsilon\mathbf{k}$	$-\varepsilon\mathbf{1}$	$\varepsilon\mathbf{i}$	0	0	0	0
$\varepsilon\mathbf{k}$	$\varepsilon\mathbf{k}$	$\varepsilon\mathbf{j}$	$-\varepsilon\mathbf{i}$	$-\varepsilon\mathbf{1}$	0	0	0	0

Dual quaternions know two types of conjugation. The *conjugate quaternion* and the *conjugate dual quaternion* of a dual quaternion $Q = x_0 + \varepsilon y_0 + \mathbf{x} + \varepsilon\mathbf{y}$ are defined as

$$\overline{Q} = x_0 + \varepsilon y_0 - \mathbf{x} - \varepsilon\mathbf{y} \quad \text{and} \quad Q_e = x_0 - \varepsilon y_0 + \mathbf{x} - \varepsilon\mathbf{y}, \tag{4.28}$$

respectively. The norm of a dual quaternion is

$$\|Q\| = \sqrt{Q\overline{Q}}. \tag{4.29}$$

With these definitions, the equation $\mathbf{b} = \mathbf{X} \cdot \mathbf{a}$ where $\mathbf{X}$ is a matrix of the shape (4.3) can be written as

$$B = X_e \star A \star \overline{X} \tag{4.30}$$

where $X = \mathbf{x} + \varepsilon\mathbf{y}$, $\|X\| = 1$, $\mathbf{x} = (x_0, \ldots, x_3)^T$, $\mathbf{y} = (y_0, \ldots, y_3)^T$, and $\mathbf{x} \cdot \mathbf{y} = 0$. The last condition is precisely the Study condition (4.5). A and B are dual quaternions of the type: $A = 1 + \varepsilon\mathbf{a}$, $B = 1 + \varepsilon\mathbf{b}$.

In other words, Euclidean displacements can also be described by unit dual quaternions that satisfy the Study condition and kinematic mapping maps a Euclidean displacement to the corresponding unit dual quaternion. The algebra of dual quaternions provides a convenient way of computing in Study coordinates (see for example [27, Chap. 9]).

4.1.5 Geometry of the Study Quadric

The topic of Sect. 4.1.2 was the geometry of the Study quadric S induced by coordinate changes in the fixed and in the moving space. Here we study the projective properties of S as hyper-quadric of seven dimensional projective space P^7. Our description follows [27, Sect. 11.2].

Lines in the Study quadric S correspond either to a one parameter set of rotations (see Example 4.1 resp. Example 4.3) or to a one parameter set of translations.

Lines through the identity ($[1:0:\cdots:0]$) correspond to one-parameter subgroups of SE(3) and are either rotation or translation subgroups.

The maximal subspaces of S are of dimension three ("3-planes"). More precisely, S is swept by two six dimensional families of 3-planes, called the *A-planes* and the *B-planes*. The A-planes and the B-planes are translates of the A-planes and the B-planes passing through the identity. Those 3-planes passing through the identity are the three dimensional subgroups of SE(3). They can be identified with SO(3) (the group of pure rotations) and with SE(2) (the group of planar Euclidean transformations). It is important to note that the exceptional three-space E, defined by $x_0 = x_1 = x_2 = x_3 = 0$, is an A-plane. The intersection of two A-planes or two B-planes is either empty or a one dimensional subspace. The intersection of an A-plane and a B-plane is either a point or a two dimensional plane. Whether an A-plane corresponds to SO(3) or SE(2) just depends on the intersection of the plane with E. In case of a point intersection the A-planes correspond to SO(3) and its translates; A-planes having line intersection with E correspond to SE(2) and its translates. General B-planes correspond to rotations about the axes in a plane, composed with a fixed displacement. The only B-plane that intersects the exceptional generator in a plane corresponds to the subgroup of all translations. All these cases belong of course to interesting kinematic configurations, but it would be beyond the scope of this paper to discuss all the possibilities. From algebraic point of view most attention has to be paid to the exceptional generator E because points in this space do not correspond to valid transformations in the pre-image space.

4.2 Some Basics from Algebraic Geometry

Before we can go into the discussion of how algebraic concepts can be used in mechanism analysis or synthesis we need to collect some basic concepts of this field. In this introduction only the most important definitions and theorems are given. We follow closely [7], which is an excellent introduction to algebraic geometry. More detailed descriptions and also the proofs for the theorems can be found there. Another source on the basics of this topic with references to engineering problems is [29, Chap. 12].

Examples in this section were computed using *Maple 15* with its packages `Groebner` and `PolynomialIdeals`.[4] The first package contains the low-level commands, the second package is newer and contains the more sophisticated ones. There are also other software packages like e.g. *Mathematica*, *Singular* or *Macaulay 2* which could have been used for these computations.

In the following all algebraic equations are polynomials in the ring $\mathbf{K}[\underline{x}] = \mathbf{K}[x_1, \ldots, x_n]$ where $\mathbf{K}$ is a field like $\mathbb{Q}$ (the rational numbers) or $\mathbb{C}$ (the complex numbers).

[4]Note that in the examples of this section often only the input of maple is displayed. To obtain the results one has to type these commands into Maple.

4.2.1 Ideals and Affine Varieties

At first polynomial ideals are defined which are the basic objects for everything else.

Definition 4.1 A set $I \subseteq \mathbf{K}[\underline{x}]$ is called an **ideal** if the following conditions are fulfilled:

- $\forall f, g \in I : f + g \in I$
- $\forall f \in I$ and $\forall h \in \mathbf{K}[\underline{x}] : hf \in I$

It follows that almost all ideals are infinite sets of polynomials and cannot be written down as a whole. The sole exception is the ideal $\{0\}$ which is also a proper subset resp. subideal of all other ideals because 0 is contained in every ideal. There is also an ideal which is a proper superset resp. superideal of them, namely the ideal which contains the constant polynomial 1 and with it all polynomials of $\mathbf{K}[\underline{x}]$.

Using Definition 4.1 it is possible now to define the ideal generated by a set of given polynomials $f_1, \ldots, f_s$.

Definition 4.2 Let $f_1, \ldots, f_s$ be polynomials in $\mathbf{K}[\underline{x}]$. Then the set

$$\langle f_1, \ldots, f_s \rangle = \left\{ g \in \mathbf{K}[\underline{x}] : g = \sum_{i=1}^{s} h_i f_i \text{ and } h_1, \ldots, h_s \in \mathbf{K}[\underline{x}] \right\}$$

is the **ideal generated by** $f_1, \ldots, f_s$.

The ideal generated by the given polynomials is the set of all combinations of these polynomials using coefficients from $\mathbf{K}[\underline{x}]$. The polynomials $f_1, \ldots, f_s$ form a so called *basis* of the ideal. Due to the fact that the same ideal can be generated by another set of polynomials, such a basis is not unique. Furthermore the ideal is obviously *finitely generated* and it can be shown that every ideal of $\mathbf{K}[\underline{x}]$ can be generated by a finite set of polynomials (Hilbert Basis Theorem). So the two special ideals mentioned above can be written as $\langle 0 \rangle$ and $\langle 1 \rangle$.

Example 4.4 A circle is to be intersected with an ellipse. The algebraic equations of both objects are $f_1 = (x_1 - 1)^2 + (x_2 - 2)^2 - 4 = 0$ and $f_2 = x_1^2 + 3x_2^2 - 5 = 0$. Using Maple one has to type the following to define the corresponding ideal:

```
with(PolynomialIdeals);
I1:=<(x[1]-1)^2+(x[2]-2)^2-4,x[1]^2+3*x[2]^2-5>;
```

All commands in the package `Groebner` allow to use the notation $[\ldots]$ instead of $<\cdots>$.

As it was mentioned above such a basis is not unique. For example the ideals $\langle f_1, f_2 \rangle$ and $\langle f_1 - f_2, f_2 \rangle$ are the same. But how can this be found out for two given ideals, if the are equal or not?

Two ideals I and J are equal if each element of I is contained in J and vice versa. It is sufficient to test if the basis of one ideal is contained in the other, and vice versa.

To find out if a given polynomial is a member of an ideal it is necessary to test if the polynomial can be written as a combination of the ideal's basis. How this can be done in a systematic way will be explained later.

Before that affine varieties are introduced.

Definition 4.3 For a given ideal $I = \langle f_1, \ldots, f_s \rangle \subseteq \mathbf{K}[\underline{x}]$ the set

$$\mathbf{V}(I) = \left\{(a_1, \ldots, a_n) \in \mathbf{K}^n : f_i(a_1, \ldots, a_n) = 0 \text{ for all } 1 \leq i \leq s\right\} \subseteq \mathbf{K}^n$$

is called the **affine variety** of the ideal I.

For each ideal $I = \langle f_1, \ldots, f_s \rangle$ there exist a unique variety $\mathbf{V}(I)$ which is the set of all solutions of the polynomials equations $f_1 = 0, \ldots, f_s = 0$, the so called *vanishing set*. It follows immediately that all bases of the ideal describe the same variety. In general the variety of an ideal is the more interesting thing, not the ideal itself, because the variety is exactly the set of solutions of the input equations $f_1, \ldots, f_s$. It has to be mentioned explicitly that the variety does not contain information about the multiplicity of solutions. It is just a set of points in $\mathbf{K}[\underline{x}]$, nothing more.

Two special varieties are $\emptyset$ and $\mathbf{K}^n$ which are the vanishing sets of the ideals $\langle 1 \rangle$ and $\langle 0 \rangle$ which appeared earlier.

Example 4.5 A circle with center $(0, 0)$ and a line are given by $x_1^2 + x_2^2 - 1 = 0$ and $x_1 + x_2 - 1 = 0$. Then the ideal generated by these two equations is given by $I = \langle x_1^2 + x_2^2 - 1, x_1 + x_2 - 1 \rangle$ and the corresponding variety is $\{(1, 0), (0, 1)\}$.

It is also possible that different ideals describe the same variety. This is related to the fact that solutions can appear with higher multiplicities.

Example 4.6 The following polynomial ideals I and I' are given, each by two possible bases.

$$I = \left\langle x_1^2 + x_2^2 - 1, x_1 + x_2 - 1 \right\rangle = \left\langle x_2^2 - x_2, x_1 + x_2 - 1 \right\rangle,$$
$$I' = \left\langle \left(x_1^2 + x_2^2 - 1\right)^2, x_1 + x_2 - 1 \right\rangle = \left\langle x_2^4 - 2x_2^3 + x_2^2, x_1 + x_2 - 1 \right\rangle.$$

It can easily be seen that $\mathbf{V}(I) = \mathbf{V}(I') = \{(1, 0), (0, 1)\}$ but the ideals are not equal because $x_2^2 - x_2$ cannot be written as a combination of $x_2^4 - 2x_2^3 + x_2^2$ and $x_1 + x_2 - 1$.

To test if two ideals describe the same variety *radicals* are introduced.

Definition 4.4 Let $I \subseteq \mathbf{K}[\underline{x}]$ be an ideal. The set

$$\sqrt{I} := \left\{ f \in \mathbf{K}[\underline{x}] : \exists m \in \mathbb{N}, m \geq 1 \text{ with } f^m \in I \right\}$$

is called the **radical** of I.

The computation of the radical of an ideal I can be seen as reducing I down to the most important things, relevant for its vanishing set. In the example above it is $\sqrt{I} = \sqrt{I'} = I$.

Example 4.7 The ideal $I = \langle (2x_1 - x_2 - 2)x_1, (2x_1 - x_2 - 2)x_2^2 \rangle$ is given, where its vanishing set $\mathbf{V}(I)$ is the line described by $2x_1 - x_2 - 2$ and the isolated point $(0, 0)$. To be exact, there are two copies of the point $(0, 0)$ when multiplicities are taken into account.

Computation of the radical using Maple leads to the slightly simpler ideal $\sqrt{I} = \langle -(2x_1 + x_2)(2x_1 - x_2 - 2), -(2x_1 - x_2 - 2)x_1 \rangle$ which has the same vanishing set, but now the point $(0, 0)$ does not appear with higher multiplicity. The code for Maple is the following:

```
with(PolynomialIdeals);
I1:=<(2*x[1]-x[2]-2)*x[1], (2*x[1]-x[2]-2)*x[2]^2>;
rad:=factor(Radical(I1));
```

$$\text{rad} := \big\langle -(2x_1 - x_2 - 2)x_1, -(2x_1 + x_2)(2x_1 - x_2 - 2) \big\rangle.$$

Next some operations are given which can be applied to varieties.

Let $I = \langle f_1, \ldots, f_s \rangle$ and $J = \langle g_1, \ldots, g_t \rangle$ be ideals with corresponding varieties $V = \mathbf{V}(I)$ and $W = \mathbf{V}(J)$. Then the **union** and **intersection** of V and W can be described as follows:

$$V \cap W = \mathbf{V}\big(\langle f_1, \ldots, f_s, g_1, \ldots, g_t \rangle\big),$$
$$V \cup W = \mathbf{V}\big(\langle f_i g_j : 1 \le i \le s, 1 \le j \le t \rangle\big).$$

The first equality is quite clear, if one is searching for the solutions two systems have in common, the equations are combined and the resulting system is examined. The second equality can be used to construct varieties which are a composition of simpler varieties.

Example 4.8 Three very simple varieties are given to show what happens, when varieties are intersected or joined.

$$V_1 = \mathbf{V}\big(\langle x_1 \rangle\big), \qquad V_2 = \mathbf{V}\big(\langle x_2 \rangle\big),$$
$$V_1 \cap V_2 = \mathbf{V}\big(\langle x_1, x_2 \rangle\big) = \big\{(0, 0)\big\}, \qquad V_1 \cup V_2 = \mathbf{V}\big(\langle x_1 x_2 \rangle\big).$$

What happens when two varieties are joined where one is a subset of the other variety?

$$V_1 \cup \mathbf{V}\big(\langle x_1, x_2 \rangle\big) = \mathbf{V}\big(\langle x_1^2, x_1 x_2 \rangle\big).$$

It can easily be seen that the vanishing set is the same, but when multiplicities are taken into account the point $(0, 0)$ appears twice.

We come back to the different ways to generate an ideal. As already mentioned there are lots of different bases which describe all the same ideal, e.g. the ideals

$$I = \langle f_1, f_2, f_3 \rangle \subseteq \mathbf{K}[x_1, x_2, x_3, x_4],$$
$$I' = \langle f_1, x_2^2 f_1 - f_2, 2f_3 + (x_3 + 5) f_2 - f_1 \rangle.$$

It can easily be verified that each combination of the generators of I' can be written as a combination of generators of I and vice versa.

But what to do when the ideals are more complex? It is necessary to have a systematic way for testing if a polynomial is a combination of some other polynomials. Therefore the concept of *multivariate division with remainder* is introduced, which is similar to the well known *univariate division with remainder* which shall be treated first. Let $f, g \in \mathbf{K}[x_1]$ be univariate polynomials with $g \neq 0$. Then there exist unique polynomials q and r such that

$$f = qg + r$$

with either $r = 0$ or $\deg(r) < \deg(g)$. In the corresponding algorithm an appropriate multiple of g is subtracted from f such that the monomial with highest degree is canceled from f. This procedure is repeated until the remainder is either 0 or has degree less than $\deg(g)$.

Example 4.9 Here an example with $f = 2x^2 - 3x - 7$ and $g = x + 5$:

$$f - \mathbf{2x}g = 2x^2 - 3x - 7 - 2x(x + 5) = -13x - 7,$$
$$(-13x - 7) - (-\mathbf{13})g = -13x - 7 + 13x + 65 = \mathbf{58}.$$

It follows that $q = 2x - 13$ and 58. To get these results with Maple the commands would be

```
quo(f,g,x); rem(f,g,x);
```

The process stops when the highest monomial of the remainder is not divisible by the highest monomial of g. So in the univariate case the degree of monomials can be seen as a natural *order* on the set of monomials, which guides the user trough the algorithm.

In the following *termorders* are introduced which allow ordering of a multivariate polynomial's monomials. With these termorders an analogous algorithm can be defined for multivariate polynomials.

Definition 4.5 Let $\underline{x}^\alpha = x_1^{\alpha_1} \dots x_n^{\alpha_n}$ and $\underline{x}^\beta = x_1^{\beta_1} \dots x_n^{\beta_n}$ be monomials in $\mathbf{K}[\underline{x}] = \mathbf{K}[x_1, \dots, x_n]$. To order these monomials a **monomial ordering** or **termorder** $>_{\underline{x}}$ on the set of monomials in $\mathbf{K}[\underline{x}]$ is defined by an ordering $>$ on the n-tuples $\alpha, \beta \in \mathbb{Z}^n_{\geq 0}$ which has to fulfill the following conditions:

- is a total ordering on $\mathbb{Z}^n_{\geq 0}$

- if $\alpha > \beta$ and $\gamma \in \mathbb{Z}^n_{\geq 0}$, then $\alpha + \gamma > \beta + \gamma$
- every nonempty subset of $\mathbb{Z}^n_{\geq 0}$ has a smallest element under $>$.

If such an ordering $>$ on $\mathbb{Z}_{\geq 0}$ is given the monomials are ordered using the following equivalence:

$$\underline{x}^{\alpha} >_{\underline{x}} \underline{x}^{\beta} \quad \Longleftrightarrow \quad \alpha > \beta.$$

Therefore monomials are ordered by comparing the ordered n-tuples constructed from the powers of each variable. Next the most important termorderings are given.

Definition 4.6 (Lexicographic Order) Let $\alpha = (\alpha_1, \ldots, \alpha_n)$ and $\beta = (\beta_1, \ldots, \beta_n)$ be elements of $\mathbb{Z}^n_{\geq 0}$. We define $\alpha >_{lex} \beta$ if the leftmost nonzero entry of the vector-difference $\alpha - \beta \in \mathbb{Z}^n$ is positive.

In Maple this ordering specified by `plex`, for example a lexicographic termorder for polynomials containing the unknowns $\{x_1, x_2, x_3\}$ could be specified to be `plex(x[3],x[1],x[2])`.

Example 4.10 How this ordering looks like for monomials in $\mathbf{K}[x_1, x_2]$ can be seen in the following. It is a sketch how the set of all monomials is ordered, first the 2-tuples are given, then the corresponding monomials starting with the smallest.

$$(0,0) <_{lex} (0,1) <_{lex} (0,2) \ldots <_{lex} (1,0) <_{lex} (1,1) <_{lex} (1,2) \ldots,$$
$$1 <_{lex} x_2 <_{lex} x_2^2 \cdots <_{lex} x_1 <_{lex} x_1 x_2 <_{lex} x_1 x_2^2 \ldots.$$

Maple has the command `TestOrder` to test if a monomial is smaller than another one.

```
with(Groebner);
TestOrder(x[1]*x[2],x[2]^5,plex(x[1],x[2]));
TestOrder(x[2]^4,x[1]^2*x[2],plex(x[1],x[2]));
```

The result of the first test will be *false*, the second result will be *true*.

There are other term orderings such as Graded Lex Order (in Maple `grlex`) or Graded Reverse Lex Order (in Maple `tdeg`). For their definition the reader is referred to [7, pp. 54–61].

All these orderings can also be combined which leads to the so called *Product Orders*. An example for a product order on $\mathbf{K}[x_1, x_2, x_3, x_4]$ in Maple would be `prod(plex(x[1],x[2]),tdeg(x[3],x[4]))`. This means that monomials are first compared using the `plex` order, ties are broken using the `tdeg` order. Even more than two partial orders are allowed.

It has to be noted explicitly that also the ordering of the variables can be varied, not only the type. All in all there are lots of different ways to define an order for ordering monomials.

Before the multivariate polynomial division can be defined another definition is necessary.

Definition 4.7 Let $f \in \mathbf{K}[\underline{x}]$ be a polynomial with $f = \sum_\alpha a_\alpha x^\alpha$ and let $>_{\underline{x}}$ be a monomial ordering on $\mathbf{K}[\underline{x}]$. We define the **leading monomial** $\mathrm{LM}(f)$ as the highest monomial of f with respect to $>_{\underline{x}}$, the **leading coefficient** $\mathrm{LC}(f)$ as the coefficient of the highest monomial, and the **leading term** as $\mathrm{LT}(f) = \mathrm{LC}(f) \cdot \mathrm{LM}(f)$.

The most important notion in this definition is the leading monomial. It will appear quite often in the following definitions and examples.

Example 4.11 Determine the degree $\deg(f)$, $\mathrm{LM}(f)$, $\mathrm{LC}(f)$ and $\mathrm{LT}(f)$ of the polynomial $f = x_1^2x_2^3 - 5x_1x_2x_3 + 4x_1^3x_3^2$ using the termorder $>_{grlex}$ on $\mathbf{K}[\underline{x}]$. The result is

$$\deg(f) = 5, \qquad \mathrm{LM}(f) = x_1^3x_3^2, \qquad \mathrm{LC}(f) = 4, \qquad \mathrm{LT}(f) = 4x_1^3x_3^2.$$

To obtain these results with Maple the following commands have to be used:

```
with(Groebner);
f:=x[1]^2*x[2]^3-5*x[1]*x[2]*x[3]+4*x[1]^3*x[3]^2;
degree(f,[x[1],x[2],x[3]]);
LeadingMonomial(f,grlex(x[1],x[2],x[3]));
LeadingCoefficient(f,grlex(x[1],x[2],x[3]));
LeadingTerm(f,grlex(x[1],x[2],x[3]));
```

For the leading term Maple does not return the product but the pair $\mathrm{LC}(f), \mathrm{LM}(f)$. If the termorder `plex(x[2],x[3],x[1])` is used instead the results are as follows:

$$\deg(f) = 5, \qquad \mathrm{LM}(f) = x_1^2x_2^3, \qquad \mathrm{LC}(f) = 1, \qquad \mathrm{LT}(f) = x_1^2x_2^3.$$

Now all ingredients are defined to introduce the multivariate division.

Definition 4.8 Let $F = [f_1, \ldots, f_s]$ be an ordered list of polynomials in $\mathbf{K}[\underline{x}]$ and $>_{\underline{x}}$ a monomial order. Then every polynomial $f \in \mathbf{K}[\underline{x}]$ can be written in the form

$$f = a_1 f_1 + \cdots + a_s f_s + r$$

where all a_i and r are elements of $\mathbf{K}[\underline{x}]$ and r is either 0 or a polynomial where no monomial is divisible by any of $\mathrm{LM}(f_1), \ldots, \mathrm{LM}(f_s)$. r is called **a remainder** of f on division by F.

Example 4.12 As an example the polynomial $f = x_1^2x_2 + x_1x_2^2 + x_2^2$ is divided by the polynomials $f_1 = x_1x_2 - 1$ and $f_2 = x_2^2 - 1$, where the termorder $>_{lex}$ is used in $\mathbf{K}[x_1, x_2]$.

$$f = x_1^2x_2 + x_1x_2^2 + x_2^2, \quad r = 0,\ a_1 = 0,\ a_2 = 0,$$
$$f \leftarrow x_1x_2^2 + x_1 + x_2^2, \quad r = 0,\ a_1 = x_1,\ a_2 = 0,$$

$$
\begin{aligned}
f &\leftarrow x_1 + x_2^2 + x_2, \quad r = 0,\ a_1 = x_1 + x_2,\ a_2 = 0,\\
f &\leftarrow x_2^2 + x_2, \quad r = x_1,\ a_1 = x_1 + x_2,\ a_2 = 0,\\
f &\leftarrow x_2 + 1, \quad r = x_1,\ a_1 = x_1 + x_2,\ a_2 = 1\\
f &\leftarrow 1, \quad r = x_1 + x_2,\ a_1 = x_1 + x_2,\ a_2 = 1,\\
f &\leftarrow 0, \quad r = x_1 + x_2 + 1,\ a_1 = x_1 + x_2,\ a_2 = 1.
\end{aligned}
$$

It follows that f can be written as

$$f = a_1 f_1 + a_2 f_2 + r = (x_1 + x_2)(x_1 x_2 - 1) + (1)\left(x_2^2 - 1\right) + (x_1 + x_2 + 1)$$

where no monomial in the remainder $x_1 + x_2 + 1$ is divisible by $\mathrm{LM}(f_1)$ or $\mathrm{LM}(f_2)$.

It has to be said clearly that the result r is *a remainder* of f on division by the list F. If f_1 is exchanged with f_2 the following result is obtained:

$$f = a_1' f_1 + a_2' f_2 + r' = (x_1 + 1)\left(x_2^2 - 1\right) + (x_1)(x_1 x_2 - 1) + (2x_1 + 1).$$

So the remainder r depends on the order of the polynomials in the list F and of course, on the monomial order which has to be chosen first of all.

Using the multivariate division the notion of *reduction* can be defined.

Definition 4.9 Let $F = [f_1, \ldots, f_s]$ be an ordered list of polynomials in $\mathbf{K}[\underline{x}]$, $f \in \mathbf{K}[\underline{x}]$ and $>_{\underline{x}}$ a monomial order. Then we call the process of dividing f by F **reduction** and denote the remainder with $\overline{f}^F$. The choice of a monomial order is required to be able to compute the remainder.

This reduction will be used quite often in the following definitions and examples. But before that the corresponding Maple command is given.

Example 4.13 The polynomial $f = x_1^2 x_2 + x_1 x_2^2 + x_2^2$ has to be divided by the polynomials $f_1 = x_1 x_2 - 1$ and $f_2 = x_2^2 - 1$, using the termorder $>_{lex}$ in $\mathbf{K}[x_1, x_2]$.

```
with(Groebner);
f:=x[1]^2*x[2]+x[1]*x[2]^2+x[2]^2;
f1:=x[1]*x[2]-1; f2:=x[2]^2-1;
r:=Reduce(f,[f1,f2],plex(x[1],x[2]),'s','a');
```

The result is a remainder r, a list of quotients a and a number s such that

$$f = \sum_{i=1}^{2} a_i f_i + \frac{r}{s}.$$

For this example:

$$r = x_1 + x_2 + 1, \qquad a = [x_1 + x_2, 1], \qquad s = 1.$$

The necessity of a monomial order will not be mentioned explicitly from now on. Next we define *interreduction*.

Definition 4.10 Let $F = [f_1, \ldots, f_s]$ be an ordered list of polynomials in $\mathbf{K}[\underline{x}]$. The process of replacing each polynomial f_i by $\overline{f_i}^{F\setminus\{f_i\}}$ is called **interreduction** of the list F.

This means that every polynomial in F is reduced with respect to all the other elements of the list. An important property if an interreduction is that the original set of polynomials and the result of the interreduction generate the same ideal. Interreduction can sometimes be used to simplify generating sets (bases) of an ideal, to obtain shorter polynomials. The right choice of the monomial order is important.

Example 4.14 The ideal $I = \langle (x_1 - 1)^2 + (x_2 + 5)^2 - 6, 2x_1^2 + 2x_2^2 - 4\rangle$ is interreduced. The appropriate commands are the following:

```
with(Groebner);
I1:=[(x[1]-1)^2+(x[2]+5)^2-6,2*x[1]^2+2*x[2]^2-5];
ir:=InterReduce(I1,plex(x[1],x[2]));
```

And the result is

$$ir = \left[416x_2^2 + 1800x_2 + 1985, 4x_1 - 20x_2 - 45\right].$$

We come back to ideals generated by a set of polynomials. There was already the question posed how one could decide if a given polynomial f is an element of $I = \langle f_1, \ldots, f_s\rangle$. The concept of reduction would be a good method to answer that question. That this concept is not the best solution is shown explicitly in [7, p. 67], because if all remainders of the reduction are zero, then one knows that the tested polynomial is in the given ideal, but if some remainders are not zero the question is still open. The zero result of the reduction is just a sufficient but not a necessary condition for ideal membership.

Now *standard bases* are defined which are "much better" representatives (generators) for an ideal. They are still dependent from a chosen monomial order but nevertheless very useful to deduce information about the ideal and the corresponding variety.

4.2.2 Standard Bases

Definition 4.11 For a fixed monomial order and an ideal $I \in \mathbf{K}[\underline{x}]$ a finite subset $G = \{g_1, \ldots, g_t\}$ of I is called a **Groebner basis** or **standard basis** if

$$\left\langle \mathrm{LM}(g_1), \ldots, \mathrm{LM}(g_t)\right\rangle = \left\langle \mathrm{LM}(I)\right\rangle$$

where $\mathrm{LM}(I)$ is the ideal generated by all the leading terms of the elements of I.

With other words a basis is also a Groebner basis if the leading monomials of the generators generate the same ideal as the leading monomials of all ideal elements.

Using a Groebner basis we get a better result for the ideal-membership-question.

Theorem 4.1 *Let $G = \{g_1, \ldots, g_t\} \subseteq \mathbf{K}[\underline{x}]$ be a Groebner basis of an ideal I and $f \in \mathbf{K}[\underline{x}]$. The polynomial f is an element of I if and only if $\overline{f}^G = 0$.*

Summarizing the procedure for the ideal-membership-question is the following: first a termorder is fixed, then a Groebner basis of the ideal is computed and after that the polynomial f is reduced with respect to this basis. f is exactly only then an element of I if the result of the reduction is 0.

It has to be mentioned that the result of a reduction with respect to a Groebner basis is independent of the order of the basis elements, this was not the case when the reduction was done with respect to a normal basis.

Example 4.15 Let $I = \langle f_1, f_2\rangle = \langle x_1x_2 + 1, x_2^2 - 1\rangle$ be an ideal in $\mathbf{K}[\underline{x}]$ and $p_1 = x_1 f_1 + x_2 f_2$ and $p_2 = x_2 f_1 + x_1 f_2$ polynomials which are definitely elements of I. Now a Groebner basis is computed wrt. `plex(x[1],x[2])` and p_1, p_2 are reduced with that basis.

```
with(Groebner);with(PolynomialIdeals):
f1:=x[1]*x[2]+1; f2:=x[2]^2-1;
G:=Basis(<f1,f2>,plex(x[1],x[2]));
p1:=x[1]*f1+x[2]*f2; p2:=x[2]*f1+x[1]*f2;
Reduce(p1,G,plex(x[1],x[2]));
Reduce(p2,G,plex(x[1],x[2]));
```

The Groebner basis is

$$G = \left\langle x_2^2 - 1, x_1 + x_2\right\rangle$$

and now the expected results are obtained:

$$\overline{p_1}^F = 0, \qquad \overline{p_2}^F = 0.$$

The package `PolynomialIdeals` contains also two commands for testing if a polynomial or an ideal is contained in another ideal. They are used as follows:

```
IdealMembership(p1,G); IdealContainment(<p1,p2>,G);
```

The result of both commands will be *true*.

Now some remarks about Groebner bases:

- The number of polynomials in a Groebner basis can be very large, it depends on the complexity of the ideal and, of course, on the chosen monomial order. It is quite possible that only a part of the Groebner basis would be enough to generate the ideal I, but then the relevant condition $\langle \mathrm{LM}(g_1), \ldots, \mathrm{LM}(g_t)\rangle = \langle \mathrm{LM}(I)\rangle$ is no more fulfilled.

- There are different methods to compute Groebner bases.
- The monomial order $>_{lex}$ (in Maple `plex`) tends to be expensive in general, whereas the order $>_{grevlex}$ (in Maple `tdeg`) tends to be "relatively" cheap. If the type of order is chosen the computational costs can again be influenced by the order of unknowns.
- The typical way to order the polynomials in a basis is by sorting them wrt. the leading monomials, starting with the smallest one.

Example 4.16 Now as an example reduced Groebner bases are computed for the ideal

$$I = \left\langle x_1^2 x_2 + x_1 x_2^2 + x_2^2 x_3, x_1 x_2 - x_3, x_2^2 - 1 \right\rangle$$

using different termorders:

$>_{lex}$ in $\mathbf{K}[x_1, x_2, x_3]$:

$$G = \left\{ x_3^3 + 2x_3^2, x_2 x_3 + x_3^2 + x_3, x_2^2 - 1, x_1 + x_3^2 + x_3 \right\}.$$

$>_{lex}$ in $\mathbf{K}[x_3, x_1, x_2]$:

$$G = \left\{ x_2^2 - 1, x_1^2 + x_1 x_2 + x_1, x_3 - x_1 x_2 \right\}.$$

$>_{grlex}$ in $\mathbf{K}[x_1, x_2, x_3]$:

$$G = \left\{ x_3^2 + x_1 + x_3, x_2 x_3 - x_1, x_2^2 - 1, x_1 x_3 + x_1 + x_3, x_1 x_2 - x_3, x_1^2 + x_1 + x_3 \right\}.$$

The code for Maple looks as follows:

```
f1:=x[1]^2*x[2]+x[1]*x[2]^2+x[2]^2*x[3];
f2:=x[1]*x[2]-x[3]; f3:=x[2]^2-1;
Basis(<f1,f2,f3>,plex(x[1],x[2],x[3]));
Basis(<f1,f2,f3>,plex(x[3],x[1],x[2]));
Basis(<f1,f2,f3>,grlex(x[1],x[2],x[3]));
```

It is no coincidence that in all the bases wrt. to $>_{lex}$ the first polynomial is univariate. This is because the lex-orders have the so called *elimination property*.

4.2.3 Elimination

First of all the so called *elimination ideals* are defined.

Definition 4.12 Let I be an ideal in $\mathbf{K}[\underline{x}] = \mathbf{K}[x_1, \ldots, x_n]$ and $1 \leq l < n$. Then the ideal $I_l = I \cap \mathbf{K}[x_{l+1}, \ldots, x_n]$ is called the l-**th limination ideal** of I. I_l contains all elements of I which do not contain the variables $x_1, \ldots, x_l$.

If a termorder has the elimination property, then a basis wrt. this order can be used to extract bases for the elimination ideals.

Theorem 4.2 *Let $G = \{g_1, \ldots, g_t\} \subseteq \mathbf{K}[x_1, \ldots, x_n]$ be a Groebner basis of an ideal I with respect to $>_{lex}$. Furthermore let $H = \{h_1, \ldots, h_k\}$ be the first k polynomials of G which do not contain the unknowns $x_1, \ldots, x_l$. Then H is a Groebner basis of the l-th elimination ideal I_l.*

It follows an example where it can be seen more clearly what this means.

Example 4.17 The ideal $I = \langle x_1^2 x_2 + x_1 x_2^2 + x_2^2 x_3, x_1 x_2 - x_3, x_2^2 - 1\rangle$ is given with the Groebner basis wrt. `plex(x[1],x[2],x[3])`

$$G = \left\langle x_3^3 + 2x_3^2, x_2 x_3 + x_3^2 + x_3, x_2^2 - 1, x_1 + x_3^2 + x_3 \right\rangle.$$

Then the following generators are all Groebner bases of the corresponding elimination ideal:

$$I_2 = \left\langle x_3^3 + 2x_3^2 \right\rangle, \qquad I_1 = \left\langle x_3^3 + 2x_3^2, x_2 x_3 + x_3^2 + x_3, x_2^2 - 1 \right\rangle.$$

There is also another command to do the elimination directly. It is contained in the package `PolynomialIdeals` and to compute I_1 directly from the input polynomials it is used as follows:

```
EliminationIdeal(<f1,f2,f3>,{x[2],x[3]});
```

The second argument gives the unknowns which shall not be eliminated. Furthermore no termorder has to be chosen, this is done by Maple internally. Unfortunately this choice is session-dependent.

It can easily be seen that with these elimination ideals it is quite easy to solve a system of equations with only finitely many solutions.

Example 4.18 Here once again the Groebner basis G from above including I_2 and I_1.

$$I_2 = \left\langle x_3^3 + 2x_3^2 \right\rangle, \qquad I_1 = \left\langle x_3^3 + 2x_3^2, x_2 x_3 + x_3^2 + x_3, x_2^2 - 1 \right\rangle,$$
$$G = \left\langle x_3^3 + 2x_3^2, x_2 x_3 + x_3^2 + x_3, x_2^2 - 1, x_1 + x_3^2 + x_3 \right\rangle.$$

Now the system can be solved step by step by solving the partial systems and extending the solutions.

```
with(Groebner):with(PolynomialIdeals):
f1:=x[1]^2*x[2]+x[1]*x[2]^2+x[2]^2*x[3];
f2:=x[1]*x[2]-x[3]; f3:=x[2]^2-1;
I0:=<f1,f2,f3>;
G:=<op(Basis(I0,plex(x[1],x[2],x[3])))>;
```

```
NumberOfSolutions(I0);
I2:=EliminationIdeal(<f1,f2,f3>,{x[3]});
I1:=EliminationIdeal(<f1,f2,f3>,{x[2],x[3]});
L1:={solve(Generators(I2),{x[3]})};
L2:=map(y->op(map(z->z union y,
     {solve(eval(Generators(I1),y), {x[2]})})),L1);
L3:=map(y->op(map(z->z union y,
     {solve(eval(Generators(G),y), {x[1]})})),L2);
```

The result for the vanishing set is $\mathbf{V}(I) = \{(-2, 1, -2), (0, -1, 0), (0, 1, 0)\}$, where the second solution has multiplicity 2.

How does the variety of the l-th elimination ideal $\mathbf{V}(I_l)$ correspond to the original variety $\mathbf{V}(I)$?

Theorem 4.3 *The variety* $\mathbf{V}(I_l) \in \mathbf{K}^{n-l}$ *is the smallest variety* (*wrt. inclusion*) *which contains* $\pi(\mathbf{V}(I))$, *where* $\pi(\mathbf{V}(I))$ *is the orthonormal projection of* $\mathbf{V}(I)$ *onto the subspace generated by equations* $x_1 = \cdots = x_l = 0$.

It is important to note that the equality $\mathbf{V}(I_l) = \pi(\mathbf{V}(I))$ only holds when I is a *projective variety* and I_l a *projective elimination ideal*. This means that here it can happen that a solution of I_l can not be extended to a solution of I_{l-1}.

Another application of elimination is implicitization. The following example shows how a variety can be deduced from a parametrisation.

Example 4.19 A parametrisation of a planar curve is given.

$$x_1 = \frac{6t^2}{t^3+1}, \qquad x_2 = \frac{6t}{t^3+1}.$$

For all values of $t \in \mathbb{R}$ a point of the curve is obtained. To compute the smallest variety which contains all these points (should be a cubic curve), the following code could be used:

```
with(Groebner);with(PolynomialIdeals):
par1:=x[1]-6*t^2/(t^3+1);
par2:=x[2]-6*t/(t^3+1);
J:=<numer(par1),numer(par2)>;
G:=Basis(J,plex(t,x[1],x[2]));
J1:=<G[1]>;
```

The first elimination ideal $J_1 = \langle x[1]^3 + x[2]^3 + 6 * x[1] * x[2] \rangle$ has exactly the cubic curve as vanishing set.

4.2.4 Dimension, Primary Decomposition

It happens quite often that one is primarily interested in the *dimension* of a variety. Here is an example where the variety contains parts with different dimensions, and it is shown how the dimension is computed.

Example 4.20 The ideal $I = \langle (2x_1 - x_2 - 2)x_1, (2x_1 - x_2 - 2)x_2^2 \rangle$ is given. $\mathbf{V}(I)$ consists of a line and an isolated point. Using the Hilbert polynomial (see [7, Chap. 9] the dimension is computed (which should be 1).

```
with(PolynomialIdeals):
I1:=<(2*x[1]-x[2]-2)*x[1], (2*x[1]-x[2]-2)*x[2]^2>;
HilbertDimension(I1,{x[1],x[2]});
```

If a variety contains parts with different dimensions, then the dimension of the whole variety is defined to be the largest of these numbers.

As already mentioned it is possible that an ideal describes a variety which is made up of some simpler varieties, e.g. the variety from the example above. It is the union of a line and an isolated point. The question is how such a decomposition can be found, if there is one.

Definition 4.13 A **primary decomposition** of a given ideal I is an expression of I as an intersection of primary ideals, namely $I = \bigcap_{i=1}^{r} Q_i$. Such a decomposition is called **minimal** if the radicals $\sqrt{Q_i}$ are all different and $Q_i \not\supseteq \bigcap_{i \neq j} Q_j$. Furthermore if no radical $\sqrt{Q_i}$ is strictly contained in another radical $\sqrt{Q_j}$, then the primary components Q_i are uniquely determined.

The radicals $\sqrt{Q_i} =: P_i$ are the corresponding prime ideals.

It follows an example where the variety can be decomposed into three different parts.

Example 4.21 A rather large ideal J is given.

$$\begin{aligned} J = \big\langle & 4{x_3}^2{x_1}^3 + 4{x_3}^2x_1{x_2}^2 + 4{x_3}^4x_1 - 16x_1{x_3}^2 + 5{x_3}^2x_2{x_1}^2 + 5{x_3}^2{x_2}^3 \\ & + 5{x_3}^4x_2 - 20x_2{x_3}^2 - 6{x_3}^2{x_1}^2 - 6{x_3}^2{x_2}^2 - 6{x_3}^4 + 24{x_3}^2, \\ & 4{x_1}^4 + 4{x_1}^2{x_2}^2 + 4{x_3}^2{x_1}^2 + 2{x_1}^2 + 5{x_1}^3x_2 + 5x_1{x_2}^3 + 5x_1x_2{x_3}^2 \\ & - 20x_1x_2 - 18{x_1}^3 - 18x_1{x_2}^2 - 18x_1{x_3}^2 + 72x_1 - 15x_2{x_1}^2 - 15{x_2}^3 \\ & - 15x_2{x_3}^2 + 60x_2 + 18{x_2}^2 + 18{x_3}^2 - 72 \big\rangle. \end{aligned}$$

Using the command

```
PrimaryDecomposition(J);
```

Table 4.1 Important joint types

Name	Abbr.	Dof	Relative motion
Revolute	R	1	Rotation about fixed axis
Prismatic	P	1	Translation in fixed direction
Cylindrical	C	2	Rotation about and translation along fixed axis
Helical	H	1	Rotation about and translation along fixed, linear relation between translation distance and rotation angle
Spherical	S	3	Rotation about axes through fixed point

the primary decomposition is computed and the result is

$$Q_1 = \langle 4x_1 + 5x_2 - 6\rangle, \qquad Q_2 = \langle {x_1}^2 + {x_2}^2 + {x_3}^2 - 4\rangle, \qquad Q_3 = \langle {x_3}^2, x_1 - 3\rangle,$$

which means that $\mathbf{V}(I)$ can be decomposed into a line, a sphere and an isolated point which appears with multiplicity 2.

Such decompositions are quite convenient if the variety has to be intersected with other varieties, because then each of the components can be treated separately. The worst case is that one has to deal with an ideal which is primary or even prime. In this case one has to take the ideal as a whole. We shall see later, that the exactly this decomposition of ideal leads to surprising new results in the analysis of lower dimensional parallel manipulators.

4.3 Mechanism Theory

We start this section with a brief definition of basic concepts in mechanism science. Our terminology follows that of [32, Sect. 1.2]. The fundamental object in computational kinematics is a *mechanism*. This is an object consisting of several links that are connected by joints.

A *link* is a collection of mechanical parts such that no relative motion between the individual members can occur. A *joint* is a connection between two links. It restricts the relative motion that is possible between the two links. The joints can be classified according to the nature of this restriction. The number of free parameters to describe this relative motion is called the *degree of freedom* of the joint. A listing of the most important joint types, their usual abbreviation, their degree of freedom, and a short description is given in Table 4.1.

It is important to note that the kinematic image of all joints in Table 4.1—with exception of the helical joint—is an algebraic variety. We restrict ourselves to algebraic joints only. Luckily helical joints are of little relevance in practice.

A collection of links that are connected by joints is called a *kinematic chain*. A kinematic chain can be represented by a graph [32, Sect. 7.3.2] where the links are the vertices and the joints are the edges. In a *closed-loop kinematic chain* every

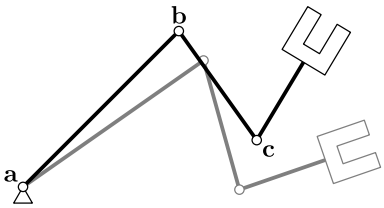

Fig. 4.2 3R-linkage

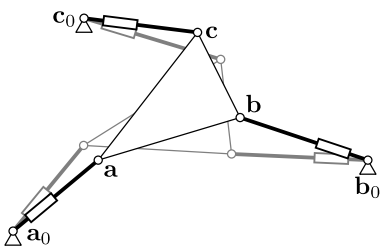

Fig. 4.3 3RPR-platform

link is connected to every other link by at least two paths, in an *open-loop kinematic chain* every link is connected to every other link by exactly one path. Of course there are also hybrid versions.

Finally, a *mechanism* is a kinematic chain where one of the links (the *base*) is fixed to the ground or, in mathematical terminology, to a base frame coordinate system. The remaining links are grouped into input links and output links. Input links are actuated and move with respect to the fixed link and the output links perform an according motion.

An example of a mechanism, a so-called planar 3R-linkage, is depicted in Fig. 4.2. It consists of three revolute joints **a**, **b**, and **c**, connected by links of constant lengths. The joint **a** is fixed to the ground, **b** and **c** can move along the paths imposed by the links **ab** and **bc**, respectively. Attached to the last joint is the end effector tool. Typically, one is interested in the motion of the end effector tool with respect to the base. The set of all poses the end effector can attain is called the mechanism's *workspace*. The workspace is a subset of the Study quadric (or of planar or spherical kinematic image space).

In Fig. 4.3 we see a planar 3RPR-platform. It consists of three legs, each composed of a revolute joint (R), a prismatic joint (P) and a further revolute joint (R). Three revolute joints ($\mathbf{a}_0$, $\mathbf{b}_0$, $\mathbf{c}_0$) are fixed to the ground, three of them (**a**, **b**, **c**) are attached to the end effector frame. This mechanism is actuated by changing the lengths of the prismatic joints. It has a three dimensional workspace, that is represented by a three dimensional variety on the Study quadric.

The spatial counterpart to a 3RPR-platform is known as Stewart-Gough platform. It consists of six legs and each leg is composed of a spherical, a prismatic and a spherical joint (Fig. 4.4). Between any two corresponding spherical joints a prismatic joint is inserted. The spherical joints can rotate freely about their center, the prismatic joints can extend or shrink in one direction (the direction of the link in our case).

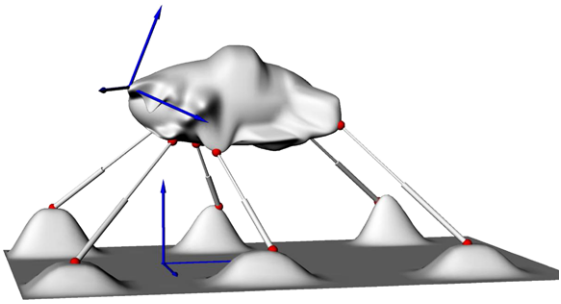

Fig. 4.4 A general Stewart-Gough platform

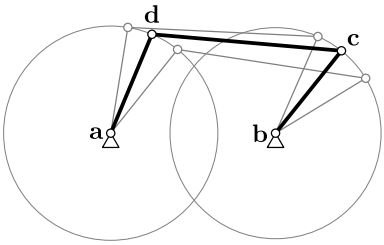

Fig. 4.5 A planar four-bar mechanism

Figure 4.5 depicts a planar four-bar linkage, a further common linkage type. It consists of four revolute joints connected by bars of fixed lengths. Two revolute joints **a**, **b** are fixed to the base frame, the two remaining joints **c**, **d** are attached to the end effector frame. The "missing" fourth bar is the ideal connection between **a** and **b**. The four-bar motion depends only on one free parameter, the rotation of the driving crank. We say that the mechanism has *one degree of freedom*. This is in contrast to 3R- and 3RPR-manipulators which have three degrees of freedom and can, at least theoretically, generate the complete group of planar Euclidean displacements. The kinematic image of the four-bar linkage is a curve on the Study quadric

4.4 Constraint Varieties

In this section we demonstrate how kinematic mapping can be used to translate mechanisms to algebraic varieties[5] in P^7. These varieties describe the possible configurations of the mechanism and are called *constraint varieties*. We start by computing the kinematic images of fundamental building blocks of mechanisms (see Table 4.1). Then we demonstrate how to combine these elements in order to describe more complex mechanisms. The corresponding algebraic operations involve intersection of varieties and implicitization.

[5]In Sect. 4.2 we have defined affine varieties. When all defining polynomials of the variety are homogeneous then the zero set of these polynomials is called projective variety. Because in mechanism analysis affine as well as projective varieties occur we use the generic term algebraic variety in this section.

4.4.1 Kinematic Image of Elementary Joints

4.4.1.1 Revolute Joints

A parametrized representation of the kinematic image of a revolute joint has already been computed in Examples 4.1 and 4.3. It is a straight line and computing its algebraic equations is elementary. Still, we will show how to carry out these computations explicitly because this demonstrates a general procedure for obtaining constraint varieties. Consider the kinematic image (4.11). It is given in a normal form and we see that it is described by six linear equations

$$\begin{aligned} &H_1(\mathbf{x})\colon x_1 = 0, \qquad H_2(\mathbf{x})\colon x_2 = 0, \qquad K_0(\mathbf{x})\colon y_0 = 0, \\ &K_1(\mathbf{x})\colon y_1 = 0, \qquad K_2(\mathbf{x})\colon y_2 = 0, \qquad K_3(\mathbf{x})\colon y_3 = 0. \end{aligned} \tag{4.31}$$

In order to obtain the constraint variety of a revolute joint in general position we have to transform the hyperplanes $H_i(\mathbf{x})$, $K_j(\mathbf{x})$ via the projective transformation $\mathbf{T}_f$. This is done by substituting $\mathbf{T}_f^{-1}\mathbf{x}$ for $\mathbf{x}$. The new equations are

$$H_i'(\mathbf{x}) = H_i\big(\mathbf{T}_f^{-1}\mathbf{x}\big), \qquad K_j'(\mathbf{x}) = K_j\big(\mathbf{T}_f^{-1}\mathbf{x}\big). \tag{4.32}$$

This procedure not only works for linear equations but for algebraic equations of arbitrary degree. Changes of coordinates in the moving frame are performed by using $\mathbf{T}_m$ instead of $\mathbf{T}_f$.

4.4.1.2 Concatenation of Elementary Joints

A mechanism generally will consist of combinations of elementary joints which act either in series or parallel. Therefore it is crucial to devise a procedure in which the constraint variety of a given concatenation of elementary joints can be computed. Such a procedure was developed in [34] and is called implicitization algorithm. We give here a brief outline of this algorithm. For a more elaborate treatment we refer to the paper.

We know already that the kinematic image of every concatenation of an arbitrary number of elementary joints will correspond to an algebraic variety, a subset of the Study quadric. By performing the forward kinematics using the usual procedure in multiplying rotation or translation matrices and coordinate transformation matrices we end up with a parametric representation of the chain. Note that for this process on can use the best adapted coordinate system, because a general pose of the chain with respect to an arbitrary coordinate system can be obtained later by performing transformations (4.17), which will not change the degree of the constraint polynomials. The algebraic variety is obtained by eliminating the parameters from the parametric representation. A simple example was shown in Example 4.19. In multi-parameter systems elimination is in general not possible, because the degree of the system increases with every elimination step. Therefore we present an alternative approach.

From the parametric representation of the chain in Cartesian space the representation in the kinematic image space has to be computed using (4.7) and (4.8). Half tangent substitution transforms the rotation angles u_i into algebraic parameters t_i and one ends up with eight parametric equations of the form:

$$x_0 = f_0(t_1, \ldots, t_n), \qquad x_1 = f_1(t_1, \ldots, t_n), \quad \ldots, \quad y_3 = f_8(t_1, \ldots, t_n).$$

These equations will be rational having a denominator of the form $(1 + t_1^2) \cdots (1 + t_n^2)$ which can be canceled because the Study parameters x_i, y_i are homogeneous. The same can be done with a possibly appearing common factor of all parametric expressions. We assume now that we have been arriving at the simplest possible parametric representation of the kinematic chain.

We have already seen that there exists a one-to-one correspondence from all spatial transformations to the Study quadric which lives in P^7. Particularly this means that a tuple of Study parameters describing a transformation is a projective point and consequently always only unique up to scalar multiples. If we have a transformation parametrized by n parameters $t_1, \ldots, t_n$ we obtain by kinematic mapping a set of corresponding points in P^7 and we ask now for the smallest variety $\mathscr{V} \in P^7$ (with respect to inclusion) which contains all these points.

What do we know about this variety? What can be said definitely is that its ideal consists of homogeneous polynomials and contains $x_0y_0 + x_1y_1 + x_2y_2 + x_3y_3$, i.e. the equation for the Study quadric S. In the following it is shown how additional equations can be computed which are necessary to describe $\mathscr{V}$. It should be noted that the minimum number necessary to describe $\mathscr{V}$ corresponds to the number of parameters, which in turn correspond to the degrees of freedom (dof) of the kinematic chain. If the number of generic parameters is n then $m = 6 - n$ polynomials are necessary to describe $\mathscr{V}$. This is of course a rough statement, because different numbers can appear when special situations (e.g. redundant dofs) are in place.

Now we are searching for homogeneous polynomials which vanish on all points that can be obtained from the parameterization of the kinematic chain, i.e. polynomials in $x_0, x_1, x_2, x_3, y_0, y_1, y_2, y_3$ which are 0 when the expressions of the parameterization are substituted. One possibility to find such polynomials is the following: A general ansatz of a homogeneous polynomial in $x_0, x_1, x_2, x_3, y_0, y_1, y_2, y_3$ with given degree n is made and then the Study parameters of the parametric representation are substituted. The resulting expression f is treated as a polynomial $f(t_1, \ldots t_n)$. Due to the fact that f has to vanish for all values of the t_i, it has to be the zero polynomial. It follows that all coefficients of f have to vanish. This means that, after extraction of these coefficients, one obtains a system of linear equations where the unknowns are the $\binom{n+7}{n}$ coefficients from the general ansatz. This system can be solved (assuming that the design parameters a_i, d_i and α_i are generic) and the solution can be substituted into the ansatz. The result is an expression r describing all homogeneous polynomials of degree n which vanish on the points of $\mathscr{V}$. An important point is that if the solution of the linear system is positive dimensional, the corresponding parameters also appear in the final expression, i.e. the expression r itself is parametrized.

More details on this algorithm can be found in [34] and as an example how it can be used for the description of the constraints of a 5-RPUR parallel manipulator is shown in [21].

4.4.1.3 Path Constraints

So far, we have demonstrated how to operate on a "joint level" in order to compute constraint varieties. This is suitable for serial manipulators. When describing parallel manipulators it is often favorable to start with a "path constraint" and then the implicitization algorithm can be avoided. Consider, for example, the four-bar mechanism of Fig. 4.5. The coupler motion is completely defined by the condition that the two points have circular trajectories. Every "circle constraint" translates into a constraint surface in the quasielliptic space of planar Euclidean displacements. The kinematic pre-image of their intersection curve is the four-bar motion.

As an example we compute the algebraic equation of the surface of all planar displacements, such that the point $(a, b)^T$ moves on a circle with center $(\xi, \eta)^T$ and of radius ϱ. Using the matrix $\mathbf{X}$ of (4.22) the circle constraint reads

$$\left\| \mathbf{X} \cdot (1, a, b)^T - (1, \xi, \eta)^T \right\|^2 - \varrho^2 = 0. \tag{4.33}$$

This is equivalent to a homogeneous polynomial of degree two in x_0, x_3, y_1, and y_2. Hence the circle constraint surface is a quadric surface in P^3.

4.4.2 Mechanism Analysis

The topic of mechanism analysis is the investigation of properties a certain mechanism exhibits. Thereby, the mechanism type and its dimensions are known. Questions of interest concern the relation of joint parameters to the position and orientation of the end effector, the topology and size of the workspace, and its singular positions (singular in kinematic sense, not in the sense of algebraic geometry).

4.4.2.1 Direct and Inverse Kinematics

Direct and inverse kinematics are two basis tasks of mechanism analysis. Usually the direct kinematics problem is relatively easy for serial manipulators but often difficult for parallel manipulators. Conversely, the inverse kinematics problem is usually simple for parallel manipulators and often complicated for parallel manipulators.

Consider for example an 6R serial chain. If the rotation angles of the individual joints are known, computing the end effector frame is just a matter of multiplying consecutive transformation matrices [23, Sect. 4.4] (direct kinematics). Conversely,

it is not obvious at all how to choose the joint angles such that the end effector attains a certain specified pose (inverse kinematics).

On the other hand, computing the leg lengths of a Stewart-Gough platform (SGP) is trivial when the pose of the moving platform—and hence also the locations of the anchor points—in space is given (inverse kinematics). The direct kinematics problem of finding the possible poses to a given sequence of leg lengths is difficult. It amounts to computing the intersection points of six sphere constraint surfaces and the Study quadric and has 40 solutions over $\mathbb{C}$. We give a short sketch of the solution algorithm.

If a point of the moving system is constrained to remain on a sphere we obtain the following "canonical" constraint equation using the implicitization algorithm:

$$\left(y_0^2+y_1^2+y_2^2+y_3^2-\frac{1}{4}R^2\left(x_0^2+x_1^2+x_2^2+x_3^2\right)\right)\lambda + (x_0y_0+x_1y_1+x_2y_2+x_3y_3)\mu=0. \tag{4.34}$$

In the canonical form the origin of moving and fixed coordinate system coincide with the centers of the spherical joint in base and platform. To obtain the constraint equation of a general leg one has to perform the coordinate transformations (4.7) and (4.8) which translate the origins to the center of the spherical joints in base (A, B, C) and platform (a, b, c) of the general leg.

$$\begin{aligned} h\colon\ & R\left(x_0^2+x_1^2+x_2^2+x_3^2\right)+4\left(y_0^2+y_1^2+y_2^2+y_3^2\right)-2x_0^2(Aa+Bb+Cc)\\ &+2x_1^2(-Aa+Bb+Cc)+2x_2^2(Aa-Bb-Cc)+2x_3^2(Aa+Bb+Cc)\\ &+2x_3^2(Aa+Bb-Cc)+4\big[x_0x_1(Bc-Cb)+x_0x_2(Ca-Ac)\\ &+x_0x_3(Ab-Ba)-x_1x_2(Ab+Ba)-x_1x_3(Ac+Ca)\\ &-x_2x_3(Bc+Cb)+(x_0y_1-y_0x_1)(A-a)+(x_0y_2-y_0x_2)(B-b)\\ &+(x_0y_3-y_0x_3)(C-c)+(x_1y_2-y_1x_2)(C+c)-(x_1y_3-y_1x_3)(B+b)\\ &+(x_2y_3-y_2x_3)(A+a)\big]=0. \end{aligned} \tag{4.35}$$

In this equation we have seven design constants: the length of the leg is encoded in R, the coordinates of the sphere center in the base are A, B, C and the center of the spherical joint on the platform are a, b, c. The direct kinematics problem is now transformed into an algebraic intersection problem of seven quadratic varieties (six constraint equations and the Study quadric S). The count of the number of solutions is not as easy because a simple check of (4.35) shows that each of the equations contains the absolute quadric F in the exceptional generator $E\colon x_0=x_1=x_2=x_3=0$. A proof for the existence of 40 solutions in the allowed part of S can be found in [36] or [27]. The solution algorithm is straightforward: take differences of the constraint equations, which are linear in y_i, solve for the y_i, substitute in the remaining equations. Three essentially different equations remain. They are in the

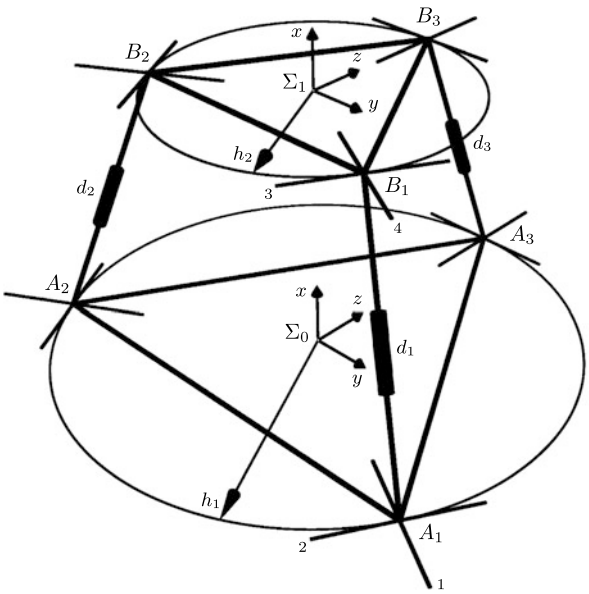

Fig. 4.6 SNU-3-UPU. The numbers at the first limb describe the order of the rotational axes of the U-joints

general case of degree $(8, 4, 4)$. Using resultants or Gröbner bases the univariate polynomial of degree 40 can be computed and solved numerically.

The use of primary decomposition of the ideal of constraint equations will be shown with the analysis of the so called SNU-3-UPU parallel manipulator. It consists of three identical *UPU*-legs (universal-prismatic-universal-joint). The anchor points on base and platform are located at the vertices of an equilateral triangle. First and fourth revolute joint as well as second and third revolute joint are parallel (Fig. 4.6).

It can easily be seen that each of the leg link-combinations reduces the degrees of freedom of the platform by two. The first restriction is the condition of constant distance between A_i and B_i. Therefore we can use the constraint equation (4.35) and obtain three sphere constraint equations g_1, g_2, g_3. The second constraint is induced by the two U-joints: the platform cannot rotate about the axis of the limb. From this fact it follows that the vertices $\mathbf{A}_i$, $\mathbf{B}_i$ and the circum-centres of base and platform have to form a planar quadrangle. But such a condition can easily be translated to an equation, because it is fulfilled if and only if the determinant of the 4×4-matrix built by these four points vanishes.

So for each limb we take the coordinates of $\mathbf{A}_i$, $\mathbf{B}_i$, the origin of Σ_0 and the origin of Σ_1 with respect to Σ_0, build the 4×4-matrix and compute its determinant. Here it is not necessary to normalize the coordinates. After removal of non-vanishing factors these determinants are reduced with the polynomial $x_0y_0 + x_1y_1 + x_2y_2 + x_3y_3$ with respect to the total degree order $x_0 \succ x_1 \succ x_2 \succ x_3 \succ y_0 \succ y_1 \succ y_2 \succ y_3$ which has the effect that the result can be again factorized and the smaller factor $-(x_0^2 + x_1^2 + x_2^2 + x_3^2)$ can be removed. We obtain the following equations which

are again quadratic and completely independent from all design parameters.

$$g_4\colon\ 4x_1y_1 + x_2y_2 + \sqrt{3}x_2y_3 + \sqrt{3}x_3y_2 + 3x_3y_3 = 0, \tag{4.36}$$

$$g_5\colon\ 4x_1y_1 + x_2y_2 - \sqrt{3}x_2y_3 - \sqrt{3}x_3y_2 + 3x_3y_3 = 0, \tag{4.37}$$

$$g_6\colon\ x_1y_1 + x_2y_2 = 0. \tag{4.38}$$

The Study-quadric equation and a normalization condition

$$g_7\colon\ x_0y_0 + x_1y_1 + x_2y_2 + x_3y_3 = 0, \qquad g_8\colon\ x_0^2 + x_1^2 + x_2^2 + x_3^2 - 1 = 0$$

complete the system and we have the ideal

$$\mathscr{I} = \langle g_1, g_2, g_3, g_4, g_5, g_6, g_7, g_8\rangle.$$

One could try to solve this system immediately, but in this case it makes sense to perform some simplification before. An inspection of the equations in the ideal shows that g_4, g_5, g_6 are free of design parameters. Therefore we look at the ideal

$$\mathscr{J} = \langle g_4, g_5, g_6, g_7\rangle$$

and perform a primary decomposition. This shows that it can be written in a very simple way:

$$\mathscr{J} = \bigcap_{i=1}^{10} \mathscr{J}_i$$

with

$$\mathscr{J}_1 = \langle y_0, y_1, y_2, y_3\rangle, \qquad \mathscr{J}_2 = \langle x_0, y_1, y_2, y_3\rangle,$$
$$\mathscr{J}_3 = \langle y_0, x_1, y_2, y_3\rangle, \qquad \mathscr{J}_4 = \langle x_0, x_1, y_2, y_3\rangle,$$
$$\mathscr{J}_5 = \langle y_0, y_1, x_2, x_3\rangle, \qquad \mathscr{J}_6 = \langle x_0, y_1, x_2, x_3\rangle, \qquad \mathscr{J}_7 = \langle y_0, x_1, x_2, x_3\rangle,$$
$$\mathscr{J}_8 = \langle x_2 - ix_3, y_2 + iy_3, x_0y_0 + x_3y_3, x_1y_1 + x_3y_3\rangle,$$
$$\mathscr{J}_9 = \langle x_2 + ix_3, y_2 - iy_3, x_0y_0 + x_3y_3, x_1y_1 + x_3y_3\rangle,$$
$$\mathscr{J}_{10} = \langle x_0, x_1, x_2, x_3\rangle.$$

To compute this decomposition the software *Singular* was used, a very powerful tool to do computations with polynomials. Actually all these ideals are prime ideals and there are no embedded components. It has to be noted that an ideal has to be very special to allow such a decomposition in so many small components. For the zero set or vanishing set $\mathscr{V}(\mathscr{J})$ of $\mathscr{J}$ it follows that

$$\mathscr{V}(\mathscr{J}) = \bigcup_{i=1}^{10} \mathscr{V}(\mathscr{J}_i).$$

Table 4.2 Dimensions of component intersections

	$\mathscr{K}_1$	$\mathscr{K}_2$	$\mathscr{K}_3$	$\mathscr{K}_4$	$\mathscr{K}_5$	$\mathscr{K}_6$	$\mathscr{K}_7$
$\mathscr{K}_1$	3	2	2	1	1	0	0
$\mathscr{K}_2$	2	3	1	2	0	1	−1
$\mathscr{K}_3$	2	1	3	2	0	−1	1
$\mathscr{K}_4$	1	2	2	3	−1	−1	−1
$\mathscr{K}_5$	1	0	0	−1	3	2	2
$\mathscr{K}_6$	0	1	−1	−1	2	3	−1
$\mathscr{K}_7$	0	−1	1	−1	2	−1	3

Now we add the remaining equations and by writing $\mathscr{K}_i := \mathscr{J}_i \cup \langle g_1, g_2, g_3, g_8 \rangle$ the vanishing set of the essential system $\mathscr{I}$ can be written as

$$\begin{aligned}\mathscr{V}(\mathscr{I}) &= \mathscr{V}\big(\mathscr{J} \cup \langle g_1, g_2, g_3, g_8\rangle\big) = \mathscr{V}(\mathscr{J}) \cap \mathscr{V}\big(\langle g_1, g_2, g_3, g_8\rangle\big) \\ &= \left(\bigcup_{i=1}^{10} \mathscr{V}(\mathscr{J}_i)\right) \cap \mathscr{V}\big(\langle g_1, g_2, g_3, g_8\rangle\big) = \bigcup_{i=1}^{10} \big(\mathscr{V}(\mathscr{J}_i) \cap \mathscr{V}\big(\langle g_1, g_2, g_3, g_8\rangle\big)\big) \\ &= \bigcup_{i=1}^{10} \mathscr{V}\big(\mathscr{J}_i \cup \langle g_1, g_2, g_3, g_8\rangle\big) = \bigcup_{i=1}^{10} \mathscr{V}(\mathscr{K}_i).\end{aligned}$$

So, instead of studying the system as a whole, we can look for solutions of the smaller systems $\mathscr{K}_i$. Then the solution of system $\mathscr{I}$ is the union of the solutions of the sub-systems.

It can easily be seen that the last set $\mathscr{V}(\mathscr{K}_{10})$ is empty because $\mathscr{K}_{10}$ contains equations $\{x_0, x_1, x_2, x_3, x_0^2 + x_1^2 + x_2^2 + x_3^2 - 1\}$ which cannot vanish simultaneously. Moreover the systems $\mathscr{V}(\mathscr{K}_8)$ and $\mathscr{V}(\mathscr{K}_9)$ yield only complex solutions. Therefore it is only necessary to study systems $\mathscr{K}_1, \ldots, \mathscr{K}_7$. We can say that the workspace of the manipulator consists of seven components, whose complete description can be obtained by adding the remaining polynomials g_1, g_2, g_3, g_8 to the polynomials of each component. A complete kinematic description of all components can be found in [33]. The dimensions of the different intersections of the components are listed in Table 4.2. The numbers in this table refer to the dimension of the respective variety where a transition from one component into the other component is possible: 0 stands for a single point, 1 for a curve and 2 for a two dimensional variety.

4.4.2.2 Algebraic Definition of Degrees of Freedom

There is a long history in defining and computing the degree of freedom of a mechanical system. Historically most of the developed formulas determine the topological structure and fail whenever special design parameters cause anomalies. Our informal definition at the beginning of Sect. 4.3 is an example of that. Exceptional, pathological or overconstrained mechanisms need special treatment. An overview

of most of the classical concepts starting with Euler's formula up to the most recent developments can be found in [1].

Within the setting of algebraic geometry and the theory developed in this chapter it is natural to define the degree of freedom of a mechanism as the Hilbert dimension of the algebraic variety associated with the mechanical device. Caution has to be taken with respect to reality of the variety and its intersection with the exceptional generator E.

Applying this definition to the direct kinematics of the Stewart-Gough platform we obtain a zero dimensional component which determines the 40 discrete solutions. That is, for fixed leg lengths the degree of freedom is, in general, zero. However, the Hilbert dimension of the ideal spanned by the six sphere constraint equations and the Study condition (4.5) is two because every sphere constraint variety contains the exceptional quadric F. This problem can be overcome easily by adding a normalizing condition (either $x_0 = 1$ or $x_0^2 + x_1^2 + x_2^2 + x_3^2 = 1$) which removes the exceptional generator from the ideal. Note that the actual degree of freedom of a Stewart-Gough platform with fixed leg lengths can be greater than zero. This interesting phenomenon will be the topic in Sect. 4.4.2.3.

4.4.2.3 Mechanism Singularities

The singular configurations of a mechanism are an important topic in mechanism analysis. The precise definition and classification of mechanism singularities is far beyond the scope of this article (compare [38] and the references therein). In particular, singular configurations of a mechanism do not necessarily correspond to singularities of the mechanism's constraint varieties. To obtain a formal definition of singularity in kinematics we can follow the exposition in [8] and apply the results herein to the constraint varieties of the mechanism. Let $V \in k^n$ be a constraint variety and let $p = [p_0, \ldots, p_7]^T$ be a point on V. The *tangent space* of V at p, denoted $T_p(V)$, is the variety

$$T_P(V) = \mathbf{V}\big(d_p(f)\big) : f \subset \mathbf{I}(\mathbf{V}) \tag{4.39}$$

of linear forms of all polynomials contained in the ideal $\mathbf{I}(\mathbf{V})$ in point p (see [8, p. 486]). With this definition we can immediately link the tangent space to the local degree of freedom of the mechanism: The local degree of freedom is defined as $\dim T_p(V)$ (see also [35]). Computationally the differentials are to be taken with respect to the Study parameters x_i, y_i. In kinematics these differentials are collected in the *Jacobian matrix* of the manipulator

$$\mathbf{J}(f_j) = \left(\frac{\partial f_j}{x_i}, \frac{\partial f_j}{y_i}\right), \tag{4.40}$$

where f_j are polynomials describing the constraints, the Study condition, and a normalizing condition. The normalizing condition has to be added to avoid dimensional problems coming from the exceptional generator E. In a nonsingular position of the

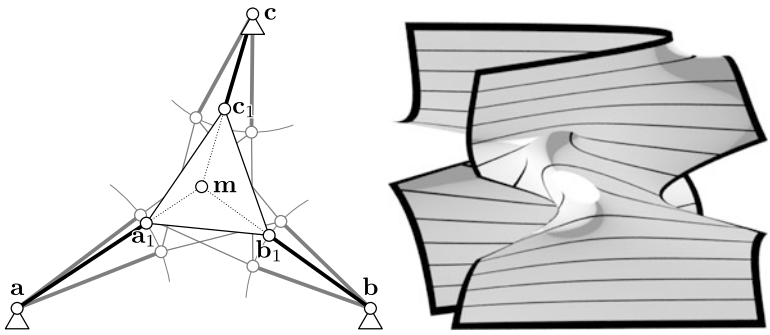

Fig. 4.7 Singular configuration of a planar 3RPR-mechanism and singularity surface

mechanism the Jacobian **J** will have maximal rank. A singular position is characterized by rank deficiency of **J** and the defect is directly related to the local degree of freedom.

It should be noted that singularity of mechanisms has different meaning when applied to serial or parallel robots. In case of a serial manipulator singularity means loss of mobility, whereas in case of parallel manipulators singularity means gain of mobility. Singular or near-singular configurations have to be avoided because of unpredictable behavior of the platform, because its resistance towards forces in certain directions becomes very weak, and because the effect to manufacturing tolerances increases. The kinematic image of all singular configurations constitutes the manipulator's singularity surface.

There is a vast literature on singularities of mechanisms. In this paper we confine ourselves to discussing singularities by means of a few examples. Some of them will show that not always the tangent space of the constraint varieties has to be computed. In these cases geometric consideration can replace the computation.

A planar 3RPR-platform (Fig. 4.3) is in a singular configuration, if the straight lines determined by the axes of its three legs intersect in a common point. It can be shown that this corresponds to configurations where two solutions of the direct kinematics problem coincide. Therefore, the mechanisms behavior in a singular configuration is unpredictable. This is illustrated in Fig. 4.7. The manipulator is in a singular configuration because the three legs meet in a common point **m**. Suppose now that we want to actuate the manipulator by changing the length of the leg through $\mathbf{c}_0$ while keeping fixed the remaining two leg lengths. This inverse kinematics problem has two solutions in the vicinity of the singular configurations.

The singularity surface Φ of a planar 3RPR-manipulator is depicted in Fig. 4.7. Its equation is found by writing the positions of $\mathbf{a}_1$, $\mathbf{b}_1$, and $\mathbf{c}_1$ in general form (using (4.22)) and expanding the concurrency condition of three lines. In [14] it was shown that the algebraic variety describing the singularities in the kinematic image space is a rational surface of degree four. Knowledge of geometric properties of Φ is helpful for singularity avoiding motion planing.

A SGP parallel manipulator is in a singular configuration when the Jacobian matrix (4.40) is rank deficient. There is again a simple geometric explanation for the

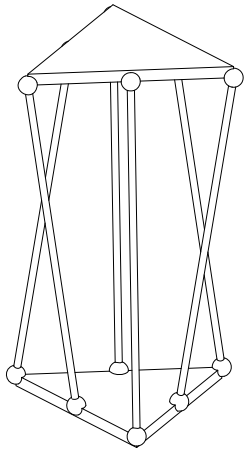

Fig. 4.8 Griffis-Duffy platform

singularity. Consider the axes of the legs of the manipulator. They are linearly dependent if they lie in a linear complex, a linear congruence or are lines on a quadric surface (see [24] for a definition of these concepts). There are more degenerate cases, which will not be mentioned here, but all cases are treated exhaustively in [22]. Because of the condition $\det \mathbf{J} = 0$ all singular positions of the manipulator belonging to rank deficiency 1 of $\mathbf{J}$ are on a degree 12 hyper-surface in P^7. Higher rank defect of $\mathbf{J}$ can be expressed by the vanishing of certain sub-determinants and corresponds to an algebraic variety as well. Little is known on that.

If $\det \mathbf{J} \equiv 0$, which means that the manipulator is singular independently of the position, then the manipulator is called *architectural singular*. One would expect that there are too many conditions that have to be fulfilled to allow this phenomenon. But surprisingly this is not the case. In [15] and [17] it is shown that for general SGP with arbitrarily distributed centers of the spherical joints architectural singularity is only possible for very degenerate designs. In the case of spherical joint centers being distributed in two planes four algebraic conditions are found which determine the locations of the anchor points in the two planes.

Self-motions of SGP occur when the mechanism moves without changing the leg length, that is with locked actuators. Algebraically this happens when the six constraint varieties and the Study quadric S determine at least a one dimensional ideal. The most famous example of this behavior is the Griffis-Duffy platform (Fig. 4.8). The ideal of constraint equations for some special design parameters of this platform reads

$$
\begin{aligned}
G := \Big[& -4x_2y_3 + 12x_1y_0 + 4y_2x_3 + 4\sqrt{3}x_1x_2, 8\sqrt{3}x_2y_0, -4x_2y_3 - 12x_1y_0 \\
& + 4y_2x_3 + 4\sqrt{3}x_1x_2, -\frac{2}{3}\sqrt{3}\big(\sqrt{3}x_2y_3 - 3\sqrt{3}x_1y_0 - \sqrt{3}y_2x_3 + \sqrt{3}x_2^2 \\
& + \sqrt{3}x_3^2 - 3x_1x_2 + 3x_2y_0 - 3y_3x_1 + 3x_3y_1\big), 4\sqrt{3}y_0(\sqrt{3}x_1 + x_2),
\end{aligned}
$$

$$4y_0^2+4y_1^2+4y_3^2+4y_2^2+x_3^2(2-R)+x_1^2(2-R)+x_2^2(2-R)$$
$$+2\sqrt{3}x_3y_1+6x_1y_0+2y_2x_3+2\sqrt{3}x_2y_0-2x_2y_3-2\sqrt{3}y_3x_1+x_1^2-x_3^2$$
$$+2\sqrt{3}x_1x_2-x_2^2, x_1y_1+x_2y_2+x_3y_3, -1+x_1^2+x_2^2+x_3^2\Big]$$

computing the Hilbert Dimension yields

```
H:=HilbertDimension(F,tdeg(x1,x2,x3,y0,y1,y2,y3))
```

$$H := 1.$$

Depending on the special design variables the constraint varieties determine various types of one dimensional ideals (see [16] and [28]). It also can happen that the ideal consist of different components having different dimensions.

A simple example is the planar 3RPR-platform, when the base anchor points and the platform anchor points form two congruent triangles and the legs have the same length. The three constraint quadrics in the kinematic image space have a circle in common and four more points, of which two are the absolute points. The circle corresponds to the possible parallel-bar motion and the two points correspond to two rigid assembly modes. Self motions of platforms can be linked to an old and famous question in kinematics which was the topic of a competition of the French academy of science in 1904. For historical references see [13].

Acknowledgement The authors thank M. Pfurner and D. Walter for their agreement to use common results for this paper.

References

1. Alizade, R., Bayram, C., Gezgin, E.: Structural synthesis of serial platform manipulators. Mech. Mach. Theory **42**, 580–599 (2007)
2. Angeles, J.: Fundamentals of Robotic Mechanical Systems: Theory, Methods, and Algorithms. Springer, Berlin (2007)
3. Blaschke, W.: Euklidische Kinematik und Nichteuklidische Geometrie. Z. Angew. Math. Phys. **60**, 61–91 (1911); 203–204
4. Blaschke, W.: Kinematik und Quaternionen. Mathematische Monographien. Springer, Berlin (1960)
5. Bottema, O., Roth, B.: Theoretical Kinematics. Dover, New York (1979)
6. Bottema, O., Roth, B.: Theoretical Kinematics. Dover, New York (1990)
7. Cox, D.A., Little, J.B., O'Shea, D.: Ideals, Varieties, and Algorithms: An Introduction to Computational Algebraic Geometry and Commutative Algebra. Springer, Berlin (1997)
8. Cox, D.A., Little, J.B., O'Shea, D.: Ideals, Varieties and Algorithms, 3rd edn. Springer, Berlin (2007)
9. Coxeter, H.S.M.: Non-Euclidean Geometry, 6th edn. Math. Assoc. Amer. (1988)
10. Golub, G.H., Van Loan, C.F.: Matrix Computations, 3rd edn. Johns Hopkins University Press, Baltimore (1996)

11. Grünwald, J.: Ein Abbildungsprinzip, welches die ebene Geometrie und Kinematik mit der räumlichen Geometrie verknüpft. Österreich. Akad. Wiss. Math.-Natur. Kl. S.-B. II **80**, 677–741 (1911)
12. Husty, M., Schröcker, H.-P.: Nonlinear Computational Geometry. The IMA Volumes in Mathematics and Its Applications, vol. 151, pp. 85–107. Springer, Berlin (2010). Chap. Algebraic geometry and kinematics
13. Husty, M.L.: E. Borel's and R. Bricard's papers on displacements with spherical paths and their relevance to self-motions of parallel manipulators. In: Ceccarelli, M. (ed.) International Symposium on History of Machines and Mechanisms-Proceedings HMM 2000, pp. 163–172. Kluwer Acad., Dordrecht (2000)
14. Husty, M.L., Gosselin, C.: On the singularity surface of planar 3-RPR parallel mechanisms. Mech. Based Des. Struct. Mach. **36**, 411–425 (2008)
15. Husty, M.L., Karger, A.: Architecture singular parallel manipulators and their self-motions. In: Lenarcic, J., Stanisic, M.M. (eds.) Advances in Robot Kinematics, pp. 355–364. Kluwer Acad., Dordrecht (2000)
16. Husty, M.L., Karger, A.: Self-motions of Griffis-Duffy type platforms. In: Proceedings of IEEE conference on Robotics and Automation (ICRA 2000), San Francisco, USA, pp. 7–12 (2000)
17. Husty, M.L., Karger, A.: Architecture singular planar Stewart-Gough platforms. In: Proceedings of the 10th Workshop RAAD, Vienna, Austria, p. 6 (2001). CD-Rom Proceedings
18. Husty, M.L., Karger, A., Sachs, H., Steinhilper, W.: Kinematik und Robotik. Springer, Berlin, Heidelberg, New York (1997)
19. Husty, M.L., Pfurner, M., Schröcker, H.-P.: A new and efficient algorithm for the inverse kinematics of a general serial 6R manipulator. Mech. Mach. Theory **42**, 66–81 (2007)
20. Husty, M.L., Pfurner, M., Schröcker, H.-P., Brunnthaler, K.: Algebraic methods in mechanism analysis and synthesis. Robotica **25**, 661–675 (2007)
21. Masouleh, M.T., Gosselin, C., Husty, M., Walter, D.R.: Forward kinematic problem of 5-RPUR parallel mechanisms (3T2R) with identical limb structures. Mech. Mach. Theory **46**, 945–959 (2011)
22. Merlet, J.-P.: Singular configurations of parallel manipulators and Grassmann geometry. Int. J. Robot. Res. **8**, 150–162 (1992)
23. Pfurner, M.: Analysis of spatial serial manipulators using kinematic mapping. Ph.D. Thesis, University Innsbruck (2006)
24. Pottmann, H., Wallner, J.: Computational Line Geometry. Springer, Berlin (2001)
25. Rath, W.: Matrix groups and kinematics in projective spaces. Abh. Math. Semin. Univ. Hamb. **63**, 177–196 (1993)
26. Schröcker, H.-P., Husty, M.L., McCarthy, J.M.M.: Kinematic mapping based assembly mode evaluation of planar four-bar mechanisms. J. Mech. Des. **129**, 924–929 (2007)
27. Selig, J.M.: Geometric Fundamentals of Robotics. Monographs in Computer Science. Springer, New York (2005)
28. Sommese, A., Verschelde, J., Wampler, C.: Advances in polynomial continuation for solving problems in kinematics. ASME J. Mech. Des. **126**, 262–268 (2004)
29. Sommese, A.J., Wampler, C.W. II: The Numerical Solution of Systems of Polynomials Arising in Engineering and Science. World Scientific, Singapore (2005)
30. Study, E.: Von den Bewegungen und Umlegungen. Math. Ann. **39**, 441–566 (1891)
31. Study, E.: Geometrie der Dynamen. B.G. Teubner, Leipzig (1903)
32. Tsai, L.-W.: Robot Analysis: The Mechanics of Serial and Parallel Manipulators. Wiley, New York (1999)
33. Walter, D., Husty, M., Pfurner, M.: Contemporary Mathematics, vol. 496. American Mathematical Society, Providence (2009), pp. 331–346. Chap. A complete kinematic analysis of the SNU 3-UPU parallel manipulator
34. Walter, D.R., Husty, M.L.: On implicitization of kinematic constraint equations. Mach. Des. Res. **26**, 218–226 (2010)

35. Wampler, C., Hauenstein, J., Sommese, A.: Mechanism mobility and a local dimension test. Mech. Mach. Theory **46**, 1193–1206 (2011)
36. Wampler, C.W.: Forward displacement analysis of general six-in-parallel SPS (Stewart) platform manipulators. Mech. Mach. Theory **31**, 331–337 (1996)
37. Wunderlich, W.: Ein vierdimensionales Abbildungsprinzip für ebene Bewegungen. Z. Angew. Math. Mech. **66**, 421–428 (1986)
38. Zlatanov, D., Fenton, R.G., Benhabib, B.: Identification and classification of the singular configurations of mechanisms. Mech. Mach. Theory **33**, 743–760 (1998)

Chapter 5
Applying Numerical Algebraic Geometry to Kinematics

Charles W. Wampler and Andrew J. Sommese

5.1 Introduction

Advances in algorithms and computer speed have brought about a new paradigm in kinematics. The proportion of effort a kinematician must exert in heavy manipulations of algebraic expressions is greatly diminished through the use of computer algorithms, and instead the kinematician may concentrate on formulating the problem and interpreting the answer so as to analyze a geometrically constrained motion or to design a device to produce desired motions. This way of working requires, however, an understanding of what kind of results the computer algorithms are capable of providing and how to use them effectively. This article condenses material from [48] providing the schema of a *mechanism space* that encapsulates most of the sorts of questions arising in kinematics and then summarizes how numerical algebraic geometry, a computational approach based on polynomial continuation, can be applied to solving such problems. In addition to [48], the application of polynomial continuation to kinematics has been addressed specifically in the tutorials [36, 45] and in substantial portions of the monograph [38].

Some notable milestones in the application of polynomial continuation to kinematics include early demonstrations that the inverse kinematics problem of general six-revolute serial-chain manipulators has 16 solutions [41], that the forward kinematics problem of general Stewart-Gough platforms has 40 solutions [32], and that the nine-point path synthesis problem for four-bar linkages has 1442 triples of Roberts-cognate solutions [46, 47]. Some indication of the difficulty of these problems is that the one with the lowest root count, the "6R problem," was once declared,

C.W. Wampler (✉)
Manufacturing Systems Laboratory, General Motors Global R&D Center, Warren, MI, USA
e-mail: charles.w.wampler@gm.com

A.J. Sommese
Applied and Computational Mathematics and Statistics, University of Notre Dame, Notre Dame IN, USA
e-mail: sommese@nd.edu

J.M. McCarthy (ed.), *21st Century Kinematics*,
DOI 10.1007/978-1-4471-4510-3_5,

in the equivalent form of the 7R spatial loop, the "Mount Everest of kinematics" [12]. While the nine-point path synthesis problem was not fully solved until nearly 70 years after its first statement in 1923 [1], the eventual cracking of the problem was presaged by partial solutions generated in 1963, in the early days of applying computers to kinematics, with a heuristic version of continuation [34]. With subsequent improvements in the technique of continuation and increases in computer speed, even the nine-point problem is now a routine calculation used as a test case for software packages in numerical continuation. (At present, it is still beyond the range of symbolic methods in computer algebra.)

These early successes all share the property that the questions to be answered have a finite number of solutions. In other words, the solution sets to be computed are *zero-dimensional*. But it is common in kinematics to explore problems having higher-dimensional solution sets. Examples include the motion curve traced out by a 1-degree-of-freedom (1DOF) mechanism, the boundary of the reachable workspace of a robot, or sets of design alternatives that satisfy an under-specified precision-point mechanism synthesis problem. (An example of the latter case is the classical center-point/circle-point Burmester curves for four given locations of a body in the plane [10].) Algebraic curves, surfaces, and beyond are all of interest in the field.

An approach for consistent treatment of higher-dimensional cases was begun in [37], where the term "numerical algebraic geometry" was coined. The essential construct in the approach is a *witness set*, in which general linear equations are appended to slice out a finite number of representative points, called *witness points*, on a higher-dimensional algebraic set. Many properties of the set can be gleaned from its witness set, and the set can be explored by tracking the witness points as the linear slicing space is moved continuously. The solution set of a system of polynomial equations can be factored into its irreducible components, each represented by a witness set, and given witness sets for two or more irreducible components, algorithms exist for finding their intersection.

The main techniques of numerical algebraic geometry are freely available in the software package Bertini [4, 5]. PHCpack [42] also implements some algorithms of the field, while Hom4PS2 [16], POLSYS_PLP [50], and POLSYS_GLP [40] offer only algorithms for computing isolated solutions.

This chapter first describes a way of viewing problems from kinematics in terms of mappings between algebraic spaces. Mechanisms, including robots, that consist of rigid links connected by the most common kinds of joints have kinematic relations that are naturally polynomial. After establishing this basic framework, attention shifts to the algorithms of numerical algebraic geometry and how to use them. Beginning with the following section, the remainder of this chapter is excerpted from [48], with permission, edited for continuity.

5.2 Notation

This chapter uses the following notations.

- $\mathbf{I} = \sqrt{-1}$, the imaginary unit.

- For polynomial system $F = \{f_1, \ldots, f_n\}$, $F : \mathbb{C}^N \to \mathbb{C}^n$, and $y \in \mathbb{C}^n$,

$$\mathscr{V}(F) = \mathscr{V}(f_1, \ldots, f_n) := \left\{ x \in \mathbb{C}^N \;\middle|\; F(x) = 0 \right\}.$$

- "DOF" means "degree(s)-of-freedom."
- $\mathbb{T}^k$ is the k-dimensional torus, the cross product of k circles.
- $\mathbb{C}^*$, pronounced "Cee-star," is $\mathbb{C} \setminus 0$, the complex plane omitting the origin.
- $\mathbb{P}^n$ is n-dimensional projective space, the set of lines through the origin of $\mathbb{C}^{n+1}$.
- Points in $\mathbb{P}^n$ may be written as homogeneous coordinates $[x_0, \ldots, x_n]$, not all zero. The coordinates are interpreted as ratios, so $[x_0, \ldots, x_n] = [\lambda x_0, \ldots, \lambda x_n]$ for any $\lambda \in \mathbb{C}^*$.
- A quaternion u is written in terms of the elements $\mathbf{1}, \mathbf{i}, \mathbf{j}, \mathbf{k}$ as

$$u = u_0\mathbf{1} + u_1\mathbf{i} + u_2\mathbf{j} + u_3\mathbf{k}, \quad u_0, u_1, u_2, u_3 \in \mathbb{C}.$$

  A quaternion u with $u_0 = 0$ can be interpreted as an ordinary spatial vector. We use $u * v$ to denote the quaternion product and u' to denote quaternion conjugation.

5.3 Algebraic Kinematics

Kinematicians are quite accustomed to writing problems as systems of polynomial equations. For example, we often begin with a standard Denavit-Hartenberg formulation in which for each rotational joint angle θ_i, the trigonometric functions $\sin\theta_i$ and $\cos\theta_i$ appear. But by the simple maneuver of defining variables

$$c_i = \cos\theta_i, \qquad s_i = \sin\theta_i,$$

and appending the trigonometric identity

$$c_i^2 + s_i^2 = 1,$$

such expressions become polynomial. In this section, we step back a moment to see why so many problems in kinematics are algebraic at their core.

5.3.1 Rigid-Body Motion Spaces

Consider first that the six-dimensional set of rigid-body transformations in three-space, $SE(3)$. The defining properties of $SE(3)$ are that each transformation must:

- preserve distances between points (the body is rigid), and
- preserve handedness (the body does not transmute into its mirror image).

The notation $SE(3)$ stands for 'special Euclidean transforms on 3-space'.

At root, rigid-body transforms are algebraic because squared distances are algebraic. Translation by a vector $\mathbf{p} \in \mathbb{R}^3$ and orthogonal transformation by a matrix $C \in O(3) = \{C \in \mathbb{R}^{3\times 3} \mid C^T C = I\}$ preserve distance, but to preserve handedness, C must be restricted to $SO(3)$ by requiring $\det C = 1$.

The most useful representations of $SE(3)$ are as follows.

- $(\mathbf{p}, C) \in \mathbb{R}^3 \times SO(3)$, where $SO(3) = \{C \in \mathbb{R}^{3\times 3} \mid C^T C = I, \det C = 1\}$. This acts on a vector $\mathbf{v} \in \mathbb{R}^3$ to transform it to $\mathbf{u} = C\mathbf{v} + \mathbf{p}$.
- The 4×4 homogeneous transform version of this, where $(\mathbf{p}, C)$ are placed in a matrix so that the transform operation becomes

$$\begin{bmatrix} \mathbf{u} \\ 1 \end{bmatrix} = \begin{bmatrix} C & \mathbf{p} \\ 0 & 1 \end{bmatrix} \begin{bmatrix} \mathbf{v} \\ 1 \end{bmatrix}.$$

- Study coordinates $[e, g] \in S_6^2 \subset \mathbb{P}^7$, where $e = (e_0, e_1, e_2, e_3)$, $g = (g_0, g_1, g_2, g_3)$ and S_6^2 is the six-dimensional hypersurface given by the equation

$$e_0 g_0 + e_1 g_1 + e_2 g_2 + e_3 g_3 = 0, \tag{5.1}$$

  known as the Study quadric. Interpreting e and g as quaternions, the transform operation is

$$\mathbf{u} = \big(e * \mathbf{v} * e' + g * e'\big)/\big(e * e'\big).$$

In all three cases, the representations live on an algebraic set. The transform operation is also algebraic in the first two cases and equations involving the Study transform operation become algebraic after clearing $e * e'$ from denominators.

There are several subgroups of $SE(3)$ that are of interest. Most prominent is $SE(2)$, the set of planar rigid-body transformations, with representations as follows.

- $(\mathbf{p}, C) \in \mathbb{R}^2 \times SO(2)$, where $SO(2) = \{C \in \mathbb{R}^{2\times 2} \mid C^T C = I, \det C = 1\}$. The transform rule looks identical to the spatial case: $\mathbf{u} = C\mathbf{v} + \mathbf{p}$.
- The unit-circle form $\{(x, y, s, c) \in \mathbb{R}^4 \mid c^2 + s^2 = 1\}$. This is the same as the former with $\mathbf{p} = x\mathbf{i} + y\mathbf{j}$ and

$$C = \begin{bmatrix} c & -s \\ s & c \end{bmatrix}.$$

- The tangent half-angle form $(x, y, t) \in \mathbb{R}^3$, in which rotations become

$$C = \frac{1}{1+t^2} \begin{bmatrix} 1-t^2 & -2t \\ 2t & 1-t^2 \end{bmatrix}.$$

- Isotropic coordinates $\{(p, \bar{p}, \theta, \bar{\theta}) \in \mathbb{C}^4 \mid \theta\bar{\theta} = 1\}$. Real transforms must satisfy $p^* = \bar{p}$ and $\theta^* = \bar{\theta}$. The action of transform $(p, \bar{p}, \theta, \bar{\theta})$ on a vector given by isotropic coordinates $(v, \bar{v})$ is the vector $(u, \bar{u})$ given by

$$(u, \bar{u}) = (p + \theta v, \bar{p} + \bar{\theta}\bar{v}).$$

Again, each of these representations lives on an algebraic set and has an algebraic transform operation (after clearing denominators in the tangent half-angle form). Clearly, $SE(2)$ is a three-dimensional space.

Another subspace of interest is the set of *spherical transforms*, that is, just $SO(3)$, another three-dimensional space. This is $SE(3)$ with the translational portion set identically to zero. The terminology "spherical" derives from the fact that this is the set of motions allowed by a spherical ball set in a spherical socket of the same diameter.

It is useful to note that since points transform algebraically, so do lines and planes, as these may be formed as linear combinations of two or three points, respectively. Labeling the points that define them, the order of the points defines an orientation for the lines and planes. Unbound unit vectors also transform algebraically, that is, by ignoring translation and applying only rotation.

5.3.2 Algebraic Joints

A mechanism is a collection of rigid bodies connected by joints. Without the joints, each body could move with six degrees of freedom anywhere in $SE(3)$. Typically, we declare one body to be "ground" and measure the locations of all the other bodies relative to it, so a collection of n bodies lives in $SE(3)^{n-1}$. Joints are surfaces of contact between bodies that constrain the motion of the mechanism to a subset of $SE(3)^{n-1}$. *Algebraic joints* are those which constrain a mechanism to *algebraic subsets* of $SE(3)^{n-1}$.

The most important joints for building mechanisms are the *lower-order pairs*. These are pairs of identical surfaces that can stay in full contact while still allowing relative motion. In other words, they are formed by a surface that is invariant under certain continuous sets of displacements. The lower-order pairs form six possible joint types, having the following standard symbols: R, revolute; P, prismatic; H, helical (screw); C, cylindrical; E, plane; and S, Spherical. The importance of the lower-order pairs derives from the fact that surface-to-surface contact spreads forces of contact over a larger area, reducing stresses that might wear out the machinery.

Fortunately—from the viewpoint of an algebraic geometer—five of these six joint types are algebraic. The exception is the H joint, which produces a translation proportional to rotation angle θ along with a rotation that depends on $\cos\theta$ and $\sin\theta$. The mixture of θ with $\cos\theta$ and $\sin\theta$ makes the motion non-algebraic. An alternative line of reasoning is to observe that a helix and a plane containing its symmetry axis intersect in an infinite number of isolated points. Any algebraic curve in $\mathbb{R}^3$ intersects a plane in at most a finite number of isolated points. However, helical joints are rarely used as a direct motion constraint in a manner that impacts kinematic analysis. Instead, screws are usually used to transmit power along a prismatic joint. Consequently, the geometric motion of a great many mechanisms is governed by algebraic joints.

To demonstrate that a joint type is algebraic, one may write down the constraint conditions it imposes between the transforms for the two bodies in contact, say A

and B. The algebraic lower-order pairs can be reduced to equating some combination of points, lines, or planes. As these are all transformed algebraically, equating them gives an algebraic constraint. In brief, one may confirm algebraicity for each joint by noting the following equivalences:

R: equate a point and an oriented line through it in A to similar in B,
P: equate a line and an oriented plane containing it in A to similar in B,
C: equate a line of A to one of B,
E: equate a plane of A to one of B, and
S: equate a point of A to one of B.

This suffices to show that the lower-order pairs R, P, C, E, and S are all algebraic.

Each joint can be described either *extrinsically* in terms of the constraint it imposes, as above, or *intrinsically* in terms of the freedom it allows between the transform for, say, body B relative to body A. Using 4×4 transform notation, and letting ${}^{i}T^{j}$ be the transform for frame j relative to frame i, one has

$$ {}^{0}T^{B} = {}^{0}T^{A}\,{}^{A}T^{B}. \tag{5.2} $$

Suppose that the joint between A and B is the kth joint of a mechanism, an algebraic lower-order pair. Then, the relative transform ${}^{A}T^{B}$ can be written as

$$ {}^{A}T^{B} = A_k X B_k, \tag{5.3} $$

where A_k and B_k are constant transforms describing the location of the joint in bodies A and B, resp., and X is variable of the form

$$ X = \begin{bmatrix} \cos\theta & -\sin\theta & 0 & a \\ \sin\theta & \cos\theta & 0 & b \\ 0 & 0 & 1 & c \\ 0 & 0 & 0 & 1 \end{bmatrix}. \tag{5.4} $$

For each joint type, the contents of X vary as follows.

R: Use (5.4) with $a = b = c = 0$, leaving θ as the joint variable.
P: Use (5.4) with $\theta = a = b = 0$, leaving c as the joint variable.
C: Use (5.4) with $a = b = 0$, leaving θ and c both as joint variables.
E: Use (5.4) with $c = 0$, leaving θ, a, and b all as joint variables.
S: Use

$$ X = \begin{bmatrix} C & 0 \\ 0 & 1 \end{bmatrix} $$

with $C \in SO(3)$ as the joint freedom.

The foregoing descriptions are meant mainly to show that the kinematic relations of rigid-body mechanisms involving only algebraic joints are all algebraic. Other formulations can sometimes be more succinct or convenient. When modeling the joints with a low number of freedoms (R, P, C) it is usually more convenient to use an

intrinsic formulation, while S joints are usually best modeled extrinsically. In some cases, one may avoid introducing transforms for some of the links altogether. For example, see Sect. 5.3.5.5 for a formulation of the kinematics of the Stewart-Gough platform that avoids introducing any transforms for the links that compose the legs.

5.3.3 Mechanism Types, Families, and Spaces

Having shown that mechanisms built with rigid links and algebraic joints have kinematic relations that are polynomial, we move on to show that a wide variety of kinematics problems can be placed into a common format involving mappings between algebraic sets. To do so, we need the definitions of a mechanism type and a mechanism family.

Definition 5.1 A *mechanism type* is defined by the number of links, n_L, and a symmetric $n_L \times n_L$ adjacency matrix T whose (i, j)th element denotes the type of joint between links i and j, one of R, P, H, C, E, S, or $\emptyset$, where $\emptyset$ indicates no connection. By convention, all diagonal elements are $\emptyset$.

(Each joint appears twice in the matrix: $T_{i,j} = T_{j,i}$ are the same joint.) We assume here that the joints are limited to the lower-order pairs, but the list of possibilities could be extended. The enumeration of all possible mechanism types for each value of n_L without double-counting mechanisms that are isomorphic under renumbering of the links is a problem in discrete mathematics. Choosing a prospective mechanism type is the first step in a mechanism design effort, and methods for guiding the enumeration of promising alternatives fall into the category of *type synthesis*. In this paper, we assume that this crucial step is already done so that we begin with a mechanism type.

Each mechanism type has an associated parameter space. We have seen in Sect. 5.3.2 one way to model each of the algebraic lower-order pairs, R, P, C, E, and S, extrinsically in terms of feature points, oriented lines, and oriented planes. Alternatively, in the intrinsic formulation of (5.3), the transforms A_k and B_k parameterize the joints. The cross-product space of all these geometric features forms a universal parameter space for the mechanism type. One may choose to model the joints in a more parsimonious way, but we assume that in the alternative model there still exists a parameterization for each joint and an associated parameter space for all the joints taken together. For example, for a succession of R and P joints, the Denavit-Hartenberg (D-H) formalism gives a minimal parameterization. (See [22] or any modern kinematics textbook for a definition.) The D-H parameters are link lengths, link offsets, and link twist angles. Treating the twists as unit circles, the parameter space becomes algebraic.

Definition 5.2 A *universal mechanism family* (T, Q) is a mechanism type T with an associated parameter space Q describing the geometry of the joints. We assume that Q is irreducible.

If one has a parameter space Q that is not irreducible, each irreducible component should be considered to define a separate universal mechanism family.

Definition 5.3 A *mechanism family* (T, Q') is a subset of a universal mechanism family (T, Q) restricted to an irreducible algebraic subset $Q' \subset Q$.

Examples of the common sorts of algebraic restrictions that define a mechanism family include the condition that the axes of two R joints in a certain link must be parallel, perpendicular, or intersecting, etc. As a particular example, consider that the universal family of spatial 3R serial-link chains includes the family of 3R planar robots, wherein the R joints are all parallel. One should appreciate that there can be subfamilies within families, and so on.

For certain mechanisms, all points of the links move in parallel planes, hence the links move in $SE(2)$ and the mechanism is said to be *planar*. In particular, a mechanism family wherein all joints are either rotational R with axis parallel to the world **z**-direction or prismatic P with axis perpendicular to the world **z**-direction is planar.

Definition 5.4 The *link space* Z for an n link mechanism is $SE(3)^{n-1}$, where one of the links is designated as ground $(\mathbf{p}, C) = (0, I)$. Any of the isomorphic representations of $SE(3)$ from Sect. 5.3.1 can be used as models of $SE(3)$. If the mechanism family is planar, then $Z = SE(2)^{n-1}$ in any of its isomorphic representations from Sect. 5.3.1.

Definition 5.5 The *mechanism space* M of a mechanism family (T, Q) is the subset of $Z \times Q$ that satisfies the joint constraints.

Proposition 5.1 *If a mechanism family is built with only the algebraic joints R, P, C, E, and S, then its mechanism space is algebraic.*

Proof Section 5.3.1 shows that Z is algebraic and Q is algebraic by assumption. That is, Z and Q are sets defined by algebraic equations. Section 5.3.2 shows that the algebraic joints impose algebraic constraints on the coordinates of Z and Q, and hence all the defining equations for M are algebraic. □

Definition 5.6 A *mechanism* is a member of a mechanism family (T, Q) given by a set of parameters $q \in Q$.

5.3.4 Kinematic Problems in a Nutshell

In this section, we present an abstract formulation that summarizes all the main types of geometric problems that arise in kinematics. In the next section, we will discuss more concretely how to map a mechanism into this formulation.

The key to our formulation is the following diagram:

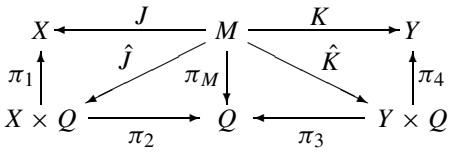

(5.5)

The main elements of the diagram are four sets X, M, Y, Q and three maps J, K, π_M. The four sets are as follows.

- X is the *input space* of the mechanism. In robotics, it is usually called the "joint space." Its coordinates are typically quantities that we command by controlling motors or other actuators.
- Y is the *output space*, often called the "operational space" in robotics. Its coordinates are the final output(s) we wish to obtain from the mechanism, such as the location of a robot's hand.
- Q is the *parameter space* of a family of mechanisms. It is the set of parameters necessary to describe the geometry of the joints in each link. Each point in Q is therefore a specific mechanism with designated link lengths, etc. The whole set Q constitutes a family of mechanisms, such as the set of all 6R robot arms, with the coordinates of Q representing all possible link lengths, etc. We assume that Q is an irreducible algebraic subset of some $\mathbb{C}^m$, that is, it is an irreducible component of $\mathcal{V}(G)$ for some system of algebraic functions $G : \mathbb{C}^m \to \mathbb{C}^{m'}$. If $\mathcal{V}(G)$ has more than one irreducible component, then each such component is considered a different family of mechanisms.
- M is the *mechanism space*, which describes all possible configurations of the mechanism for all possible parameters. Let Z be the space of all possible locations of the links when they are disconnected. That is, for an N-link spatial mechanism with one link designated as ground, $Z = SE(3)^{N-1}$. Then, M is the subset of $Z \times Q$ where the link locations satisfy the constraints imposed by the joints between them. Let $F : Z \times Q \to \mathbb{C}^c$ be a set of polynomials defining the joint constraints. Then, $M = \mathcal{V}(F) \cap \mathcal{V}(G)$ is an extrinsic representation of M. Each point $(z, q) \in M$ is a specific mechanism $q \in Q$ in one of its assembly configurations $z \in Z$. In some cases, it is more natural to describe M intrinsically via an irreducible set, say Θ, that parameterizes the freedoms of the joints of the mechanism, so that Z becomes $\Theta \times SE(3)^{N-1}$. We will use this, for example, to describe M for 6R serial-link robots. In such a representation, F includes the equations that define Θ along with the equations relating link poses to joint freedoms and equations for the constraints imposed by closing kinematic loops. Formulating such equations is part of the art of kinematics, and we will not delve into it in this paper beyond what is necessary to present specific examples.

After choosing a representation for $SE(3)$, and if present, for the joint freedom space Θ, the space Z is a subspace of some Euclidean space, $Z \subset \mathbb{C}^v$, and $z \in Z$ has coordinates $z = (z_1, \ldots, z_v)$.

Three maps are defined on M, as follows.

- $J : M \to X$ is the *input map*, which extracts from M the input values. The symbol J acknowledges that the inputs are usually a set of joint displacements.
- $K : M \to Y$ is the *output map*, which extracts from M the output values.
- $\pi_M : M \to Q$ is a projection that extracts the parameters from M. It is the natural projection operator on $Z \times Q$ restricted to M given by $\pi_M : (z, q) \mapsto q$.

If the maps F, G, J, K are merely analytic (instead of algebraic) and the spaces X, M, Y, Q are analytic, the above framework still applies, and we may pose questions in the analytic setting. In particular, H joints are analytic but not algebraic. The advantage of restricting to the algebraic setting is the existence of a much more powerful algebraic theory that enables the use of algebraic techniques, including numerical algebraic geometry, to be employed in answering the questions.

The commutative diagram is completed by defining $\hat{J} := (J, \pi_M)$ and $\hat{K} := (K, \pi_M)$ and the associated natural projections $\pi_1, \pi_2, \pi_3, \pi_4$.

It should be understood that M characterizes a family of mechanisms, such as the family of spatial 6R serial-link robots, the family of planar four-bar linkages, or the family of Stewart-Gough platforms. Maps J and K are tailored to an application of the mechanism. For a four-bar function generator, J gives the input angle and K gives the output angle, while for a four-bar path generator, K gives instead the position of the coupler point.

Using the diagram of (5.5) succinctly summarizes the algebraic setting of almost all kinematic problems. The problems can be broadly classified into three types of problems:

- Analysis (mobility analysis, forward and inverse kinematics, workspace analysis),
- Synthesis (precision point problems), and
- Exceptional mechanisms.

We describe each of these in more detail next.

5.3.4.1 Analysis

In analysis problems, one has a specific mechanism, say $q^* \in Q$, and one wishes to analyze some aspect of its motion.

Definition 5.7 The *motion of a mechanism* given by parameters $q^* \in Q$ in a family with mechanism space M is $\pi_M^{-1}(q^*) = M \cap \mathscr{V}(q - q^*) \subset Z \times Q$. This can also be called the *motion fiber over* q^*.

In the following, it is also convenient to define the inverses of J and K:

$$J^{-1}(x) = \{(z, q) \in M \mid J(z, q) = x\}, \qquad K^{-1}(y) = \{(z, q) \in M \mid K(z, q) = y\}.$$

These are defined for $x \in X$ and $y \in Y$, respectively. In the set $J^{-1}(x)$ for a particular $x \in X$, q is not fixed, so this inverse applies across a whole mechanism family.

When we wish to address just one particular mechanism, q^*, we want to consider the inverse of $\hat{J}$ instead:

$$\hat{J}^{-1}(x, q^*) = \{(z, q) \in M \mid \hat{J}(z, q) = (x, q^*)\}.$$

Similarly, we have:

$$\hat{K}^{-1}(y, q^*) = \{(z, q) \in M \mid \hat{K}(z, q) = (y, q^*)\}.$$

The basic problems in analysis are as follows.

- **Motion decomposition** of a *mechanism* breaks $\pi_M^{-1}(q^*)$ into its irreducible components, often called assembly modes by kinematicians. (See Sect. 5.6 for a description of irreducible components.) The numerical irreducible decomposition of $\pi_M^{-1}(q^*)$ finds the dimension and degree of each assembly mode and provides a set of witness points on each.
- **Motion decomposition** of a *mechanism family* breaks M into its irreducible components. If $A \subset M$ is one of these components, then $\pi_M(A) \subset Q$ is the subfamily of mechanisms that can be assembled in that mode, $\dim \pi_M(A)$ is the dimension of the subfamily, and $\dim A - \dim \pi_M(A)$ is the mobility of that mode.
- **Mobility analysis** seeks to find the degrees of freedom (DOFs) of the mechanism, that is, mobility is $\dim \pi_M^{-1}(q^*)$. As the dimension of an algebraic set is always taken to be the largest dimension of any of its components, this definition of mobility picks out the assembly mode (or modes) having the largest number of DOFs. There are simple formulas, known as the Gruebler-Kutzbach formulas, that correctly estimate the mobility for a wide range of mechanisms, and even more mechanisms submit to refined analysis based on displacement group theory, but there exist so-called "paradoxical" mechanisms that have higher mobility than these methods predict. To handle all cases, one needs to analyze the equations defining M in more detail taking into account that q^* may be on a subset of Q having exceptional mobility.
- **Local mobility analysis** finds the mobility of a mechanism in a given assembly configuration. That is, given $(z^*, q^*) \in Z \times Q$, one wishes to find

$$\text{Local mobility} := \dim_{(z^*, q^*)} \pi_M^{-1}(q^*). \tag{5.6}$$

  A mechanism can have more than one assembly mode, corresponding to the irreducible components of $\pi_M^{-1}(q^*)$. The local mobility is the dimension of the assembly mode that contains the given configuration, z^*, or if there is more than one such mode, the largest dimension among these.
- **Forward kinematics** seeks to find the output that corresponds to a given input x^* for a mechanism q^*. That is, for $x^* \in X$ and $q^* \in Q$, one wishes to find

$$FK(x^*, q^*) := K(\hat{J}^{-1}(x^*, q^*)). \tag{5.7}$$

  Example: given the joint angles of a particular 6R serial-link robot, find its hand pose.

- **Inverse kinematics** is similar to forward kinematics but goes from output to input. For $y^* \in Y$ and $q^* \in Q$ find

$$IK(y^*, q^*) := J\left(\hat{K}^{-1}(y^*, q^*)\right). \tag{5.8}$$

  Example: given the hand pose of a particular 6R serial-link robot, find all sets of joint angles that reach that pose.
- **Singularity analysis** finds configurations where the maps lose rank. If we have found a motion decomposition of the mechanism, then for each assembly mode $A \subset \pi_M^{-1}(q^*)$ there is an associated input space $J(A)$ and an output space $K(A)$. The input and output maps have Jacobian matrices $\partial J/\partial z$ and $\partial K/\partial z$. Assume for the moment that A is a reduced algebraic set. (For example, $\mathscr{V}(x-y)$ is a reduced line in the (x, y)-plane, while the double line $\mathscr{V}((x-y)^2)$ is non-reduced.) For generic points $(z, q^*) \in A$, the Jacobian matrices have a constant rank, say $\operatorname{rank}[\partial J/\partial z(z, q^*)] = r_J$ and $\operatorname{rank}[\partial K/\partial z(z, q^*)] = r_K$. Then, there may be input and output singularities, as follows.

  Input Singularities: $\{(z, q^*) \in A \mid \operatorname{rank} \frac{\partial J}{\partial z}(z, q^*) < r_J\}$. In the common case that $\partial J/\partial z$ is square and generically full rank, these are the special configurations where, to first order, the mechanism can move without any change in its input.

  Output Singularities: $\{(z, q^*) \in A \mid \operatorname{rank} \frac{\partial K}{\partial z}(z, q^*) < r_K\}$. In the common case that $\partial K/\partial z$ is square and generically full rank, these are the special configurations where, to first order, the mechanism can move without any change in its output.

  If A is a non-reduced assembly mode, one might wish to consider the input and output singularities of the reduction of A, which can be analyzed via a deflation of A. (See Sect. 5.6.3.)
- **Workspace analysis** seeks to find all possible outputs of a robot or mechanism. Ignoring limits on the inputs, this is just the set $K(\pi_M^{-1}(q^*))$. The main concern in practice is the set of outputs for real assembly configurations, so letting $A_{\mathbb{R}}$ denote the real points in an assembly mode A, the corresponding workspace is $K(A_{\mathbb{R}})$. Output singularities and joint limits induce boundaries in the workspace.
  Example 1: for a 6R serial-link robot, find all possible poses that the hand can reach.
  Example 2: for a given four-bar linkage with output defined as the position of its coupler point, find the coupler curve.
  Example 3: for a 6-SPS (Stewart-Gough) platform robot with limits on the leg lengths, find all possible poses of the moving platform.

The motion of a mechanism over the complexes contains its real motion, but the extraction of the real motion from the complex one can be difficult, all the more so as the dimensionality of the motion grows. See Sect. 5.6.5 for a discussion.

The problems presented above mainly concern the geometry of a mechanism's motion, where principally angles, positions, and poses enter the picture. As indicated by the questions of singularity analysis, one may also be concerned with differential relations between these, so that joint rates, linear velocity, and angular velocity may become objects of study. Since these are all related to the mechanism

space M through its derivatives, these too fit into the algebraic setting, as do static forces and torques, through the principles of virtual work.

5.3.4.2 Synthesis

While analysis determines how a mechanism moves, synthesis finds mechanisms that move in a specified way. Synthesis problems begin with a set of desired outputs or a set of input/output pairs and seek to find the mechanisms that will produce these. Synthesis tends to be harder than analysis because one must consider the ability of the mechanism to reach each desired state. In essence, we must consider multiple copies of M simultaneously. The relevant construction in algebraic geometry is called the *fiber product*. Instead of studying M, one works with $M \times_Q M = \mathcal{V}(F(z_1; q), F(z_2; q))$, which comprises two copies of the motion for the same mechanism. Clearly, the fiber product operation can be extended to triple fiber products and higher. Forming the k-fold fiber product

$$M_Q^k := \underbrace{M \times_Q \cdots \times_Q M}_{k \text{ times}},$$

if $\pi_{M,k}$ is the projection from M_Q^k that picks out its parameters, q, then $\pi_{M,k}^{-1}(q^*)$ for $q^* \in Q$ gives back k copies of the motion fiber over q^*. We may also define a map K_k acting on M_Q^k to produce k outputs and a map JK_k acting on M_Q^k to produce k input/output pairs.

With these maps, we may define several kinds of synthesis problems. The following problems are known as *precision point* problems, since there is a set of specified points which the mechanism must interpolate exactly.

- **Output synthesis** seeks mechanisms that can reach a set of specified outputs. For $(y_1, \ldots, y_k) \in Y^k$, we wish to find the set

$$\left\{q \in Q \mid K_k\left(\pi_{M,k}^{-1}(q)\right) = (y_1, \ldots, y_k)\right\}.$$

  Kinematicians distinguish between different types of output synthesis.

  Path synthesis finds mechanisms where the path of a point of the mechanism interpolates a set of given points. In this case, K is defined on M such that $Y \subset \mathbb{C}^3$.

  Body guidance In this case, the output is the pose of one body of the mechanism, that is, $Y \subset SE(3)$. The purpose of the mechanism is to guide that body through a set of specified poses.

- **Input/output synthesis** seeks mechanisms that produce a coordinated input/output relationship specified by a set of input/output pairs. For $((x_1, y_1), \ldots, (x_k, y_k)) \in (X \times Y)^k$, we wish to find the set

$$\left\{q \in Q \mid JK_k\left(\pi_{M,k}^{-1}(q)\right) = \left((x_1, y_1), \ldots, (x_k, y_k)\right)\right\}.$$

A common case is a 1DOF mechanism, such as a four-bar, with the input being the angle of one link with respect to ground. Then, with K defined as in a path synthesis problem, the input/output problem becomes *path synthesis with timing*. Similarly, one can have *body guidance with timing*. (The nomenclature derives from an assumption that the input moves at a constant rate.) If the input and output are both angles of the mechanism, then input/output synthesis becomes *function generation*, as the precision points approximate some desired functional relationship between input and output.

What makes these problems difficult is that the whole system of equations defining M is repeated k times, increasing the total degree of the system exponentially in k.

For any precision point problem, there is a maximum number of precision points that can be specified. Roughly speaking, this is the total number of independent parameters in the mechanism family under consideration divided by the number of constraints placed on the parameters by each precision point. If more than the maximum number of precision points is specified, then there will in general be no mechanism that interpolates them exactly. One may then reformulate the problem by defining an error metric and seek mechanisms whose motion best fits the specified approximation points. This is analogous to finding a best-fit line that approximates three or more points.

We should note that all these synthesis problems have been formulated only at the geometric level. It is also possible to specify motions at the level of velocity or acceleration or to mix specifications at several levels. For a 1DOF motion, differential relations can be approximated by limits as precision points approach each other. For this reason, classical synthesis theory sometimes distinguishes between *finitely-separated precision points* and *infinitesimally-separated precision points*. We will not discuss synthesis problems involving differential relations further here.

5.3.4.3 Exceptional Mechanisms

While M describes the motion of an entire family of mechanisms, $\pi_M^{-1}(q^*)$ is the motion of a particular mechanism in the family. For any generic $q \in Q$, attributes such as the mobility of the mechanism or the local mobilities of its assembly modes all stay constant. However, there may be algebraic subsets of Q where mobilities increase. These exceptional mechanisms are often called "overconstrained mechanisms," as a slight perturbation of the parameters off of the exceptional set into a generic position suddenly brings in extra constraints that reduce mobility. One may define subsets of M where the local mobility is constant, that is,

$$\mathscr{D}_k^* = \left\{(z,q) \in M \;\middle|\; \dim_{(z,q)} \pi_M^{-1}(q) = k\right\}. \tag{5.9}$$

The closures of these, $\mathscr{D}_k = \overline{\mathscr{D}_k^*}$, are algebraic sets. When $\mathscr{D}_j \subset \mathscr{D}_k$, $j > k$, we say that $\mathscr{D}_j$ is an exceptional set of mechanisms, a family of overconstrained mechanisms.

The discovery of exceptional mechanisms is perhaps the most difficult kind of kinematics problem. One may think of these as a kind of synthesis problem where the only thing that is specified about the motion is its mobility. As in the precision-point synthesis problems, it turns out that fiber products play a central role. We leave further discussion of this to Sect. 5.6.6.

5.3.5 Fitting into the Nutshell

Sections 5.3.1 and 5.3.2 show that any mechanism composed of n rigid links connected by any combination of R, P, C, E, or S joints leads to a set of constraint equations that is algebraic in the link locations $(\mathbf{p}_j, C_j) \in SE(3)$, $j = 1, \ldots, n$ and is also algebraic in the parameters defining the joints. In Sects. 5.3.3, 5.3.4, we put forward a schema that formulates a wide variety of kinematics problems in terms of spaces X, M, Y, Q and maps J, K, π between them. In this section, we will detail how some example mechanism types fit into this schema.

5.3.5.1 Planar 3R Robots

Consider first the universal family of 3R planar serial-link robots. These have $n_L = 4$ links, one of which is ground. The adjacency matrix has R in each element of the super- and sub-diagonals and $\emptyset$ everywhere else. Since the mechanism is planar, the link space is $Z = SE(2)^3$. Using the reference frames as indicated in Fig. 5.1, we have coordinates for Z as

$$\begin{aligned} z_1 &= (P_x, P_y, x_1, y_1), \qquad z_2 = (Q_x, Q_y, x_2, y_2), \\ z_3 &= (R_x, R_y, x_3, y_3), \end{aligned} \tag{5.10}$$

where (P_x, P_y) are the coordinates of point P, etc., and $x_j = \cos\phi_j$, $y_j = \sin\phi_j$, $j = 1, 2, 3$. Here, ϕ_1, ϕ_2, ϕ_3 are the absolute rotation angles of the links. Accordingly, the algebraic equations defining the link space Z are

$$x_j^2 + y_j^2 - 1 = 0, \quad j = 1, 2, 3. \tag{5.11}$$

The parameters of the mechanism are just the link lengths (a, b, c), so the parameter space Q is $\mathbb{C}^3$. In the plane, the constraint imposed on two links by a rotational joint is the coincidence of the point of connection. Point $O = (0, 0)$ in the ground must coincide with point $(-a, 0)$ in the reference frame of link 1:

$$(0, 0) = (P_x - ax_1, P_y - ay_1). \tag{5.12}$$

Similarly, the other two joints impose the constraints

$$(P_x, P_y) = (Q_x - bx_2, Q_y - by_2) \quad \text{and} \quad (Q_x, Q_y) = (R_x - cx_3, R_y - cy_3). \tag{5.13}$$

Accordingly, (5.11)–(5.13) define the mechanism space M.

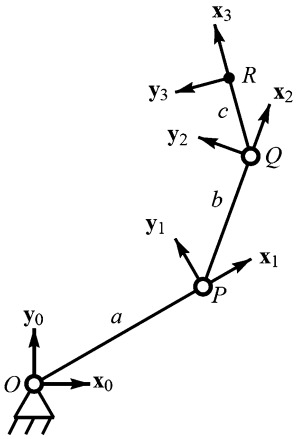

Fig. 5.1 Planar 3R robot with reference frames

To complete the picture, we need the maps π_M, J, K. The projection $\pi_M : M \to Q$ simply picks out the parameters:

$$\pi : (z_1, z_2, z_3, a, b, c) \mapsto (a, b, c). \tag{5.14}$$

Assuming the input space $X = \mathbb{T}^3$ is the relative rotation angles $(\theta_1, \theta_2, \theta_3)$ represented by cosine/sine pairs, the difference formulas for cosine and sine give

$$\begin{aligned} J : (z_1, z_2, z_3, a, b, c) \mapsto \big((x_1, y_1), (x_2 x_1 + y_2 y_1, y_2 x_1 - x_2 y_1), \\ (x_3 x_2 + y_3 y_2, y_3 x_2 - x_3 y_2)\big). \end{aligned} \tag{5.15}$$

Finally, assuming the output space $Y = SE(2)$ is the location of reference frame 3, the output map is

$$K : (z_1, z_2, z_3, a, b, c) \mapsto (z_3). \tag{5.16}$$

If instead the robot is applied to just positioning point R in the plane, we have $Y = \mathbb{C}^2$ with the output map

$$K' : (z_1, z_2, z_3, a, b, c) \mapsto (R_x, R_y). \tag{5.17}$$

With these definitions, the problems of forward kinematics, inverse kinematics, reachable workspace, and exceptional sets all fit neatly into the nutshell schema.

5.3.5.2 Spatial 6R Robots

The case of spatial 6R robots is quite similar to the 3R planar case, but we shall choose to handle the joint constraints by introducing variables implicitly modeling the freedom of the joints rather than explicitly writing constraint equations. A 6R serial-link chain has $n_L = 7$ links, one of which is ground. The adjacency

matrix has entries of R on the super- and sub-diagonals and $\emptyset$ elsewhere. Let the link space be $Z = \mathbb{T}^6 \times SE(3)^6$, with unit circle representations of the joint angles and 4×4 homogeneous transforms for the link locations, so that Z is represented as $z = \{(c_j, s_j, {}^0T^j),\ j = 1, \ldots, 6\}$ with

$$c_j^2 + s_j^2 - 1 = 0, \quad j = 1, \ldots, 6. \tag{5.18}$$

The first factor of Z is precisely the joint space $X = \mathbb{T}^6$ and the output is the location of the "hand," the last frame in the chain, ${}^0T^6$. The link parameters are 4×4 transforms $A_j \in SE(3)$, $j = 0, 1, \ldots, 6$. One can use general transforms, but the Denavit-Hartenberg formalism shows that by choosing reference directions aligned with joint axes and their common normals, it suffices to parameterize the A_j as

$$A_j = \begin{bmatrix} 1 & 0 & 0 & a_j \\ 0 & \alpha_j & -\beta_j & -\beta_j d_j \\ 0 & \beta_j & \alpha_j & \alpha_j d_j \\ 0 & 0 & 0 & 1 \end{bmatrix}, \quad j = 0, \ldots, 6. \tag{5.19}$$

In this expression, (α_j, β_j) are a cosine/sine pair for the twist of link j, a_j is the length of the link (along its $\mathbf{x}$-direction), and d_j is the link offset distance (along its $\mathbf{z}$-direction). To keep A_j in $SE(3)$, these must satisfy

$$\alpha_j^2 + \beta_j^2 - 1 = 0, \quad j = 0, \ldots, 6. \tag{5.20}$$

With this parameterization, the parameter space is $Q = \mathbb{T}^7 \times \mathbb{C}^{14}$ with coordinates $q = \{(\alpha_j, \beta_j, a_j, d_j),\ j = 0, \ldots, 7\}$. Joint rotations $R_z(c_j, s_j)$ of the form

$$R_z(c, s) = \begin{bmatrix} c & -s & 0 & 0 \\ s & c & 0 & 0 \\ 0 & 0 & 1 & 0 \\ 0 & 0 & 0 & 1 \end{bmatrix} \tag{5.21}$$

alternate with relative link displacements A_j to give the transforms of the link locations as

$${}^0T^1 = A_0 R_z(c_1, s_1) A_1, \qquad {}^0T^j = {}^0T^{j-1} R(c_j, s_j) A_j, \quad j = 2, \ldots, 6. \tag{5.22}$$

Combining these gives

$${}^0T^6 = K_{6R}(z, q) := A_0 \prod_{j=1}^{6} R_z(c_j, s_j) A_j. \tag{5.23}$$

Equations (5.18)–(5.21) define the mechanism space M in terms of coordinates (z, q). The associated maps from M to Q, $X = \mathbb{T}^6$, and $Y = SE(3)$ are

$$\begin{aligned} &\pi_M : (z, q) \mapsto q, \qquad J : (z, q) \mapsto \big((c_j, s_j), j = 1, \ldots, 6\big), \\ &K = K_{6R} : (z, q) \mapsto {}^0T^6. \end{aligned} \tag{5.24}$$

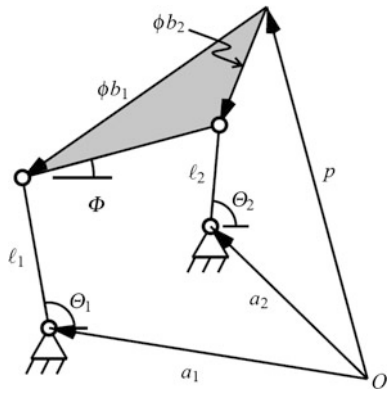

Fig. 5.2 Vector diagram of a four-bar linkage

5.3.5.3 Four-Bar Linkages

The four-bar has four links with four R joints. If we call the ground link 0, the two links connected to ground as links 1 and 2, and the coupler as link 3, then the adjacency matrix has entries $T_{1,3} = T_{2,3} = T_{0,1} = T_{0,2} = \mathrm{R}$. Using isotropic coordinates (see Sect. 5.3.1), let $(\phi, \bar{\phi})$ represent the orientation of the coupler link and let $(\theta_1, \bar{\theta}_1)$ and $(\theta_2, \bar{\theta}_2)$ be the rotations of links 1 and 2, and let $(p, \bar{p})$ be the coupler point position. [Recall that in isotropic coordinates, we represent a vector, say $\mathbf{a} = \alpha\mathbf{i} + \beta\mathbf{j}$, by a complex number $a = \alpha + \beta\mathbf{I}$ and its conjugate $\bar{a} = \alpha - \beta\mathbf{I}$.] Hence, the link space Z is given by coordinates $z = (p, \bar{p}, \phi, \bar{\phi}, \theta_1, \bar{\theta}_1, \theta_2, \bar{\theta}_2)$ subject to the unit length conditions of

$$\phi\bar{\phi} = \theta_1\bar{\theta}_1 = \theta_2, \qquad \bar{\theta}_2 = 1. \tag{5.25}$$

Referring to Fig. 5.2, a four-bar can be parameterized by $Q = \mathbb{C}^{10}$ with coordinates $q = (a_1, \bar{a}_1, a_2, \bar{a}_2, b_1, \bar{b}_1, b_2, \bar{b}_2, \ell_1, \ell_2)$. With these notations, the mechanism space for four-bar linkages is the solution set of the equations

$$\begin{aligned}
&\ell_1\theta_1 = p + \phi b_1 - a_1, \qquad && \ell_1\bar{\theta}_1 = \bar{p} + \bar{\phi}\bar{b}_1 - \bar{a}_1, \\
&\ell_2\theta_2 = p + \phi b_2 - a_2, \qquad && \ell_2\bar{\theta}_2 = \bar{p} + \bar{\phi}\bar{b}_2 - \bar{a}_2, \\
&\theta_1\bar{\theta}_1 = 1, \qquad \theta_2\bar{\theta}_2 = 1, \qquad && \phi\bar{\phi} = 1.
\end{aligned} \tag{5.26}$$

The input and output spaces and their associated maps depend on the application of the mechanism. For path generation, we have output $Y = \mathbb{C}^2$ with map $K = K_{\text{path}} : (z, q) \mapsto (p, \bar{p})$. For body guidance, $Y = SE(2)$ with $K = K_{\text{guide}} : (z, q) \mapsto (p, \bar{p}, \phi, \bar{\phi})$. If timing along the coupler curve or timing of the body motion are of concern, we may name the angle of one of the links connected to ground as input, say $X = \mathbb{T}^1$ given by $J : (z, q) \mapsto (\theta_1, \bar{\theta}_1)$. For function generation, the input is the angle of link 1 and the output is the angle of link 2, so $J : (z, q) \mapsto (\theta_1, \bar{\theta}_1)$ and $K = K_{\text{fcn}} : (z, q) \mapsto (\theta_2, \bar{\theta}_2)$.

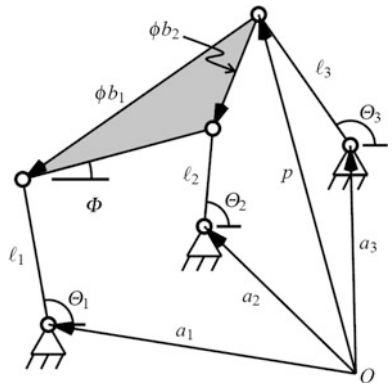

Fig. 5.3 3-RPR planar platform robot

The raw equation sets that come out of the above formulation often benefit from further algebraic manipulation before submitting the system to a numerical solution procedure. In particular, for the path synthesis problem, it can be beneficial to eliminate some variables. In the nine-point path synthesis problem—in general, nine is the maximal number of precision points that can be exactly interpolated—we wish to find parameters q such that the coupler curve $K_{\text{path}}(\pi_M^{-1}(q)) \subset \mathbb{C}^2$ passes through points $(p_i, \bar{p}_i)$, $i = 0, \ldots, 8$. With a little algebra, this can be reduced to solving a system of eight polynomials

$$f_{cc}(p_j, \bar{p}_j; q) = 0, \quad j = 1, \ldots, 8, \tag{5.27}$$

each of degree seven. See [46, 48] for derivations, based on a similar formulation from Roth and Freudenstein [34].

5.3.5.4 Planar 3-RPR Platforms

A 3-RPR planar platform robot has a moving triangle supported from a stationary triangle by three RPR legs, as in Fig. 5.3. Coordinates for the mechanism space M of the 3-RPR planar platform are an extension of those for the four-bar with $a_3, \bar{a}_3, \theta_3, \bar{\theta}_3, \ell_3$ appended with the additional equations:

$$\ell_3\theta_3 = p - a_3, \qquad \ell_3\bar{\theta}_3 = \bar{p} - \bar{a}_3, \quad \text{and} \quad \theta_3\bar{\theta}_3 = 1. \tag{5.28}$$

However, there is a shuffle in which coordinates are parameters and which are variables of the motion. The new maps are

$$\begin{aligned} \pi &: (z, q) \mapsto (a_1, \bar{a}_1, a_2, \bar{a}_2, a_3, \bar{a}_3, b_1, \bar{b}_1, b_2, \bar{b}_2), \\ J &: (z, q) \mapsto (\ell_1, \ell_2, \ell_3), \\ K &: (z, q) \mapsto (p, \bar{p}, \phi, \bar{\phi}). \end{aligned} \tag{5.29}$$

5.3.5.5 Stewart-Gough Platforms

For the forward and inverse kinematics problems of the 6-SPS platform, we do not need to explicitly represent transforms for the upper and lower leg segments. It is enough to use the leg lengths and the transform for the moving platform. Hence, the link space is $Z = \mathbb{C}^6 \times SE(3)$, and if we use Study coordinates for $SE(3)$, the space is $Z = \mathbb{C}^6 \times S_6^2$, where $S_6^2 \subset \mathbb{P}^7$ is the Study quadric given by (5.1). With leg lengths $L_1, \ldots, L_6$, the coordinates of Z are $(L_1, \ldots, L_6), [e, g]$. The parameter space Q consists of the vectors $\mathbf{a}_j, \mathbf{b}_j \in \mathbb{C}^3$, $j = 1, \ldots, 6$, that specify the centers of the S joints in the base and moving platforms. The mechanism space M is given by the Study quadric along with the leg-length equations

$$L_i^2 = \left\| \left(g * e' + e * \mathbf{b}_j * e'\right) / \left(e * e'\right) - \mathbf{a}_j \right\|_2^2, \quad j = 1, \ldots, 6, \tag{5.30}$$

which after expanding and clearing denominators becomes for $j = 1, \ldots, 6$

$$\begin{aligned} 0 = {} & g * g' + \left(\mathbf{b}_j * \mathbf{b}_j' + \mathbf{a}_j * \mathbf{a}_j' - L_j^2\right) e * e' + \left(g * \mathbf{b}_j' * e' + e * \mathbf{b}_j * g'\right) \\ & - \left(g * e' * \mathbf{a}_j' + \mathbf{a}_j * e * g'\right) - \left(e * \mathbf{b}_j * e' * \mathbf{a}_j' + \mathbf{a}_j * e * \mathbf{b}_j' * e'\right). \end{aligned} \tag{5.31}$$

The input space $X = \mathbb{C}^6$ is the set of leg lengths $L_1, \ldots, L_6$, and the output space is $Y = S_6^2$ is the Study quadric for the transform of the moving platform. The maps J, K are the associated natural projections.

5.4 Overview: Numerical Algebraic Geometry

The fundamental problem in numerical algebraic geometry is to numerically compute and manipulate the solution set of a system of polynomials

$$f(x) := \left[f_1(x), \ldots, f_n(x)\right], \tag{5.32}$$

where $x = (x_1, \ldots, x_N) \in \mathbb{C}^N$. As we have seen in the preceding sections, problems in kinematics often concern parameterized systems, that is, polynomial systems of the form

$$f(x, q) := \left[f_1(x, q), \ldots, f_n(x, q)\right] \tag{5.33}$$

with $x \in \mathbb{C}^N$ and $q \in Q$, where Q is an irreducible algebraic set. We may have simply $Q = \mathbb{C}^M$, a Euclidean space of M independent parameters, but we may also have a Q formed with elements from $SE(3)$ or the unit circle. It is important to note that in practice, an engineer might not know the exact twist angle of a link, but when it comes to solving the associated polynomial system, it is known that the sine/cosine pair of the angle must lie on the unit circle.

Historically, within numerical algebraic geometry, the problem of finding isolated solutions for *square systems*, i.e., systems such as (5.32) in the case $n = N$,

came first. The most basic tool is homotopy continuation (or continuation for short), which consists of studying a square system of polynomials $f(x)$ by starting with a simpler system $g(x)$ that we know how to solve and deforming $g(x)$ and the solutions of $g(x) = 0$ to $f(x)$ and the solutions of $f(x) = 0$. A good source for explication of this basic approach is the book [24], with more modern treatments given in [19, 38].

The solution of non-square systems ($n \neq N$ in (5.32)) came considerably later than methods for square systems. The techniques we employ always reformulate such problems to reduce them once again to finding isolated solutions.

At first sight, the case of $n > N$ (more equations than unknowns) would seem to be numerically unstable, as a small perturbation of the system can obliterate a solution. The is true for any solution sets of dimension greater than $N - n$. The fact that saves the day is that the existence of such solutions depends on the parameters lying exactly on a parameter space, and we assume we know the exact equations that define that space. Consider a pair of parameters that should lie on a unit circle. When we work numerically, the pair will rarely lie exactly on the circle, but the exact unit circle condition is known, and by using extra digits, the pair of parameters can be placed as close as needed to the true parameter space. Thus, to make the computation of sets of dimension greater than $N - n$ robust, the Bertini software package [4] implements *adaptive multiprecision arithmetic* (see Sect. 5.5.5) that adjusts the number of digits as needed. This same technology stabilizes the numerics of isolated singular and near-singular roots of square systems.

To provide a complete ability to solve systems of polynomials, one must be able to deal not just with isolated roots but also with higher-dimensional solution sets (curves, surfaces, etc.). Obviously, this arises when $n < N$, as there are not enough equations to determine an isolated root.[1] The approach of dealing with this in numerical algebraic geometry is a data structure called a *witness set* in which extra linear equations are introduced in order to cut out general isolated points on the higher dimensional sets. These points can then be computed using the techniques for finding isolated solution points. To cut out isolated points on a set of dimension m, one must augment the original system with $N - m$ general linear equations. Thus, if the solution set is has dimension $m > N - n$, the augmented system has $n + m > N$ equations, which has the potential for being numerically unstable. The procedure for stabilizing this situation depends on *randomization*, as described in Sect. 5.5.11.

5.5 Finding Isolated Roots

In this section we briefly discuss the continuation method of finding isolated solutions of a polynomial system (5.32). Various aspects of how this process is made

[1] At least not in complex space. In real space, singular isolated roots are possible with $n < N$. See Sect. 5.6.5.

robust and efficient are highlighted. From the viewpoint of a user of software packages for continuation, a few things, particularly the division of variables into groups for multihomogenization, requires some level of expertise from the user, but most of these measures can be automated without user input. The motivation for a user to understand the basic solution processes is for making an informed choices of which software to use, as discussed further in Sect. 5.7, and which algorithms to use within a chosen software package. Although it will not be addressed here, advanced users may also change configuration settings that can affect the speed and robustness to adapt performance to the specific needs of their applications.

5.5.1 Homotopy

For the square case of N polynomials in N unknowns, one of the most classical homotopies is the total-degree homotopy that uses the "γ trick" of [26]:

$$H(x,t) := (1-t)\begin{bmatrix} f_1(x) \\ \vdots \\ f_N(x) \end{bmatrix} + \gamma t \begin{bmatrix} g_1(x) \\ \vdots \\ g_N(x) \end{bmatrix}, \tag{5.34}$$

where each polynomial g_j has degree the same as f_j and the solution set of the system $(g_1(x), \ldots, g_N(x)) = 0$ consists of $d_1 \cdots d_N$ nonsingular isolated solutions. When γ is chosen as a random complex number, then with probability one, the homotopy satisfies the properties:

1. $\{(x,t) | t \in (0,1]; x \in \mathbb{C}^N; H(x,t) = 0\}$ is a union of $d_1 \cdots d_N$ full-rank paths, say $x_1(t), \ldots, x_{d_1 \cdots d_N}(t)$, starting at the solutions of $H(x,1) = 0$; and
2. the set of limits $\lim_{t \to 0} x_j(t)$ that are finite include all the isolated solutions of $H(x,0) = 0$.

This theory justifies the use of the very simple start system defined by $g_j(x) = x_j^{d_j} - 1$, $j = 1, \ldots, N$.

5.5.2 Multihomogeneous Homotopies

Constructing good homotopies with the number of paths not too different from the number of isolated solutions of f was an important research topic at the end of the 20th century. There is detailed discussion of this topic in [38, Chap. 8]. For systems that are not too large, which includes many mechanism systems, multihomogeneous formulations can be quite useful. Multihomogeneous homotopies were first proposed in [25] and discussed in [38, §8.4].

For a hint of what difference the selection of homotopy can make, consider the 3-RPR forward kinematics problem of Sect. 5.3.5.4, which is to solve the 10

equations (5.26, 5.28) for the 10 unknowns $(\theta_1, \theta_2, \theta_2, \phi, p, \bar{\theta}_1, \bar{\theta}_2, \bar{\theta}_2, \bar{\phi}, \bar{p})$. Six of the equations are linear but the four unit-length equations are degree 2, for a total degree of 16. Yet, as a 2-homogeneous system, with variables divided into two groups as $(\theta_1, \theta_2, \theta_2, \phi, p)$, $(\bar{\theta}_1, \bar{\theta}_2, \bar{\theta}_2, \bar{\phi}, \bar{p})$, the system has at most $\binom{4}{2} = 6$ isolated roots, which is in fact the exact root count for general cases. In the Bertini software package, the move from a total degree homotopy to a 2-homogeneous one is done by simply using two separate `variable_group` statements to declare the variables.

A more impressive example is the nine-point path synthesis problem mentioned in Sect. 5.3.5.3. In the Roth-Freudenstein formulation of (5.27), the total degree of the system is $7^8 = 5,764,801$. An alternative in [46] uses a 2-homogeneous formulation of the problem that has a root count of just 286,720. A special homotopy that takes advantage of a 2-way symmetry reduces the number of paths to 143,360, which is about one-fortieth $(1/40)$ that of the total degree homotopy. This formulation lead to the first complete solution of this classical problem in kinematics.

5.5.3 Sparse Homotopies

A polynomial of degree d in N variables can have $\binom{N+d}{N}$ different monomials but problems arising in applications typically have many fewer than this. Multihomogeneous homotopies take advantage of sparseness associated to limited mixing of products between variables within groups. This is a common occurrence in kinematics, but it does not capture all the kinds of sparseness that may arise. In particular, in a multihomogeneous formulation, variable groupings stay fixed across the whole system of polynomials.

Linear product homotopies capture sparseness at a finer scale, including, for example, groupings of variables that change from one polynomial to the next. The main alternatives are laid out in [38, Chap. 8], based on theory developed in [43] and generalized in [29]. Versions of this are available in POLSYS_PLP [50] and POLSYS_GLP [40].

Polyhedral homotopies take full advantage of any sparse structure in a polynomial system. While the multihomogeneous and linear product homotopies require the user to identify good groupings of the variables—no efficient method is known for finding the best groupings—the polyhedral method completely automates the creation of a homotopy with the minimal number of paths for systems with the sparse structure of the target system. The leading approach for polyhedral homotopies is described in [20] and is implemented in HOM4PS2 [16].

Unfortunately, the formation of a polyhedral homotopy depends on an intricate combinatorial calculation, called the mixed volume, whose complexity grows rapidly with the number of variables and which is not easily parallelizable. So while it is an excellent approach for small to medium size problems, it becomes untenable for large ones.

5.5.4 Regeneration Homotopy

For larger systems, the regeneration approach scales up more readily than the polyhedral approach [13, 14]. Moreover, it can take advantage of structure in the system beyond just sparsity. In particular, the coefficients that appear in a polynomial system may satisfy interrelationships that reduce the root count. In the kinematics context, this might arise as parameters that satisfy a unit circle condition or that lie in $SE(3)$. Regeneration does not build this structure into the homotopy from the beginning, as is done in the sparse homotopies, but rather it discovers structure by treating the system equation-by-equation. Regeneration methods are available in the Bertini software package.

5.5.5 Adaptive Multiprecision

Higher-precision arithmetic (i.e., greater than double precision) makes the basic process of path tracking more bulletproof, while adaptive multiprecision, in which precision is adjusted up or down as needed, accomplishes this goal with greater efficiency. Consider the nine-point path-synthesis problem for four-bars just mentioned above. Of the 143,360 paths in the homotopy used in [46], all but 4326 end on various degenerate sets. The 4326 roots of interest appear in a three-way symmetry, as expected from the classical result known as Roberts cognates [10, 33]. The original computations in 1992 on this problem were conducted in double precision followed by a check for any points missing from the expected symmetry groups. Reruns in extended precision cleaned up any paths having questionable numerical stability, filling in the missing points and thereby establishing with high confidence that the solution list was complete. More recent experiments with a path-tracker having adaptive multiprecision found that in order to be tracked accurately, 0.83 % of the paths required precision higher than double precision somewhere in the middle of the paths before returning to double precision (see [7, §5.3]). This approach consistently finds the entire solution set without requiring any reruns or other corrective actions. Although in the early 1990s, this was an extraordinarily difficult computation, we now use this problem as a moderately difficult test system.

5.5.6 Parallelism

One of the highly advantageous features of polynomial continuation is that all the paths of a homotopy can be tracked independently. For many algorithms in the field, this makes the bulk of the computation "embarrassingly parallel." The Bertini software package offers a parallel version for the Linux operating system [4]. Unfortunately, it is much harder to efficiently parallelize the steps that set up a polyhedral homotopy, so that, as of this writing, the leading polyhedral package, Hom4PS2 [16], is only available for single-processor systems.

5.5.7 Solutions at Infinity

One difficulty in path tracking is paths that go to infinity as $t \to 0$. Tracking such a path may be computationally expensive as it is infinitely long and numerical conditioning may be poor as the magnitudes of the solution variables grow. Morgan's projective transformation trick [23] is to work on a random coordinate patch in the projective space containing $\mathbb{C}^N$. This maneuver keeps the magnitude of the variables and the path lengths finite. It is common for polynomial continuation packages, such as Bertini, to perform homogenization automatically.

5.5.8 Multiplicities and Deflation

It is widely appreciated that for a polynomial in one variable, the multiplicity of a solution is governed by the number of derivatives that vanish there. In several variables, multiplicity still makes sense, but directional derivatives and algebraic relations between them come into play, so the situation is more complicated.

For the moment, consider only isolated solutions of a polynomial system. (We take up multiplicity as it applies to higher-dimensional sets in Sect. 5.6.3.) When the multiplicity μ of solution z^* is greater than one, z^* is said to be a singular solution. Such solutions are difficult to work with numerically. A primary problem is that the vanishing derivatives ruin the convergence properties of Newton's method near the singular point. For this reason, tracking paths to z^* from a good homotopy for z^* is computationally expensive and often impossible in double precision. To deal with these points effectively, we use endgames (see Sect. 5.5.9) and adaptive precision (see Sect. 5.5.5).

Deflation is another approach for dealing with singular points [11, 13, 17, 18, 30, 31]. Since singularities are caused by the vanishing of derivatives, deflation is a process for re-establishing regularity by including equations that are only satisfied by solutions with derivatives that vanish to the correct order at the singular point. The main difficulty with this procedure lies in determining the rank of certain matrices formed from derivatives of the equations. This leads to a vicious circle, since computing the singular solution accurately is the initial objective, and one needs an accurate value for the solution to determine the ranks. The upshot is that for isolated solution points the cost of computing a deflation system often dwarfs the cost of computing the point accurately using the endgame methods in the next subsection. Yet, deflation can be of great service when working with higher dimensional solution sets of multiplicity greater than one. (See Sect. 5.6.3.)

5.5.9 Endgames

Let $H(x, t) = 0$ be a homotopy, and let $z(t)$ with $t \in (0, t]$ be one of its solution paths. Endgames refer to the process of computing $x^* := \lim_{t \to 0} z(t)$. We may as-

sume by using Morgan's projective transformation trick, Sect. 5.5.7, that x^* is finite, i.e., $x^* \in \mathbb{C}^N$. However, when x^* is singular, more than one path may be converging to the same spot, and all those paths become more and more difficult to track as t approaches zero.

There are several ways to circumvent this problem, but all depend on the fact that instead of just tracking t along the real line, we can consider what happens as t moves into the complex plane near the origin. One of the most effective ways of computing x^* is to track t in a small circle around the origin and to compute a Cauchy integral [28], parallelized in [2].

5.5.10 Parameter Homotopy

The schema for kinematics problems in Sect. 5.3.4 shows that they naturally arise as systems of parameterized polynomials. This fact can be used to reduce the computational cost of solving more than one problem from the same parameterized family [27]. The power of this concept when applied to finding isolated roots derives from the fact that once one has solved a single general example from a parameterized family, one has a bound on the number of isolated roots of any other member of the family. Moreover, one can find all isolated roots of any subsequent examples in a parameter homotopy that tracks solutions from the first example as the parameters are moved along a general, continuous, path in parameter space, starting at the parameters of the first example and ending at those of the new target system.

As a first example, consider the forward kinematics problem for general Stewart-Gough (6-SPS) platforms, given by (5.1, 5.31). These are 7 equations in $[e, g] \in \mathbb{P}^7$, all quadratic. One can solve a general member of this family using a total-degree homotopy having $2^7 = 128$ paths and find the problem has just 40 solutions. One can solve any other example in the family with a coefficient-parameter homotopy that has just 40 paths. Moreover, there are several different subfamilies of interest wherein some of the S joints coincide. One of these is the octahedral family where the base and moving links are both triangles, with two legs terminating at each vertex. For this family, the problem has only 16 roots, appearing in a two-way symmetry. (Reflection of the mechanism through the plane of the base does not alter the geometry.) Since a coefficient-parameter homotopy respects this symmetry, only eight paths need to be tracked. As discussed in [38, §7.7], after solving one general member of any Stewart-Gough subfamily, the remaining ones can be solved with an optimal number of paths by coefficient-parameter homotopy. Although these problems are all simple enough that a elimination approach can be devised—and this has been done for most cases—each special case requires a new derivation. In contrast, homotopy methods cover all the cases seamlessly.

A more extreme illustration of the power of the coefficient-parameter homotopy technique is provided by the nine-point path-synthesis problem for four-bars. As we mentioned earlier, the best multihomogeneous formulation found for the problem has 143,360 paths of which only 4326 have finite endpoints. So after a one-time

execution of that homotopy for a general example, all subsequent examples can be solved with a coefficient-parameter homotopy having only 4326 paths. But the story gets even better, because the 4326 solutions appear in a three-way symmetry called Robert's cognates [33]. The coefficient-parameter homotopy respects this symmetry, so only one path in each symmetry group needs to be tracked, resulting in a homotopy with only 1442 paths. This is nearly a 100-fold decrease in the number of paths compared to the original multihomogeneous homotopy (which was already a 40-fold decrease from the total degree homotopy).

5.5.11 Randomization

Situations may arise where the number of equations, n, is greater than the number of variables, N. A case in point is the $6R$ inverse kinematics problem, which is to (5.23) for (c_i, s_i), $i = 1, \ldots, 6$ subject to the unit circle conditions, $c_i^2 + s_i^2 = 1$, $i = 1, \ldots, 6$. Since the transform equation (5.23) is equivalent to 12 polynomials (the bottom row of the 4×4 matrices is trivial), we have altogether 18 equations in only 12 variables. Even so, we expect solutions, because each transform lives on $SE(3)$, so the equations are compatible. We have seen that polynomial continuation is capable of finding all isolated solutions in the square case ($n = N$), but $n > N$ requires extra measures.

Sometimes, one can pick out a subset of equations and be sure of getting all isolated roots, the remaining equations being redundant. But this takes extra knowledge about the structure of the system, because there exist systems where solving a subset does not work. An example is the system

$$xy = 0, \qquad x(x - y - 1) = 0, \qquad y(x - y - 1) = 0, \tag{5.35}$$

which has 3 isolated roots, $(0, 0)$, $(1, 0)$, and $(0, 1)$, whereas each subsystem formed by any two of the three equations has only one isolated root.

A method which does work in general is to take N random linear combinations of the equations. With probability one, this preserves all isolated roots of the original system, although it may introduce additional extraneous roots. In the case of (5.35), the randomized system has four isolated roots: the original three and an extraneous one that depends on the random coefficients chosen in forming the linear combinations. We call this process *randomization*.

An important property of randomization is that it numerically stabilizes solutions. Numerical evaluation of a polynomial inevitably introduces small perturbations: the evaluation is not exact. In a strict sense, the numerically evaluated system, consisting of $n > N$ randomly perturbed equations, will have no solutions. But a perturbed randomized system, being square, still has exact solutions, and these will be close to the solutions to the original exact system.

A similar trick works for higher dimensional sets. The case of isolated solutions for $n > N$ is the $m = 0$ special case of a solution set of dimension m with $m >$

$N-n$. With probability one, a system of $N-m$ random linear combinations of the original n equations preserves all solution sets of dimension m, but may introduce extraneous sets at that dimension as well. This leads us into the next topic: positive-dimensional solution sets.

5.6 Computing Positive-Dimensional Sets

We already mentioned in Sect. 5.4 that in numerical algebraic geometry, positive-dimensional sets (curves, surfaces, etc.) are represented by witness sets. An irreducible algebraic set is an algebraic set that cannot be expressed as a union of a finite number of proper algebraic subsets. One of the main goals in numerical algebraic geometry is to compute, for a given polynomial system F, all the irreducible components of $\mathscr{V}(F)$. This is called the *numerical irreducible decomposition*, and it consists of one witness set for each irreducible component of $\mathscr{V}(F)$. In kinematics, when $F(z,q)=0$ is the polynomial system for a mechanism family, as in the schema presented in Sect. 5.3.4, then for a particular mechanism, say $q^* \in Q$, the irreducible components of $\mathscr{V}(F(z,q^*))$ are the *assembly modes* of the mechanism. Although it may seem nonintuitive, the assembly modes might not all have the same dimension: the same mechanism can sometimes have a different number of DOFs depending on which mode it is assembled in. It is even possible for such assembly modes to meet, meaning that a mechanism could change its number of DOFs at certain special configurations. Such mechanisms have been called "kinematotropic" mechanisms [51].

A witness set, $\mathscr{A}$, for an m-dimensional irreducible algebraic set $A \subset \mathbb{C}^N$ is a data structure having three members:

- a polynomial system F such that A is an irreducible component of $\mathscr{V}(F)$,
- a generic linear space $L \subset \mathbb{C}^N$ of dimension $N-m$ (equivalently, m random linear equations), and
- the set of isolated points $W = L \cap A$.

We usually write this as the triple $\mathscr{A} = \{F, L, W\}$, and by context, L may mean either the set of linear equations or the linear space they define. In the numerical irreducible decomposition of $\mathscr{V}(F)$, F itself plays the role of the first member, the random linear equations are constructed by use of a random number generator, and the witness points W are found by polynomial continuation. When $m = N-n$, the system formed by appending m linear equations to the original n equations of F produces a square system, so W can be found using a conventional homotopy. When $m > N-n$, randomization is used, as described in Sect. 5.5.11, to produce a system of only $N-m$ equations so that once again we obtain a square system when the linear equations are appended.

A complete description of the procedures for computing a numerical irreducible decomposition are beyond the scope of this chapter. In short, one proceeds by testing every possible dimension m and factoring the witness points at each dimension

Fig. 5.4 Griffis-Duffy platform of Type I

according to the irreducible components. In numerical work, the use of intersections with a linear spaces to find higher dimensional sets was first proposed in [37], where the term *numerical algebraic geometry* was coined. See [38] for a full exposition or [48] for a briefer summary of the various techniques used to make computation of the numerical irreducible decomposition practical. The current preferred approach for descending through the dimensions is the regenerative cascade [14], which is the default method in the Bertini software package.

One interesting example of the application of the numerical irreducible decomposition is a special case of the Stewart-Gough platform called the Griffis-Duffy Type I architecturally-singular platform. These have base and moving platforms that are equilateral triangles, with legs connecting vertices of the base to midpoints of the moving platform and vice versa in a cyclic pattern [15, 36]. No matter what the leg lengths are, a general case of this type of platform has a motion curve in Study coordinates of degree 28. This is illustrated in Fig. 5.4, where the path of a small sphere attached to the moving plate is shown. This path has degree 40 in $\mathbb{R}^3$. For a special case of this in which the two triangles are congruent and the leg lengths are equal, this curve factors into five pieces: four sextics and one quartic. The numerical irreducible decomposition is able to find all of these [36].

5.6.1 Membership Tests

If one has a witness set $\mathscr{A} = \{F, L, W\}$, as above, for m-dimensional irreducible component $A \subset \mathscr{V}(F)$ and a point $z^* \in \mathscr{V}(F)$, it can sometimes be of interest to know if z^* is in A. The main membership tests used in practice are variants of the monodromy membership test (see [38, Chap. 15.4] for details). In short, we form a linear system $L'(z) = B(z - z^*) = 0$ (so z^* is a solution) with B a random matrix in $\mathbb{C}^{m \times N}$ and set up a homotopy

$$H(z,t) = \left\{F(z), tL(z) + (1-t)L'(z)\right\} = 0 \tag{5.36}$$

where L is the system of linear equations from $\mathscr{A}$. Then, $z^* \in A$ if and only if one of the homotopy paths starting from the points in W for $t = 1$ lands on z^* as $t \to 0$. The Bertini package provides this test.

5.6.2 Component Sampling

It can also be of interest to generate additional points on an irreducible component, that is, to sample the component. To do so randomly, one merely follows the same homotopy as in (5.36), except that L' is chosen completely at random. This functionality is also provided by Bertini.

5.6.3 Deflation Revisited

Just as isolated solution points may appear with multiplicity greater than one (double points, triple points, etc.), positive-dimensional irreducible solution components also may appear with higher multiplicity. Such solution components are said to be *nonreduced*. The generic multiplicity of an irreducible component is the same as the multiplicity of the witness points W considered as isolated solutions of the augmented system $\{F, L\} = 0$. The methods for deflating isolated solutions mentioned in Sect. 5.5.8 can be applied to the augmented system at the witness points, and the conditions placed on derivatives can be carried forward as L is deformed. Deflation is necessary to efficiently carry out monodromy membership or component sampling on a nonreduced irreducible component, as otherwise the homotopy paths of (5.36) would be singular at every step along t.

5.6.4 Local Dimension

Given a solution x^* of a polynomial system $f(x) = 0$, it can be of interest to determine the local dimension at x^* of the solution set $\mathscr{V}(f)$. This means the dimension of the irreducible component of $\mathscr{V}(f)$ that contains x^*, or if there is more than one such component, the largest dimension among them. This has a technical use in computing the numerical irreducible decomposition, where points must be sorted by dimension. The method in [3] handles this task.

The determination of local dimension also has direct applicability to kinematics in finding the local mobility of a mechanism in some given pose, as defined in (5.6). The rank of the Jacobian matrix tells a kinematician how many infinitesimal DOFs exist, but does not indicate how many of these extend to finite motion DOFs. To settle the issue often requires the computation of higher order derivatives. In general, without computing an irreducible decomposition for the whole solution set, one

does not have enough information to limit the number of derivatives that must be checked, but pre-specifying the order of the derivatives keeps computation finite and yields the depth-bounded local dimension [44]. For large enough depth, this is the correct local dimension, but even if one stops short of the theoretically sufficient depth, one may obtain a practically sufficient result, as the difference between an infinitesimal DOF associated to a very high multiplicity and a true finite DOF can become academic. A high multiplicity isolated root in the rigid-body model may in fact exhibit substantial motion when small elastic deformations of the links, which are always present in a physical device, enter the picture. See [44] for the method and some kinematic examples.

5.6.5 Real Sets

Throughout this article we have dealt almost exclusively with *complex* solutions, even though isolated and positive dimensional *real* solutions are the main interest for most applications.

For isolated solutions, we may simply pick the isolated real solutions out of the isolated complex solutions. For positive dimensional sets, extra work is required, and the complexity of extracting a complete description of the real set, every start and stop and every self-crossing, can be high. One illustration of the difficulty is that in singular situations, the real and complex dimensions can differ. For example, consider the equation $x^2 + y^2 = 0$, which when considered in complex space defines a pair of lines (namely, $x = \pm \mathbf{I} y$), but which only has an isolated real solution at the origin, where the lines cross in a singularity.

One-dimensional sets (curves) are relatively straightforward [21]. The key notion is to consider a family of parallel hyperplanes sweeping across $\mathbb{R}^N$. Each hyperplane that kisses the curve in a tangency marks a turning point in the real curve, and in between, the planes cut the curve transversely. Thus, every arc of the real curve is found by first solving for the tangency condition and then slicing the curve in between the turning points. Isolated real points, if they exist, are found as real tangencies that have no incoming real arcs. Recently, an algorithm has been developed along similar lines for solving the more difficult problem of finding the real points in a complex surface [9].

In Sect. 5.6, we illustrated the Griffis-Duffy Type I platform robot, a special case of the Stewart-Gough (6-SPS) platform, and mentioned that the motion for the Griffis-Duffy Type II subcase factors into five pieces: four sextics and one quartic. In [21], an even more special example of a Griffis-Duffy Type II robot is considered, one whose leg lengths are all equal to the altitude of the base and moving triangles (which are congruent equilateral triangles). This robot is unusual in that it can fold up into the plane with both triangles coinciding. Its motion is a curve that factors even more finely than general Type II cases into three double lines, three quadrics, and four quartics. (The sum of the degrees $3 \cdot 2 + 3 \cdot 2 + 4 \cdot 4 = 28$ is the same as the degree of the irreducible curve in the Type I case.) Numerical irreducible

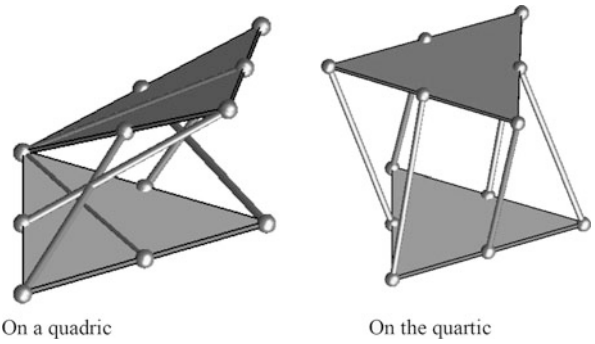

Fig. 5.5 Selected poses of the foldable Stewart-Gough platform. From [21] by permission, © AMS

decomposition finds this factorization, and the technique sketched above extracts the real curves inside these complex factors. Poses on two of these motion curves are shown in Fig. 5.5.

5.6.6 Exceptional Sets

Many problems may be rephrased as a problem of finding the set of parameters where some exceptional behavior occurs. An interesting case in kinematics is finding overconstrained mechanisms, i.e., mechanisms of a given family that have more degrees of freedom than most of the other mechanisms in the family.

A smattering of planar and spatial overconstrained mechanisms are known, including, for example, the Bennett [8] spatial four-bar and the Griffis-Duffy Type I and II 6-SPS mechanisms mentioned above. However, to date, investigations of overconstrained mechanisms have employed specialized arguments for the specific mechanism family under consideration. The fiber product approach to finding exceptional sets described in [39] has the potential to provide a general approach applicable to many mechanism families. Implementation of that approach in a form that can handle mechanisms of an interesting level of complexity is still a research topic.

5.7 Software

There are several software packages that compute isolated solutions of polynomial systems, Bertini [4], HOM4PS-2.0 [16], Hompack90 [49] and its extensions [40, 50], and PHCpack [42]. Hompack90 has general parallel tracking facilities. HOM4PS-2.0 has the best implementation of polyhedral methods, but is not a parallel code. Only Bertini and PHCpack implement algorithms of numerical algebraic geometry for positive-dimensional solution sets.

PHCpack and Bertini both allow the user to define their own homotopy and prescribed start points, but HOM4PS-2.0 currently does not.

HOM4PS-2.0 uses only double precision arithmetic to perform computations. To varying degrees, both PHCpack and Bertini have the capability of using higher precision arithmetic. PHCpack does not currently have the capability of adapting the precision based on the local conditioning of the homotopy path. This means that more human interaction is needed to verify that the precision is set appropriately to accurately and reliably perform the requested computations.

The more advanced algorithms of numerical algebraic geometry (including the powerful equation-by-equation methods for finding isolated solutions) place strong requirements on the underlying numerical software [5]. For example, without secure path-tracking and adaptive precision, computing the numerical irreducible decomposition for systems that involve more than a few variables is not possible.

Only Bertini gives the numerical irreducible decomposition directly. Exceptional features of Bertini include:

- secure path-tracking;
- adaptive multiprecision [6, 7];
- utilities for working with polynomial systems given as straight-line programs;
- the numerical irreducible decomposition [35, 38];
- equation-by-equation methods such as regeneration [13, 14];
- local dimension testing [3] (see Sect. 5.6.4); and
- various endgames (see Sect. 5.5.9) including the Cauchy endgame [28], and a parallel endgame based on it [2].

5.8 Conclusions

This chapter shows how problems in kinematics can be formulated as algebraic systems, thereby introducing the concept of a mechanism space and its associated input and output maps. This provides a framework for understanding the definitions of a variety of kinematics problems, including analysis problems, such as the forward and inverse kinematics problems for robots, and synthesis problems that seek to design mechanisms that produce a desired motion.

Since algebraic kinematics is a subset of algebraic geometry, the computational tools for systems of polynomials can be applied. In particular, numerical algebraic geometry, based on polynomial continuation, has matured into a set of tools for finding and manipulating solution sets of any dimension. Since the bulk of computation is spent tracking a large number of independent homotopy paths, the methods naturally scale to large parallel computing environments, well suited for the needs of 21st-century kinematicians.

References

1. Alt, H.: Über die erzeugung gegebener ebener kurven mit hilfe des gelenkvierecks. Z. Angew. Math. Mech. **3**(1), 13–19 (1923)
2. Bates, D.J., Hauenstein, J.D., Sommese, A.J.: A parallel endgame. Contemp. Math. **556**, 25–35 (2011)

3. Bates, D.J., Hauenstein, J.D., Peterson, P., Sommese, A.J.: A numerical local dimension test for points on the solution set of a system of polynomial equations. SIAM J. Numer. Anal. **47**, 3608–3623 (2009)
4. Bates, D.J., Hauenstein, J.D., Sommese, A.J., Wampler, C.W.: Bertini: software for numerical algebraic geometry. www.nd.edu/~sommese/bertini. Cited 26 June 2012
5. Bates, D.J., Hauenstein, J.D., Sommese, A.J., Wampler, C.W.: Software for numerical algebraic geometry: a paradigm and progress towards its implementation. In: Stillman, M.E., Takayama, N., Verschelde, J. (eds.) Software for Algebraic Geometry. IMA Volumes in Mathematics and Its Applications, vol. 148, pp. 1–14. Springer, New York (2008)
6. Bates, D.J., Hauenstein, J.D., Sommese, A.J., Wampler, C.W.: Adaptive multiprecision path tracking. SIAM J. Numer. Anal. **46**, 722–746 (2008)
7. Bates, D.J., Hauenstein, J.D., Sommese, A.J., Wampler, C.W.: Stepsize control for adaptive multiprecision path tracking. Contemp. Math. **496**, 21–31 (2009)
8. Bennett, G.T.: A new mechanism. Engineering **76**, 777–778 (1903)
9. Besana, G.M., Di Rocco, S., Hauenstein, J.D., Sommese, A.J., Wampler, C.W.: Cell decomposition of almost smooth real algebraic surfaces. Preprint (2012)
10. Bottema, O., Roth, B.: Theoretical Kinematics. North-Holland, Amsterdam (1979). Reprinted: Dover, New York (1990)
11. Dayton, B., Zeng, Z.: Computing the multiplicity structure in solving polynomial systems. In: Proc. of ISSAC 2005, pp. 116–123. ACM, New York (2005)
12. Freudenstein, F.: Kinematics: past, present and future. Mech. Mach. Theory **8**, 151–160 (1973)
13. Hauenstein, J.D., Sommese, A.J., Wampler, C.W.: Regeneration homotopies for solving systems of polynomials. Math. Comput. **80**, 345–377 (2011)
14. Hauenstein, J.D., Sommese, A.J., Wampler, C.W.: Regenerative cascade homotopies for solving polynomial systems. Appl. Math. Comput. **218**(4), 1240–1246 (2011)
15. Husty, M.L., Karger, A.: Self-motions of Griffis-Duffy type parallel manipulators. In: Proc. 2000 IEEE ICRA, CDROM, San Francisco, CA, April 24–28 (2000)
16. Lee, T.-L., Li, T.-Y., Tsai, C.H.: HOM4PS-2.0: a software package for solving polynomial systems by the polyhedral homotopy continuation method. Computing **83**, 109–133 (2008)
17. Leykin, A., Verschelde, J., Zhao, A.: Newton's method with deflation for isolated singularities of polynomial systems. Theor. Comput. Sci. **359**, 111–122 (2006)
18. Leykin, A., Verschelde, J., Zhao, A.: Higher-order deflation for polynomial systems with isolated singular solutions. In: Dickenstein, A., Schreyer, F.-O., Sommese, A.J. (eds.) Algorithms in Algebraic Geometry, pp. 79–97. Springer, New York (2008)
19. Li, T.-Y.: Numerical solution of multivariate polynomial systems by homotopy continuation methods. In: Acta Numerica, vol. 6, pp. 399–436. Cambridge Univ. Press, Cambridge (1997)
20. Li, T.-Y.: Numerical solution of polynomial systems by homotopy continuation methods. In: Handbook of Numerical Analysis XI, pp. 209–304. North-Holland, Amsterdam (2003)
21. Lu, Y., Bates, D., Sommese, A.J., Wampler, C.W.: Finding all real points of a complex curve. In: Proc. Midwest Algebra, Geometry and Its Interactions Conference, Contemporary Math., vol. 448, pp. 183–205. AMS, Providence (2007)
22. McCarthy, J.M.: Geometric Design of Linkages. Springer, New York (2000)
23. Morgan, A.P.: A transformation to avoid solutions at infinity for polynomial systems. Appl. Math. Comput. **18**(1), 77–86 (1986)
24. Morgan, A.P.: Solving Polynomial Systems Using Continuation for Engineering and Scientific Problems. Prentice Hall, Englewood Cliffs (1987)
25. Morgan, A.P., Sommese, A.J.: A homotopy for solving general polynomial systems that respects m-homogeneous structures. Appl. Math. Comput. **24**, 101–113 (1987)
26. Morgan, A.P., Sommese, A.J.: Computing all solutions to polynomial systems using homotopy continuation. Appl. Math. Comput. **24**, 115–138 (1987). Errata: Appl. Math. Comput. **51**, 209 (1992)
27. Morgan, A.P., Sommese, A.J.: Coefficient-parameter polynomial continuation. Appl. Math. Comput. **29**(2), 123–160 (1989). Errata: Appl. Math. Comput. **51**, 207 (1992)

28. Morgan, A.P., Sommese, A.J., Wampler, C.W.: Computing singular solutions to nonlinear analytic systems. Numer. Math. **58**(7), 669–684 (1991)
29. Morgan, A.P., Sommese, A.J., Wampler, C.W.: A product-decomposition bound for Bezout numbers. SIAM J. Numer. Anal. **32**(4), 1308–1325 (1995)
30. Ojika, T.: Modified deflation algorithm for the solution of singular problems. I. A system of nonlinear algebraic equations. J. Math. Anal. Appl. **123**, 199–221 (1987)
31. Ojika, T., Watanabe, S., Mitsui, T.: Deflation algorithm for the multiple roots of a system of nonlinear equations. J. Math. Anal. Appl. **96**, 463–479 (1983)
32. Raghavan, M.: The Stewart platform of general geometry has 40 configurations. ASME J. Mech. Des. **115**, 277–282 (1993)
33. Roberts, S.: On three-bar motion in plane space. Proc. Lond. Math. Soc. **VII**, 14–23 (1875)
34. Roth, B., Freudenstein, F.: Synthesis of path-generating mechanisms by numerical means. ASME J. Eng. Ind. **85**(Series B), 298–306 (1963)
35. Sommese, A.J., Verschelde, J., Wampler, C.W.: Numerical decomposition of the solution sets of polynomial systems into irreducible components. SIAM J. Numer. Anal. **38**(6), 2022–2046 (2001)
36. Sommese, A.J., Verschelde, J., Wampler, C.W.: Advances in polynomial continuation for solving problems in kinematics. ASME J. Mech. Des. **126**(2), 262–268 (2004)
37. Sommese, A.J., Wampler, C.W.: Numerical algebraic geometry. In: Renegar, J., Shub, M., Smale, S. (eds.) The Mathematics of Numerical Analysis (Park City, UT, 1995). Lectures in Appl. Math., vol. 32, pp. 749–763. AMS, Providence (1996)
38. Sommese, A.J., Wampler, C.W.: The Numerical Solution of Systems of Polynomials Arising in Engineering and Science. World Scientific, Singapore (2005)
39. Sommese, A.J., Wampler, C.W.: Exceptional sets and fiber products. Found. Comput. Math. **28**, 171–196 (2008)
40. Su, H.-J., McCarthy, J.M., Sosonkina, M., Watson, L.T.: Algorithm 857: POLSYS_GLP—a parallel general linear product homotopy code for solving polynomial systems of equations. ACM TOMS **32**(4), 561–579 (2006)
41. Tsai, L.-W., Morgan, A.P.: Solving the kinematics of the most general six- and five-degree-of-freedom manipulators by continuation methods. ASME J. Mech. Transm. Autom. Des. **107**, 48–57 (1985)
42. Verschelde, J.: Algorithm 795: PHCpack: A general-purpose solver for polynomial systems by homotopy continuation. ACM TOMS **25**(2), 251–276 (1999)
43. Verschelde, J., Cools, R.: Symbolic homotopy construction. Appl. Algebra Eng. Commun. Comput. **4**(3), 169–183 (1993)
44. Wampler, C.W., Hauenstein, J.D., Sommese, A.J.: Mechanism mobility and a local dimension test. Mech. Mach. Theory **46**(9), 1193–1206 (2011)
45. Wampler, C.W., Morgan, A.P., Sommese, A.J.: Numerical continuation methods for solving polynomial systems arising in kinematics. **112**(1), 59–68 (1990)
46. Wampler, C.W., Morgan, A.P., Sommese, A.J.: Complete solution of the nine-point path synthesis problem for four-bar linkages. ASME J. Mech. Des. **114**, 153–159 (1992)
47. Wampler, C.W., Morgan, A.P., Sommese, A.J.: Complete solution of the nine-point path synthesis problem for four-bar linkages—Closure. ASME J. Mech. Des. **119**, 150–152 (1997)
48. Wampler, C.W., Sommese, A.J.: Numerical algebraic geometry and algebraic kinematics. Acta Numer. **20**, 469–567 (2011). doi:10.1017/s0962492911000067
49. Watson, L.T., Sosonkina, M., Melville, R.C., Morgan, A.P., Walker, H.F.: Algorithm 777: HOMPACK90: a suite of Fortran 90 codes for globally convergent homotopy algorithms. ACM TOMS **23**(4), 514–549 (1997)
50. Wise, S.M., Sommese, A.J., Watson, L.T.: Algorithm 801: POLSYS_PLP: A partitioned linear product homotopy code for solving polynomial systems of equations. ACM TOMS **26**(1), 176–200 (2000)
51. Wohlhart, K.: Kinematotropic linkages. In: Lenarcic, J., Parenti-Castelli, V. (eds.) Recent Advances in Robot Kinematics, pp. 359–368. Kluwer Academic, Dordrecht (1996)

Chapter 6
The Kinematics of 3-D Cable-Towing Systems

Qimi Jiang and Vijay Kumar

6.1 Introduction

Helicopters are used to transport payloads suspended via cables to hard-to-access environments in emergency response, construction, mining and military operations [1, 6, 20]. The dynamics and stability of aerial towed-cable-body systems are discussed in [20] and the trajectory control for a payload suspended from a cable from a helicopter is analyzed in [14]. In this chapter, we are interested in the mechanics of payloads suspended by multiple cables in three dimensions. The case with six cables with stationary anchors is addressed in the literature on cable-actuated platforms [5, 19]. Indeed the kinematic analysis has much in common with the analysis of cable-actuated parallel manipulators in three dimensions [2, 4, 5]. However, the key difference is that the payload pose in our case is determined by the robots' positions and the payload pose in parallel mechanisms is realized by changing the lengths of multiple cables.

When the number of cables is reduced from six to five, the conditions for equilibrium become more interesting. If the line vectors are linearly independent and the cables are taut, the line vectors and the gravity wrench axis must belong to the same linear complex [7]. The payload is free to instantaneously twist about the reciprocal screw axis. With four cables, under similar assumptions on linear independence and positive tension, the line vectors and the gravity wrench must belong to the same linear congruence. The unconstrained freedoms correspond (instantaneously) to a set of twists whose axes lie on a cylindroid. In the three-cable case, all three cables and the gravity wrench axis must lie on the same regulus—the generators of a hyperboloid which is a ruled surface [16]. Of course, in all of these cases there are special

Q. Jiang (✉)
Automation Specialist, Mining Technologies International Inc., Greater Sudbury, Ontario, Canada
e-mail: qimi.jiang@mti.ca

V. Kumar
Department of Mechanical Engineering, University of Pennsylvania, Philadelphia, PA, USA
e-mail: kumar@seas.upenn.edu

J.M. McCarthy (ed.), *21st Century Kinematics*,
DOI 10.1007/978-1-4471-4510-3_6,

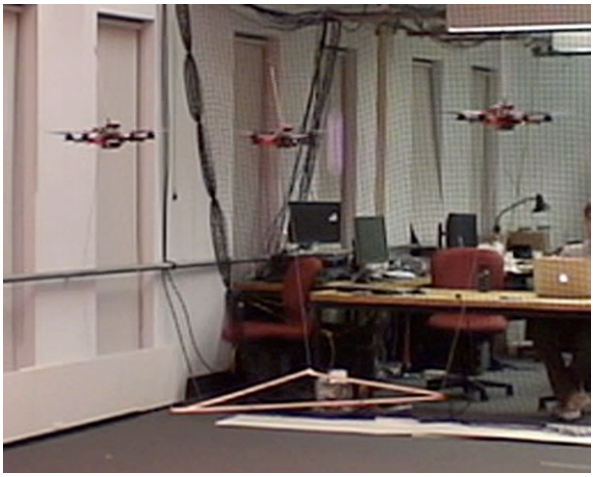

Fig. 6.1 3-D towing of a triangular payload with three aerial robots [13]

configurations in which the screw systems assume special forms [7]. The arguments for the single cable and the two cable cases are similar, but in these cases, the cables and the center of mass must lie on the same vertical plane for equilibrium.

In this chapter, we address the manipulation and transportation of a payload suspended from aerial robots via cables. In previous work [3, 13][1] (also see Fig. 6.1) we formulated the dynamics, control and planning problems for such systems. In this chapter, we present an overview of the kinematics of 3-D aerial manipulation. We are interested in (a) the inverse kinematics problem, the problem of determining the positions of the aerial robots to which the cables are attached given the desired position and orientation of the payload suspended by cables; and (b) the direct kinematics problem, the problem of determining the position and orientation of the suspended payload for a given position of the aerial robots.

In Sect. 6.2, we formulate the conditions for static equilibrium and the geometric constraints that are at the heart of this analysis. In Sect. 6.3, we address the direct kinematics problem where we will limit ourselves to the case with vertical planes of symmetry. We show how to solve the inverse kinematics using dialytic elimination in Sect. 6.4. In Sect. 6.5 we discuss constraints on solutions imposed by limitations on cable tensions. Finally, we conclude the chapter with a few remarks about open problems in Sect. 6.7.

6.2 The Conditions of Equilibrium and Constraint

In Fig. 6.2 we show the general case of a payload suspended by cables from n aerial robots. Suppose that the position of robot Q_i in the inertial frame is $\mathbf{q}_i = [x_{qi}, y_{qi}, z_{qi}]^T$. The positions of the attachment point P_i in the inertial and body-

[1] Taken from [3], reprinted with kind permission © Sage 2012.

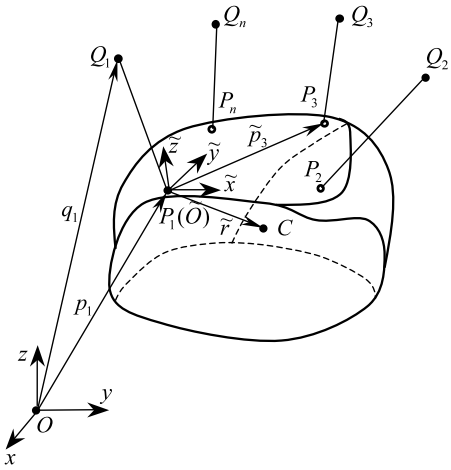

Fig. 6.2 A payload suspended in three dimensions by multiple aerial robots

fixed frames are $\mathbf{p}_i = [x_{pi}, y_{pi}, z_{pi}]^T$ and $\tilde{\mathbf{p}}_i = [\tilde{x}_{pi}, \tilde{y}_{pi}, \tilde{z}_{pi}]^T$ respectively. The positions of the center of mass of the payload in the inertial and body-fixed frames are $\mathbf{r} = [x, y, z]^T$ and $\tilde{\mathbf{r}} = [\tilde{x}, \tilde{y}, \tilde{z}]^T$ respectively. If the length of cable i is given by l_i, the unit wrench of cable i with respect to the origin O of the inertial frame can be given as

$$\mathbf{w}_i = \frac{1}{l_i} \begin{bmatrix} \mathbf{q}_i - \mathbf{p}_i \\ \mathbf{p}_i \times \mathbf{q}_i \end{bmatrix}. \tag{6.1}$$

The wrench caused by the weight of the payload with respect to the origin O is

$$\mathbf{G} = -mg \begin{bmatrix} \mathbf{e}_3 \\ \mathbf{r} \times \mathbf{e}_3 \end{bmatrix}, \tag{6.2}$$

where mg is the weight of the payload and $\mathbf{e}_3$ is the unit vector $[0, 0, 1]^T$. If the tension of cable i is given by T_i, the static equilibrium condition of the payload can be given as

$$[\mathbf{w}_1 \ \mathbf{w}_2 \ \ldots \ \mathbf{w}_n] \begin{bmatrix} T_1 \\ T_2 \\ \vdots T_n \end{bmatrix} + \mathbf{G} = 0. \tag{6.3}$$

Also, the cable lengths should satisfy the following geometric constraints:

$$\|\mathbf{q}_i - \mathbf{p}_i\| = l_i \quad (i = 1, 2, \ldots, n). \tag{6.4}$$

6.3 Direct Kinematics

This section addresses the direct kinematics problem which can be described as follows [10, 11]: *Given the positions of the aerial robots, find the possible positions and orientations of the payload, that satisfy* (6.3) *and* (6.4).

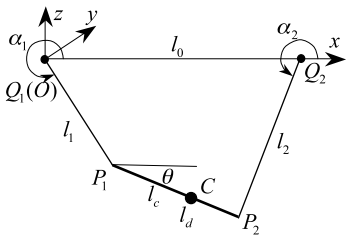

Fig. 6.3 Four-bar linkage (payload suspended from two robots)

The general case with three robots was formulated in [11]. The resulting set of equations is quite unwieldy and does not lend itself to a closed form solution. For simplicity, we address the direct kinematics problem for the symmetric case here. The payload is a regular polygon suspended from n identical cables and we consider the case where the n robots form a regular polygon on a horizontal plane. The motion of such a 3-D cable system has several vertical planes of symmetry. In each plane the motion can be described in terms of the motion of an equivalent planar 4-bar linkage. Hence, an analytic algorithm based on resultant elimination can be used to determine all possible equilibrium configurations of the planar 4-bar linkage, which then offers a basis for solving the direct kinematics problem of the 3-D cable system with symmetric geometry.

We start with the planar abstraction which takes the form of a four bar linkage in Fig. 6.3, in which we assume Q_1 and Q_2, the two robots, are on the same horizontal plane. The lengths of the four bars are $|Q_1Q_2| = l_0$, $|P_1Q_1| = l_1$, $|P_2Q_2| = l_2$, and $|P_1P_2| = l_d$ respectively. The center of mass of the payload, the coupler P_1P_2, is C and $|P_1C| = l_c$. Also, the masses of the cables (the input and output bars) can be neglected. If Q_1 is chosen as the origin O and Q_1Q_2 as the x axis of the frame, the coordinates of P_1 and P_2 can be respectively given as

$$\begin{aligned} \mathbf{p}_1 &= \mathbf{q}_1 + l_1[\cos\alpha_1, \sin\alpha_1]^T = \mathbf{q}_1 + l_1[x_1, z_1]^T, \\ \mathbf{p}_2 &= \mathbf{q}_2 + l_2[\cos\alpha_2, \sin\alpha_2]^T = \mathbf{q}_2 + l_2[x_2, z_2]^T, \end{aligned} \tag{6.5}$$

where

$$\begin{aligned} x_1^2 + z_1^2 &= 1, \\ x_2^2 + z_2^2 &= 1. \end{aligned} \tag{6.6}$$

Referring to (6.3), the equilibrium condition for the planar 4-bar linkage can be given as

$$\begin{aligned} x_1T_1 + x_2T_2 &= 0, \\ z_1T_1 + z_2T_2 + mg &= 0, \\ l_0l_dz_2T_2 + mg\big[l_1(l_d - l_c)x_1 + l_2l_cx_2 + l_0l_c\big] &= 0. \end{aligned} \tag{6.7}$$

From the third equation of (6.7), one gets

$$T_2 = -mg\big[l_1(l_d - l_c)x_1 + l_2l_cx_2 + l_0l_c\big]/(l_0l_dz_2). \tag{6.8}$$

Substituting T_2 into the first equation of (6.7), one gets

$$T_1 = -mg\big[l_1(l_d - l_c)x_1 + l_2 l_c x_2 + l_0 l_c\big]x_2/(l_0 l_d x_1 z_2). \tag{6.9}$$

Then, substituting T_1 and T_2 into the second equation of (6.7), one gets

$$\begin{aligned}&\big[l_1(l_c - l_d)x_1 x_2 - l_2 l_c x_2^2 - l_0 l_c x_2\big]z_1\\ &\quad - [l_1(l_c - l_d)x_1^2 - l_2 l_c x_1 x_2 + l_0(l_d - l_c)x_1)z_2 = 0.\end{aligned} \tag{6.10}$$

Also, the coordinates of P_1 and P_2 should satisfy the geometric constraint $|P_1P_2| = l_d$, hence

$$l_1 l_2 z_1 z_2 + l_1 l_2 x_1 x_2 + l_0(l_1 x_1 - l_2 x_2) + g_0 = 0, \tag{6.11}$$

where

$$g_0 = \big[l_d^2 - l_0^2 - l_1^2\big(x_1^2 + z_1^2\big) - l_2^2\big(x_2^2 + z_2^2\big)\big]/2. \tag{6.12}$$

From the trigonometric identities given by (6.6), it is clear that g is a constant. Now, we have four equations consisting of (6.6), (6.10) and (6.11) in four unknowns (x_1, z_1, x_2, z_2). In order to solve this nonlinear system, elimination algorithms are used. From (6.11), one gets

$$z_2 = -\big[l_1 l_2 x_1 x_2 + l_0(l_1 x_1 - l_2 x_2) + g\big]/(l_1 l_2 z_1). \tag{6.13}$$

Substituting (6.13) into (6.10) and the second equation of (6.6), one gets

$$\begin{aligned}&\big[l_1^2 l_2(l_c - l_d)x_1 x_2 - l_1 l_2^2 l_c x_2^2 - l_1 l_2 l_c l_0 x_2\big]z_1^2 + \big[l_1^2 l_2(l_c - l_d)x_2 + l_1^2(l_c - l_d)l_0\big]x_1^3\\ &\quad + \big[l_0 l_1 l_2(2l_d - 3l_c)x_2 - l_1 l_2^2 l_c x_2^2\big]x_1^2 + l_1\big[(l_d - l_c)l_0^2 + (l_c - l_d)g\big]x_1^2\\ &\quad + l_2^2 l_c l_0 x_1 x_2^2 + l_2\big[(l_c - l_d)l_0^2 - l_c g\big]x_1 x_2 + (l_d - l_c)l_0 g x_1 = 0,\\ &\big(l_1^2 l_2^2 x_2^2 + 2l_1^2 l_2 l_0 x_2 + l_1^2 l_0^2\big)x_1^2 - 2l_1 l_2^2 l_0 x_1 x_2^2 + 2l_1 l_2\big(g - l_0^2\big)x_1 x_2 + 2l_1 l_0 g x_1\\ &\quad + \big(l_1^2 l_2^2 x_2^2 - l_1^2 l_2^2\big)z_1^2 + l_2^2 l_0^2 x_2^2 - 2l_2 l_0 b x_2 + g^2 = 0.\end{aligned} \tag{6.14}$$

It can be seen that there is only one quadratic term in z_1 in every equation of (6.14). Referring to the first equation of (6.6), z_1^2 can be substituted by $(1 - x_1^2)$. Hence, (6.14) becomes

$$\begin{aligned}&l_2\big\{2l_0 l_1(l_d - l_c)x_1^2 + \big[(l_c - l_d)\big(l_0^2 + l_1^2\big) - l_c g\big]x_1 - l_1 l_c l_0\big\}x_2\\ &\quad + \big(l_2^2 l_c l_0 x_1 - l_1 l_2^2 l_c\big)x_2^2 + (l_d - l_c)\big[-l_0 l_1^2 x_1^3 + l_1\big(l_0^2 - g\big)x_1^2 + l_0 g x_1\big] = 0,\\ &l_2^2\big(l_0^2 + l_1^2 - 2l_1 l_0 x_1\big)x_2^2 + 2l_2\big[l_1^2 l_0 x_1^2 + l_1\big(g - l_0^2\big)x_1 - l_0 g\big]x_2\\ &\quad + \big(l_1^2 l_0^2 + l_1^2 l_2^2\big)x_1^2 + 2l_1 l_0 g x_1 - l_1^2 l_2^2 + g^2 = 0.\end{aligned} \tag{6.15}$$

Table 6.1 Real solutions of the equilibrium problem of the planar 4-bar linkage shown in Fig. 6.4

No.	x_1	x_2	z_1	z_2	No.	x_1	x_2	z_1	z_2
1	0.826	0.127	0.564	0.992	9	0.332	−0.777	0.943	0.630
2	0.826	0.127	−0.564	−0.992	**10**	**0.332**	**−0.777**	**−0.943**	**−0.630**
3	0.777	−0.332	0.630	0.943	11	0.180	−0.180	0.984	0.984
4	**0.777**	**−0.332**	**−0.630**	**−0.943**	**12**	**0.180**	**−0.180**	**−0.984**	**−0.984**
5	0.620	−0.620	0.785	0.785	13	−1	NA	NA	NA
6	**0.620**	**−0.620**	**−0.785**	**−0.785**	14	−1	NA	NA	NA
7	−0.127	−0.826	0.992	0.564	15	1	2.116	0	NA
8	−0.127	−0.826	−0.992	−0.564	16	1	2.116	0	NA

In order to eliminate x_2 from (6.15), the resultant algorithm is used [17]. This leads to the following 8 degree polynomial equation in x_1:

$$G_8 x_1^8 + G_7 x_1^7 + G_6 x_1^6 + G_5 x_1^5 + G_4 x_1^4 + G_3 x_1^3 + G_2 x_1^2 + G_1 x_1 + G_0 = 0, \quad (6.16)$$

where $G_0, G_1, \ldots, G_8$ are constant coefficients.

In principle, up to 8 solutions in x_1 can be found from (6.16). For every solution of x_1 substituted into (6.15), one corresponding solution in x_2 can be obtained. Then, up to two solutions of z_1 can be obtained by substituting a solution of x_1 into the first equation of (6.6). Finally, a corresponding solution of z_2 can be obtained by (6.13). It seems that the total number of solutions are 16. However, the computational results show that the maximal number of real solutions is no more than 12, a result that is consistent with the reasoning in [12]. This point can be demonstrated by an example for which the geometric parameters are $l_0 = 4$ m, $l_1 = 5$ m, $l_2 = 5$ m, $l_d = 2.2$ m, $l_c = 1.1$ m, $mg = 10$ N and the results are listed in Table 6.1.

When $x_1 = -1$, two real solutions $(1.800, \ -1.124)$ can be obtained for x_2 from the first equation of (6.15). However, no real solutions can be found for x_2 from the second equation of (6.15). When $x_1 = 1$, the corresponding real solutions can be found for x_2 and z_1, but no real solutions can be found for z_2. In other words, when $x_1 = \pm 1$, there is no real solutions for the problem. Hence, the total number of real solutions of the considered problem is only 12. The corresponding equilibrium configurations are shown in Fig. 6.4 in which the thick solid lines represent the coupler, the thin solid lines represent the input or output links (cables) with positive tensions, and the dashed lines represent the input or output links (cables) with negative tensions. Since cable tensions cannot be negative, only the four solutions (Nos. 4, 6, 10 and 12) listed in Table 6.1 make physical sense.

We use the methodology for determining equilibrium configurations of the planar 4-bar linkage to solve the direct kinematics problem of a homogeneous, regular, polygonal payload suspended by n identical cables with n robots forming a regular, horizontal polygon. Take the case with six robots as an example. Thus, the six aerial robots (Q_1, Q_2, Q_3, Q_4, Q_5, Q_6) lie in the same horizontal plane and form a regular hexagon with side length l_q. The attachment points (P_1, P_2, P_3, P_4, P_5, P_6) of the

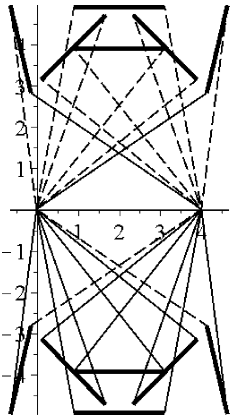

Fig. 6.4 Twelve equilibrium configurations of the planar 4-bar linkage

Table 6.2 Geometric parameters of equivalent planar 4-bar linkages for case with 6 robots

No.	l_0	l_1	l_2	l_d	l_c
1	$2l_q$	l	l	$2l_p$	l_p
2	$\sqrt{3}l_q$	$\frac{\sqrt{4l^2-(l_q-l_p)^2}}{2}$	$\frac{\sqrt{4l^2-(l_q-l_p)^2}}{2}$	$\sqrt{3}l_p$	$\frac{\sqrt{3}l_p}{2}$

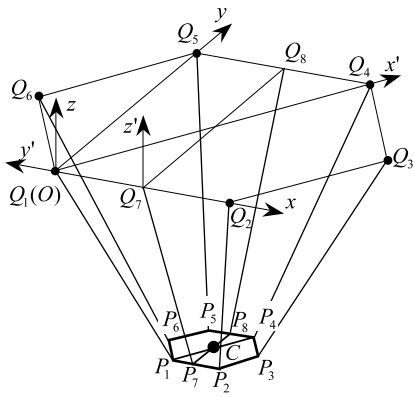

Fig. 6.5 A homogeneous, regular polygonal payload ($P_1P_2P_3P_4P_5P_6$) suspended from six robots Q_1, Q_2, Q_3, Q_4, Q_5, and Q_6 arranged on the verticals of a horizontal regular polygon

payload also form a regular hexagon with side length l_p, and the center of mass of the payload coincides with the centroid of hexagon $P_1P_2P_3P_4P_5P_6$. Also, the cables have the same length l.

An equilibrium configuration for this geometry is shown in Fig. 6.5. There are six vertical planes of symmetry that fall into two classes. In the first class, every vertical plane of symmetry, e.g., $Q_1P_1P_4Q_4$, passes through the diagonal lines of regular hexagons $Q_1Q_2Q_3Q_4Q_5Q_6$ and $P_1P_2P_3P_4P_5P_6$. In the second class, every vertical plane of symmetry, e.g., $Q_7P_7P_8Q_8$, passes through the middle points of the opposite sides of regular hexagons $Q_1Q_2Q_3Q_4Q_5Q_6$ and $P_1P_2P_3P_4P_5P_6$. If the payload swings in one of these six vertical planes of symmetry, it is equivalent

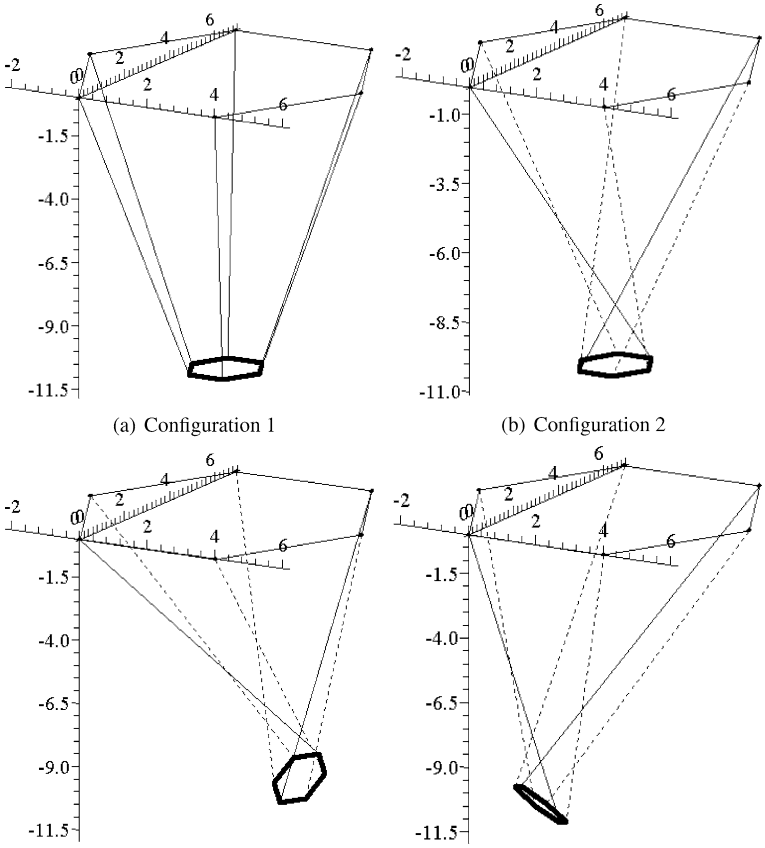

(a) Configuration 1 (b) Configuration 2

(c) Configuration 3 (d) Configuration 4

Fig. 6.6 Four equilibrium configurations of a payload suspended from six robots determined by the equivalent planar four bar linkage in the plane $Q_1P_1P_4Q_4$

to the motion of a 4-bar linkage in the same plane. The geometric parameters of two classes equivalent planar 4-bar linkages are listed in Table 6.2.

If l, l_q and l_p are respectively given by 12 m, 4 m and 1 m, four equilibrium configurations can be determined in every vertical plane of symmetry of the first class using the corresponding equivalent planar 4-bar linkage. Figure 6.6 shows the four equilibrium configurations in the vertical plane $Q_1P_1P_4Q_4$. In every configuration except configuration 1 which coincides with the initial configuration, there are four cables (P_2Q_2, P_3Q_3, P_5Q_5 and P_6Q_6) are slack and represented by the dashed lines.

Also, four equilibrium configurations can be determined in every vertical plane of symmetry of the second class using the corresponding equivalent planar 4-bar linkage. Figure 6.7 shows the four equilibrium configurations in the vertical plane $Q_7P_7P_8Q_8$. In every configuration except configuration 1 which coincides with the

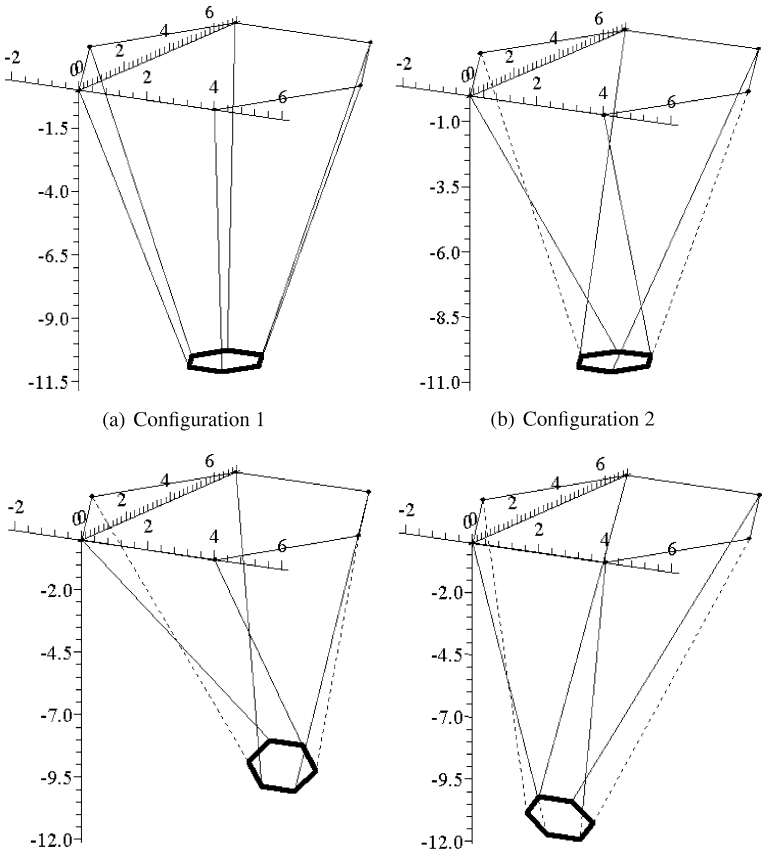

(a) Configuration 1 (b) Configuration 2

(c) Configuration 3 (d) Configuration 4

Fig. 6.7 Four equilibrium configurations of a payload suspended from six robots determined by the equivalent planar four bar linkage in the plane $Q_7P_7P_8Q_8$

initial configuration, there are two cables (P_3Q_3 and P_6Q_6) are slack and represented by the dashed lines.

However, configurations found by the four-bar linkage abstraction are only a subset of equilibrium configurations. This is easily seen in Fig. 6.8 in which every pair opposite cables intersects. Hence, the total number of equilibrium configurations for the case with six robots is at least 20.

In [11], we provide a more exhaustive analysis of such systems by considering case studies with $n = 3,\ 4,\ 5$, and 6.

6.4 Inverse Kinematics

In this section, we present an efficient analytic algorithm based on Dialytic elimination to solve this inverse kinematics problem which can be described as follows

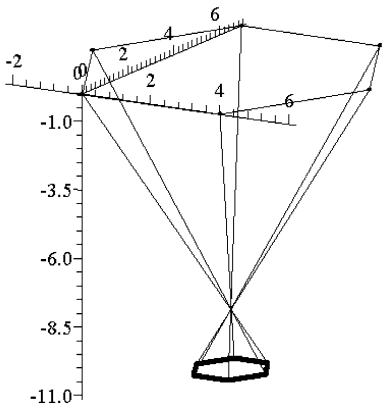

Fig. 6.8 The equilibrium configuration with six robots in which every pair of opposite cables intersect each other

[8, 9]:[2] *Given a desired position and orientation of the payload* $(\mathbf{r}, \mathbf{R})$*, find the positions of the aerial robots* $(\mathbf{q}_i,\ i = 1, 2, \ldots, n)$ *that satisfy* (6.3) *and* (6.4).

To maintain a desired position and orientation, the payload needs at least three attachment points. Thus, for the cases with 1 and 2 robots, the inverse kinematics problem, in general, has no solution. However, for the cases with 3 or more robots, there are infinitely many solutions, because the number of unknowns is greater than the sum of the number of equations of static equilibrium and the number of constraints.

For the case with three robots, if the tensions T_i $(i = 1, 2, 3)$ of three cables are given, there are 9 unknowns $(x_{qi}, y_{qi}, z_{qi}, i = 1, 2, 3)$ in 9 equations given by (6.3) and (6.4). Hence, it should be possible to find a finite number of solutions for the inverse kinematics problem.

From (6.3), one gets

$$\begin{aligned}
&s_1x_1 + s_2x_2 + s_3x_3 = 0,\\
&s_1y_1 + s_2y_2 + s_3y_3 = 0,\\
&s_1z_1 + s_2z_2 + s_3z_3 = mg,\\
&-s_6y_1 + s_5z_1 - s_9y_2 + s_8z_2 - s_{12}y_3 + s_{11}z_3 = t_1,\\
&s_6x_1 - s_4z_1 + s_9x_2 - s_7z_2 + s_{12}x_3 - s_{10}z_3 = t_2,\\
&-s_5x_1 + s_4y_1 - s_8x_2 + s_7y_2 - s_{11}x_3 + s_{10}y_3 = 0,
\end{aligned} \tag{6.17}$$

where $s_1, s_2, \ldots, s_{12}$, t_1, t_2 are constants or functions of T_i $(i = 1, 2, 3)$, and $x_i = x_{qi} - x_{pi}$, $y_i = y_{qi} - y_{pi}$ and $z_i = z_{qi} - z_{pi}$ $(i = 1, 2, 3)$. From (6.4), one gets

$$x_i^2 + y_i^2 + z_i^2 = l_i^2 \quad (i = 1, 2, 3). \tag{6.18}$$

[2] Taken from [8, 9], reprinted with kind permission © ASME 2012.

Hence, the problem reduces to solving the 9 unknowns $(x_i, y_i, z_i,\ i = 1, 2, 3)$ using the 9 equations given by (6.17) and (6.18). Once x_i, y_i, z_i $(i = 1, 2, 3)$ are known, the position coordinates x_{qi}, y_{qi}, z_{qi} $(i = 1, 2, 3)$ of the robots can be easily obtained.

As long as the tensions of the cables are not zero, the six equations in (6.17) are linear independent in $z_1, y_2, z_2, x_3, y_3, z_3$. Hence, we can eliminate these six unknowns from (6.17) and (6.18). From (6.17), one obtains

$$\begin{aligned} z_1 &= t_{17}x_1 + t_{18}y_1 + t_{19}x_2 + t_{20}, \\ y_2 &= -(t_4x_1 + t_8y_1 + t_6x_2)/t_9, \\ x_3 &= -(s_1x_1 + s_2x_2)/s_3, \\ y_3 &= t_{11}x_1 + t_{12}y_1 + t_{13}x_2, \\ z_2 &= t_{21}x_1 + t_{22}y_1 + t_{23}x_2 + t_{24}, \end{aligned} \tag{6.19}$$

where t_i are constants for given tensions. Then, substituting (6.19) into (6.18), one gets

$$a_ix_1^2 + b_iy_1^2 + c_ix_2^2 + d_ix_1y_1 + e_iy_1x_2 + f_ix_2x_1 + g_ix_1 + h_iy_1 + i_ix_2 + j_i = 0, \tag{6.20}$$

where $a_i, b_i, \ldots, j_i$ $(i = 1, 2, 3)$ are constants for given tensions.

The polynomial system given by (6.20) consists of 3 quadratic equations in x_1, y_1 and x_2. The total degree of this polynomial system is 8. According to Bezout's theorem, this system has at most 8 isolated solutions in the complex space.

This section presents an analytic algorithm to address the general case of the above inverse kinematics problem. The proposed algorithm is based on Roth's Dialytic elimination approach [18]. The three equations given by (6.20) are actually the general expressions of three quadratic surfaces. To find the solutions of (6.20) is to find all common intersection points of three quadratic surfaces. In [18], Roth proposed a Dialytic elimination approach to eliminate two unknowns without increasing the power products and without increasing the degree of the system. The principle is based on the fact that the derivatives of the determinant of the Jacobian of a system of equations written in terms of homogeneous coordinates have the same zeros as the original system of equations. Here, Roth's approach is modified and used to solve (6.20) for the general case.

Suppose that x_2 is suppressed, (6.20) can be written as

$$a_ix_1^2 + b_iy_1^2 + d_ix_1y_1 + k_ix_1 + u_iy_1 + v_i = 0, \tag{6.21}$$

where $k_i = f_ix_2 + g_i$, $u_i = e_ix_2 + h_i$ and $v_i = c_ix_2^2 + i_ix_2 + j_i$ $(i = 1, 2, 3)$.

Now, there are three equations and six power products. Hence, at least three more equations are needed. Rewriting (6.21) into the form with homogeneous coordinates by substituting $x_1 = X/T$, $y_1 = Y/T$ and then multiplying by T^2, one gets

$$a_iX^2 + b_iY^2 + d_iXY + k_iXT + u_iYT + v_iT^2 = 0. \tag{6.22}$$

If the left-hand side of (6.22) is given by F_i $(i = 1, 2, 3)$, (6.22) can be re-written as

$$F_{iX}X + F_{iY}Y + F_{iT}T = 0, \tag{6.23}$$

where

$$\begin{aligned} F_{iX} &= \frac{\partial F_i}{\partial X} = 2a_iX + d_iY + k_iT, \\ F_{iY} &= \frac{\partial F_i}{\partial Y} = 2b_iY + d_iX + u_iT, \\ F_{iT} &= \frac{\partial F_i}{\partial T} = k_iX + u_iY + 2v_iT. \end{aligned} \tag{6.24}$$

Hence, (6.23) can be re-written in the following matrix form:

$$\mathbf{J}\mathbf{X}_1 = \mathbf{0}, \tag{6.25}$$

where $\mathbf{X}_1 = [X, Y, T]^T$ and $\mathbf{J}$ is the Jacobian matrix:

$$\mathbf{J} = \begin{bmatrix} F_{1X} & F_{1Y} & F_{1T} \\ F_{2X} & F_{2Y} & F_{2T} \\ F_{3X} & F_{3Y} & F_{3T} \end{bmatrix}. \tag{6.26}$$

In order to make $\mathbf{X}_1$ to be not a zero vector, the determinant of the above Jacobian matrix must be zero:

$$|\mathbf{J}| = 0. \tag{6.27}$$

Thus,

$$\begin{aligned} \frac{\partial |\mathbf{J}|}{\partial X} &= 3AX^2 + 2BXY + 2CXT + DY^2 + ET^2 + FYT = 0, \\ \frac{\partial |\mathbf{J}|}{\partial Y} &= BX^2 + 2DXY + FXT + 3GY^2 + 2HYT + IT^2 = 0, \\ \frac{\partial |\mathbf{J}|}{\partial T} &= CX^2 + 2EXT + FXY + HY^2 + 2IYT + 3JT^2 = 0, \end{aligned} \tag{6.28}$$

where $A, B, \ldots, K$ are functions of x_2. The six equations in (6.22) and (6.28) can be written in the following matrix form:

$$\mathbf{M}\mathbf{X}_2 = \mathbf{0}, \tag{6.29}$$

where $\mathbf{X}_2 = [X^2, Y^2, XY, XT, YT, T^2]^T$. In order to make $\mathbf{X}_2$ to be not a zero vector, the determinant of matrix $\mathbf{M}$ must be zero. This determinant is an eight-degree polynomial in x_2. The coefficients of this polynomial are functions of the coefficients of the original three equations. Hence, x_2 can be easily solved with Matlab. For every real root x_2 substituted into (6.29), a linear system in $(x_1^2, y_1^2, x_1y_1, x_1, y_1)$ will be available by setting T to 1. Then, a solution of x_1 and y_1 can be obtained

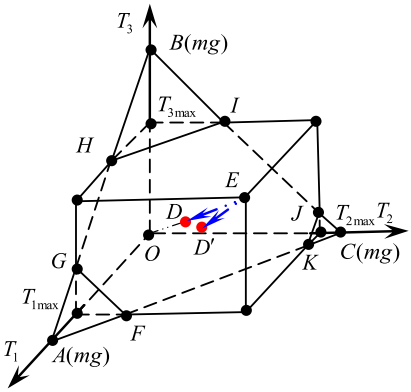

Fig. 6.9 Possible workspace of the tensions (mg is the weight of the payload)

by solving this linear system. When x_1, y_1 and x_2 are available, the other six unknowns $(z_1,\ y_2, z_2,\ x_3,\ y_3,\ z_3)$ can be calculated with (6.19). When x_i, y_i and z_i $(i = 1, 2, 3)$ are available, the position coordinates $(x_{qi}, y_{qi}, z_{qi},\ i = 1, 2, 3)$ of the robots can be obtained. Theoretically speaking, there are up to eight common intersection points of three quadratic surfaces. The case studies conducted later show that usually only six or less real solutions can be found by (6.20) for the 3-D cable towing.

The above algorithm can solve the general inverse kinematics problem. Unfortunately, it fails in the special case with the attachment points lie in the horizontal plane which is discussed in greater detail in [9].

Referring to Fig. 6.9, in order to address the cooperation in the manipulation task, it is useful to define the so-called *tension ratio*. If the payload capacity of robot Q_i is T_{imax}, the tension ratio of cable i can be defined as

$$c_{ri} = T_i / T_{imax}. \tag{6.30}$$

If all robots were to share the load equally, normalized to their strengths, the tension ratios c_{ri} $(i = 1, 2, 3)$ should be the same. Otherwise, the robots are not, strictly speaking, cooperating in a fair way. In the case with three robots, we want $c_{r1} = c_{r2} = c_{r3} = c_r$, which corresponds to the line $\overline{EO}$ inside the rectangular cuboid in Fig. 6.9. E represents the point with the maximal tension ratio $c_r = 1$. At this point, the tension of every cable reaches the payload capacity of every robot. In this condition of maximal cooperation, the tensions can be directly obtained from the tension ratio c_r.

For the 3-D cooperative towing with three aerial robots, the body-fixed frame can be chosen by taking P_1 as the origin $\tilde{O}$, P_1P_2 as the $\tilde{x}$ axis and triangle $P_1P_2P_3$ as the $\tilde{O}\tilde{x}\tilde{y}$ plane.

Suppose that the attachment points $(P_1,\ P_2,\ P_3)$ of the payload form an arbitrary triangle. Their coordinates in the body-fixed frame are given by $\tilde{\mathbf{p}}_1 = [0, 0, 0]^T m$, $\tilde{\mathbf{p}}_2 = [1, 0, 0]^T m$ and $\tilde{\mathbf{p}}_3 = [0.8, 0.7, 0]^T m$. The center of mass does not lie in the plane of triangle $P_1P_2P_3$. Instead, its position in the body-fixed frame is given by $\tilde{\mathbf{r}} = [0.7, 0.2, -0.3]^T m$. The lengths of three cables are $l_1 = l_2 = l_3 = 1.5$ m. The

Table 6.3 Solutions for a general payload with $c_r = 0.9$, $\phi = 25°$, $\theta = 15°$ and $\psi = -5°$

No.	1	2	3	4	5	6
$x_{q1}(m)$	−0.024	−0.590	1.783	1.469	−0.111	−0.456
$y_{q1}(m)$	1.473	−0.319	0.527	1.294	1.428	1.159
$z_{q1}(m)$	2.621	1.845	1.738	2.196	2.618	2.560
$x_{q2}(m)$	2.385	0.650	0.030	1.039	2.548	2.489
$y_{q2}(m)$	1.453	1.464	0.085	1.656	−0.166	−0.244
$z_{q2}(m)$	1.790	2.186	1.630	2.195	0.937	0.911
$x_{q3}(m)$	0.588	2.531	1.293	0.646	0.510	0.821
$y_{q3}(m)$	0.071	1.405	1.977	0.028	1.522	1.791
$z_{q3}(m)$	1.979	2.214	2.781	1.944	2.728	2.794

weight of the payload is $mg = 100$ N. The payload capacities of three robots are respectively $T_{1max} = 60$ N, $T_{2max} = 70$ N and $T_{3max} = 80$ N. In this very general case, if the position of the payload is chosen as $\mathbf{r} = [1, 1, 1]^T m$ and the tension ratios are chosen as the same with $c_r = 0.9$ and the desired orientation is given by ($\phi = 25°$, $\theta = 15°$, $\psi = -5°$), six solutions for the inverse kinematics problem can be found and listed in Table 6.3, which corresponds to the four configurations as shown in Fig. 6.10.

Six sequences of configurations can be obtained by reducing c_r from 1 along line EO in Fig. 6.9. These sequences are shown in Fig. 6.11 in which sequences 1 and 2 correspond to a range of $c_r \in [0.532, 1]$, sequences 3 and 4 correspond to a range of $c_r \in [0.575, 1]$, and sequences 5 to 6 correspond to a range of $c_r \in [0.9, 1]$. In other words, when the tension ratio c_r is less than 0.9 and greater than 0.575, the inverse kinematics problem has only four solutions. When the tension ratio c_r is less than 0.575, the inverse kinematics problem has only two solutions. In this general case, the minimal tension ratio $c_r = 0.532$ can also be obtained numerically using a line search. Obviously, in the general case, the minimal tension ratio 0.532 is greater than 0.472 calculated with $c_r \sum_{i=1}^{3} T_{imax} = mg$. Also, when c_r reaches its minimal valid value 0.532, the three cables do not lie in vertical positions, see the dashed lines in Figs. 6.11(a) and (b).

6.5 The Set of Valid Tensions

For a given set of tensions, we can find several equilibrium configurations. However, the tensions cannot be chosen arbitrarily. The tension of every cable should be in a range from a positive lower threshold to the payload capacity T_{imax} of the robot, i.e., $T_i \in [0, T_{imax}]$. In the case with three robots, it would seem that any point in the rectangular cuboid with side length T_{imax} ($i = 1, 2, 3$) as shown in Fig. 6.9 is a valid choice of tensions. However, this is not true. First, the tensions of three cables

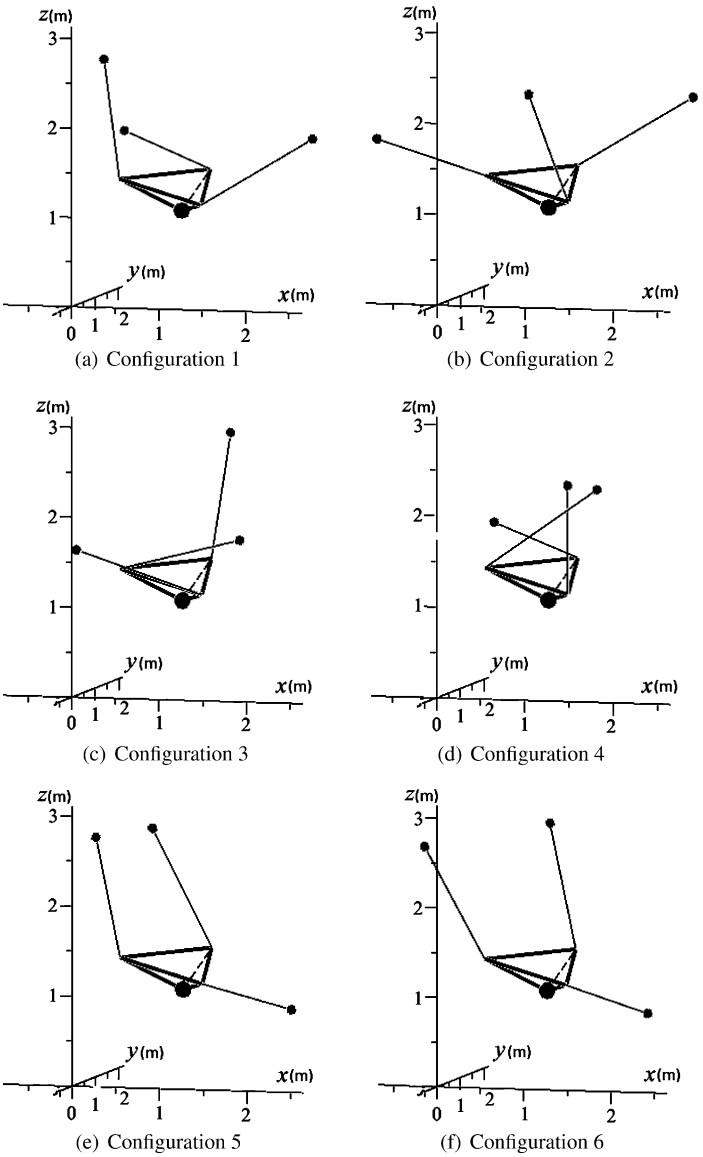

(a) Configuration 1 (b) Configuration 2

(c) Configuration 3 (d) Configuration 4

(e) Configuration 5 (f) Configuration 6

Fig. 6.10 Configurations for a general payload in a general configuration ($\mathbf{r} = [1, 1, 1]^T m$, $\phi = 25°, \theta = 15°$ and $\psi = -5°$), with $c_r = 0.9$

should satisfy the following condition:

$$\sum_{i=1}^{3} T_i \geq mg. \tag{6.31}$$

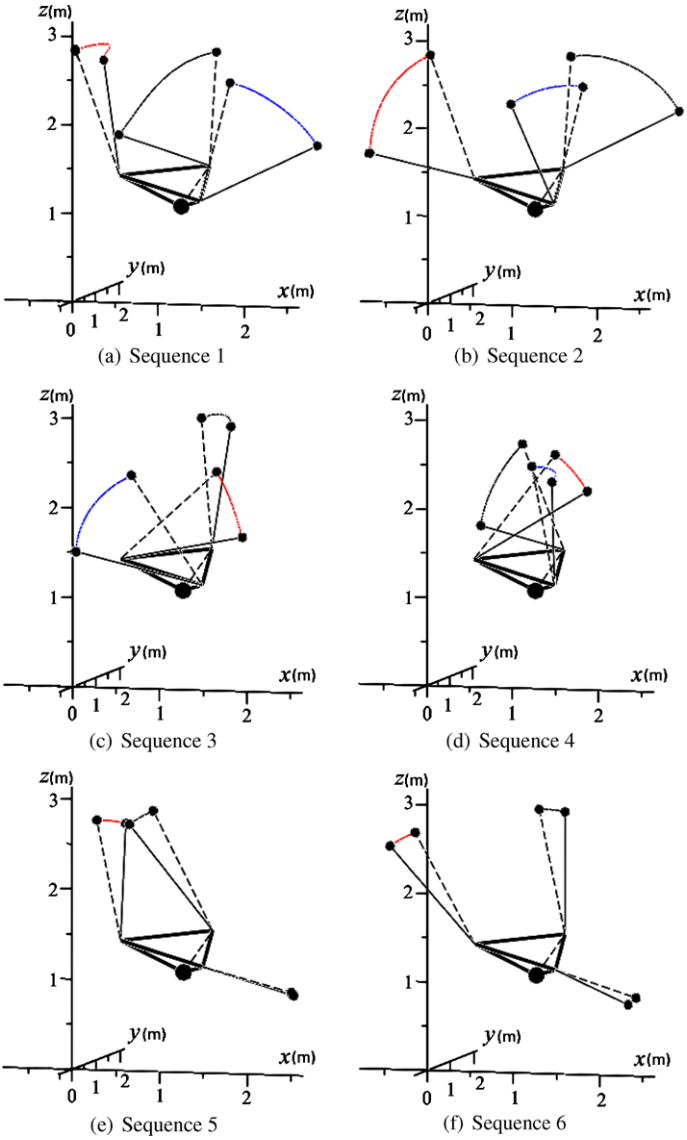

Fig. 6.11 Sequences of configurations for a general configuration ($\mathbf{r} = [1, 1, 1]^T m$, $\phi = 25°, \theta = 15°$ and $\psi = -5°$), with different tension ratios

This condition shows that the possible work point for the tensions should be in the region above the plane ABC with $\sum_{i=1}^{3} T_i = mg$. However, even in this region, not every point represents a valid set of tensions. For instance, in general, points on the boundary $FGHIJKF$ are not realistic if a desired orientation is specified.

Accordingly, we determine the *tension workspace*, the set of valid tensions. First, the vertex E in Fig. 6.9 should be a valid point. Otherwise, the tension workspace

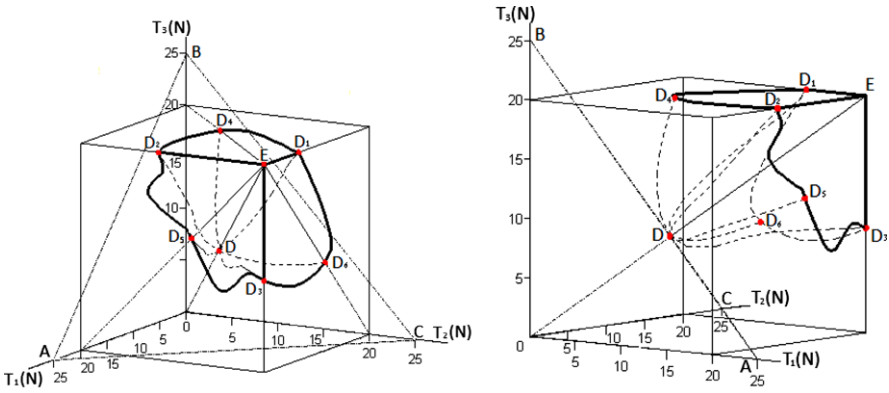

Fig. 6.12 Tension workspace for an equilateral triangle payload with $\phi = 25°$, $\theta = 15°$, $\psi = -5°$

is the null set. Second, the tension workspace should lie in the half plane above the plane ABC defined $\sum_{i=1}^{3} T_i = mg$. Hence, it should be closed by three planes, each perpendicular to one of the axes, and a surface that lies above ABC as shown in Fig. 6.12. To compute the boundary of this workspace, we start from $c_r = 1$ (which corresponds to point E in Fig. 6.9) and gradually decrease c_r with a small step size, Δc_r, along different rays in the workspace numerically. See Fig. 6.12. More details are available in [9].

6.6 Stability Analysis

The equilibrium configurations have been obtained from the case studies in both direct and inverse kinematics analysis. However, we have not discussed the stability of the equilibrium points. Clearly the payload will not stay in configurations that are unstable. Thus it is necessary to able to find solutions that are stable.

The obvious approach to analyze the stability is to derive the Hessian matrix of the system. If all eigenvalues λ_i $(i = 1, 2, \ldots, n)$ of the Hessian matrix are strictly positive, the corresponding equilibrium configuration can be regarded as stable. Otherwise, the configuration is either unstable (one of the eigenvalues is strictly negative) or requires higher order analysis (all eigenvalues are non negative).

The position and orientation of the payload can be defined by the position $\mathbf{r} = [x, y, z]^T$ of its center of mass and the rotation matrix $\mathbf{R}$ in which there are three orientation angles (ϕ, θ, ψ). Hence, six variable $(x, y, z, \phi, \theta, \psi)$ can be used to define the position and orientation of the payload.

6.6.1 Case with Two Cables

In the equilibrium configurations as shown in Figs. 6.6(b), (c) and (d), the payload is suspended by only two cables. Considering the geometric constraints imposed by

the two cables, the payload has four degrees of freedom. Hence, only four of the six variables $(x, y, z, \phi, \theta, \psi)$ are independent. Referring to the geometric constraints given by (6.4), the coordinate x can be eliminated and z can be expressed as the function of (y, ϕ, θ, ψ), which are used as four independent variables. The potential energy of the payload can be given by

$$V = mgz = mgz(y, \phi, \theta, \psi). \tag{6.32}$$

Hence, the Hessian matrix can be given as

$$\mathbf{H} = mg \begin{bmatrix} \frac{\partial^2 z}{\partial y^2} & \frac{\partial^2 z}{\partial y \partial \phi} & \frac{\partial^2 z}{\partial y \partial \theta} & \frac{\partial^2 z}{\partial y \partial \psi} \\ \frac{\partial^2 z}{\partial \phi \partial y} & \frac{\partial^2 z}{\partial \phi^2} & \frac{\partial^2 z}{\partial \phi \partial \theta} & \frac{\partial^2 z}{\partial \phi \partial \psi} \\ \frac{\partial^2 z}{\partial \theta \partial y} & \frac{\partial^2 z}{\partial \theta \partial \phi} & \frac{\partial^2 z}{\partial \theta^2} & \frac{\partial^2 z}{\partial \theta \partial \psi} \\ \frac{\partial^2 z}{\partial \psi \partial y} & \frac{\partial^2 z}{\partial \psi \partial \phi} & \frac{\partial^2 z}{\partial \psi \partial \theta} & \frac{\partial^2 z}{\partial \psi^2} \end{bmatrix}. \tag{6.33}$$

Now, the focus is how to obtain the above Hessian matrix. From (6.4), one gets

$$\begin{aligned} (x + u_{11})^2 + (y + u_{12})^2 + (z + u_{13})^2 &= l_1^2, \\ (x + u_{21})^2 + (y + u_{22})^2 + (z + u_{23})^2 &= l_2^2, \end{aligned} \tag{6.34}$$

where

$$\begin{aligned} u_{11} &= r_{11}(\tilde{x}_{p1} - \tilde{x}) + r_{12}(\tilde{y}_{p1} - \tilde{y}) + r_{13}(\tilde{z}_{p1} - \tilde{z}) - x_{q1}, \\ u_{12} &= r_{21}(\tilde{x}_{p1} - \tilde{x}) + r_{22}(\tilde{y}_{p1} - \tilde{y}) + r_{23}(\tilde{z}_{p1} - \tilde{z}) - y_{q1}, \\ u_{13} &= r_{31}(\tilde{x}_{p1} - \tilde{x}) + r_{32}(\tilde{y}_{p1} - \tilde{y}) + r_{33}(\tilde{z}_{p1} - \tilde{z}) - z_{q1}, \\ u_{21} &= r_{11}(\tilde{x}_{p2} - \tilde{x}) + r_{12}(\tilde{y}_{p2} - \tilde{y}) + r_{13}(\tilde{z}_{p2} - \tilde{z}) - x_{q2}, \\ u_{22} &= r_{21}(\tilde{x}_{p2} - \tilde{x}) + r_{22}(\tilde{y}_{p2} - \tilde{y}) + r_{23}(\tilde{z}_{p2} - \tilde{z}) - y_{q2}, \\ u_{23} &= r_{31}(\tilde{x}_{p2} - \tilde{x}) + r_{32}(\tilde{y}_{p2} - \tilde{y}) + r_{33}(\tilde{z}_{p2} - \tilde{z}) - z_{q2}, \end{aligned} \tag{6.35}$$

and r_{ij} $(i, j = 1, 2, 3)$ are the entries of the rotation matrix $\mathbf{R}$ and given as follows:

$$\begin{aligned} r_{11} &= \cos\theta \cos\psi, \\ r_{12} &= \sin\phi \sin\theta \cos\psi - \cos\phi \sin\psi, \\ r_{11} &= \cos\phi \sin\theta \cos\psi + \sin\phi \sin\psi, \\ r_{21} &= \cos\theta \sin\psi, \\ r_{22} &= \sin\phi \sin\theta \sin\psi + \cos\phi \cos\psi, \\ r_{23} &= \cos\phi \sin\theta \sin\psi - \sin\phi \cos\psi, \\ r_{31} &= -\sin\theta, \end{aligned} \tag{6.36}$$

$$r_{32} = \sin\phi\cos\theta,$$
$$r_{33} = \cos\phi\cos\theta.$$

Subtracting the first equation of (6.34) from the second equation of (6.34), one gets

$$2(u_{21}-u_{11})x + 2(u_{22}-u_{12})y + 2(u_{23}-u_{13})z = U_2 - U_1, \tag{6.37}$$

where

$$\begin{aligned} U_1 &= l_1^2 - u_{11}^2 - u_{12}^2 - u_{13}^2, \\ U_2 &= l_2^2 - u_{21}^2 - u_{22}^2 - u_{23}^2. \end{aligned} \tag{6.38}$$

From (6.37), one gets

$$\begin{aligned} x = \big[\big(l_2^2 - u_{21}^2 - u_{22}^2 - u_{23}^2 - l_1^2 + u_{11}^2 + u_{12}^2 + u_{13}^2\big)/2 \\ - (u_{22}-u_{12})y - (u_{23}-u_{13})z\big]/(u_{21}-u_{11}). \end{aligned} \tag{6.39}$$

Substituting (6.39) into the first equation of (6.34), one gets

$$F = F(y, z, u_{11}, \ldots, u_{23}) = F(y, z, \phi, \theta, \psi). \tag{6.40}$$

So,

$$\begin{aligned} \frac{\partial z}{\partial y} &= -F_y/F_z, & \frac{\partial z}{\partial \phi} &= -F_\phi/F_z, \\ \frac{\partial z}{\partial \theta} &= -F_\theta/F_z, & \frac{\partial z}{\partial \psi} &= -F_\psi/F_z. \end{aligned} \tag{6.41}$$

Therefore,

$$\begin{aligned} \frac{\partial^2 z}{\partial y^2} &= -\frac{F_{yy}F_z - F_y F_{zy}}{F_z^2}, & \frac{\partial^2 z}{\partial y \partial \phi} &= -\frac{F_{y\phi}F_z - F_y F_{z\phi}}{F_z^2}, \\ \frac{\partial^2 z}{\partial y \partial \theta} &= -\frac{F_{y\theta}F_z - F_y F_{z\theta}}{F_z^2}, & \frac{\partial^2 z}{\partial y \partial \psi} &= -\frac{F_{y\psi}F_z - F_y F_{z\psi}}{F_z^2}, \\ \frac{\partial^2 z}{\partial \phi \partial y} &= -\frac{F_{\phi y}F_z - F_\phi F_{zy}}{F_z^2}, & \frac{\partial^2 z}{\partial \phi^2} &= -\frac{F_{\phi\phi}F_z - F_\phi F_{z\phi}}{F_z^2}, \\ \frac{\partial^2 z}{\partial \phi \partial \theta} &= -\frac{F_{\phi\theta}F_z - F_\phi F_{z\theta}}{F_z^2}, & \frac{\partial^2 z}{\partial \phi \partial \psi} &= -\frac{F_{\phi\psi}F_z - F_\phi F_{z\psi}}{F_z^2}, \\ \frac{\partial^2 z}{\partial \theta \partial y} &= -\frac{F_{\theta y}F_z - F_\theta F_{zy}}{F_z^2}, & \frac{\partial^2 z}{\partial \theta \partial \phi} &= -\frac{F_{\theta\phi}F_z - F_\theta F_{z\phi}}{F_z^2}, \\ \frac{\partial^2 z}{\partial \theta^2} &= -\frac{F_{\theta\theta}F_z - F_\theta F_{z\theta}}{F_z^2}, & \frac{\partial^2 z}{\partial \theta \partial \psi} &= -\frac{F_{\theta\psi}F_z - F_\theta F_{z\psi}}{F_z^2}, \end{aligned} \tag{6.42}$$

Table 6.4 Eigenvalues of the Hessian matrices of the equilibrium configurations with two cables

Configuration	Fig. 6.6(a)	Fig. 6.6(b)	Fig. 6.6(c)	Fig. 6.6(d)
λ_1	1.635	0.092	0.091	0.091
λ_2	0.344	+0.000	0.000	9.214
λ_3	0.086	9.039	−0.150	−0.150
λ_4	+0.000	−0.367	−0.153	−0.153

$$\frac{\partial^2 z}{\partial \psi \partial y} = -\frac{F_{\psi y} F_z - F_\psi F_{zy}}{F_z^2}, \qquad \frac{\partial^2 z}{\partial \psi \partial \phi} = -\frac{F_{\psi \phi} F_z - F_\psi F_{z\phi}}{F_z^2},$$

$$\frac{\partial^2 z}{\partial \psi \partial \theta} = -\frac{F_{\psi \theta} F_z - F_\psi F_{z\theta}}{F_z^2}, \qquad \frac{\partial^2 z}{\partial \psi^2} = -\frac{F_{\psi \psi} F_z - F_\psi F_{z\psi}}{F_z^2}.$$

If F is directly expressed as the function of $(y, z, \phi, \theta, \psi)$, the expression of F is so complicated that standard symbolic manipulation packages cannot handle the derivation. Hence, all derivatives (F_y, F_z, F_ϕ, F_θ, F_ψ, F_{zy}, $F_{z\phi}$, $F_{z\theta}$, $F_{z\psi}$, F_{yy}, $F_{y\phi}$, $F_{y\theta}$, $F_{y\psi}$, $F_{\phi y}$, $F_{\phi\phi}$, $F_{\phi\theta}$, $F_{\phi\psi}$, $F_{\theta y}$, $F_{\theta\phi}$, $F_{\theta\theta}$, $F_{\theta\psi}$, $F_{\psi y}$, $F_{\psi\phi}$, $F_{\psi\theta}$, $F_{\psi\psi}$) of F with respect to $(y, z, \phi, \theta, \psi)$ have to be computed individually and pieced together using the chain rule. Even so, the expressions of some second order derivatives are still very complicated. Substituting (6.42) into (6.33), the Hessian matrix is obtained and the eigenvalues of the Hessian matrix are determined.

Now the above developed approach is used to analyze the stability of the equilibrium configurations as shown in Fig. 6.6. Although the configuration of the payload as shown Fig. 6.6(a) coincides with its initial configuration as shown in Fig. 6.5, this configuration is obtained by supposing that the payload is suspended with two cables. Hence, the stability analysis of this configuration can be conducted by supposing that the payloads is suspended with only two relevant cables. If this configuration under this condition is stable, its corresponding initial configuration should be more stable.

For every equilibrium configuration as shown in Fig. 6.6, the positions of two relevant robots and two relevant attachment points and the center of mass as well as the orientation angles of the payload are know. Substituting all these parameters into (6.42) and then into (6.33), a Hessian matrix is available. The eigenvalues of the Hessian matrix can be easily evaluated by the package Matlab.

Table 6.4 lists the eigenvalues of the Hessian matrices of these equilibrium configurations. From this table, it can be seen that the configurations as shown in Fig. 6.6(a) are stable. But other configurations are unstable.

6.6.2 Case with Three Cables

In the equilibrium configurations as shown in Fig. 6.10, the payload is suspended by three cables. Considering the geometric constraints imposed by the three ca-

bles, the payload has three degrees of freedom. Hence, three of the six variables $(x, y, z, \phi, \theta, \psi)$ are independent.

Referring to the geometric constraints given by (6.4), the coordinates (x, y) can be eliminated and z can be expressed as the function of the orientation angles (ϕ, θ, ψ), which are used as three independent variables. The potential energy of the payload can be given by

$$V = mgz = mgz(\phi, \theta, \psi). \tag{6.43}$$

Hence, the Hessian matrix can be given as

$$\mathbf{H} = mg \begin{bmatrix} \frac{\partial^2 z}{\partial \phi^2} & \frac{\partial^2 z}{\partial \phi \partial \theta} & \frac{\partial^2 z}{\partial \phi \partial \psi} \\ \frac{\partial^2 z}{\partial \theta \partial \phi} & \frac{\partial^2 z}{\partial \theta^2} & \frac{\partial^2 z}{\partial \theta \partial \psi} \\ \frac{\partial^2 z}{\partial \psi \partial \phi} & \frac{\partial^2 z}{\partial \psi \partial \theta} & \frac{\partial^2 z}{\partial \psi^2} \end{bmatrix}. \tag{6.44}$$

Now, the focus is how to obtain the above Hessian matrix. From (6.4), one gets

$$\begin{aligned} (x + u_{11})^2 + (y + u_{12})^2 + (z + u_{13})^2 &= l_1^2, \\ (x + u_{21})^2 + (y + u_{22})^2 + (z + u_{23})^2 &= l_2^2, \\ (x + u_{31})^2 + (y + u_{32})^2 + (z + u_{33})^2 &= l_3^2, \end{aligned} \tag{6.45}$$

where

$$\begin{aligned} u_{11} &= r_{11}(\tilde{x}_{p1} - \tilde{x}) + r_{12}(\tilde{y}_{p1} - \tilde{y}) + r_{13}(\tilde{z}_{p1} - \tilde{z}) - x_{q1}, \\ u_{12} &= r_{21}(\tilde{x}_{p1} - \tilde{x}) + r_{22}(\tilde{y}_{p1} - \tilde{y}) + r_{23}(\tilde{z}_{p1} - \tilde{z}) - y_{q1}, \\ u_{13} &= r_{31}(\tilde{x}_{p1} - \tilde{x}) + r_{32}(\tilde{y}_{p1} - \tilde{y}) + r_{33}(\tilde{z}_{p1} - \tilde{z}) - z_{q1}, \\ u_{21} &= r_{11}(\tilde{x}_{p2} - \tilde{x}) + r_{12}(\tilde{y}_{p2} - \tilde{y}) + r_{13}(\tilde{z}_{p2} - \tilde{z}) - x_{q2}, \\ u_{22} &= r_{21}(\tilde{x}_{p2} - \tilde{x}) + r_{22}(\tilde{y}_{p2} - \tilde{y}) + r_{23}(\tilde{z}_{p2} - \tilde{z}) - y_{q2}, \\ u_{23} &= r_{31}(\tilde{x}_{p2} - \tilde{x}) + r_{32}(\tilde{y}_{p2} - \tilde{y}) + r_{33}(\tilde{z}_{p2} - \tilde{z}) - z_{q2}, \\ u_{31} &= r_{11}(\tilde{x}_{p3} - \tilde{x}) + r_{12}(\tilde{y}_{p3} - \tilde{y}) + r_{13}(\tilde{z}_{p3} - \tilde{z}) - x_{q3}, \\ u_{32} &= r_{21}(\tilde{x}_{p3} - \tilde{x}) + r_{22}(\tilde{y}_{p3} - \tilde{y}) + r_{23}(\tilde{z}_{p3} - \tilde{z}) - y_{q3}, \\ u_{33} &= r_{31}(\tilde{x}_{p3} - \tilde{x}) + r_{32}(\tilde{y}_{p3} - \tilde{y}) + r_{33}(\tilde{z}_{p3} - \tilde{z}) - z_{q3}, \end{aligned} \tag{6.46}$$

and r_{ij} $(i, j = 1, 2, 3)$ are the entries of the rotation matrix $\mathbf{R}$ and given by (6.36). Respectively subtracting the first equation of (6.45) from the second and the third equations of (6.45), one gets

$$\begin{aligned} 2(u_{21} - u_{11})x + 2(u_{22} - u_{12})y + 2(u_{23} - u_{13})z &= U_2 - U_1, \\ 2(u_{31} - u_{11})x + 2(u_{32} - u_{12})y + 2(u_{33} - u_{13})z &= U_3 - U_1, \end{aligned} \tag{6.47}$$

where

$$\begin{aligned} U_1 &= l_1^2 - u_{11}^2 - u_{12}^2 - u_{13}^2, \\ U_2 &= l_2^2 - u_{21}^2 - u_{22}^2 - u_{23}^2, \\ U_3 &= l_3^2 - u_{31}^2 - u_{32}^2 - u_{33}^2. \end{aligned} \tag{6.48}$$

From (6.47), one gets

$$\begin{aligned} x &= \frac{-u_{32}u_{23} + u_{32}u_{13} + u_{12}u_{23} + u_{22}u_{33} - u_{22}u_{13} - u_{12}u_{33}}{u_{21}u_{32} - u_{21}u_{12} - u_{11}u_{32} - u_{22}u_{31} + u_{22}u_{11} + u_{12}u_{31}} z \\ &\quad + \frac{u_{32}U_2 - u_{32}U_1 - u_{12}U_2 - u_{22}U_3 + u_{22}U_1 + u_{12}U_3}{2(u_{21}u_{32} - u_{21}u_{12} - u_{11}u_{32} - u_{22}u_{31} + u_{22}u_{11} + u_{12}u_{31})}, \\ y &= \frac{u_{31}u_{23} - u_{31}u_{13} - u_{11}u_{23} - u_{21}u_{33} + u_{21}u_{13} + u_{11}u_{33}}{u_{21}u_{32} - u_{21}u_{12} - u_{11}u_{32} - u_{22}u_{31} + u_{22}u_{11} + u_{12}u_{31}} z \\ &\quad - \frac{u_{31}U_2 - u_{31}U_1 - u_{11}U_2 - u_{21}U_3 + u_{21}U_1 + u_{11}U_3}{2(u_{21}u_{32} - u_{21}u_{12} - u_{11}u_{32} - u_{22}u_{31} + u_{22}u_{11} + u_{12}u_{31})}. \end{aligned} \tag{6.49}$$

Substituting (6.49) into the first equation of (6.45), one gets

$$F(z, u_{11}, \ldots, u_{33}) = F(z, \phi, \theta, \psi) = 0. \tag{6.50}$$

So,

$$\frac{\partial z}{\partial \phi} = -F_\phi / F_z, \qquad \frac{\partial z}{\partial \theta} = -F_\theta / F_z, \qquad \frac{\partial z}{\partial \psi} = -F_\psi / F_z. \tag{6.51}$$

Hence,

$$\begin{aligned} \frac{\partial^2 z}{\partial \phi^2} &= -\frac{F_{\phi\phi}F_z - F_\phi F_{z\phi}}{F_z^2}, \\ \frac{\partial^2 z}{\partial \phi \partial \theta} &= -\frac{F_{\phi\theta}F_z - F_\phi F_{z\theta}}{F_z^2}, \\ \frac{\partial^2 z}{\partial \phi \partial \psi} &= -\frac{F_{\phi\psi}F_z - F_\phi F_{z\psi}}{F_z^2}, \\ \frac{\partial^2 z}{\partial \theta \partial \phi} &= -\frac{F_{\theta\phi}F_z - F_\theta F_{z\phi}}{F_z^2}, \\ \frac{\partial^2 z}{\partial \theta^2} &= -\frac{F_{\theta\theta}F_z - F_\theta F_{z\theta}}{F_z^2}, \end{aligned} \tag{6.52}$$

Table 6.5 Eigenvalues of Hessian matrices of the equilibrium configurations in Fig. 6.10

No.	1	2	3	4	5	6
λ_1	2.789	1.345	1.101	0.625	11.001	29.549
λ_2	0.495	0.729	0.428	0.080	0.823	0.844
λ_3	0.009	0.196	0.043	−0.350	0.450	0.689

$$\frac{\partial^2 z}{\partial\theta\partial\psi} = -\frac{F_{\theta\psi}F_z - F_\theta F_{z\psi}}{F_z^2},$$
$$\frac{\partial^2 z}{\partial\psi\partial\phi} = -\frac{F_{\psi\phi}F_z - F_\psi F_{z\phi}}{F_z^2},$$
$$\frac{\partial^2 z}{\partial\psi\partial\theta} = -\frac{F_{\psi\theta}F_z - F_\psi F_{z\theta}}{F_z^2},$$
$$\frac{\partial^2 z}{\partial\psi^2} = -\frac{F_{\psi\psi}F_z - F_\psi F_{z\psi}}{F_z^2}.$$

Equation (6.50) shows that F is a function of (z, ϕ, θ, ψ). Its derivatives with respect to (z, ϕ, θ, ψ) can be derived using the chain rule. Substituting (6.52) into (6.44), we can obtain a Hessian matrix which can be used to analyze the stability of the equilibrium configurations. For every equilibrium configuration, the positions of three relevant robots and three relevant attachment points and the center of mass as well as the orientation angles of the payload are know. Substituting all these parameters into (6.52) and then into (6.44), a Hessian matrix is available. The eigenvalues of the Hessian matrix can be easily evaluated by the package Matlab.

Table 6.5 lists the eigenvalues of the Hessian matrices of the six equilibrium configurations as shown in Fig. 6.10. From this table, it can be seen that configurations 1, 2, 3, 5 and 6 are stable. Only configuration 4 is unstable.

6.6.3 Case with Four Cables

In the equilibrium configurations as shown in Figs. 6.7(b), (c) and (d), the payload is suspended by four cables. Considering the geometric constraints imposed by the four cables, the payload has two degrees of freedom. Hence, only two of the six variables $(x, y, z, \phi, \theta, \psi)$ are independent. If (θ, ψ) are used as the two independent variables, the Hessian matrix can be given by

$$\mathbf{H} = mg\begin{bmatrix} \frac{\partial^2 z}{\partial\theta^2} & \frac{\partial^2 z}{\partial\theta\partial\psi} \\ \frac{\partial^2 z}{\partial\psi\partial\theta} & \frac{\partial^2 z}{\partial\psi^2} \end{bmatrix}. \tag{6.53}$$

Now, the focus is how to obtain the above Hessian matrix. From (6.4), one gets

$$\begin{aligned}
(x+u_{11})^2+(y+u_{12})^2+(z+u_{13})^2&=l_1^2,\\
(x+u_{21})^2+(y+u_{22})^2+(z+u_{23})^2&=l_2^2,\\
(x+u_{31})^2+(y+u_{32})^2+(z+u_{33})^2&=l_3^2,\\
(x+u_{41})^2+(y+u_{42})^2+(z+u_{43})^2&=l_4^2,
\end{aligned} \tag{6.54}$$

where

$$\begin{aligned}
u_{11}&=r_{11}(\tilde{x}_{p1}-\tilde{x})+r_{12}(\tilde{y}_{p1}-\tilde{y})+r_{13}(\tilde{z}_{p1}-\tilde{z})-x_{q1},\\
u_{12}&=r_{21}(\tilde{x}_{p1}-\tilde{x})+r_{22}(\tilde{y}_{p1}-\tilde{y})+r_{23}(\tilde{z}_{p1}-\tilde{z})-y_{q1},\\
u_{13}&=r_{31}(\tilde{x}_{p1}-\tilde{x})+r_{32}(\tilde{y}_{p1}-\tilde{y})+r_{33}(\tilde{z}_{p1}-\tilde{z})-z_{q1},\\
u_{21}&=r_{11}(\tilde{x}_{p2}-\tilde{x})+r_{12}(\tilde{y}_{p2}-\tilde{y})+r_{13}(\tilde{z}_{p2}-\tilde{z})-x_{q2},\\
u_{22}&=r_{21}(\tilde{x}_{p2}-\tilde{x})+r_{22}(\tilde{y}_{p2}-\tilde{y})+r_{23}(\tilde{z}_{p2}-\tilde{z})-y_{q2},\\
u_{23}&=r_{31}(\tilde{x}_{p2}-\tilde{x})+r_{32}(\tilde{y}_{p2}-\tilde{y})+r_{33}(\tilde{z}_{p2}-\tilde{z})-z_{q2},\\
u_{31}&=r_{11}(\tilde{x}_{p3}-\tilde{x})+r_{12}(\tilde{y}_{p3}-\tilde{y})+r_{13}(\tilde{z}_{p3}-\tilde{z})-x_{q3},\\
u_{32}&=r_{21}(\tilde{x}_{p3}-\tilde{x})+r_{22}(\tilde{y}_{p3}-\tilde{y})+r_{23}(\tilde{z}_{p3}-\tilde{z})-y_{q3},\\
u_{33}&=r_{31}(\tilde{x}_{p3}-\tilde{x})+r_{32}(\tilde{y}_{p3}-\tilde{y})+r_{33}(\tilde{z}_{p3}-\tilde{z})-z_{q3},\\
u_{41}&=r_{11}(\tilde{x}_{p4}-\tilde{x})+r_{12}(\tilde{y}_{p4}-\tilde{y})+r_{13}(\tilde{z}_{p4}-\tilde{z})-x_{q4},\\
u_{42}&=r_{21}(\tilde{x}_{p4}-\tilde{x})+r_{22}(\tilde{y}_{p4}-\tilde{y})+r_{23}(\tilde{z}_{p4}-\tilde{z})-y_{q4},\\
u_{43}&=r_{31}(\tilde{x}_{p4}-\tilde{x})+r_{32}(\tilde{y}_{p4}-\tilde{y})+r_{33}(\tilde{z}_{p4}-\tilde{z})-z_{q4},
\end{aligned} \tag{6.55}$$

and r_{ij} $(i,j=1,2,3)$ are the entries of the rotation matrix $\mathbf{R}$ and given by (6.36). From (6.54), one gets

$$\begin{aligned}
x^2+2u_{11}x+y^2+2u_{12}y+z^2+2u_{13}z&=U_1,\\
x^2+2u_{21}x+y^2+2u_{22}y+z^2+2u_{23}z&=U_2,\\
x^2+2u_{31}x+y^2+2u_{32}y+z^2+2u_{33}z&=U_3,\\
x^2+2u_{41}x+y^2+2u_{42}y+z^2+2u_{43}z&=U_4,
\end{aligned} \tag{6.56}$$

where

$$\begin{aligned}
U_1&=l_1^2-u_{11}^2-u_{12}^2-u_{13}^2,\\
U_2&=l_2^2-u_{21}^2-u_{22}^2-u_{23}^2,\\
U_3&=l_3^2-u_{31}^2-u_{32}^2-u_{33}^2,\\
U_4&=l_4^2-u_{41}^2-u_{42}^2-u_{43}^2.
\end{aligned} \tag{6.57}$$

From the first three equations of (6.56), one gets

$$\begin{aligned} 2(u_{21}-u_{11})x+2(u_{22}-u_{12})y+2(u_{23}-u_{13})z&=U_2-U_1,\\ 2(u_{31}-u_{11})x+2(u_{32}-u_{12})y+2(u_{33}-u_{13})z&=U_3-U_1. \end{aligned} \tag{6.58}$$

Hence,

$$\begin{aligned} x=&\frac{-u_{32}u_{23}+u_{32}u_{13}+u_{12}u_{23}+u_{22}u_{33}-u_{22}u_{13}-u_{12}u_{33}}{u_{21}u_{32}-u_{21}u_{12}-u_{11}u_{32}-u_{22}u_{31}+u_{22}u_{11}+u_{12}u_{31}}z\\ &+\frac{u_{32}U_2-u_{32}U_1-u_{12}U_2-u_{22}U_3+u_{22}U_1+u_{12}U_3}{2(u_{21}u_{32}-u_{21}u_{12}-u_{11}u_{32}-u_{22}u_{31}+u_{22}u_{11}+u_{12}u_{31})},\\ y=&\frac{u_{31}u_{23}-u_{31}u_{13}-u_{11}u_{23}-u_{21}u_{33}+u_{21}u_{13}+u_{11}u_{33}}{u_{21}u_{32}-u_{21}u_{12}-u_{11}u_{32}-u_{22}u_{31}+u_{22}u_{11}+u_{12}u_{31}}z\\ &-\frac{u_{31}U_2-u_{31}U_1-u_{11}U_2-u_{21}U_3+u_{21}U_1+u_{11}U_3}{2(u_{21}u_{32}-u_{21}u_{12}-u_{11}u_{32}-u_{22}u_{31}+u_{22}u_{11}+u_{12}u_{31})}. \end{aligned} \tag{6.59}$$

Substitute (6.59) into the first and the fourth equations of (6.56), one gets

$$\begin{aligned} F(z,u_{11},\ldots,u_{43})&=F(z,\phi,\theta,\psi)=0,\\ G(z,u_{11},\ldots,u_{43})&=G(z,\phi,\theta,\psi)=0. \end{aligned} \tag{6.60}$$

From (6.60), one gets

$$\begin{aligned} \frac{\partial z}{\partial\theta}&=(F_\phi G_\theta-F_\theta G_\phi)/(F_z G_\phi-F_\phi G_z),\\ \frac{\partial z}{\partial\psi}&=(F_\phi G_\psi-F_\psi G_\phi)/(F_z G_\phi-F_\phi G_z). \end{aligned} \tag{6.61}$$

Hence,

$$\begin{aligned} \frac{\partial^2 z}{\partial\theta^2}=&\big[(F_{\phi\theta}G_\theta+F_\phi G_{\theta\theta}-F_{\theta\theta}G_\phi-F_\theta G_{\phi\theta})(F_zG_\phi-F_\phi G_z)\\ &-(F_\phi G_\theta-F_\theta G_\phi)(F_{z\theta}G_\phi+F_zG_{\phi\theta}-F_{\phi\theta}G_z-F_\phi G_{z\theta})\big]\\ &/(F_zG_\phi-F_\phi G_z)^2,\\ \frac{\partial^2 z}{\partial\theta\partial\psi}=&\big[(F_{\phi\psi}G_\theta+F_\phi G_{\theta\psi}-F_{\theta\psi}G_\phi-F_\theta G_{\phi\psi})(F_zG_\phi-F_\phi G_z)\\ &-(F_\phi G_\theta-F_\theta G_\phi)(F_{z\psi}G_\phi+F_zG_{\phi\psi}-F_{\phi\psi}G_z-F_\phi G_{z\psi})\big]\\ &/(F_zG_\phi-F_\phi G_z)^2,\\ \frac{\partial^2 z}{\partial\psi\partial\theta}=&\big[(F_{\phi\theta}G_\psi+F_\phi G_{\psi\theta}-F_{\psi\theta}G_\phi-F_\psi G_{\phi\theta})(F_zG_\phi-F_\phi G_z)\\ &-(F_\phi G_\psi-F_\psi G_\phi)(F_{z\theta}G_\phi+F_zG_{\phi\theta}-F_{\phi\theta}G_z-F_\phi G_{z\theta})\big]\\ &/(F_zG_\phi-F_\phi G_z)^2, \end{aligned} \tag{6.62}$$

Table 6.6 Eigenvalues of Hessian matrices of the equilibrium configurations in Fig. 6.7

Configuration	1	2	3	4
λ_1	1.549	8.852	0.203	−0.024
λ_2	0.159	0.289	−0.499	−0.340

$$\frac{\partial^2 z}{\partial \psi^2} = \big[(F_{\phi\psi}G_\psi + F_\phi G_{\psi\psi} - F_{\psi\psi}G_\phi - F_\psi G_{\phi\psi})(F_z G_\phi - F_\phi G_z) - (F_\phi G_\psi - F_\psi G_\phi)(F_{z\psi}G_\phi + F_z G_{\phi\psi} - F_{\phi\psi}G_z - F_\phi G_{z\psi})\big] / (F_z G_\phi - F_\phi G_z)^2.$$

Equation (6.60) shows that both F and G are functions of (z, ϕ, θ, ψ). Their derivatives with respect to (z, ϕ, θ, ψ) can be derived using the chain rule. Substituting (6.62) into (6.53), we can obtain a Hessian matrix which can be used to analyze the stability of the equilibrium configurations as shown in Fig. 6.7. Although the configuration of the payload as shown in Fig. 6.7(a) coincides with its initial configuration as shown in Fig. 6.5, this configuration is obtained by supposing that the payload is suspended with four cables. Hence, the stability analysis of this configuration can be conducted by supposing that the payload is suspended with only four relevant cables. If this configuration under this condition is stable, its corresponding initial configuration should be more stable.

For every equilibrium configuration, the positions of four relevant robots and four relevant attachment points and the center of mass as well as the orientation angles of the payload are know. Substituting all these parameters into (6.62) and then into (6.53), a Hessian matrix is available. The eigenvalues of the Hessian matrix can be easily evaluated by the package Matlab.

Table 6.6 lists the eigenvalues of the Hessian matrices of the four equilibrium configurations as shown in Fig. 6.7. From this table, it can be seen that configurations 1 and 2 are stable. But the other two configurations are unstable.

6.7 Conclusions

Aerial manipulation and transport with multiple aerial robots has many applications. We derived a mathematical model that captures the kinematic constraints and conditions of static equilibrium. We showed how to obtain solutions for the direct kinematics and inverse kinematics, and provided a methodology to analyze the mechanics underlying stable equilibria of the underactuated system. The application of these ideas to multi-quadrotor control and planning are discussed in [3, 13]. Experimental studies of the stability of the system are presented in [11] and conditions for uniqueness of the direct kinematics solution are established in [3].

This line of inquiry has several possible directions of future research. Clearly the general direct kinematics problem is still unsolved, even for the three robot case.

Because the system is under actuated, it is necessary to consider the dynamics of the system to determine the stability of the true dynamical system instead of merely considering the static stability. This has important implications for control. More generally, one can envision cable-actuated parallel manipulators where the anchor point is position controlled in two or three dimensions allowing the payload to be manipulated without spooling cables to change the cable length or requiring mechanical linkages directly attached to the payload.

Acknowledgements The authors gratefully acknowledge the support from NSF grants IIS-0413138, IIS-0427313 and IIP-0742304, ARO Grant W911NF-05-1-0219, ONR Grant N00014-08-1-0696, and ARL Grant W911NF-08-2-0004. The first author was supported in part by the PDF fellowship from the Natural Sciences and Engineering Research Council of Canada (NSERC).

References

1. Bernard, E.: Stability of a towed body. J. Aircr. **35**(2), 197–205 (1998)
2. Carricato, M., Merlet, J.-P.: Direct geometrico-static problem of under-constrained cable-driven parallel robots with three cables. In: Proceedings of 2011 IEEE International Conference on Robotics and Automation (ICRA), 9–13 May 2011, pp. 3011–3017 (2011)
3. Fink, J., Michael, N., Kim, S., Kumar, V.: Planning and control for cooperative manipulation and transportation with aerial robots. Int. J. Robot. Res. **30**(3), 324–334 (2011)
4. Gosselin, C., Lefrançois, S., Zoso, N.: Underactuated cable-driven robots: machine, control and suspended bodies. Adv. Intell. Soft Comput. **83**, 311–323 (2010)
5. Gouttefarde, M., Daney, D., Merlet, J.-P.: Interval-analysis-based determination of the wrench-feasible workspace of parallel cable-driven robots. IEEE Trans. Robot. **5**(1), 1–13 (2010)
6. Henderson, J.F., Potjewyd, J., Ireland, B.: The dynamics of an airborne towed target system with active control. Proc. Inst. Mech. Eng., G J. Aerosp. Eng. **213**, 305–319 (1999)
7. Hunt, K.H.: Kinematic Geometry of Mechanisms. Oxford University Press, London (1978)
8. Jiang, Q., Kumar, V.: The inverse kinematics of 3-D towing. In: Proceedings of the 12th International Symposium: Advances in Robot Kinematics, Piran-Portoroz, Slovenia, June 27–July 1 (2010)
9. Jiang, Q., Kumar, V.: The inverse kinematics of cooperative transport with multiple aerial robots. Conditionally accepted by IEEE Trans. Robot.
10. Jiang, Q., Kumar, V.: The direct kinematics of payloads suspended from cables. In: Proceedings of the ASME 2010 International Design Engineering Technical Conferences & Computers and Information in Engineering Conference DETC2010-28036, Montreal, Quebec, Canada, August 15–18 (2010)
11. Jiang, Q., Kumar, V.: Determination and stability analysis of equilibrium configurations of payloads suspended from multiple aerial robots. ASME J. Mech. Robot. **4**(2), 021005 (2012)
12. Michael, N., Kim, S., Fink, J., Kumar, V.: Kinematics and statics of cooperative multi-robot aerial manipulation with cables. In: Proceedings of the ASME 2009 International Design Engineering Technical Conferences & Computers and Information in Engineering Conference, DETC2009-87677, San Diego, USA, Aug. 30–Sep. 2 (2009)
13. Michael, N., Fink, J., Kumar, V.: Cooperative manipulation and transportation with aerial robots. Auton. Robots **30**(1) (2011)
14. Murray, R.M.: Trajectory generation for a towed cable system using differential flatness. In: IFAC World Congress, San Francisco, CA, July (1996)
15. Oh, S.R., Agrawal, S.K.: A control Lyapunov approach for feedback control of cable-suspended robots. In: Proceedings of the IEEE International Conference on Robotics and Automation, Rome, Italy, April, pp. 4544–4549 (2007)

16. Phillips, J.: Freedom in Machinery, vol. 1. Cambridge University Press, Cambridge (1990)
17. Pohst, M., Zassenhaus, H.: Algorithmic Algebraic Number Theory. Cambridge University Press, Cambridge (1989)
18. Roth, B.: Computations in kinematics. In: Angeles, J., Hommel, G., Kovacs, P. (eds.) Computational Kinematics, pp. 3–14. Kluwer Academic, Dordrecht (1993)
19. Stump, E., Kumar, V.: Workspaces of cable-actuated parallel manipulators. ASME J. Mech. Des. **128**(1), 159–167 (2006)
20. Williams, P., Sgarioto, D., Trivailo, P.: Optimal control of an aircraft-towed flexible cable system. In: Proceedings of the 11th Australian International Aerospace Congress, Melbourne, Mar. 12–17, pp. 1–21 (2005)

Chapter 7
Compliant Mechanisms

Larry L. Howell

7.1 Introduction

Compliant mechanisms[1] gain their motion from the deflection of elastic members. Examples of compliant mechanisms are shown in Fig. 7.1. Because compliant mechanisms gain their motion from the constrained bending of flexible parts, they can achieve complex motion from simple topologies. Traditional mechanisms use rigid parts connected at articulating joints (such as hinges, axles, or bearings), which usually requires assembly of components and results in friction at the connecting surfaces [21, 31, 46]. Because traditional bearings are not practical in many situations (e.g. microelectro-mechanical systems) and lubrication can be problematic, friction and wear present major difficulties. Compliant mechanisms also offer an opportunity to achieve complex motions within the limitations of micro- and nano-fabrication.

Nature provides an example of how to effectively create controlled motion. Most moving components in nature are flexible instead of stiff, and the motion comes from bending the flexible parts instead of rigid parts connected with hinges (for example, consider hearts, elephant trunks, and bee wings). The smaller the specimen, the more likely it is to use the deflection of flexible components to obtain its motion [21].

7.1.1 Advantages of Compliant Mechanisms

Some of the advantages of compliant mechanisms include the following:

[1]This section is based on "Compliant Mechanisms" by L.L. Howell in *Encyclopedia of Nanotechnology*, Editor: B. Bhusham, © Springer, 2012, used with permission.

L.L. Howell (✉)
Brigham Young University, Provo, UT, USA
e-mail: lhowell@byu.edu

J.M. McCarthy (ed.), *21st Century Kinematics*,
DOI 10.1007/978-1-4471-4510-3_7, © Springer-Verlag London 2013

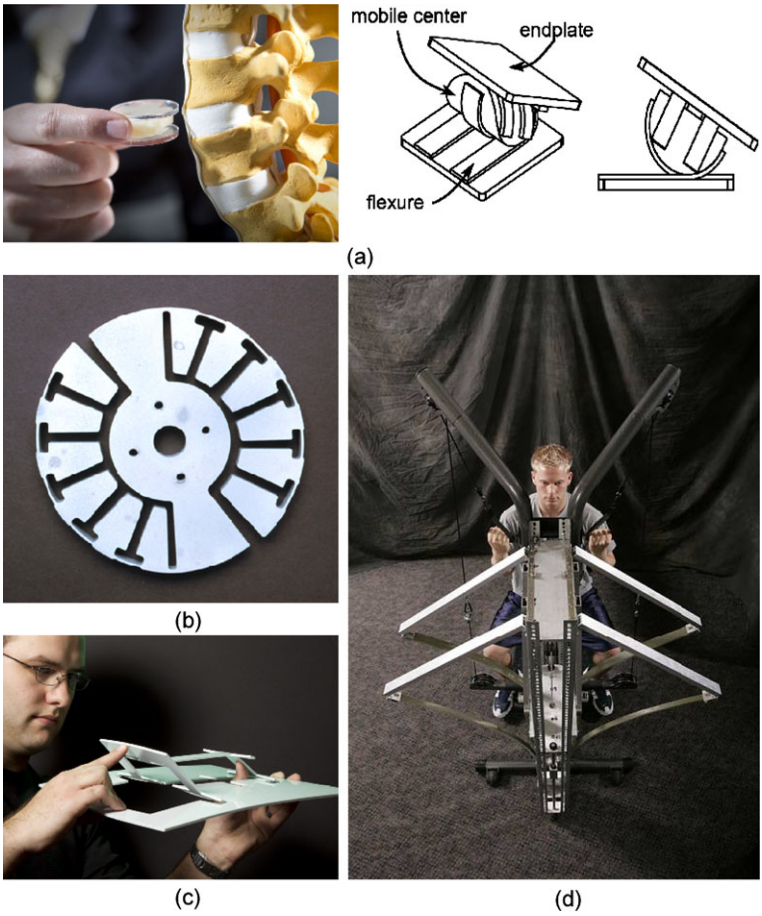

Fig. 7.1 Example compliant mechanisms. (**a**) An artificial spinal disc. (**b**) A compliant centrifugal clutch. (**c**) A lamina emergent mechanism. (**d**) A compliant constant-force exercise machine

Can Be Made From One Layer of Material Compliant mechanisms can be fabricated from a single layer. This makes them compatible with many common microelectromechanical system (MEMS) fabrication methods, such as surface micromachining, bulk micromachining, and LIGA. For example, consider the folded beam suspension shown in Fig. 7.2. This device is often used as a suspension element in MEMS systems. It offers a simple approach for constrained linear motion, and also integrates a return spring function. The device can achieve large deflections with reasonable off-axis stiffness. The compliant mechanism makes it possible to do these functions with a single layer of material.

No Assembly Required Compliant mechanisms that gain all of their motion from the deflection of flexible components are "fully compliant mechanisms," where devices that combine both traditional and compliant elements are called "partially

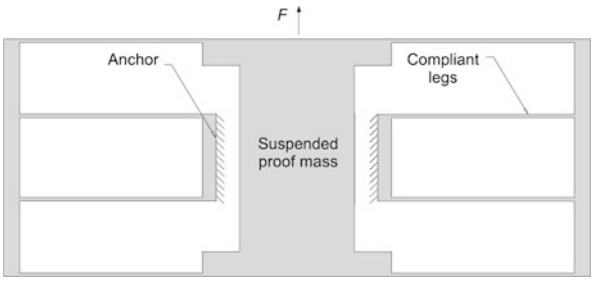

Fig. 7.2 A folded-beam suspension is an example of a widely used compliant mechanism in microelectromechanical systems (MEMS) applications

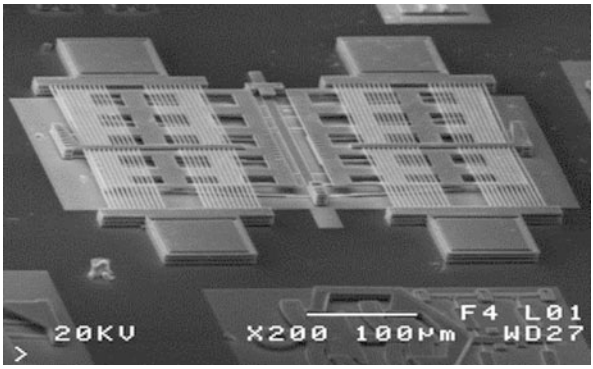

Fig. 7.3 This scanning electron micrograph shows a thermal actuator that uses multiple layers of compliant elements to achieve large amplification with a small footprint

compliant mechanisms". Fully compliant mechanism can usually be fabricated without assembly of different components.

Compact Some compliant mechanisms can also be designed to have a small footprint. Various strategies can be used to decrease the size of a mechanism. Figure 7.3 shows a thermal actuator that uses multiple layers to achieve a small footprint.

Friction-Free Motion Because compliant mechanisms gain their motion from deflection of flexible members rather than from traditional articulating joints, it is possible to reduce or eliminate the friction associated with rubbing surfaces. This results in reduced wear and eliminates the need for lubrication, as described next.

Wear-Free Motion Wear can be particularly problematic in biomedical applications, precision mechanisms, and at small scales. The elimination of friction can result in the elimination of wear at the connecting surfaces of joints. For devices that are intended to undergo many cycles of motion, eliminating friction can dramatically increase the life of the system.

No Need for Lubrication Another consequence of eliminating friction is that lubricants are not needed for the motion. This is particularly important in biomedical implants, space applications, and at small scales where lubrication can be problematic.

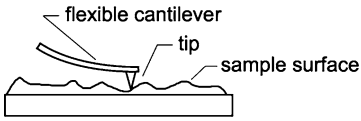

Fig. 7.4 The cantilever of an atomic force microscope (AFM) is an example of compliance employed in high precision instruments

High Precision Flexures have long been used in high precision instruments because of the repeatability of their motion. Some reasons for compliant mechanisms precision are the backlash-free motion inherent in compliant mechanisms and the wear-free and friction-free motion described above. The cantilever associated with an atomic force microscope (Fig. 7.4) is an example application.

Integrated Functions Like similar systems in nature, compliant mechanisms have the ability to integrate multiple functions into few components. For example, compliant mechanisms often provide both the motion function and a return-spring function. Thermal actuators are another example of integration of functions, as described later.

High Reliability The combination of highly constrained motion of compliant mechanisms and wear-free motion result in high reliability of compliant mechanisms.

7.1.2 Challenges of Compliant Mechanisms

Compliant mechanisms have many advantages, but they also have some significant challenges. A few of these are discussed below [21]:

Limited Rotation One drawback of compliant mechanisms is that most are unable to undergo continuous rotation. Also, if a fully compliant mechanism is constructed from a single layer of material, then special care has to be taken to ensure that moving segments of the compliant mechanism do not collide with other segments of the same mechanism.

Dependence on Material Properties The performance of compliant mechanisms is highly dependent on the material properties, which are not always well known.

Nonlinear Motions The deflections experienced by compliant mechanisms of-ten extend beyond the range of linearized beam equations. This can make their analysis and design more complicated.

Fatigue Analysis Because most compliant mechanisms undergo repeated loading, it is important to consider the fatigue life of the device. An understanding of how to achieve controlled compliant mechanism motion and the associated stresses,

makes it possible to design compliant mechanisms with the desired fatigue life. Interestingly, because of the types of materials used and their purity, many MEMS compliant mechanisms will either fail on their first loading cycle or will have infinite fatigue life. Because of the low inertia of MEMS devices, it is often easy to quickly test a MEMS device to many millions of cycles. Factors such as stress concentrations, the operating temperature, and other environment conditions can affect the fatigue life.

Difficult Design Integration of functions into fewer components, nonlinear displacements, dependence on material properties, the need to avoid self collisions during motion, and designing for appropriate fatigue life, all combine to make the design of compliant mechanisms nontrivial and often difficult.

7.1.3 Analysis and Design of Compliant Mechanisms

Multiple approaches are available for the analysis and design of compliant mechanisms. Three of the most developed approaches are described below.

7.1.3.1 Finite Element Analysis

Finite element methods are the most powerful and general methods available to analyze compliant mechanisms. Commercial software is currently available that has the capability of analyzing the large, nonlinear deflections often associated with compliant mechanisms. The general nature of the method makes it applicable for a wide range of geometries, materials, and applications. Increasingly powerful computational hardware has made it possible to analyze even very complex compliant mechanisms. It is also possible to use finite element methods in the design of compliant mechanisms, particularly once a preliminary design has been determined. But in the early phases of design, other methods (or hybrid methods) are often preferred so that many design iterations can be quickly analyzed.

7.1.3.2 Topology Optimization

Suppose that all that is known about a design is the desired performance and design domain. Topology optimization shows promise for designing compliant mechanisms under such conditions. The advantage is that very little prior knowledge about the resulting compliant mechanism is needed, and any biases of the designer are eliminated [10]. Topology optimization is often integrated with finite element methods to consider many possible ways of distributing material with the design domain. This has the potential to find designs that would not otherwise be discovered by other methods. Infinite possible topologies are possible and finite element

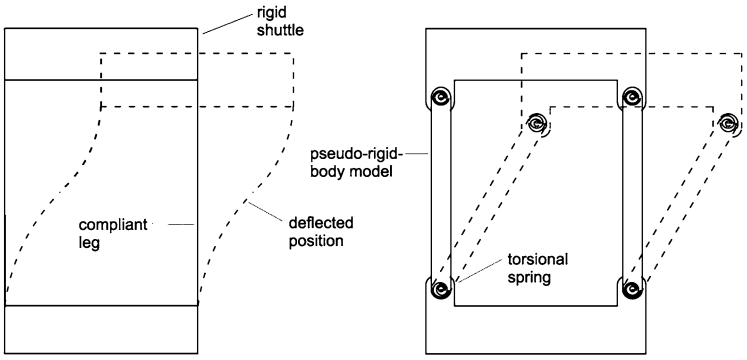

Fig. 7.5 The pseudo-rigid-body model of the compliant parallel-guiding mechanism consists of appropriately located pin joints and torsional springs. (This device is a building block of other devices, such as the folded-beam suspension)

methods can be employed to evaluate the different possibilities. The resolution of the design domain mesh can be a limiting factor, but once a desirable topology is identified, it can be further refined using other approaches.

7.1.3.3 Pseudo-Rigid-Body Model

The pseudo-rigid-body model is used to model compliant mechanisms as traditional rigid-body mechanisms, which opens up the possibility of using the design and analysis methods developed for rigid-body mechanisms in the design of compliant mechanisms [10]. With the pseudo-rigid-body model approach, flexible parts are modeled as rigid links connected at appropriately placed pins, with springs to represent the compliant mechanisms resistance to motion. Extensive work has been done to develop pseudo-rigid-body models for a wide range of geometries and loading conditions. Consider a simple example. The mechanism shown in Fig. 7.5 has a rigid shuttle that is guided by two flexible legs. (Note that the folded-beam suspension in Fig. 7.2 has four of these devices connected in series and parallel.) The pseudo-rigid-body model of the mechanism models the flexible legs as rigid links connected at pin joints with torsional springs. Using appropriately located joints and appropriately sized springs, this model is very accurate well into the nonlinear range. For example, if the flexible legs are single walled carbon nanotubes, comparisons to molecular simulations have shown the pseudo-rigid-body model to provide accurate results [18]. The advantages of the pseudo-rigid-body model are realized during the early phases of design where many design iterations can be quickly evaluated, traditional mechanism design approaches can be employed, and motions can be easily visualized.

The pseudo-rigid-body model approach is described in more detail in the following section. When the configuration of a compliant device is already known, nonlinear finite element analysis may be used to analyze its behavior. However, if instead

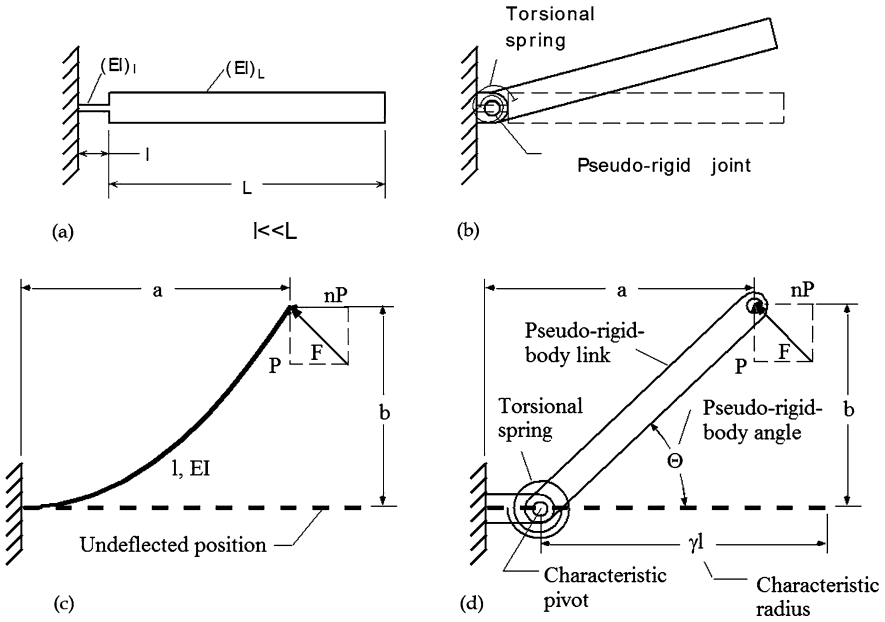

Fig. 7.6 Examples of flexible segments and their pseudo-rigid-body models. (**a**) A small-length flexural pivot, (**b**) its pseudo-rigid-body model, (**c**) a fixed-pinned segment, (**d**) its pseudo-rigid-body model

of knowing the device configuration, all that is known is the task that must be performed and the configuration and dimensions must be synthesized, then nonlinear finite element analysis alone is not a realistic approach because of the many iterations and computation required. Recently, the pseudo-rigid-body model has been developed for the analysis and design of compliant mechanisms. The pseudo-rigid-body model concept analyzes large-deflection beams as rigid links with appropriately placed pin joints and torsional springs. The result is that an otherwise complicated compliant mechanism may be modeled as a rigid-link mechanism. This unification of compliant mechanism theory and traditional rigid-link mechanism theory allows the vast amount of knowledge available for the design of rigid-link mechanisms to be applied to compliant mechanisms.

Individual Flexible Segments Pseudo-rigid-body models have been developed for various types of compliant segments, two of which will be reviewed here.

Small-Length Flexural Pivots [20] The simplest segment is the small-length flexural pivot. Consider a flexible segment that has a much smaller length than the more rigid section, as illustrated in Fig. 7.6(a). The motion of the end of the beam is due to elastic deflection of the flexible segment, which is amplified by the rigid-body rotation of the rigid segment. This motion can be modeled by a pin joint located at the center of the flexible segment, as shown in Fig. 7.6(b). The resistance to motion

is modeled by a torsional spring. The length of the pseudo-rigid link, r, is

$$r = L + \frac{l}{2}, \tag{7.1}$$

where l is the length of the flexible segment and L is the length of the rigid segment. The value of the torsional spring constant, K, is

$$K = \frac{EI}{l}, \tag{7.2}$$

where E is the Youngs modulus, and I is the area moment of inertia. This model is quite accurate for large deflections for cases where L is much greater than l.

Fixed-Pinned Segment [19] A long, flexible, cantilever beam with a force at the free end is shown in Fig. 7.6(c). The end of the beam follows a path that is very nearly circular for a very large deflection. This implies that the deflection can be accurately modeled by two rigid links pinned at the center of the circular path. Figure 7.6(d) shows the pseudo-rigid-body model for the beam. The location of the characteristic pivot is defined by the nondimensional "characteristic radius factor," γ. The length of the pseudo-rigid link, r, is

$$r = \gamma l. \tag{7.3}$$

The resistance to deflection is modeled by a torsional spring with a torsional spring constant, K, of

$$K = \gamma K_\Theta \frac{EI}{l}. \tag{7.4}$$

The deflections of the beam are now easily calculated. The vertical deflection, b, is

$$b = \gamma l \sin \Theta, \tag{7.5}$$

where Θ is the angle of the pseudo-rigid-link. The horizontal deflection, a, is

$$a = l(1 - \gamma) \cos \Theta. \tag{7.6}$$

Typical values of K_γ and Θ are 0.85 and 2.65, respectively. The boundary conditions for the fixed-pinned beam described earlier are one end fixed (force and moment reactions), and the other end pinned (force reactions only).

Other Segments Pseudo-rigid-body models have been developed for other types of segments, including fixed-guided segments, functionally binary pinned-pinned segments, beams loaded with a moment at the end, and beams with follower loads.

Mechanisms. The real power of the pseudo-rigid-body model for individual segments is realized when they are applied to compliant mechanisms that contain such elements. For example, consider the compliant bistable mechanism illustrated in

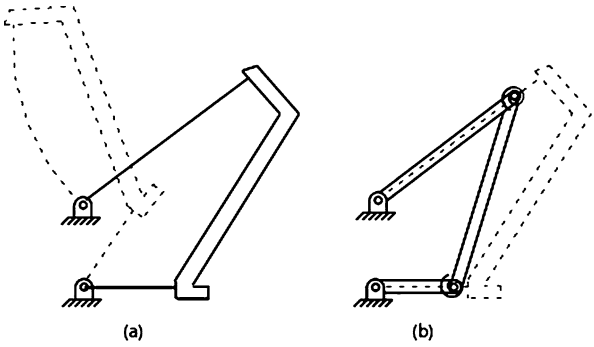

Fig. 7.7 (**a**) A bistable compliant mechanism and (**b**) its pseudo-rigid-body model

Fig. 7.7(a). Since the flexible segments have the geometry and boundary conditions of the fixed-pinned segment discussed earlier, they can be modeled using the pseudo-rigid-body model for that segment. The resulting pseudo-rigid-body model for the mechanism is shown in Fig. 7.7(b). This mechanism will be discussed in more detail as an example.

Example model. Consider a brief example for the compliant, micro, bistable mechanism illustrated in Fig. 7.7(a) [29]. Its corresponding pseudo-rigid-body model is shown in Fig. 7.7(b). The torsional spring constants are calculated from the geometry and material properties. The potential energy, V, for the mechanism is

$$V = \frac{1}{2}(K_2\psi_2 + K_3\psi_3), \tag{7.7}$$

where K_i is the spring constant for joint i, and

$$\psi_2 = (\theta_2 - \theta_{20}) - (\theta_3 - \theta_{30}) \quad \text{and} \quad \psi_3 = (\theta_4 - \theta_{40}) - (\theta_3 - \theta_{30}) \tag{7.8}$$

and θ_i is the angle of link i, which can be found using traditional kinematic analysis. The input torque, M_2, is

$$M_2 = \frac{dV}{d\theta_2} = K_2\psi_2(1 - h_{32}) + K_3\psi_3(h_{42} - h_{32}), \tag{7.9}$$

where

$$h_{32} = \frac{r_2\sin(\theta_4 - \theta_2)}{r_3\sin(\theta_3 - \theta_4)} \quad \text{and} \quad h_{42} = \frac{r_2\sin(\theta_3 - \theta_2)}{r_4\sin(\theta_4 - \theta_3)}. \tag{7.10}$$

The second derivative of the potential energy (the stiffness) is

$$\begin{aligned}\frac{d^2V}{d\theta_2^2} &= K_2\left(1 - 2h_{32} + h_{32}^2 - \psi_2 h'_{32}\right) \\ &\quad + K_3\left[h_{42}^2 - 2h_{42}h_{32} + h_{32}^2 + \psi_3\left(h'_{42} - h'_{23}\right)\right],\end{aligned} \tag{7.11}$$

where

$$h'_{32} = \frac{dh_{32}}{d\theta_2} = \frac{r_2}{r_3}\left[\frac{\cos(\theta_4 - \theta_2)}{\sin(\theta_3 - \theta_4)}(h_{42} - 1) - \frac{\sin(\theta_4 - \theta_2)\cos(\theta_3 - \theta_4)}{\sin^2(\theta_3 - \theta_4)}(h_{32} - h_{42})\right], \tag{7.12}$$

$$h'_{42} = \frac{dh_{42}}{d\theta_2} = \frac{r_2}{r_4}\left[\frac{\cos(\theta_3 - \theta_2)}{\sin(\theta_3 - \theta_4)}(h_{32} - 1) - \frac{\sin(\theta_3 - \theta_2)\cos(\theta_3 - \theta_4)}{\sin^2(\theta_3 - \theta_4)}(h_{32} - h_{42})\right]. \tag{7.13}$$

The potential energy curve (equation (7.9)), the required crank torque (equation (7.11)), and the second derivative of potential energy (equation (7.13)) are particularly useful in defining the mechanism behavior. The input torque is zero at points of relative minimum (stable equilibrium position) or maximum (unstable equilibrium) potential energy. The global minimum of potential energy occurs when the mechanism is in its undeflected position. This position is shown in solid lines in Fig. 7.7(a). The second stable equilibrium position has some energy stored but is a local minimum of potential energy and therefore is a stable equilibrium position. The energy stored is evident in the deflected member shown in dashed lines in Fig. 7.7(a).

7.2 Example Compliant Mechanism Research Areas

There are many active research topics in compliant mechanisms and new areas continue to be discovered. A subset of topics is mentioned here and then three examples are discussed in more depth. Compliant mechanism design methods have been an important area of research. This includes optimization methods [10, 11, 23, 27, 43, 45, 48, 50, 56], design of precision flexures [6, 16, 17, 31, 46, 54], building blocks [30], and the pseudo-rigid-body model approach discussed previously. Classes of compliant mechanisms studied include multistable mechanisms [4, 5, 28, 33, 41], metamorphic mechanisms [8, 9, 52], contact-aided compliant mechanisms [3, 13, 34, 35], compliant joints [40, 49, 55], medical devices [7, 36], origami inspired mechanisms [12] and statically balanced mechanisms [14, 42]. Analysis of nonlinear deflections [2, 15] and dynamics of compliant mechanisms [51, 53] are two of many analysis topics under study. Three examples of compliant mechanism research areas are provided next, including microelectromechanical systems (MEMS), biomedical implants, and lamina emergent mechanisms.

7.2.1 Microelectromechanical Systems (MEMS)

Compliant mechanisms[2] are well suited for application at the micro scale. The fact that they can be fabricated from a single layer makes them compatible with many

[2]This section is based on Compliant Mechanisms, by L.L. Howell in *Encyclopedia of Nanotechnology*, Editor: B. Bhusham, Springer, 2012, used with permission.

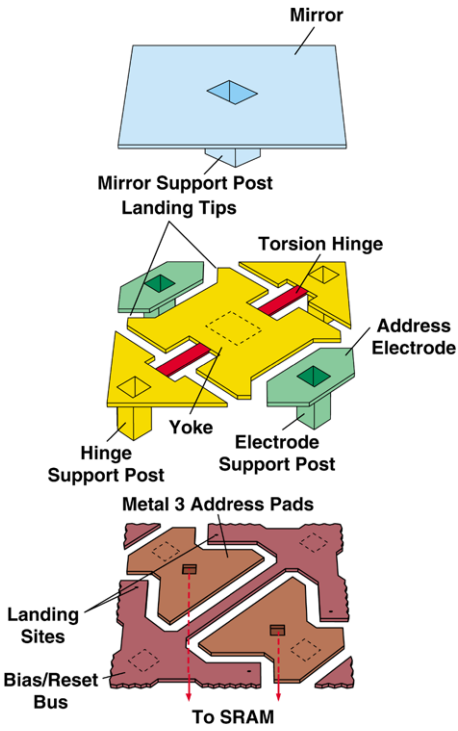

Fig. 7.8 Texas Instruments Digital Micromirror Device (DMD™) uses compliant torsion hinges to facilitate mirror motion. (Illustration courtesy of Texas Instruments)

MEMS fabrication methods. The elimination of assembly and friction is also important for micro devices. Examples of MEMS compliant mechanisms are shown here to illustrate their properties and to demonstrate a few applications.

Digital Micromirrors One of the most visible commercially available microelectromechanical systems is Texas Instruments Digital Micromirror Device (DMD™) which is used in applications such as portable projectors. The DMD is a rectangular array of moving micromirrors that is combined with a light source, optics, and electronics to project high quality color images. Figure 7.8 shows the architecture of a single DMD pixel. A 16 micrometer square aluminum mirror is rigidly attached to a platform (the "yoke"). Flexible torsion hinges are used to connect the yoke to rigid posts. An applied voltage creates an electrostatic force that causes the mirror to rotate about the torsion hinges. When tilted in the on position, the mirror directs light from the light source to the projection optics and the pixel appears bright. When the mirror is tilted in the off position, the light is directed away from the projection optics and the pixel appears dark. The micromirrors can be combined in an array on a chip, and each micromirror is associated with the pixel of a projected image. The torsion hinges use compliance to obtain motion while avoiding rubbing parts that cause friction and wear. The hinges can be deflected thousands of times per second and infinite fatigue life is essential.

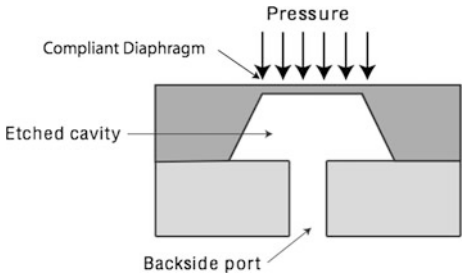

Fig. 7.9 The strain on a compliant diaphragm of a piezoresistive pressure sensors results in a detectable change in resistance, which is correlated with the pressure

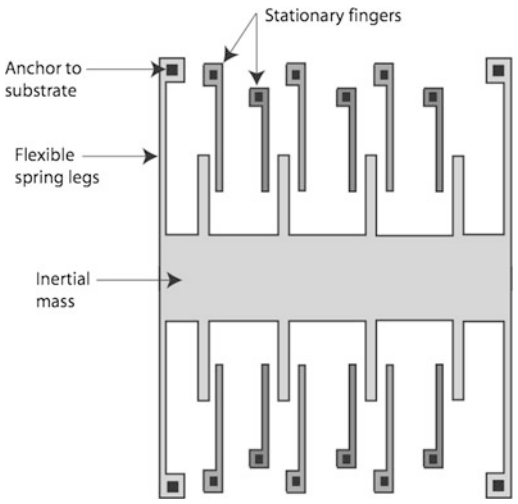

Fig. 7.10 This accelerometer makes use of compliant legs that deflect under inertial loads. The deflection results in a detectable change in capacitance and is correlated with the corresponding acceleration

Piezoresistive Pressure Sensors A sensor is a device that responds to a physical input (such as motion, radiation, heat, pressure, magnetic field), and transmits a resulting signal that is usually used for detection, measurement, or control. Advantages of MEMS sensors are their size and their ability to be more closely integrated with their associated electronics. Piezoresistive sensing methods are among the most commonly employed sensing methods in MEMS. Piezoresistance is the change in resistivity caused by mechanical stresses applied to a material. Bulk micromachined pressure sensors have been commercially available since the 1970s. A typical design is illustrated in Fig. 7.9. A cavity is etched to create a compliant diaphragm that deflects under pressure. Piezoresistive elements on the diaphragm change resistance as the pressure increases; this change in resistance is measured and is correlated with the corresponding pressure.

Capacitive Acceleration Sensors Accelerometers are another example of commercially successful MEMS sensors. Applications include automotive airbag safety systems, mobile electronics, hard drive protection, gaming, and others. Figure 7.10 illustrates an example of a surface micromachined capacitive accelerometer. Acceleration causes a displacement of the inertial mass connected to the compliant suspension, and the capacitance change between the comb fingers is detected.

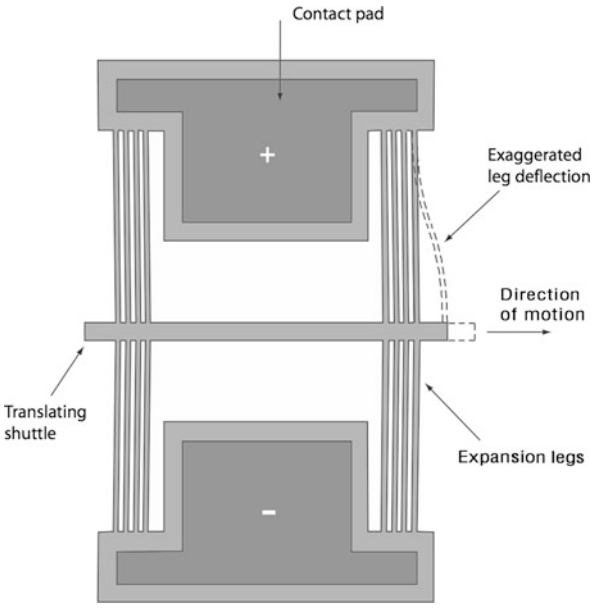

Fig. 7.11 A schematic of a thermomechanical in-plane microactuor (TIM) that uses compliant expansion legs to amplify the motion caused by thermal expansion

Thermal Actuators A change in temperature causes an object to undergo a change in length, where the change is proportional to the material coefficient of thermal expansion [22]. This length change is usually too small to be useful in most actuation purposes. Therefore, compliant mechanisms can be used to amplify the displacement of thermal actuators. Figure 7.11 illustrates an example of using compliant mechanisms to amplify thermal expansion in microactuators. Figure 7.12 shows a scanning electron micrograph of a Thermomechanical In-plane Microactuator (TIM) illustrated in Fig. 7.11. It consists of thin legs connecting both sides of a center shuttle. The leg ends not connected to the shuttle are anchored to bond pads on the substrate and are fabricated at a slight angle to bias motion in the desired direction. As voltage is applied across the bond pads, electric current flows through the thin legs. The legs have a small cross sectional area and thus have a high electrical resistance, which causes the legs to heat up as the current passes through them. The shuttle moves forward to accommodate the resulting thermal expansion. Advantages of this device include its ability to obtain high deflections and large forces, as well as its ability to provide a wide range of output forces by changing the number of legs in the design.

7.2.2 Biomedical Compliant Mechanisms

Compliant mechanisms are well suited for application in biomedical applications because of their low wear, the ability to be fabricated of biocompatible materials,

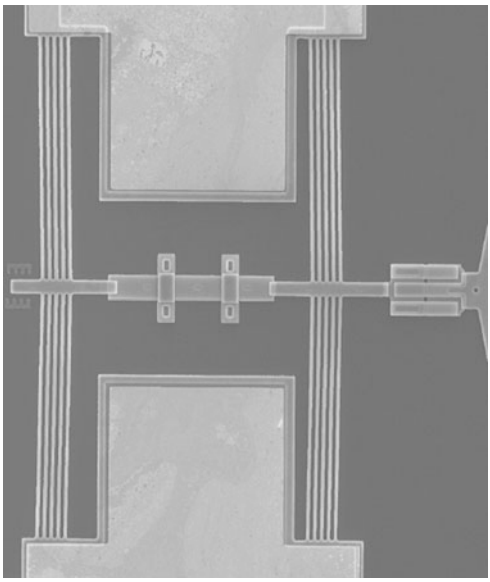

Fig. 7.12 A scanning electron micrograph of a thermal actuator illustrated in Fig. 7.11

and their compactness. There are many possible research areas and applications, and one implant is described here as a illustrative example.

The design objective of the spinal implant is to restore healthy physiologic biomechanics to the degenerated spinal segment. Because the healthy motion and the degree of mechanical dysfunction of the spine varies significantly from person to person [37, 39], the device is tailorable to the needs of the patient via surgeon-selectable inserts. There may also be therapeutic benefits to intentional adjustment of the devices stiffness to induce and support remodeling of the surrounding tissue architecture [44]. This example discusses the design and validation of a spinal implant capable of nonlinear stiffness and adjustability, including analytical and numerical models, benchtop, and cadaveric testing results.

Example Implant Design A compliant mechanism[3] was designed as a spinal implant to share load with a damaged or diseased intervertebral spinal disc, as shown in Fig. 7.13.

The baseline configuration of the spinal implant is based on the lamina emergent torsional (LET) joint [47]. The LET geometry offers advantages in terms of manufacturability and independently controlled flexibility in multiple directions [24, 25]. The device consists of a LET joint that has been split into two parts that are independently attached to the vertebral pedicles. The vertebra themselves act as semirigid connections between the two parts of the LET joint. The attachment to the vertebral pedicles is accomplished via pedicle screws. Each half of the baseline device

[3]This section is based on "Spinal Implant Development, Modeling, and Testing to Achieve Customizable and Nonlinear Stiffness" by E. Dodgen, E. Stratton, A.E. Bowden, L.L. Howell, in *Journal of Medical Devices*, vol. 6, doi:10.1115/1.4006543, 2012. Used with kind permission © ASME.

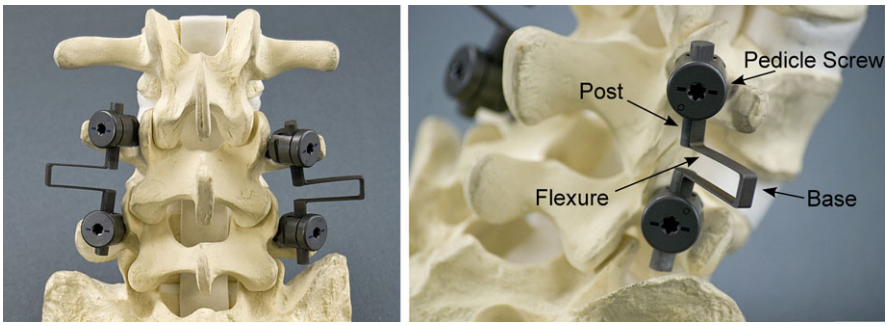

Fig. 7.13 Prototype of the baseline configuration

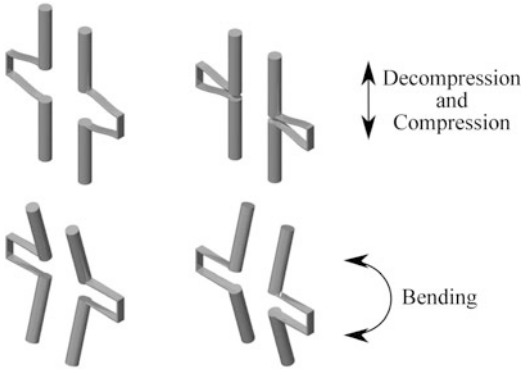

Fig. 7.14 Deflected positions of the baseline configuration

configuration is composed of two attachment posts, two flexures, and a central connecting beam. The two flexures and the central connecting beam form a C-shape. The bilateral components are positioned on either side of the two vertebral bodies to which they are attached. Optional inserts adjust the force-deflection response of the flexures to meet the target spinal kinetic response deemed appropriate for the individual patient. Figure 7.14 shows the baseline configuration deflected in the two modes of loading for which it was designed.

The optional contact-aided insert design is configured as two parts which connect together and attach to the central connecting beams of the baseline device. The elliptical contact surfaces of the inserts are designed such that as the flexures of the baseline configuration deflect during spinal motion, they come into contact with the surfaces, altering the force deflection relationship in a controlled and specific manner, as shown in Figs. 7.15 and 7.16.

Through alteration of the elliptical parameters for the contact surfaces, the insert can be modified to provide a wide range of variability in stiffness. The intended use is for clinicians to select the desired insert configurations appropriate to the patient pathology. If the response of the implant needs to be modified due to changes in the patient pathology, then the insert can be replaced without changes to the pedicular attachment sites. Figure 7.17 displays a prototype of the insert and how it attaches to

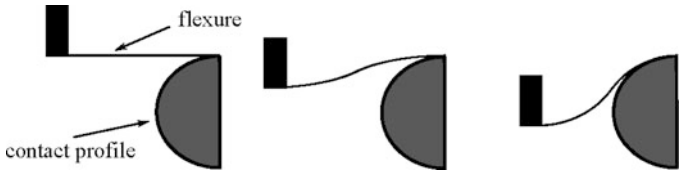

Fig. 7.15 Contact-aided flexure shown deflected on a circular contact profile

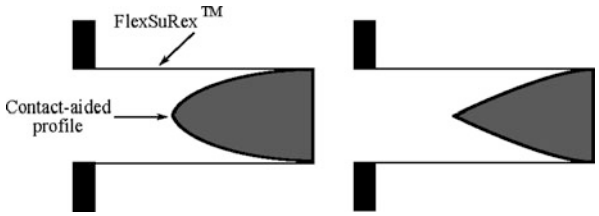

Fig. 7.16 Contact-aided flexure and two different contact profiles

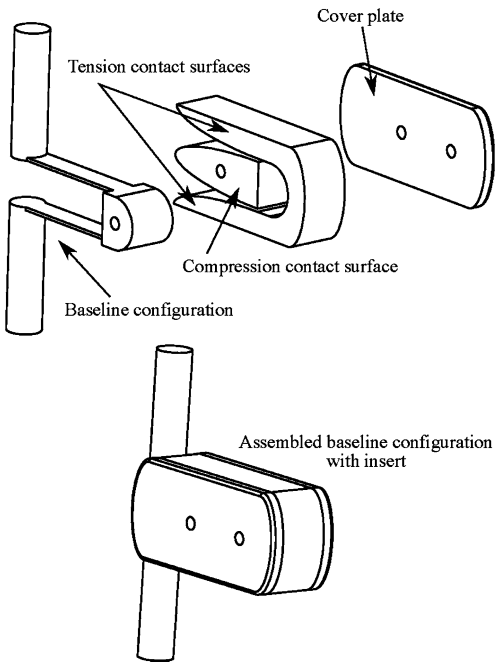

Fig. 7.17 Contact-aided attachment for baseline configuration

the baseline configuration of the implant. The dimensions of the baseline configuration and the semimajor a and semiminor b axes of the elliptic surfaces are shown in Fig. 7.18. The surfaces of the insert are positioned such that the flexures come into contact with them as the device is pulled in tension (i.e., during flexion and during contralateral bending) or compressed (i.e., during extension and during ipsi-

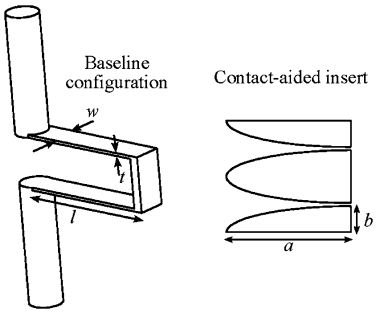

Fig. 7.18 Baseline configuration with contact surface dimensions defined

lateral bending). The elliptical geometry of the insert used in conjunction with the flexures geometry defines the stiffness of the implant. The ideal design performance of the device was evaluated using analytical modeling, finite element modeling, and benchtop testing of prototypes.

7.2.3 Lamina Emergent Mechanisms (LEMS)

Lamina emergent mechanisms (LEMs)[4] are mechanical devices fabricated from planar materials (laminae) with motion that emerges out of the fabrication plane. They achieve their motion from the deflection of flexible members (and are therefore compliant mechanisms [21]) and are monolithic within each planar layer. The attraction of LEMs lies in their potential to perform sophisticated mechanical tasks with simple topology. The ability to fabricate them from planar layers of material makes it possible to pursue manufacturing using simplified processes common to sheet materials. Thus, LEMs offer the potential for high performance, compact devices that can be fabricated at low manufacturing cost, but with the tradeoff of challenging design issues. The development of fundamental principles in LEMs has the potential to release a flood of new LEM applications [26]. Consider some generic examples of LEMs. Figure 7.19(a) shows a pantograph mechanism (a multidegree-of-freedom device used for scaling force or motion) and Fig. 7.19(b) shows a multistage mechanism. Plan views of the devices are shown on the left and prototypes on the right. Figure 7.20(a) is a scanning electron micrograph of a rigid-link, three-degrees-of-freedom micromechanism[32] that is fabricated using planar layers of material and has motion out of the plane. A compliant counterpart is shown in Fig. 7.20(b).

[4]This section is based on "Lamina Emergent Mechanisms and Their Basic Elements," by J.O. Jacobsen, B.G. Winder, L.L. Howell, and S.P. Magleby, *Journal of Mechanisms and Robotics*, vol. 2, No. 1, 011003-1 to 011003-9, 2010. Used with kind permission © ASME.

7.2.3.1 Advantages of LEMs

The interest in LEMs comes from the advantages inherent in their nature: being fabricated in a plane, having a flat initial state, and being monolithic. Each of these characteristics and its associated advantages are briefly described below.

Fabricated in a Plane The fact that LEMs can be fabricated from planar layers influences both what processes can be used for their manufacture and what materials may be used in their construction. The use of low-cost, high-quality sheet goods has the potential to dramatically reduce cost for high-volume production. At the microlevel, LEMS can be fabricated using single-layer MEMS fabrication methods and materials, which offers significant cost and reliability advantages. It also provides opportunities for complex out-of-plane motion with only a single layer.

At the macrolevel, manufacturing processes used to make static structures or components for assembly can be used to create mechanisms capable of sophisti-

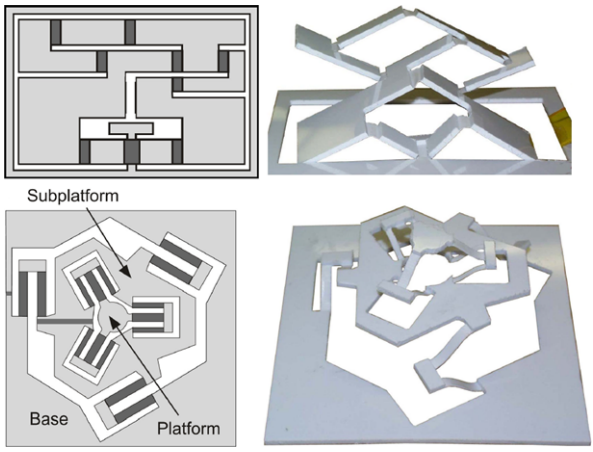

Fig. 7.19 Examples of LEMs, including (**a**) a pantograph mechanism, and (**b**) a multiple stage platform. In both (**a**) and (**b**) the darker sections in the schematics are flexible elements. The pictures on the right are polypropylene models

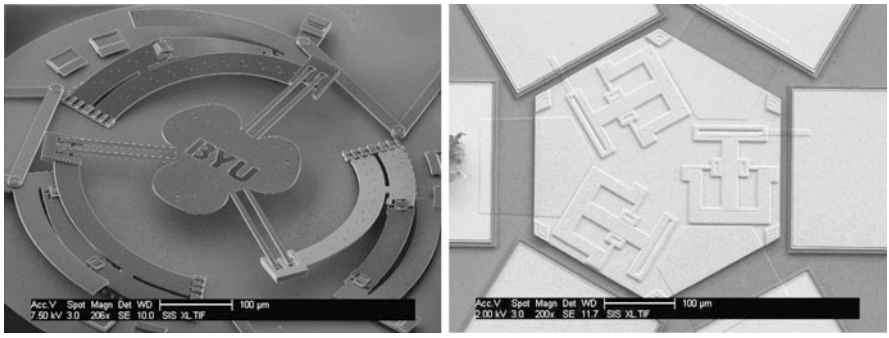

Fig. 7.20 Scanning electron micrographs (SEMs) of (**a**) a rigid-link three-degrees-of-freedom microplatform made using multiplelayers, and (**b**) a compliant counterpart

cated motions and complex tasks. Example processes include stamping, fine blanking, laser cutting, water jet cutting, plasma cutting, and wire electrical discharge machining (EDM). Some of these processes, such as stamping, offer significant cost advantages for high-volume production.

Flat Initial State The potential for many LEMs to have a flat initial state provides opportunities for extreme compactness. Compact mechanisms are particularly attractive in applications with highly constrained space. Another advantage is found in applications where it is important for the device to be compact during transport and then deployed when at its location of operation. An obvious advantage of a flat initial state is compact packaging and shipping, which can mean a significant reduction in the cost of handling, storing, and shipping high volumes of devices.

Not all LEMs will be flat after fabrication because some may be shaped using the same processes used to create the mechanism (e.g., stamping operations). There is also the possibility of using residual stresses in MEMS processes to move the after-fabricated position out of plane. But the nonflat mechanisms still have the characteristic of being monolithic, which is discussed next.

Monolithic The single-piece, or monolithic, nature of LEMs brings with it many of the characteristics of compliant mechanisms in general. The creation of controlled motion without pin joints provides opportunities for increased precision because of the elimination of backlash and wear. Weight can be reduced by using compliant mechanisms, and friction between rubbing parts can be reduced or eliminated. While multilayer LEMs require assembly, for monolithic devices, assembly of mechanism parts is often unnecessary.

7.2.3.2 Challenges of Lamina Emergent Mechanism Design

Taking advantage of the benefits of lamina emergent mechanisms often requires overcoming their inherent challenges. First, the desired motions are often too large to be modeled using linearized equations such as those commonly used in beam equations or linear finite element analysis. Thus, any successful modeling approach must be capable of addressing the intrinsic nonlinearities of the problem. Second, there are singularities inherent in LEM analysis because of the planar nature of the fabricated position. LEMs are change-point mechanisms in their fabricated state, and multiple motions are possible for a given input. Third, unlike those in rigid-body mechanisms, the motions in LEMs are highly coupled with stress, fatigue, and energy stored in a system.

By leveraging the unique performance and cost-saving characteristics possible with LEMs, many innovations become possible. Improvements can be made to existing products, and new products with unprecedented performance can be created. Products that were economically impractical with other technologies could become viable in a competitive marketplace with LEM technology.

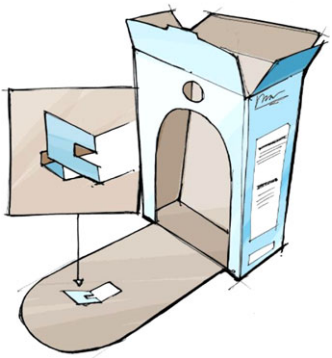

Fig. 7.21 Cereal boxes and other packaging could be used to create entertaining games for children

7.2.3.3 Potential Applications of LEMs

Various categories of opportunities[5] are enabled by combining the advantages of the different functional characteristics of LEMs. Descriptions of these opportunities are below.

Disposable Mechanisms By using low-cost, planar manufacturing techniques to create mechanisms with little or no assembly required, production of LEMs can be very inexpensive. Flat initial states can further reduce costs through compact shipping. Such low-cost mechanisms could be considered disposable.

There are many possible applications for disposable LEMs. Sterile products could use emerging packaging so that opening the packaging causes a motion to present the non-sterile end to the user for easy removal. Cereal boxes and other cardboard packaging could have LEMs that emerge into entertaining games for children (see Fig. 7.21).

Radio frequency identification is becoming more common in credit cards, allowing users to complete transactions more quickly and easily. However, this can also be a source for identity theft by scanning a card in someones pocket. A LEM could be used as a credit card Faraday cage to cover the chip until the device is deployed for use (see Fig. 7.22). Alternatively, the receiving or signaling circuits could remain open until the user actuates a LEM to make electrical contact during a credit card transaction. The low cost of these devices allows companies to continue mailing credit card offers that are often viewed as disposable.

Novel Arrays An array in this context is defined as a patterned arrangement, normally in rows and columns. LEMs that are composed of an array of mechanisms

[5]This section is based on "Identifying Potential Applications for Lamina Emergent Mechanisms Using Technology Push Product Development," by N.B. Albrechtsen, S.P. Magleby, and L.L. Howell, in *Proceedings of the ASME International Design Engineering Technical Conferences*, Montreal, Quebec, Aug. 15–18, 2010, DETC2010-28531, used with permission. Used with kind permission © ASME.

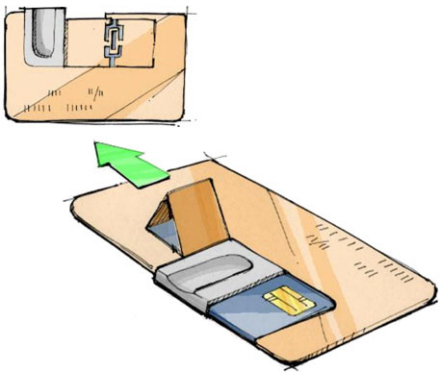

Fig. 7.22 A LEM used as a Faraday cage to cover the radio frequency identification chip on credit cards to prevent identity theft

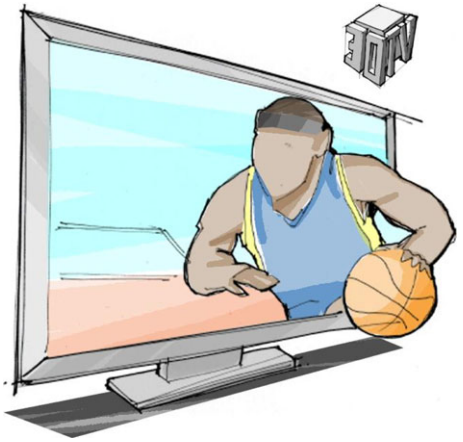

Fig. 7.23 A television where each pixel is a LEM, creating a moving, three-dimensional image

could benefit from all three functional characteristics. If a large array with many mechanisms required manual assembly, the labor costs associated with production might preclude that product from becoming economically viable. By using a stamping process, eliminating assembly through compliance, and transporting compactly in the flat initial state, price can be reduced significantly. LEMs may enable many novel arrays that were previously cost prohibitive.

LEMs that use arrays are perhaps the largest group of potential applications for the technology. A LEM printed circuit board could integrate a qwerty key-board with its underlying circuitry into a single piece device. A television screen in which each pixel could emerge from the viewing plane would create a more realistic three dimensional experience (see Fig. 7.23). A similar array could be used to give tactile responses to users in a virtual reality environment.

LEM arrays would experience widespread use if applied to electricity generation. Energy could be harvested from urban pedestrian traffic, wind, waves, or highway pavement compression.

Creating an array of small surfaces that can be oriented to face in different directions would be useful in many application areas. A guided LEM solar array would

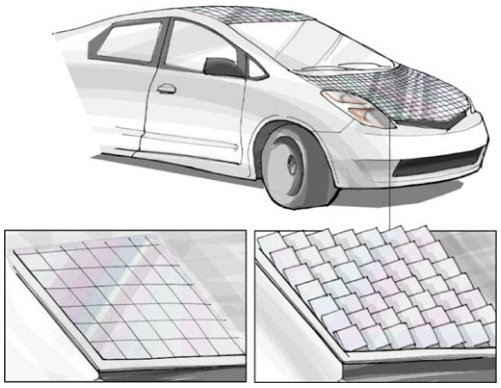

Fig. 7.24 A guided array of solar panels mounted on a vehicle

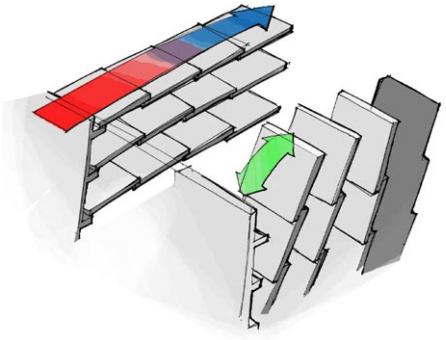

Fig. 7.25 Using LEMs, heat fins could be reconfigured into insulation, allowing a dynamic thermal resistance

dramatically reduce the bulk of current solar trackers, perhaps allowing them to be mounted on the surfaces of vehicles or buildings (see Fig. 7.24). A directional array could be used to reflect, combine, and diffract various media such as waves, signals, or light. A directional array could create dynamic acoustics, radar-diverting stealth surfaces, improved satellites, or artistic lighting effects. The mechanism would even have the ability provide a variable surface texture. This might be used to manipulate drag characteristics for guiding projectiles, create air resistance for rapid braking, or regulate flow rates in pipes. It could also be used to change the traction of contact surfaces.

LEM arrays could become powerful tools to influence thermal properties. By stacking layers of LEMs, a kinetic insulation could be possible. Deploying the mechanisms would increase the amount of air contained in the insulation, thereby increasing the thermal resistance. This is advantageous over existing kinetic insulations because it only requires a simple mechanical input instead of pressurization [38]. The layers of LEM insulation could even be reconfigured into heat fins, converting the device from a heat shield into a heat sink (see Fig. 7.25).

Deployable rebar structures are another application that could benefit from a pattern of co-planar joints. Current rebar structures require extensive manual assembly that consists of fastening rods together using wire and hand tools. Instead, large sections of rebar structures could be stamped and deployed into the desired config-

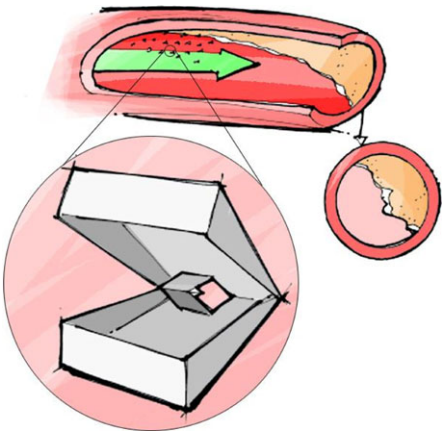

Fig. 7.26 Microscopic LEMs could be placed in the bloodstream to erode plaques from arteries

uration with one or two simple inputs. This could dramatically reduce labor costs and the duration of construction projects, which may be particularly important for rebuilding after a disaster.

Scaled Mechanisms The planar fabrication and potential to eliminate assembly through compliance allows for scaling to very small sizes. Using micromachining techniques, LEMs can be developed on the micro scale. In addition, mechanisms that have been developed at the micro level can be scaled to fit larger applications.

Autonomous micro LEM devices could perform various operations on individual cells. Cells could be physically manipulated, tested for various diseases, and individually medicated. A large number of micro cutting mechanisms in the bloodstream could erode plaques from arterial walls, avoiding the need for invasive stents or bypass surgery (see Fig. 7.26). Similar mechanisms could be used to clean industrial piping. The devices could be removed from the process flow with magnets in order to maintain production rates.

Surprising Motion LEMs can have complex, unusual, and non-intuitive motion. A flat initial state causes LEM designs to have a very simple topology, and compliance allows LEMs to be monolithic. Therefore, the complex motion emerging from a single sheet of material is often impressive to users.

The complex motion that springs from a simple LEM can surprise users and attract attention. This could be used in pop-up advertising that deploys when users open a products packaging for the first time. This could also create entertaining three dimensional board game layouts (see Fig. 7.27). Kits could be sold to help crafters create emerging images in scrap book pages. LEM business cards would increase interest and be memorable to potential customers.

Shock Absorbing The compliant nature of LEMs induces energy storage during motion. Not all of the energy is stored in LEMs. Some of the energy can be dissipated by conversion into heat and friction, giving LEMs an ability to dissipate energy as well.

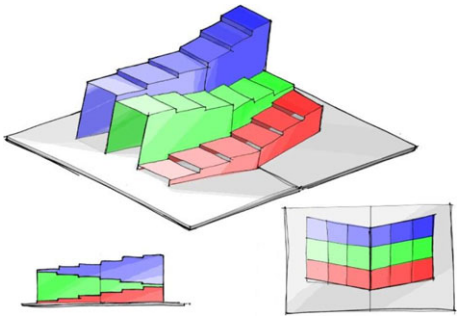

Fig. 7.27 A surprising three-dimensional board game made with a LEM

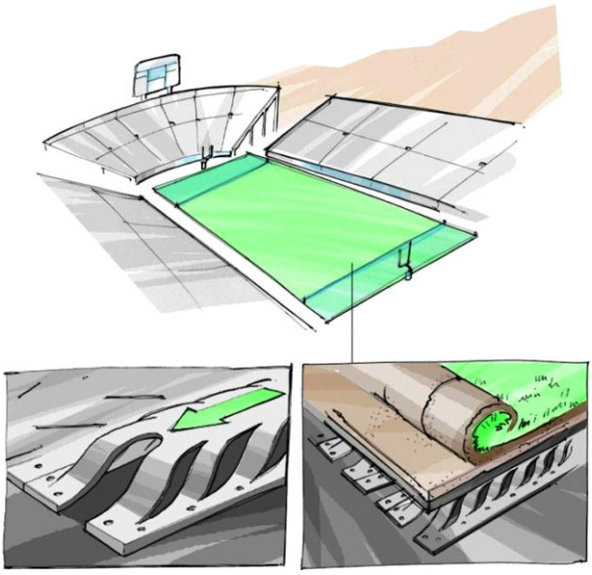

Fig. 7.28 Shock absorbing LEMs could allow better control over the spring and damping properties of athletic turf or flooring

The energy absorption of LEMs can be useful in many shock-absorbing products. Athletic flooring, turf, and footwear with a layer of energy absorbing LEMs could allow more control over the spring and damping properties than current padding (see Fig. 7.28).

This could reduce sports injuries that develop due to repeated impact. Protective armor could be manufactured with multiple layers of energy absorbing and dissipating LEMs, possibly improving upon current bullet-proof technologies [1]. A deploying spring system that encases sensitive electronics could cushion against drops that typically cause damage, and a flexible suspension matrix for crates of produce could also reduce bruising and cracking in the fruit and egg industries. Cushioning LEMs could be stamped into metal seating surfaces to allow a more comfortable distribution of body pressure.

Deployable Mechanisms LEMs can be transported in their flat initial state and then deployed onsite into an expanded configuration. This has the potential to dra-

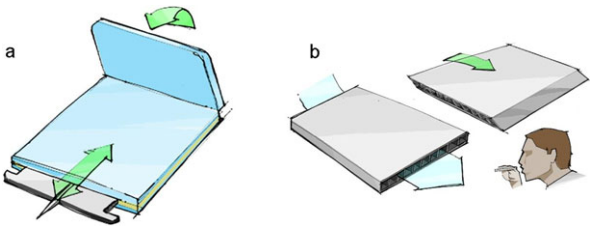

Fig. 7.29 Deployable mechanisms could be the size of a credit card to fit into a wallet for emergencies. Examples include (**a**) an adrenaline injector or (**b**) an inhaler

matically increase portability and decrease the cost of handling, storing, and shipping LEMs.

Mechanisms and structures with significant empty space are prime candidates to become deployable mechanisms. A deploying desk and chair could eliminate the need for an extra room for a home office, making them more available to the general population. International barge containers could be collapsed during return transport to reduce the cost associated with shipping empty space. Temporary structures could be LEMs, allowing innovative,deploying camping shelters, green houses, and field medical rooms.

Many deployable devices could be the size of a credit card and easily carried in a wallet for unexpected situations (see Fig. 7.29). A compact blood lancet for blood testing would be useful for diabetes patients. Credit card sized adrenaline injectors could be useful for people with serious allergies. A small inhaler could easily be carried by asthma patients for use in case of emergencies. Even a single-exposure, disposable camera could fit inside a wallet in case of unplanned photograph opportunities.

7.3 Conclusion

Compliant mechanisms provide significant benefits for motion applications. They can be compatible with many fabrication methods, may not require assembly, have friction-free and wear-free motion, provide high precision and high reliability, and they can integrate multiple functions into fewer components. The major challenges associated with compliant mechanisms come from the difficulty associated with their design, limited rotation, and the need to ensure adequate fatigue life. It is likely that compliant mechanisms will see increasing use in mechanical systems at all size scales and in many application domains as more people understand their advantages and have tools available for their development.

Acknowledgements This chapter is based on work done in collaboration with many other people, and the contributions of the co-authors on those works are gratefully acknowledged. This includes Spencer Magleby, Anton Bowden, Nathan Albrechtsen, Eric Dodgen, Eric Stratton, Joseph Jacobsen, and Brian Winder. The assistance of Danielle Peterson, Kevin Francis, Holly Greenberg and Larrin Wada are also appreciated. The author gratefully acknowledges support from Crocker Ventures, the Utah Technology Commercialization and Innovation Program, and the National Science Foundation through grant CMMI-0800606.

References

1. Andersen, C., Magleby, S., Howell, L.: Principles and preliminary concepts for compliant mechanically reactive armor. In: ASME/IFToMM International Conference on Reconfigurable Mechanisms and Robots (2009)
2. Awtar, S., Sen, S.: A generalized constraint model for two-dimensional beam flexures: nonlinear load-displacement formulation. J. Mech. Des. **132**(8)
3. Cannon, J.R., Howell, L.L.: A compliant contact-aided revolute joint. Mech. Mach. Theory **40**(11), 1273–1293 (2005)
4. Chen, G., Aten, Q.T., Zirbel, S., et al.: A tristable mechanism configuration employing orthogonal compliant mechanisms. J. Mech. Robot. **2**(1) (2010)
5. Chen, G., Gou, Y., Zhang, A.: Synthesis of compliant multistable mechanisms through use of a single bistable mechanism. J. Mech. Des. **133**(8) (2011)
6. Chen, S.-C., Culpepper, M.L.: Design of a six-axis micro-scale nanopositioner-hexflex. Precis. Eng. **30**(3), 314–324 (2006)
7. Cronin, J.A., Frecker, M.I., Mathew, A.S.: Design of a compliant endoscopic suturing instrument. J. Med. Dev. **2**(2) (2008)
8. Dai, J.S., Jones, J.R.: Matrix representation of topological changes in metamorphic mechanism. J. Mech. Des. **127**(4), 837–840 (2005)
9. Dai, J.S., Jones, J.R.: Mobility in metamorphic mechanisms of foldable/erectable kinds. J. Mech. Des. **121**(3), 375–382 (1999)
10. Frecker, M., Ananthasuresh, G., Nishiwaki, S., Kikuchi, N., Kota, S.: Topological synthesis of compliant mechanisms using multi-criteria optimization. J. Mech. Des. **11**(9), 238–245 (1997)
11. Frecker, M., Canfield, S.: Optimal design and experimental validation of compliant mechanical amplifiers for piezoceramic stack actuators. J. Intell. Mater. Syst. Struct. **11**(5), 360–369 (2000)
12. Greenberg, H.C., Gong, M.L., Howell, L.L., Magleby, S.P.: Origami and compliant mechanisms. J. Mech. Sci. **2**, 217–225 (2011)
13. Halverson, P.A., Howell, L.L., Magleby, S.P.: Tension-based multi-stable compliant rolling-contact elements. Mech. Mach. Theory **45**(2), 147–156 (2010)
14. Hoetmer, K., Woo, G., Kim, C., Herder, J.: Negative stiffness building blocks for statically balanced compliant mechanisms: design and testing. J. Mech. Robot. **2**(4) (2010)
15. Holst, G.L., Teichert, G.H., Jensen, B.D.: Modeling and experiments of buckling modes and deflection of fixed-guided beams in compliant mechanisms. J. Mech. Des. **133**(5) (2011)
16. Hopkins, J.B., Culpepper, M.L.: Synthesis of multi-degree of freedom, parallel flexure system concepts via freedom and constraint topology (FACT)—part I: Principles. Precis. Eng. **34**(2), 259–270 (2010)
17. Hopkins, J.B., Culpepper, M.L.: Synthesis of multi-degree of freedom, parallel flexure system concepts via freedom and constraint topology (FACT)—part II: Practice. Precis. Eng. **34**(2), 271–278 (2010)
18. Howell, L., DiBiasio, C., Cullinan, M., Panas, R., Culpepper, M.: A pseudo-rigid-body model for large deflections of fixed-clamped carbon nanotubes. J. Mech. Robot. **2**, 034501 (2010)
19. Howell, L., Midha, A.: Parametric deflection approximations for end-loaded, large-deflection beams in compliant mechanisms. J. Mech. Des. **117**, 156–165 (1995)
20. Howell, L., Midha, A.: A method for the design of compliant mechanisms with small-length flexural pivots. J. Mech. Des. **116**, 280–290 (1994)
21. Howell, L.L.: Compliant Mechanisms. Wiley, New York (2001)
22. Howell, L.L., McLain, T.W., Baker, M.S., Lott, C.D.: MEMS/NEMS Handbook, Techniques and Applications. Springer, New York (2006), pp. 187–200
23. Hull, P., Canfield, S.: Optimal synthesis of compliant mechanisms using subdivision and commercial FEA. J. Mech. Des. **128**(2), 337–348 (2006)
24. Jacobsen, J.O., Chen, G., Howell, L.L., Magleby, S.P.: Lamina emergent torsional (LET) joint. Mech. Mach. Theory **44**(11), 2098–2109 (2009)

25. Jacobsen, J.O., Howell, L.L., Magleby, S.P.: Lamina emergent mechanisms and their basic elements. J. Mech. Robot. **2**(1), 011003 (2010)
26. Jacobsen, J.O., Howell, L.L., Magleby, S.P.: Fundamental components for lamina emergent mechanisms. In: Proceedings of the 2007 ASME International Mechanical Engineering Congress and Exposition (2007)
27. Jain, C., Saxena, A.: An improved material-mask overlay strategy for topology optimization of structures and compliant mechanisms. J. Mech. Des. **132**(6) (2010)
28. Jensen, B.D., Howell, L.L.: Identification of compliant pseudo-rigid-body four-link mechanism configurations resulting in bistable behavior. J. Mech. Des. **125**(4), 701–708 (2003)
29. Jensen, B.D., Howell, L.L., Salmon, L.G.: Design of two-link, in-plane, bistable compliant micro-mechanisms. J. Mech. Des. **121**, 416–423 (1999)
30. Krishnan, G., Kim, C., Kota, S.: An intrinsic geometric framework for the building block synthesis of single point compliant mechanisms. J. Mech. Robot. **3**(1) (2011)
31. Lobontiu, N.: Compliant Mechanisms: Design of Flexure Hinges. CRC Press, Boca Raton (2003)
32. Lusk, C.P., Howell, L.L.: Components, building blocks, and demonstrations of spherical mechanisms in microelectromechanical systems. J. Mech. Des. **130**(3), 034503 (2008)
33. Lusk, C.P., Howell, L.L.: Spherical bistable micromechanism. J. Mech. Des. **130**, 1–6 (2008)
34. Mankame, N.D., Ananthasuresh, G.K.: Synthesis of contact-aided compliant mechanisms for non-smooth path generation. Int. J. Numer. Methods Eng. **69**(12), 2564–2605 (2007)
35. Mehta, V., Frecker, M., Lesieutre, G.A.: Stress relief in contact-aided compliant cellular mechanisms. J. Mech. Des. **131**(9), 091009 (2009)
36. Nai, T.Y., Herder, J.L., Tuijthof, G.J.M.: Steerable mechanical joint for high load transmission in minimally invasive instruments. J. Med. Dev. Trans. ASME **5**(3) (2011)
37. Natarajan, R.N., Andersson, G.B.J.: The influence of lumbar disc height and cross-sectional area on the mechanical response of the disc to physiologic loading. SPINE **24**(18), 1873–1881 (1999)
38. Nelson, P., Malecha, R., Chilenskas, A.: Variable pressure thermal insulating jacket (1994)
39. Panjabi, M.M., Goel, V., Oxland, T., Takata, K., Duranceau, J., Krag, M., Price, M.: Human lumbar vertebrae quantitative three-dimensional anatomy. SPINE **17**(3), 299–306 (1992)
40. Pei, X., Yu, J., Zong, G., Bi, S., Su, H.: The modeling of cartwheel flexural hinges. Mech. Mach. Theory **44**, 1900–1909 (2009)
41. Qiu, J., Lang, J.H., Slocum, A.H.: A curved-beam bistable mechanism. J. Microelectromech. Syst. **13**(2), 137–146 (2004)
42. Radaelli, G., Gallego, J.A., Herder, J.L.: An energy approach to static balancing of systems with torsion stiffness. J. Mech. Des. **133**(9) (2011)
43. Saxena, A., Ananthasuresh, G.K.: On an optimal property of compliant topologies. Struct. Optim. **19**(1), 3649 (2000)
44. Schnake, K.J., Putzier, M., Haas, N.P., Kandziora, F.: Mechanical concepts for disc regeneration. Eur. Spine J. **15**(Suppl. 3), 354–360 (2006)
45. Sigmund, O.: On the design of compliant mechanisms using topology optimization. Mech. Based Des. Struct. Mach. **25**(4), 493–524 (1997)
46. Smith, S.: Flexures: Elements of Elastic Mechanisms. Taylor, Francis, London (2000)
47. Stratton, E., Howell, L.L., Bowden, A.E.: Force-displacement model of the flexsure spinal implant (2010)
48. Sundaram, M.M., Limaye, P., Ananthasuresh, G.K.: Design of conjugate, conjoined shapes and tilings using topology optimization. Struct. Multidiscip. Optim. **45**(1), 65–81 (2012)
49. Trease, B.P., Moon, Y.-M., Kota, S.: Design of large-displacement compliant joints. J. Mech. Des. **127**, 788–798 (2005)
50. Wang, M.Y.: A kinetoelastic formulation of compliant mechanism optimization. J. Mech. Robot. **1**(2) (2009)
51. Wang, W., Yu, Y.: New approach to the dynamic modeling of compliant mechanisms. J. Mech. Robot. **2**(2) (2010)

52. Wuxiang, Z., Xilun, D.: A method for designing metamorphic mechanisms and its application (2009)
53. Yu, Y.Q., Howell, L.L., Lusk, C.P.: Dynamic modeling of compliant mechanisms based on the pseudo-rigid-body model. J. Mech. Des. **127**(4), 760–765 (2005)
54. Zhao, H., Bi, S., Yu, J.: A novel compliant linear-motion mechanism based on parasitic motion compensation. Mech. Mach. Theory **50**, 15–28 (2012)
55. Zhao, H., Bi, S., Yu, J.: Nonlinear deformation behavior of a beam-based flexural pivot with monolithic arrangement. Precis. Eng. **35**, 369–382 (2011)
56. Zhou, H., Killekar, P.: The modified quadrilateral discretization model for the topology optimization of compliant mechanisms. J. Mech. Des. **133**(11) (2011)

Chapter 8
Protein Molecules: Evolution's Design for Kinematic Machines

Kazem Kazerounian and Horea T. Ilieş

8.1 Introduction

Can we design protein molecules that are capable of binding to, inhibiting, or stimulating biomolecular targets within the body, enabling researchers to develop personalized pharmaceuticals, or design more effective cancer therapies? Can we create DNA strands that function as electronic switches on a chip or bioreactor? Can we predict the role of proteins in the mechanics of the living cells and cure and eradicate potentially fatal diseases like malaria? Can we use biomolecular systems to create and store energy? Or, more broadly, can we engineer biomolecular artifacts? These are some of the profound, yet largely unanswered, questions raised in recent decades. So why try to answer them again? Simply stated, finding such answers is a more critical endeavor for our society and a more tangible task than ever before. We are reaching a time when engineers and scientists can integrate the most recent advances in science, engineering, computation, and experimental capabilities to break physical scale barriers and produce revolutionary artifacts.

The biological role of a protein is determined by its function, which, in turn, is largely determined by its structure. Understanding protein folding, structure and compliance is of great importance since many neurodegenerative diseases, such as Parkinson's and Alzheimer's, as well as many cancers, Cystic fibrosis or Type II diabetes, are generated by protein misfolding and accumulation. Furthermore, such an understanding would allow researchers to develop new molecular carriers whose sole purpose would be to deliver drugs where they are needed. At the same time,

K. Kazerounian (✉)
Department of Mechanical Engineering, The University of Connecticut, Storrs, CT 06269, USA
e-mail: kazem@engr.uconn.edu

H.T. Ilieş
Departments of Computer Science and Mechanical Engineering, The University of Connecticut, Storrs, CT 06269, USA
e-mail: ilies@engr.uconn.edu

J.M. McCarthy (ed.), *21st Century Kinematics*,
DOI 10.1007/978-1-4471-4510-3_8,

the fact that proteins are the "nano devices" developed through evolution by nature suggests that the development of biomimetic artificial nano machines based on polypeptide building blocks is not only promising, but may also be the most practical approach to develop the nano-machines of the future.

A protein molecule can exist in a *denatured state* that may be loosely compared to an open string, whose particular shape has no relevance to its state. However, when placed in an appropriate environment (i.e., solvent, PH, and temperature as found, for example, in a cell environment), the protein folds to a complex 3D shape, also called the *native state* of the protein. This process may take anywhere between a few nano seconds to a few seconds. A protein in the native state can be denatured by changing some of the environment parameters such as solvent, PH or temperature. However, when placed back in the appropriate environment, the protein returns again to its native state. The repeatability of this process indicates that the final three dimensional structure (tertiary structure) of the protein is intrinsic to its primary structure (amino acid sequence). Therefore, in principle, this must be a predictable state. This prediction, however, remains a fundamental challenge in computational biology, and it is even being referred to as the "grand challenge" of the century.

Protein folding occurs under the effect of inter-atomic forces (among protein atoms as well as between protein atoms and the atoms of the solvent). The final conformation is a relatively stable configuration for which the total potential energy is globally minimized or in other words, the system is in stable static equilibrium.

There are two basic primary approaches used in *ab initio* folding simulations. The first approach attempts to change the geometry of a molecule in order to minimize its potential energy, which is often formulated as an optimization problem [18]. The major drawback of optimization-based methods is that the search usually gets trapped in the local optima of the energy landscape. The second approach is based on the dynamics of the protein chain movements and utilizes Molecular Dynamic Simulations (MDS). MDS in protein folding are also divided into two main groups: (1) All atom dynamic simulations [11] and (2) Torsion angle dynamic simulations [23]. In all atom dynamic simulations, the atoms are simulated individually. By contrast, in torsion angle (or atom group) dynamic simulations, the formulation is based on the fixed bond lengths, bond angles, chirality, and planarity, which significantly reduces the degrees of freedom and consequently the computational expense. In MDS methods, the equations of motion for individual atoms or atom groups are integrated in the time domain. A more recent method, Successive Kineto-Static Fold Compliance has been introduced as a promising alternative to Molecular Dynamic Simulations [30, 31].

As recent reviews indicate [6, 17, 22], both approaches are still far from being able to predict the structure of a protein in its native state if an approximate initial guess is not available. On the other hand, both approaches are promising contenders to the difficult task of performing global optimization on the energy landscape defined by a protein and its environment.

Moreover, the study of protein folding and interactions must take into account the protein flexibility. Clearly, rigid sub-regions within the structure of a protein

stabilize its conformation. At the same time, flexible regions allow the proteins to change their conformation in a manner consistent with the constrains imposed by rigid sub-regions, and hence perform their biological tasks. Therefore, predicting protein flexibility is a key task for understanding their function. At the same time, taking advantage of protein mobility analysis can lead to a more realistic as well as computationally faster simulation of protein molecules. The critical factor in protein mobility analysis is, arguably, the formation of hydrogen bonds.

For the remainder of this chapter, we will discuss some of the central kinematic elements that can be used to model protein chains and to study their folding and flexibility. We will conclude with a look at the challenges and opportunities of studying proteins with the help of modern kinematic tools.

8.2 Protein Model

8.2.1 Protein Molecule as a Kinematic Chain

The authors have successfully modeled the protein molecule as a kinematic chain of rigid bodies connected by revolute joints [6, 30, 31, 46–48]. Our model, which has been implemented in PROTOFOLD—our in-house protein folding simulation framework, fully defines the kinematic structure of the backbone (main chain) of the protein polymer at the Zero Position as follows. The backbone of a protein chain that contains M residues (amino acids) is defined as a serial chain of $N+1$ solid links connected by N revolute joints (see for example Fig. 8.1). Since each residue has two revolute joints $N = 2M$. The revolute joints in each amino acid are φ_i and ψ_i, $i = \overline{1, M}$. We introduce a uniform notation of these angles as θ_j, $j = \overline{1, N}$, where

$$\theta_j = \varphi_i, \tag{8.1}$$

$$\theta_{j+1} = \psi_i, \quad \forall j = 2(i-1) \text{ and } i = \overline{1, M}. \tag{8.2}$$

The N revolute joints and solid links connecting them within the N degree of freedom serial linkage are kinematically defined by a set of unit vectors $\mathbf{u}$ and body vectors $\mathbf{b}$:

- $\mathbf{u}_{0j1}$—Unit vectors along the dihedral joints θ_j. The first index indicates that we use the zero-position configuration; the second index corresponds to the joint number, and the third index indicates the chain number (e.g., the index of the main chain is 1; side chains have indices larger than 1). Thus, $\mathbf{u}_{0j1}$ corresponds to the unit vector along the ith joint of the main chain. In this paper we only focus on the main chain and, therefore, the third index will always be equal to 1.
- $\mathbf{b}_{0j1}$—Body vector connecting a point on the dihedral joint axis of the angle θ_j (specifically, a Nitrogen atom if j is odd, and α-Carbon atom if j is even) to a point on the dihedral joint axis of the angle θ_{j+1} (an α-Carbon if j is odd,

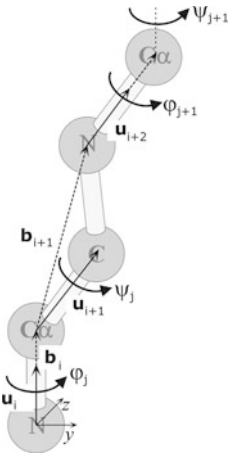

Fig. 8.1 A triad segment of an amino acid chain with dihedral angles as generalized coordinates

and a Nitrogen atom of the next residue if j is even). The indices have the same meaning as defined above.

Note that in this configuration (Zero-Position, which is *not* a native conformation) all dihedral angles θ_j are defined to be zero. Furthermore, our selection for the biological reference conformation as our Zero configuration implies that the pair of body vectors $\mathbf{b}_{0j1}$ and $\mathbf{b}_{0(j+1)1}$ are identical for all residues in the chain in this conformation. Thus, $\mathbf{u}_{0j1}$ and $\mathbf{b}_{0j1}$ need to be defined only for one residue.

The backbone structure of the protein in any Non-Zero configuration (when the values of the dihedral angles θ_j are non-zero) can be found by a series of successive rotations:

$$\mathbf{b}_{j1} = [R_{\theta_1,\mathbf{u}_{011}}][R_{\theta_2,\mathbf{u}_{021}}]\ldots[R_{\theta_j,\mathbf{u}_{0j1}}]\mathbf{b}_{0j1}, \tag{8.3}$$

where j denotes the jth solid link in the protein chain and R is the screw rotation matrix of angle θ_j about axis $\mathbf{u}_{0j1}$. In every peptide plane, assumed to be rigid body in our formulation, the above equations result in the computation of two body vectors $\mathbf{b}_{j1}$ and $\mathbf{b}_{(j+1)1}$. A similar procedure is also implemented for the side chains.

The reduction in the computational time between the linkage model that we use and the standard all-atom models is tremendous. If we assume that each amino residue in the chain, on average, has 10 atoms (most have more), then the number of optimization variables in the majority of *ab initio* methods reduces from $10 \cdot 3 \cdot N$ to $2N$ variables. Considering that most optimization methods have a computational cost proportional to the square of the number of variables (global search based methods such as simulated annealing and genetic algorithms excluded), the expected computational time (number of cost evaluations) reduction is 15^2 or 225 times. Additionally, in evaluating the cost function, the bond and angle energies are no longer needed. This argument does not take into account the computational time of the direct kinematics.

8.2.2 Amber Potential and Force Field

PROTOFOLD employs the AMBER atomic force model [10] to describe the system energy of a given conformation. AMBER describes the total potential energy of the protein chain as a sum of the electrostatic and van der Waals energies between all atoms. Note that there are several terms in the force field that represent the bond angle and length energy changes (spring like effects) that are automatically eliminated due to the rigid body assumption of the peptide planes. Therefore:

$$E_{potential} = \sum_{i<j} \left(\frac{A_{ij}}{r_{ij}^{12}} - \frac{B_{ij}}{r_{ij}^{6}} + \frac{q_i q_j}{\varepsilon r_{ij}} \right), \tag{8.4}$$

where A_{ij} and B_{ij} are the van der Waals and London dispersion terms; q_i and q_j are the partial atomic charges, and ε is the dielectric constant (see [10, 15]).

The force between any two atoms is the negative derivative of the potential energy between those same atoms. Thus,

$$F_{ij} = -\frac{12A_{ij}}{r_{ij}^{13}} + \frac{6B_{ij}}{r_{ij}^{7}} - \frac{q_i q_j}{\varepsilon r_{ij}^{2}}. \tag{8.5}$$

The combined force applied to each atom i is then the sum of the forces exerted by all other atoms j:

$$F_i = \sum_{j=1}^{N} F_{ij}, \quad i \neq j. \tag{8.6}$$

8.3 Folding via Successive Kineto-Static Fold Compliance

In our approach, known as Successive Kineto-Static Fold Compliance Method, the conformational changes of the peptide chain are driven by an inter-atomic force field without the need for Molecular Dynamic Simulation. Instead, the chain complies under the Kineto-Static effect of the force field in such a manner that each rotatable joint changes by an amount proportional to the effective torque on that joint. This process successively iterates until all of the joint torques have converged to zero. The resulting conformation is in a minimum potential energy state. PROTOFOLD, our own protein simulation platform, uses this methodology. It has been shown that PROTOFOLD is orders of magnitude more efficient and robust than traditional Molecular Dynamics Simulation [45].

The main steps in Successive Kineto-Static Fold Compliance are therefore described below:

1. At a given set of joint angles, calculate the Cartesian coordinates of all atoms in the protein molecule (Direct Kinematics using Zero-Position formulation discussed above).

2. Calculate all the inter-atomic forces in this conformation (using the Amber Force Field model discussed below).
3. Calculate the equivalent joint torques (τ_j) using the well known relation between the end-effector forces and the joint forces in robotics.
4. Calculate an effective change in each joint variable, proportional to that joint's equivalent torque τ_j ($\Delta\theta_j = k\tau_j$) and rotate each joint accordingly.
5. Go back to step 1 until all the joint equivalent torques have diminished to zero (within some small prescribed error).

8.4 Mobility

8.4.1 Formation of Hydrogen Bonds

The first class of approaches identifies rigid domains by comparing two conformations of a protein [38, 50], and require experimental observations of proteins as well as knowledge of atom coordinates obtained by crystallographic or NMR techniques. Hence, the applicability of these methods is limited to known protein conformational states.

The second class of approaches predict rigid subsets of a protein by using a single protein conformation. This class of approaches includes molecular dynamics [14, 33], normal mode analysis [13], graph theory based [28] and kinematics based [41] methods.

We have developed a novel mobility analysis based on the kinematic role of hydrogen bonds in the 3D structure of protein molecules [41, 42]. Our method predicts the formation of hydrogen bonds, and identifies the rigid regions inside the protein molecule, as well as the under-constrained flexible regions.

The hydrogen bonds that form between atoms of the main chain are identified using our geometric criteria proposed in [41], which are based on published experimental results. These bonds increase the complexity of the open loop kinematic chain of the protein structure, and form multiple closed sub-chains. We infer from the Grübler-Kutzbach criterion that the closed loops that have at most six joints are rigid, and can be therefore replaced by a single rigid link.

Lines 1 to 14 in Algorithm 8.1 outline the mobility analysis developed in [41]. This rigidity analysis method was applied to some candidate proteins to design and fabricate a nanoparticle (a new vaccine for SARS) [44]. Our procedure, based on 3D structure of protein molecules, predicted that only one of the candidates is capable of producing a stable nanoparticle, which was in agreement with the experimental results.

We have extended our existing mobility analysis framework to study bonds that form with/between atoms of the protein's side-chains, which have a prominent role in determining flexible and rigid regions of protein molecules. We have also extended the identification of rigid closed loops from [41] to include non-rigid (under-constrained) closed loops and develop constraint equations for closed loops with one or more degrees of freedom.

Table 8.1 Geometric criteria to detect hydrogen bonds

	α^o	β^o	r (Å)
Main-chain main-chain	[110, 180]	[110, 180]	<2.5
Main-chain side-chain and side-chain side-chain	[90, 180]	[90, 180]	<2.5

We show (1) how under-constraint closed loops determine rigid regions of protein molecules, and (2) that the flexible regions predicted by our method correlate well with the experimental observations for several proteins. A key advantage of the rigidity analysis is the reduction of the number of degrees of freedom in our protein model by up to 80 %.

A hydrogen bond is an interaction between a hydrogen atom with an electronegative atom (such as nitrogen and oxygen). It is increasingly recognized that these comparatively weak bonds are crucial for the stabilization and function of protein molecules as well as protein folding. Many in-depth studies of the hydrogen bonds that form in proteins [2, 5, 34, 36, 51] provided considerable insight into the geometry of hydrogen bonds, and a comprehensive review of the geometry of hydrogen bonds has been conducted in [41]. Table 8.1 represents the extended set of geometric criteria. Observe that not all side-chains are participating in hydrogen bond interactions. Specifically, donor side chains are: SER, THR, ASN, HIS, GLN, LYS, ARG, and TYR, while the acceptor side chains are SER, THR, ASN, GLU, GLN, ASP, TYR. Figures 8.2 and 8.3 show the geometry of hydrogen bonds and illustrate the formation of closed loops by these bonds.

All computations described here have been performed within the PROTOFOLD platform, our in-house developed protein simulation software [30].

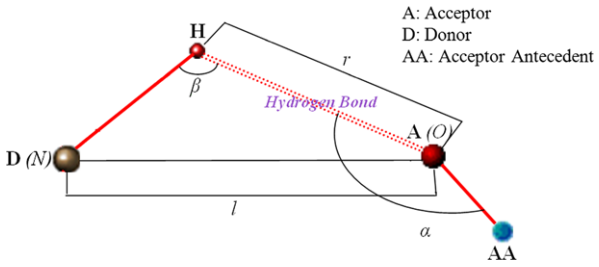

Fig. 8.2 Geometric parameters of hydrogen bonds

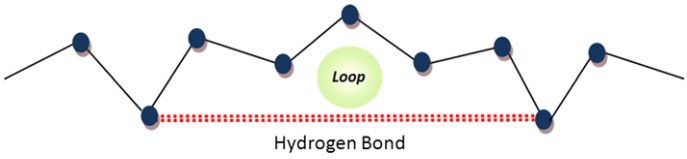

Fig. 8.3 A loop generated by a hydrogen bond

8.4.2 Mobility Analysis

The Grübler-Kutzbach criterion given in (8.7) prescribes the i degrees of freedom (DOF) of a 3D mechanism with L links and P_i joints:

$$DOF = 6(L-1) - 5P_1 - 4P_2 - 3P_3 - 2P_4 - P_5. \tag{8.7}$$

This criterion is applicable to generic structures [20] with no special symmetries that generate geometric singularities. Since there are no known non-generic structures that have been observed in experimental observations [28], we can assume, without loss of generality that protein structures do not contain such singularities.

We compute the topological (connectivity) information, which is then parsed to extract the closed loops whose degrees of freedom are determined from equation (8.7). Note that due to the fact that our kinematic model only contains revolute joints with one DOF, $P_2 = P_3 = P_4 = P_5 = 0$. Therefore, for a closed loop containing 6 links, i.e., $L \leq 6$, the resulting number of degrees of freedom of a closed loop will be zero or less. This, in turn, means that the loop is kinematically over-constrained, and it can be considered a rigid body. Consequently, the loops having more than 6 links are under-constrained and hence flexible. For instance, a loop with 8 links and 8 joints has 2 degrees of freedom, which means controlling any 2 of its joints completely determines the angles in the other joints. In some cases these loops can be connected to each other and share one or more links. In such a case, DOF of the system can not be calculated using (8.7).

For non-rigid (NR) loops with shared links, we compute the number of DOF based on (8.8):

$$DOF = \sum_{i=1}^{m} (DOF)_i - \sum_{j=1}^{n} P_j, \tag{8.8}$$

where $(DOF)_i$ is the number of degrees of freedom of the ith loop in the group of connected loops and P_j represents the degrees of freedom that are 'used' by the jth shared joint. There is no restriction on which closed loops may be used as long as they collectively involve all links and joints. One can develop a proof of (8.8) based on an analogy with geometric constraint equations [24].

We use (8.8) to calculate DOF of the group of NR loops. If the DOF of the group of NR loops is less than 1, then all links of these loops are rigid. In such a case, all links are replaced with one single rigid link. For a group of NR loops with n DOF ($n > 0$), there are n free joints and the rest of the joints are constrained.

It has been well documented in the robotics literature that the velocity state of the end effector ($\dot{X}$) in a serial chain is related to the actuated joint rates ($\dot{q}$) through the conventional manipulator Jacobian matrix (8.9).

$$\dot{\mathbf{X}} = J\dot{\mathbf{q}}. \tag{8.9}$$

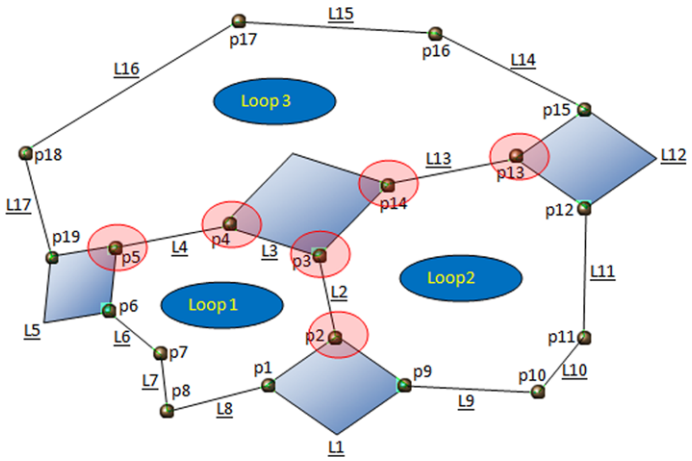

Fig. 8.4 Three non-rigid 3D loops connected to each other—*Red circles* show shared joints

For the ith revolute joint, the ith column of the Jacobian is:

$$J = \begin{pmatrix} \mathbf{u_i} \\ \mathbf{u_i} * \mathbf{P_i P_H} \end{pmatrix}, \tag{8.10}$$

where $\mathbf{u_i}$ is a unit vector along the ith joint and $\mathbf{P_i P_H}$ is a vector connecting a point on the ith joint to the end effector. For a closed loop the first link and the end effector coincide ($\mathbf{P_H} = \mathbf{P_1}$), and therefore (8.10) can be written as

$$J = \begin{pmatrix} \mathbf{u_i} \\ \mathbf{u_i} * \mathbf{P_i P_1} \end{pmatrix}. \tag{8.11}$$

Furthermore, in the system of (8.9), $\dot{\mathbf{X}}$ becomes zero and therefore system (8.9) is rewritten as:

$$J\dot{\mathbf{q}} = 0, \tag{8.12}$$

$$J(\Delta\boldsymbol{\theta}) = 0. \tag{8.13}$$

For small displacements, the system of (8.12) can be approximated by (8.13) to compute the change of the joints angles. Our specific procedure can be intuitively explained by examining a sample group of connected NR closed loops shown in Fig. 8.4. This example contains 3 loops and 6 shared joints in 3D (the example in Fig. 8.4 is shown in 2D for simplicity), and the link numbers are underlined. The number of joints, links and DOF of each loop are listed in Table 8.2. Using (8.8) the DOF for this group of NR loops is equal to 1. After computing the Jacobian for each loop (shown in Fig. 8.5), we extend each Jacobian from $6 \times n$ (n is number of joints in the loop) to $6 \times m$ (m is total number of joints in the group of loops). A zero column has been added for each joint that does not belong to that loop in the

Table 8.2 Loops in the example of Fig. 8.4

Loop #	Joints #	Links #	Loop DOF
Loop1	8	8	2
Loop2	8	8	2
Loop3	9	9	3

$$J_1 = \begin{pmatrix} u_1 & u_2 & u_3 & u_4 & u_5 & u_6 & u_7 & u_8 \\ u_1 * p_1 p_1 & u_2 * p_2 p_1 & u_3 * p_3 p_1 & u_4 * p_4 p_1 & u_5 * p_5 p_1 & u_6 * p_6 p_1 & u_7 * p_7 p_1 & u_8 * p_8 p_1 \end{pmatrix}$$

$$J_2 = \begin{pmatrix} u_3 & u_2 & u_9 & u_{10} & u_{11} & u_{12} & u_{13} & u_{14} \\ u_3 * p_3 p_3 & u_2 * p_2 p_3 & u_9 * p_9 p_3 & u_{10} * p_{10} p_3 & u_{11} * p_{11} p_3 & u_{12} * p_{12} p_3 & u_{13} * p_{13} p_3 & u_{14} * p_{14} p_3 \end{pmatrix}$$

$$J_3 = \begin{pmatrix} u_5 & u_4 & u_{14} & u_{13} & u_{15} & u_{16} & u_{17} & u_{18} & u_{19} \\ u_5 * p_5 p_5 & u_4 * p_4 p_5 & u_{14} * p_{14} p_5 & u_{13} * p_{13} p_5 & u_{15} * p_{15} p_5 & u_{16} * p_{16} p_5 & u_{17} * p_{17} p_5 & u_{18} * p_{18} p_5 & u_{19} * p_{19} p_5 \end{pmatrix}$$

$$NewJ_1 = \begin{pmatrix} u_1 & u_2 & u_3 & u_4 & u_5 & u_6 & u_7 & u_8 & 0\,0\,0\,0\,0\,0\,0\,0\,0\,0\,0\,0 \\ u_1 * p_1 p_1 & u_2 * p_2 p_1 & u_3 * p_3 p_1 & u_4 * p_4 p_1 & u_5 * p_5 p_1 & u_6 * p_6 p_1 & u_7 * p_7 p_1 & u_8 * p_8 p_1 & 0\,0\,0\,0\,0\,0\,0\,0\,0\,0\,0\,0 \end{pmatrix}$$

$$NewJ_2 = \begin{pmatrix} 0 & u_2 & u_3 & 0\,0\,0\,0\,0 & u_9 & u_{10} & u_{11} & u_{12} & u_{13} & u_{14} & 0\,0\,0\,0\,0 \\ 0 & u_2 * p_2 p_3 & u_3 * p_3 p_3 & 0\,0\,0\,0\,0 & u_9 * p_9 p_3 & u_{10} * p_{10} p_3 & u_{11} * p_{11} p_3 & u_{12} * p_{12} p_3 & u_{13} * p_{13} p_3 & u_{14} * p_{14} p_3 & 0\,0\,0\,0\,0 \end{pmatrix}$$

$$NewJ_3 = \begin{pmatrix} 0\,0\,0 & u_4 & u_5 & 0\,0\,0\,0\,0\,0\,0 & u_{13} & u_{14} & u_{15} & u_{16} & u_{17} & u_{18} & u_{19} \\ 0\,0\,0 & u_4 * p_4 p_5 & u_5 * p_5 p_5 & 0\,0\,0\,0\,0\,0\,0 & u_{13} * p_{13} p_5 & u_{14} * p_{14} p_5 & u_{15} * p_{15} p_5 & u_{16} * p_{16} p_5 & u_{17} * p_{17} p_5 & u_{18} * p_{18} p_5 & u_{19} * p_{19} p_5 \end{pmatrix}$$

Fig. 8.5 J_1, J_2, J_3 are Jacobian matrices for loops in example shown in Fig. 8.4. $NewJ_1$, $NewJ_2$ and $NewJ_3$ are the extended Jacobian matrices

extended Jacobian matrix. All extended Jacobian matrices have been combined to get the overall Jacobian matrix (shown in (8.14)).

$$NewJacobian = \begin{bmatrix} [NewJ_1] \\ [NewJ_2] \\ [NewJ_3] \end{bmatrix}. \tag{8.14}$$

Once the overall Jacobian matrix has been computed, we detect which joints can change freely. We can prescribe changes for the angles of the independent joints in (8.15) and solve the system of linear (8.16).

$$\begin{bmatrix} C_1\, C_2\, C_3 \ldots C_{19} \end{bmatrix} \begin{bmatrix} \Delta\theta_1 \\ \Delta\theta_2 \\ \Delta\theta_3 \\ \ldots \\ \Delta\theta_{19} \end{bmatrix} = 0, \tag{8.15}$$

$$\begin{bmatrix} C_2\, C_3\, C_4 \ldots C_{19} \end{bmatrix} \begin{bmatrix} \Delta\theta_2 \\ \Delta\theta_3 \\ \Delta\theta_4 \\ \ldots \\ \Delta\theta_{19} \end{bmatrix} = \begin{bmatrix} C_1 \Delta\theta_1 \end{bmatrix}. \tag{8.16}$$

The choice of independent joints cannot be arbitrary because it can lead to an ill-defined Jacobian matrix. If *all* diagonal elements in the upper triangular matrix of the combined Jacobian matrix are non-zero then the matrix is well-defined and

Algorithm 8.1: Pseudo-code of the proposed mobility analysis procedure

```
input  : Protein structure
output: Rigid subsets & Change of joint angles

Find Hydrogen bonds;
Build connectivity matrix;
Remove loose-end links and update connectivity matrix;
Build topological graph;
Find all cycles in the graph;
for every loop detected do
    Check loop rigidity according to Grübler-Kutzbach criterion
    if Loop is rigid then
        Replace links of the loop with one rigid link
        Update connectivity matrix
    else
        Continue search until all links have been considered
Search for all non-rigid loops (NR loops)
for every NR loop detected do
    Find Degrees of Freedom (n)
    if NR loops are connected then
        Calculate DOF of connected loops
        if DOF is < 1 then
            Replace links of the loop with one rigid link
        else
            Go to 25
        Combine all extended Jacobian matrices of any connected NR loop and build a
        single Jacobian matrix for a group of connected loops
    else
        Build a Jacobian matrix for a single loop
    Find the upper triangle matrix of Jacobian matrix
    if All diagonal elements of upper diagonal matrix are not zero then
        Last n loops are given joints
    else
        Change the positions of columns in Jacobian matrix
        Repeat 24 until given joints are found;
    Replace independent joints angle change
    Reduce the Jacobian matrix to new Jacobian
    Calculate the change of the remaining joints angles
```

we can assume that the last n (number of $DOF - 1$ in this example) joints are independent. Otherwise we have to switch columns until we eliminate all the zeroes of the diagonal.

Solving the system of linear equations provides us with the change of the joint angles. Assuming P_1 as an independent joint in our example, we obtain 18 equations and 18 unknowns (as shown in the system of (8.16)). Solving this system of linear equations results in the values of all other joint angles. The pseudo-code of the procedure is shown in Algorithm 8.1.

Table 8.3 Modified mobility analysis results. The percentage in row VI shows the amount of reduction in the number of DOF compared to row II. ('MC-MC Hbonds' represents main-chain/main-chain hydrogen bonds)

		Protein Name			
		1YVQ	2I88	1Z15	2HHB
I	No. of amino acids	141	176	342	141
II	Total No. of DOF	282	352	684	282
III	No. of MC-MC Hbonds	90	98	140	82
IV	No. of DOF considering just MC-MC Hbonds	52	79	303	64
V	No. of all types of Hbonds	106	110	191	95
VI	No. of DOF considering all types of Hbonds using new mobility analysis	39 (86 %)	37 (89 %)	254 (62 %)	59 (79 %)

8.4.3 Results of Our Mobility Analysis

We have applied the mobility analysis procedure discussed above to study several proteins obtained from PDB, namely 1YVQ, 2I88, 1Z15, 2HHB. The Cartesian coordinates of all atoms except hydrogen atoms were obtained from PDB, and the hydrogen atom positions were identified via PROTOFOLD. The structural properties and the DOF of each protein are shown in the first two rows of Table 8.3. The comparison between rows III and V of this table shows the contribution of the hydrogen bonds formed with side-chains atoms. By considering all types of hydrogen bonds as well as all types of loops (both over-constrained and under-constrained) we reduce the total DOF of protein molecules by an average of 80 %. This reduction in the number of degrees of freedom is in fact expected since the inclusion of hydrogen bonds formed with side chain atoms reduce the flexibility of protein molecules.

To validate the results we have compared different conformational changes from experimental observations for each protein, to infer which regions in the protein are flexible or rigid. Figure 8.6 illustrates a protein molecule with 2 known 3D structures in PDB (1YVQ and 1YVT). Figure 8.7 shows the deference between dihedral angles of the two structures of this protein molecule. By comparing these two configurations, one can conclude that relatively large changes in dihedral angles correspond to flexible regions of the protein molecule. In the same figure we label the flexible domains predicted by the method proposed in this paper with red circles. These results show that our method correctly predicts almost all of the expected flexible domains for these molecules. The same technique has been applied to another protein molecule with 2 structures in PDB (2HHB and 1HHO), shown in Figs. 8.8 and 8.9.

8.5 Mechanical Model for Hydrogen Bonds

In a broad sense, the difficulty and complexity of experimental studies aimed at measuring the stiffness of protein molecules are inversely proportional to the size of the molecules, while a larger molecules is computationally more expensive to analyze. The stiffness of protein molecules has been studied experimentally by using Atomic Force Microscopy (AFM) [19, 35, 39, 49], as well as laser tweezers [32]. Computational models have been developed to predict the mechanical properties of molecules [9, 21, 27].

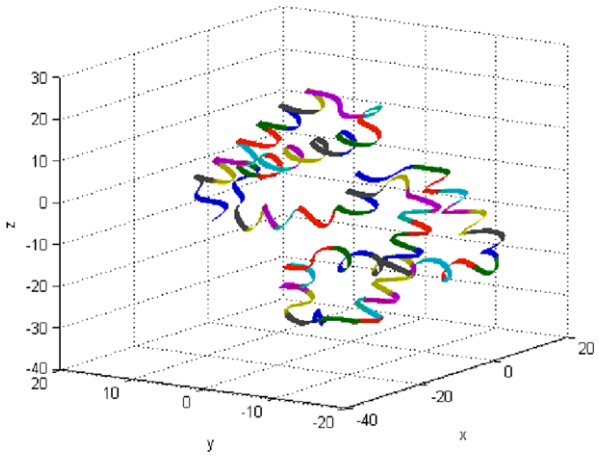

Fig. 8.6 The 3D structure of 1YVQ

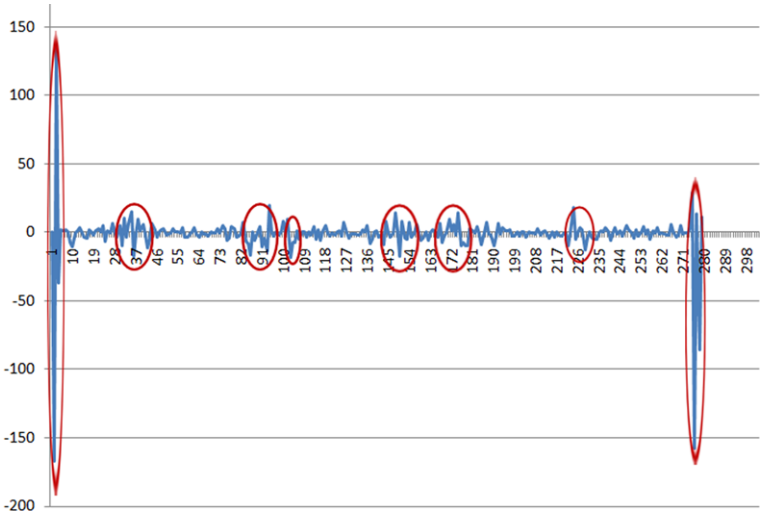

Fig. 8.7 Rigid and flexible regions of 1YVQ

One of the key mechanical properties of protein molecules is their stiffness, which, in turn, is driven by essentially non-rigid hydrogen bonds. The authors and their research group has recently proposed a novel mechanical model to capture the flexibility of the hydrogen bond in terms of three interconnected springs. Under the assumption of small displacements, the linear spring constants are determined based on the available information in the literature about the energy of a hydrogen bond. By computing the equivalent stiffness ellipsoid for each bond, one can predict the stiffness of protein molecules. We estimated the stiffness of three protein molecules

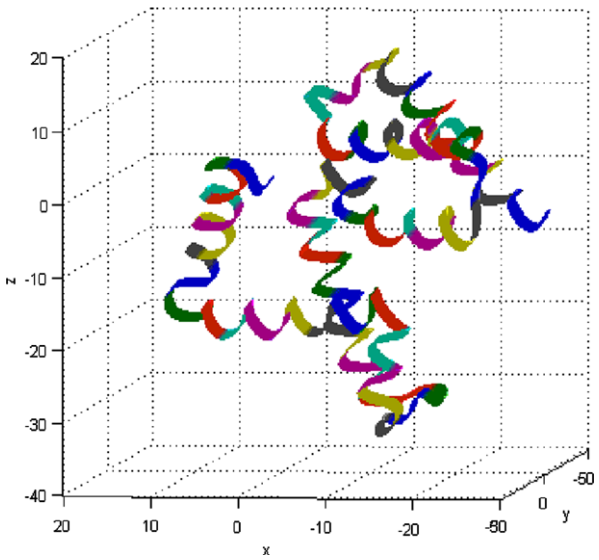

Fig. 8.8 The 3D structure of 2HHB

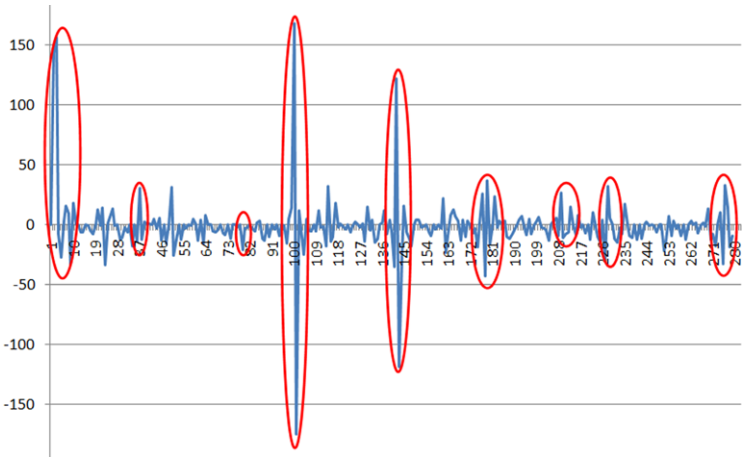

Fig. 8.9 Rigid and flexible regions of 2HHB

based on our mechanical model, which shows a reasonable agreement with data obtained experimentally.

8.5.1 Hydrogen Bond Energy in the Literature

The hydrogen bond energy depends on the chemistry of the donor and acceptor atoms as well as their relative position in space. Two commonly used energy functions for the hydrogen bonds are the Morse function and the Lennard-Jones (LJ) potential [12, 16, 25, 29], which require the determination of a number of constants.

The following model based on the LJ function has been described by Irbäck et al. in [26] to describe the energy of hydrogen bonds for proteins in water:

$$E_{LJ} = \varepsilon\left[5\left(\sum_{hb}/r\right)^{12} - 6\left(\sum_{hb}/r\right)^{10}\right] * g(\alpha,\beta),$$
$$g(\alpha,\beta) = (\cos\alpha\cos\beta)^{1/2} \quad \text{if } \alpha,\beta > 90^\circ,$$
$$g(\alpha,\beta) = 0 \quad \text{if } \alpha,\beta < 90^\circ, \tag{8.17}$$

where E_{LJ} is the proposed energy function based on the LJ potential, and most parameters are empirically defined based on protein folding simulations. In (8.17), $\sum_{hb} = 2$ Å, and $\varepsilon = 3.1$ Å for bonds formed only with main chain atoms, and $\varepsilon = 2$ Å for main chain-side chain bonds. Noted that this energy function depends on distance r and angles α and β.

Two other angle-dependent models have been proposed by Park et al. [25] based on the Morse function (8.18) and LJ function (8.19). The parameters in their models come from Density Functional Theory (DFT) calculations, complemented with genetic algorithms optimization. The model based on the Morse function is described by:

$$E_{Morse} = D_0\left[1 - e^{-\alpha(r-r_0)}\right]^2 * g(\alpha,\beta),$$
$$g(\alpha,\beta) = \sum\left(a_i\cos^i\theta + b_i\sin^i\theta\right) * \sum\left(c_j\cos^j\theta + d_j\sin^j\theta\right), \tag{8.18}$$

where $D_0 = 7.785$ kcal/mol, $\alpha = 1.234$ Å^{-1}, $a_1 = -0.106$, $b_1 = 0.671$, $c_1 = 1.494$, $d_1 = -1.494$, $a_2 = -2.953$, $b_2 = 2.976$, $c_2 = -0.059$, $d_2 = 2.906$, $a_3 = 1.494$, $b_3 = -0.224$, $c_3 = -0.482$, and $d_3 = -1.918$. Furthermore, the model using the LJ potential is described by:

$$E_{LJ} = v_0\left[5(d_0/d)^{12} - 6(d_0/d)^{10})\right] * g(\alpha,\beta),$$
$$g(\alpha,\beta) = \sum\left(a_i\cos^i\theta + b_i\sin^i\theta\right) * \sum\left(c_j\cos^j\theta + d_j\sin^j\theta\right) \tag{8.19}$$

where $D_0 = 9.663$ kcal/mol, $a_1 = 0.153$, $b_1 = -0.224$, $c_1 = -0.106$, $d_1 = -0.388$, $a_2 = -0.012$, $b_2 = -0.624$, $c_2 = 0.788$, $d_2 = -0.224$, $a_3 = 0.224$, $b_3 = 2.989$, $c_3 = -0.765$, and $d_3 = 0.341$.

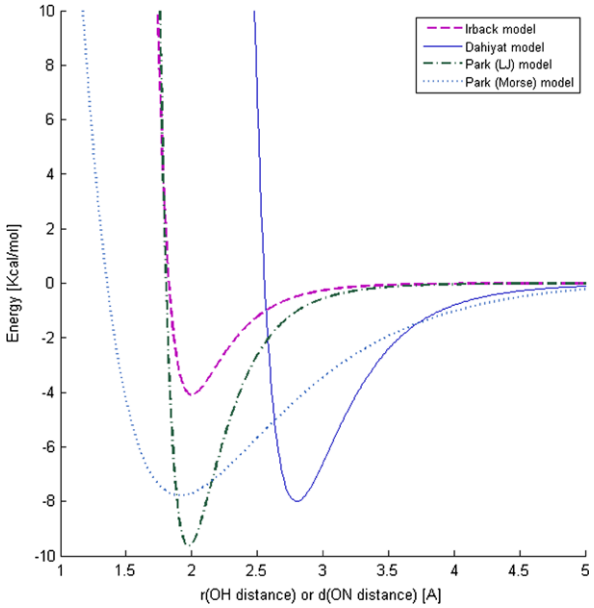

Fig. 8.10 Different energy functions of hydrogen bonds. The horizontal axis is either hydrogen bond length (r) for the functions proposed by Irbäck et al. and Park et al., or donor-acceptor distance (d) for the energy function proposed by Dahiyat et al.

Another angle-dependent model has been suggested by Dahiyat et al. [12] that is based on the potential function used in the DREIDING force field. To prevent the occurrence of unfavorable hydrogen bond geometries, their model uses more situation dependent terms in the energy function:

$$
\begin{aligned}
E_{HB} &= v_0\left[5(d_0/d)^{12} - 6(d_0/d)^{10}\right] g(\beta,\alpha,\phi),\\
g(\beta,\alpha,\phi) &= \cos^2\beta\cos^2(\alpha - 109.5), \quad \text{for } sp^3 donor - sp^3 acceptor,\\
g(\beta,\alpha,\phi) &= \cos^2\beta\cos^2\alpha, \quad \text{for } sp^3 donor - sp^2 acceptor\\
g(\beta,\alpha,\phi) &= \cos^4\beta, \quad \text{for } sp^2 donor - sp^3 acceptor,\\
g(\beta,\alpha,\phi) &= \cos^2\beta\cos^2\big(\max[\alpha,\phi]\big), \quad \text{for } sp^2 donor - sp^2 acceptor. \qquad (8.20)
\end{aligned}
$$

The constants involved in the energy function described by (8.20) assume the values $v_0 = 8$ kcal/mol and $d_0 = 2.8$ Å.

Figure 8.10 compares the energy functions from (8.17)–(8.20). In this figure we included only the terms that define the bond energy due to positional coordinates and neglect the angular coordinates, due to the fact that the latter have a considerably lower influence on the total bond energy.

Since the energy from (8.17) assumes that the solvent can only be water, we decided to focus on the models given in (8.18), (8.19) and (8.20). As already mentioned, Fig. 8.10 shows the Park et al. and Dahiyat et al.'s functions with the effect of the angular coordinates neglected. Nevertheless, our numerical experiments indicate that the angular terms in both (8.18) and (8.19) calculated with the set of constants

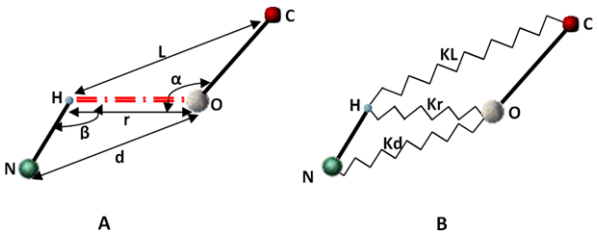

Fig. 8.11 (**A**) The geometry of hydrogen bonds. (**B**) The equivalent mechanical model of hydrogen bonds

reported in [25], as well as with a second set of constants obtained through private communications with the authors, unexplainably distort the energy function. Consequently, we decided to use the energy function proposed by Dahiyat et al. (8.20) for the remainder of this work. This function considers hydrogen bonds of protein molecules in any solvent, and the energy predicted is commonly regarded in reasonable match with experimental data [28]. Importantly, the our mechanical model presented below can be modified to fit the data provided by any other energy function.

8.5.2 Equivalent Stiffness for Individual Hydrogen Bonds

In modeling the protein molecules the authors have previously considered hydrogen bonds to act as rigid bodies (links) [41]. This assumption is valid for numerous applications when the geometry of the 3-D structure of the molecule is studied without considering the effect of external forces. However, hydrogen bonds are flexible under the effect of external and internal forces. We assume that the bond flexibility is linear over small displacements, and we can therefore use linear springs as the basis of our model. We note that we continued to treat covalent bonds as rigid bodies.

As mentioned above, we used the energy function given in (8.20) to determine the spring stiffnesses in our model. In this equation the energy is a function of three geometric parameters: donor-acceptor bond length (d), and the two angles ($\alpha\&\beta$) shown in Fig. 8.11(A). To simplify the model, angular coordinates ($\alpha\&\beta$) in energy function are replaced by the positional coordinates l and r, using the geometric identities:

$$d^2 = (NH)^2 + r^2 - 2r(NH)\cos(\beta), \tag{8.21}$$

$$l^2 = (OC)^2 + r^2 - 2r(OC)\cos(\alpha). \tag{8.22}$$

Figure 8.11(B) shows our proposed equivalent mechanical system of a hydrogen bond, which consists of three interconnected linear springs. Our aim is to determine the stiffness of each spring such that the energy of this system would be identical to the energy of the bond itself predicted by (8.20). Under the assumption of small displacements, the equivalent energy of the equivalent spring system can be calculated by using Hooke's law. The corresponding energy function can therefore be written

as:

$$E = 0.5k_l(l_2 - l_0)^2 + 0.5k_r(r_2 - r_0)^2 + 0.5k_d(d_2 - d_0)^2. \tag{8.23}$$

A complete definition of the equivalent model requires the values of the six constants $(k_r, r_0, k_l, l_0, k_d, d_0)$. These values can be obtained by setting up an optimization problem that minimizes the error between the bond energy obtained by empirical studies (8.20) and our proposed model (8.23), evaluated for each individual hydrogen bond. Observe that (8.23) contains the sum of positive values, and will therefore be always positive, while the empirical function has both negative and positive values. This discrepancy is due to different zero energy levels for calculating the energy and can be easily rectified by shifting the values of the energy along the vertical axis so that all empirical energy values become positive.

Furthermore, we imposed the following constraints on the optimization problem:

- the energy computed at the configuration prior to the small displacements by both methods ((8.20) and (8.23)) should be equal;
- the three spring constants (for the springs in Fig. 8.11) are the slope of the graph describing each spring force versus inter-atomic separation distance [37], and
- the stiffness and the free length of each spring should be positive numbers.

Therefore, we formulate the optimization problem as follows:

$$\begin{aligned}
\text{minimize:} \quad & M = 0.5k_l(l_2 - l_0)^2 + 0.5k_r(r_2 - r_0)^2 + 0.5k_d(d_2 - d_0)^2 \\
& \quad - E(d2, \alpha 2, \beta 2), \\
\text{subject to:} \quad & H1 = 0.5k_l(l_1 - l_0)^2 + 0.5k_r(r_1 - r_0)^2 + 0.5k_d(d_1 - d_0)^2 \\
& \quad - E(d1, \alpha 1, \beta 1), \\
& H2 = k_l - dE_l/(l_1 - l_0), \\
& H3 = k_r - dE_r/(r_1 - r_0), \\
& H4 = k_d - dE_d/(d_1 - d_0), \\
& -k_d + s^2 \leq 0, \\
& -k_d + p^2 \leq 0, \\
& -k_l + q^2 \leq 0, \\
& -l_0 + m^2 \leq 0, \\
& -r_0 + n^2 \leq 0, \\
& -d_0 + o^2 \leq 0.
\end{aligned} \tag{8.24}$$

This optimization problem is then solved using the Lagrange Multipliers method [3]. Figure 8.12 shows the energy of the hydrogen bond versus the bond length (r) obtained by empirical studies (first curve) and our optimized model (second curve). As shown in Fig. 8.12, the proposed function can accurately estimate the

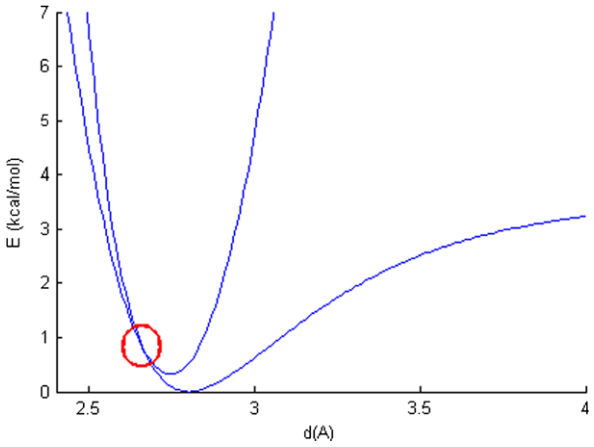

Fig. 8.12 The new energy function calculated vs. the LJ function

empirical energy function for small variations of the bond length. Similar graphs are obtained for energy versus the donor acceptor length (d) and the hydrogen acceptor ancestor (l) [40].

Importantly, Fig. 8.12 implies that each individual hydrogen bond with specific geometry can be modeled, for small displacements, as a combination of 3 linear springs which provides an equivalent stiffness in *any* direction. This is a significant step over the existing models, which considered the bond to be flexible only in the bond direction and assumed the same stiffness for all bonds with different geometry [8]. In the following section we show how we can use our model to compute the bond stiffness for *any* direction of interest.

8.5.3 Equivalent Stiffness Ellipsoid

Computing the bond stiffness in any given direction requires the determination of the stiffness matrix and, consequently, of the stiffness ellipsoid. The stiffness matrix is computed by setting up the static equilibrium equations for our equivalent mechanical system (Fig. 8.13). Link NH is assumed to be fixed and link OC is free to move (from O1C1 to O2C2). The free body diagram of the system is shown in Fig. 8.13(B). The static equilibrium equations are given by:

$$\begin{aligned} F_x = {} & k_1 dx_o \cos\alpha_1{}^2 + k_2 dx_o \cos\alpha_2{}^2 + k_3 dx_c \cos\alpha_3{}^2 \\ & + k_1 dy_o \cos\alpha_1 \cos\beta_1 + k_2 dy_o \cos\alpha_2 \cos\beta_2 + k_3 dy_c \cos\alpha_3 \cos\beta_3 \\ & + k_1 dz_o \cos\alpha_1 \cos\gamma_1 + k_2 dz_o \cos\alpha_2 \cos\gamma_2 + k_3 dz_c \cos\alpha_3 \cos\gamma_3, \end{aligned} \tag{8.25}$$

$$\begin{aligned} F_y = {} & k_1 dx_o \cos\alpha_1 \cos\beta_1 + k_2 dx_o \cos\alpha_2 \cos\beta_2 + k_3 dx_c \cos\alpha_3 \cos\beta_3 \\ & + k_1 dy_o \cos\beta_1{}^2 + k_2 dy_o \cos\beta_2{}^2 + k_3 dy_c \cos\beta_3{}^2 \\ & + k_1 dz_o \cos\beta_1 \cos\gamma_1 + k_2 dz_o \cos\beta_2 \cos\gamma_2 + k_3 dz_c \cos\beta_3 \cos\gamma_3, \end{aligned} \tag{8.26}$$

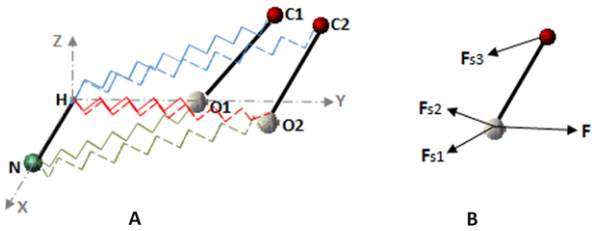

Fig. 8.13 **A**: Small displacement of atoms result in small change in the length of springs **B**: Free body diagram of link OC

$$F_z = k_1 dx_o \cos\alpha_1 \cos\gamma_1 + k_2 dx_o \cos\alpha_2 \cos\gamma_2 + k_3 dx_c \cos\alpha_3 \cos\gamma_3 + k_1 dy_o \cos\gamma_1 \cos\beta_1 + k_2 dy_o \cos\gamma_2 \cos\beta_2 + k_3 dy_c \cos\gamma_3 \cos\beta_3 + k_1 dz_o \cos{\gamma_1}^2 + k_2 dz_o \cos{\gamma_2}^2 + k_3 dz_c \cos{\gamma_3}^2. \tag{8.27}$$

The stiffness matrix can be obtained from:

$$\begin{pmatrix} F_x \\ F_y \\ F_z \end{pmatrix} = \begin{pmatrix} k_{11} & k_{12} & k_{13} & k_{14} & k_{15} & k_{16} \\ k_{21} & k_{22} & k_{23} & k_{24} & k_{25} & k_{26} \\ k_{31} & k_{32} & k_{33} & k_{34} & k_{35} & k_{36} \end{pmatrix} * \begin{pmatrix} dx_o \\ dy_o \\ dz_o \\ dx_c \\ dy_c \\ dz_c \end{pmatrix} \tag{8.28}$$

and

$$F = KX. \tag{8.29}$$

The maximum and minimum stiffness of the system at point C, and their corresponding directions can be computed from the stiffness matrix as follows: (1) a unit displacement vector at point C is assumed; (2) the corresponding force required to cause this displacement is calculated from (8.28); (3) the process of finding the minimum and maximum possible force vectors is then setup as an optimization problem:

$$\begin{aligned} &\text{minimize:} \quad F = KX, \\ &\text{subject to:} \quad XX^T = I. \end{aligned} \tag{8.30}$$

It can be shown that these maximum and minimum forces are the eigenvectors of the $K^T K$ matrix, with the magnitudes of these forces being the square root of the corresponding eigenvalues [43]. The three eigenvalues are the corresponding lengths of the semi-principal axes of the stiffness ellipsoid, and the eigen vectors are the directions of these semi-principal axes.

The stiffness of the bond in any other direction **v** can be computed by calculating the length of the line segment obtained by intersecting the stiffness ellipsoid and the line passing through the center of ellipsoid in the direction of **v**. Figure 8.14 shows a schematic representation of the stiffness ellipsoid and its orientation with respect to bond geometry.

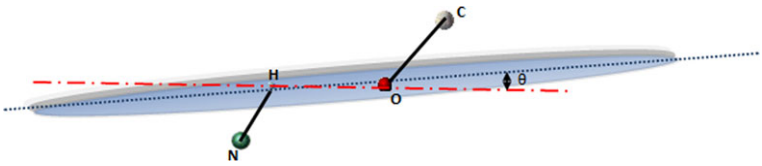

Fig. 8.14 A schematic presentation of stiffness ellipsoid and hydrogen bond

Table 8.4 Experimentally obtained stiffnesses of various bonds [4]

Bond type	Bond stiffness (N/m)
Covalent	50–180
Metallic	15–75
Ionic	8–24
Hydrogen bond	6–3
Van der Walls	0.5–1

8.5.4 Model Validation

The modeling procedure described above has been used to estimate the stiffness of several sample hydrogen bonds. Our baseline data is the experimentally obtained stiffness values published in [4] for several different types of bonds and summarized in Table 8.4. Note that the experimentally measured stiffness for hydrogen bonds is 3–6 (N/m).

The results of the estimates obtained with our model are summarized in Table 8.5 and includes the following parameters:

- the bond energy E (kCal/mol),
- the spring stiffness (N/m) for each of the three springs, k_l, k_r, and k_d,
- free length of springs (Å),
- eigen values of the stiffness matrix, which are the maximum, mean and minimum stiffnesses of the bonds (N/m),
- the angle θ^* between the direction of the maximum and the hydrogen bond direction (degrees),
- the hydrogen bond stiffness k^{**} in bond (OH) direction (N/m).

We note that our predicted stiffness values shown in Table 8.5 range between 1.19–5.74 N/m, with an average of 3.43 N/m and standard deviation of 1.3 N/m are in agreement with the experimentally obtained stiffness range of 3–6 N/m reported in [4]. The data in Table 8.5 also shows that the predicted angle between the maximum stiffness direction and the bond direction is between 5–10 degrees. Furthermore, the data shows that the corresponding stiffness ellipsoids for all these bonds are much longer in the direction of one semi-principal axis (i.e., the direction of the maximum stiffness) than in the other two principal directions. Consequently, we conclude that the stiffness of the hydrogen bond is much larger in the direction

Table 8.5 Predicted stiffness values for a number of hydrogen bonds

E (energy)	k_l	k_r	k_d	l_0	r_0	d_0	max k	mean k	min k	θ^*	k^{**}
−2.303	51	26.3	4.8	2.9	2.2	3	54.53	1.82	0.14	6.9	3.36
−2.29	40.9	8	1.7	2.8	2	2.9	34.16	0.49	0.07	10	1.19
−3.576	68.3	23.6	3	2.8	2	2.9	64.68	1.61	0.07	5.4	2.1
−3.232	111.2	37.9	6.9	2.8	1.9	2.8	104.51	2.03	0.14	7.9	4.83
−4.791	87.9	26.6	3.3	2.8	2	3	80.43	1.19	0.14	5.5	2.31
−4.843	127.7	28.8	3.9	2.8	1.8	2.9	109.69	1.26	0.21	6.4	2.73
−3.676	69.6	22.7	3.5	2.8	2	3	64.82	1.19	0.14	6.8	2.45
−2.238	57.1	41.9	6.5	2.9	2.2	3	70.56	3.15	0.14	5.1	4.55
−2.043	45.3	22.1	4.6	2.9	2.2	3	47.39	1.33	0.14	8.2	3.22
−3.04	62.1	26.4	4.4	2.9	2.1	3	62.23	1.61	0.21	6.7	3.08
−1.37	46.9	49.6	8.2	3.1	2.4	3.1	69.51	4.2	0.14	4.6	5.74
−2.856	60.1	27.7	4.8	2.9	2.1	3	61.81	1.61	0.14	6.9	3.36
−3.765	109.3	29.8	5.3	2.8	1.9	2.8	97.44	1.33	0.14	8	3.71
−1.172	39	37.3	7.7	3	2.4	3.1	54.53	2.87	0.28	6.1	5.39

of the bond than in a direction perpendicular to the bond. This implies that the α helices are stiffer in the axial direction than in the lateral direction which confirms the experimental observations [27].

Application to Protein Molecules The secondary structures of protein molecules (α helices and β sheets) are stabilized by hydrogen bonds [7]. Hence, one can infer that the stiffness of protein molecules is largely determined by hydrogen bonds. We propose two methods to calculate the stiffness of secondary structures of protein molecules.

First Approach: Hydrogen Bonds as Parallel Springs Figure 8.15(A) illustrates a schematic arrangement of hydrogen bonds in α helices. It is shown that in each turn of α helix there are 3 to 4 hydrogen bonds [1]. Each turn has 3.6 residues with 5.4 Å pitch along the helical axis [7]. The equivalent mechanical model is shown in Fig. 8.15(B). In this model, hydrogen bonds in each turn are assumed to be parallel and turns are connected in a serial form. Under these assumptions, the stiffness of the entire α helix can be obtained from Hooke's law given in (8.31).

$$K_{eq} = 1/(1/k_{turn1} + 1/k_{turn2} + \cdots + 1/k_{turn\text{-}end}). \tag{8.31}$$

Second Approach: Energy Analysis Based on the principle of superposition, the total change of energy in the protein molecule should equal the summation of the energy change of all individual hydrogen bonds. The stiffness of each hydrogen bond is known (it can be determined as described in Sect. 8.5.2). To determine the displacement of each bond from the total elongation of the secondary structure we

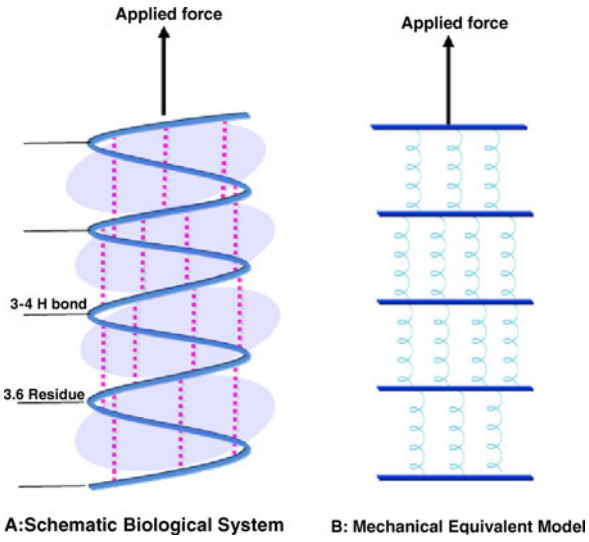

Fig. 8.15 A schematic arrangement of hydrogen bonds in α helices

assume a uniform distribution of the total elongation to each turn. Hence, if the helix is elongated by dl and the total number of turns is n, the axial elongation of each turn will be $dx = dl/n$. By assuming that each bond in a given turn act as parallel springs, the displacement of each bond will be dx. These individual bond elongations can be used together with (8.32) to compute the stiffness of the secondary structure

$$(1/2)K_{eq}(d_l)^2 = \sum (1/2)k_i(d_x)^2. \tag{8.32}$$

Stiffness Prediction for Sample Proteins Now we can use both approaches discussed above to calculate the stiffness of several secondary structures for which experimentally determined stiffness data is available in the literature. Table 8.6 lists three proteins with their PDB (Protein Data Bank) code, the number of amino acids and the number of detected hydrogen bonds (based on the geometric and energetic criteria reported in [44]). We applied both methods to these three protein molecules (Fig. 8.15).

The first molecule is a synthetic peptide, cysteine-lysine-cysteine ($C3K30C$) specifically designed to study hydrogen bonding by Lantz et al. [35]. Under the experimental conditions (explained in [35]) this synthetic peptide adopts the α helix structure as a result of hydrogen bonding (31 bonds) within the molecule. The peptide has a length of 53 Å and a diameter of approximately 15 Å. The stiffness of this protein molecule was measured using force microscopy. Each molecule was stretched from the α-helical state into a linear chain. The stiffness was found to vary with molecule displacement. In order to conduct a meaningful comparison between our predicted stiffness of this protein molecule and the empirical measurement reported in [35], only small displacements are considered. In particular, we concentrate on deformation of 1 Å or smaller of the protein.

Table 8.6 Properties of three specific proteins

PDB code	# of amino acids	# detected hydrogen bonds
Synthetic peptide	35	31
1gk6	53	42
1nkn	150	146

Table 8.7 Predicted and experimentally measured stiffnesses for different protein molecules (N/m)

PDB code	k from method # 1	k from method # 2	k reported in literature
Synthetic peptide	0.380	0.384	0.300–0.400 [35]
1gk6	0.520	0.524	0.571 [9]
1nkn	0.083	0.066	0.060–0.080 [27]

Under such a deformation, the protein molecule will maintain its helical shape and the hydrogen bonds intact. The reported experimentally measured stiffness of this protein molecule for a 1 Å elongation varies between 0.3–0.4 N/m. Our computational analysis detects 31 hydrogen bonds by using our own hydrogen bond formation criteria [41], and predicts the stiffness to be 0.38 N/m (based on the first approach above), and 0.384 N/m (from the second approach based on energy analysis), which is in good agreement with the experimentally measured stiffness.

Furthermore, the elastic properties of characterized myosin II S2 sub domain has been studied in [27] using molecular dynamics and normal mode analysis. The specific protein molecule, whose PDB code is 1NKN PDB, is an 87 residue long α-helix. We predicted 146 hydrogen bonds within this molecular structure. This resulted in 0.088 N/m stiffness employing the first method and 0.066 N/m using the second method, which are in good agreement with the stiffness predicted in [27] for this protein molecule (0.06–0.08 N/m).

Finally, the force-extension behavior of α-helices, β-sheets and tropocollagen domains has been studied in [9]. Their results are based on atomistic modeling of nano-mechanical response of protein molecules at ultra-slow deformation rates. The stiffness predicted for a molecule with helical structure (1GK6) in this study is 0.571 N/m. The predicted stiffness for this molecule using our proposed method is 0.52 N/m, see Table 8.7.

8.6 Concluding Reflections on Challenges and Opportunities

Life exists because a large number of protein nano-molecules function inside biological cells in a coordinated manner as articulated kinematic machines performing their task. While we understand the governing kinematics and, to some degree, dynamics principles, it would be naïve to think that the mechanics of these nano-machines is understood. We can however claim that we have begun to chart the

road map for studying protein mechanics in terms of the systematic application of the well-established classical mechanics (kinematics and dynamics). The simplicity and robustness of these principles in an otherwise complex and difficult to model environment (internal and external to protein molecules) is a major asset for scientists.

In this chapter, we discussed some of the central kinematic elements that can be used to model protein chains and to study their mobility, folding and flexibility. We have used rigorous principles of mechanics in systematic and efficient manners. One might fear that these rigorous kinematics methodologies deceptively present the study of protein molecules as an easy task. That was neither our intention nor it is true. However it is our hope that some of the readers of these pages come to recognize that much of the great future of natural and synthetic biology and nano technology rests in gaining an understanding of the geometry and motion of these kinematic wonders of life. This is in disagreement with the belief many young scientist may hold that kinematics does not play a fundamental role in their carriers.

A careful study of this chapter should persuade the reader of two things. First, we have made significant strides in understanding the mechanics of protein molecules. Second, there is a lot more left to be discovered. Central challenges in the study of proteins are rooted in the cross disciplinary nature of the field. Future breakthroughs will undoubtedly come from the emergence of high performance computing, advances in molecular biology and physical chemistry, science of microscopy and material characterization, statistics, and modern kinematics. Institutions of higher education must facilitate this exciting convergence of diverse disciplines, which will require the non-trivial feat of a major rethinking of the educational framework in the area of bio-nanotechnology.

Reciprocally, the science of modern kinematics will be propelled forward as new kinematic tools are developed to tackle the complexities of modeling protein molecules. In renaissance, the industrialization and emergence of complex machinery fuelled the genesis of modern kinematics. Protein molecules, these engines of life, will be the drivers of "post-modern kinematics".

Acknowledgements We would like to acknowledge the current and former graduate students involved in the research that made this publication possible: C. Alvarado, P. Bohnenkamp, K. Latif, C. Madden, J. Parker, K. Rodriguez, R. Subramanian, Z. Shahbazi, and P. Tavousi. Kazem Kazerounian was partially supported by the National Science Foundation grants CMMI-0856401, CNS-0923158, and CMMI-1053077. Horea Ilieş was supported in part by the National Science Foundation grants CMMI-0555937, CAREER award CMMI-0644769, CMMI-0856401, CMMI-0927105, and CNS-0923158. The authors would like to gratefully acknowledge this financial support.

References

1. Ackbarow, T., Chen, X., Keten, S., Buehler, M.J.: Hierarchies, multiple energy barriers, and robustness govern the fracture mechanics of alpha-helical and beta-sheet protein domains. Proc. Natl. Acad. Sci. USA **104**(42), 16,410–16,415 (2007)
2. Alexandrescu, A.T., Snyder, D.R., Abildgaard, F.: NMR of hydrogen bonding in cold-shock protein A and an analysis of the influence of crystallographic resolution on comparisons of hydrogen bond lengths. Protein Sci. **10**(9), 1856–1868 (2001)

3. Arora, J.S.: Introduction to Optimum Design. Elsevier Academic, Amsterdam (2004)
4. Ashby, M., Shercliff, H., Cebon, D.: Materials: Engineering, Science, Processing and Design. Butterworth-Heinemann, Stoneham (2007)
5. Baker, E.N., Hubbard, R.E.: Hydrogen bonding in globular proteins. Prog. Biophys. Mol. Biol. **44**(2), 97–179 (1984)
6. Bohnenkamp, P., Kazerounian, K., Ilieş, H.: Strategies to avoid energy barriers in ab initio protein folding. In: 12th IFToMM (International Federation of the Theory of Mechanisms and Machines) World Congress, Besançon, France (2007)
7. Branden, C., Tooze, J.: Introduction to Protein Structure, 2nd edn. Garland Publishing, New York (1999)
8. Brown, I.: The Chemical Bond in Inorganic Chemistry: The Bond Valence Model. Oxford University Press, London (2006)
9. Buehler, M.J., Keten, S.: Elasticity, strength and resilience: A comparative study on mechanical signatures of α helix, β sheet and tropocollagen domains. Nano Res. **1**, 63–71 (2008)
10. Cornell, W.D., Cieplak, P., Bayly, C.I., Gould, I.R., Merz, K.M., Ferguson, D.M., Spellmeyer, D.C., Fox, T., Caldwell, J.W., Kollman, P.A.: A second generation force field for the simulation of proteins, nucleic acids, and organic molecules. J. Am. Chem. Soc. **117**(3), 5179–5197 (1995). doi:10.2307/40041279
11. Daggett, V., Li, A., Fersht, A.: Combined molecular dynamics and ϕ-value analysis of structure-reactivity relationships in the transition state and unfolding pathway of Barnase: structural basis of Hammond and anti-Hammond effects. J. Am. Chem. Soc. **120**(49), 12,740–12,754 (1998)
12. Dahiyat, B., Gordon, D., Mayo, S.: Automated design of the surface positions of protein helices. Protein Sci. **6**, 1333–1337 (1997)
13. Doruker, P., Bahara, I., Baysalb, C., Erman, B.: Collective deformations in proteins determined by a mode analysis molecular dynamics trajectories. Polymer **43**, 431–439 (2002)
14. Duan, Y., Karplus, M.: Pathways to a protein folding intermediate observed in a 1-microsecond simulation in aqueous solution. Science **282**, 7404 (1998)
15. Duan, Y., Wu, C., Chowdhury, S., Lee, M.C., Xiong, G.M., Zhang, W., Yang, R., Cieplak, P., Luo, R., Lee, T., Caldwell, J., Wang, J.M., Kollman, P.: A point-charge force field for molecular mechanics simulations of proteins based on condensed-phase quantum mechanical calculations. J. Comput. Chem. **24**(16), 1999–2012 (2003)
16. Favrin, G., Irbäck, A., Mohanty, S.: Oligomerization of amyloid a β 16-22 peptides using hydrogen bonds and hydrophobicity forces. Biophys. J. **87**, 3657–3664 (2004)
17. Fetrow, J., Giammona, A., Kolinski, A., Skolnick, J.: The protein folding problem: a biophysical enigma. Curr. Pharmaceutical Biotechnol. **3**(4), 329–347 (2002)
18. Floudas, C., Klepeis, J., Pardalos, P.: Global optimization approaches in protein folding and peptide docking. DIMACS Ser. Discret. Math. Theor. Comput. Sci. **47**, 141–171 (1999)
19. Gabovich, A., Li, M.: Mechanical stability of proteins. J. Chem. Phys. **131**, 024121 (2009)
20. Guyon, E., Roux, S., Hansen, A., Bibeau, D., Troadec, J., Crapo, H.: Non-local and non-linear problems in the mechanics of disordered systems: application to granular media and rigidity problems. Rep. Prog. Phys. **53**, 3739 (1990)
21. Hamdia, M., Ferreira, A., Sharmab, G., Mavroidis, C.: Prototyping bio-nanorobots using molecular dynamics simulation and virtual reality. Microelectron. J. **39** (2008)
22. Hardin, C., Pogorelov, T., Luthey-Schulten, Z.: Ab initio protein structure prediction. Curr. Opin. Struct. Biol. **12**(2), 176–181 (2002)
23. Herrmann, T., Güntert, P., Wüthrich, K.: Protein NMR structure determination with automated NOE assignment using the new software CANDID and the torsion angle dynamics algorithm DYANA. J. Mol. Biol. **319**(1), 209–227 (2002)
24. Hoffmann, C., Joan-Arinyo, R.: A brief on constraint solving. Comput-Aided Des. Appl. **2**(5), 655–663 (2005)
25. Hwanho, C., Hongsuk, K., Hwangseo, P.: New angle-dependent potential energy function for backbone-backbone hydrogen bond in protein-protein interactions. J. Comput. Chem. **31**(5), 897–903 (2010)

26. Irbäck, A., Mitternacht, S., Mohanty, S.: An effective all-atom potential for proteins. PMC Biophys. **2**(2) (2009)
27. Ivana, A., Srboljub, M.M., Karplus, M.: The elastic properties of the structurally characterized myosin ii s2 subdomain: A molecular dynamics and normal mode analysis. Biophys. J. **94**, 3779–3789 (2008)
28. Jacobs, D.J., Rader, A.J., Kuhn, L.A., Thorpe, M.F.: Protein flexibility predictions using graph theory. Proteins Struct. Funct. Genet. **44**(2), 150–165 (2001). doi:10.1002/prot.1081
29. Jeffery, A.G., Justin, S.D., James, P.L., Randall, T.C.: Implementation of a Morse potential to model hydroxyl behavior in phyllosilicates. J. Chem. Phys. **130**, 134,713 (2009)
30. Kazerounian, K., Latif, K., Alvarado, C.: Protofold: a successive kinetostatic compliance method for protein conformation prediction. J. Mech. Des. **127**(4), 712–717 (2005)
31. Kazerounian, K., Latif, K., Rodriguez, K., Alvarado, C.: Nano-kinematics for analysis of protein molecules. J. Mech. Des. **127**(4), 699–711 (2005)
32. Kellermayer, M.S., Smith, S.B., Bustamante, C., Granzier, H.L.: Complete unfolding of the titin molecule under external force. J. Struct. Biol. **122**, 197–205 (1998)
33. Keskin, O.: Proteins with similar architecture exhibit similar large-scale dynamic behavior. Biophys. J. **78**, 2093–2106 (2000)
34. Kortemme, T., Morozov, A.V., Baker, D.: An orientation-dependent hydrogen bonding potential improves prediction of specificity and structure for proteins and protein-protein complexes. J. Mol. Biol. **326**(4), 1239–1259 (2003)
35. Mark, A.L., Suzanne, P.J., Hiroshi, T., Tomasz, M., Toshinori, K., Nakamara, C., Jun, M.: Stretching the α-helix: A direct measure of the hydrogen bond energy of a single peptide molecule. Chem. Phys. Lett. **315**, 61–68 (1999)
36. McDonald, I.K., Thornton, J.M.: Satisfying hydrogen-bonding potential in proteins. J. Mol. Biol. **238**(5), 777–793 (1994)
37. Mitchel, B.S.: An Introduction to Materials Engineering and Science. Wiley, New York (2003)
38. Nichols, W.L., Rose, G.D., Ten Eyck, L.F., Zimm, B.H.: Rigid domains in proteins: an algorithmic approach to their identification. Proteins **23**(1), 38–48 (1995)
39. Rief, M., Gautel, M., Oesterhelt, F., Fernandez, J.M., Gaub, H.E.: Reversible unfolding of individual titin immunoglobulin domains by afm. Science **276**, 1109 (1997)
40. Shahbazi, Z.: Role of hydrogen bonds in kinematics mobility and elasticity analysis of protein molecules. Ph.D. Thesis, University of Connecticut (2012)
41. Shahbazi, Z., Ilieş, H., Kazerounian, K.: Hydrogen bonds and kinematic mobility of protein molecules. J. Mech. Robot. **2**, 021009 (2010)
42. Shahbazi, Z., Ilieş, H., Kazerounian, K.: Kinematic motion constraints of the protein molecule chains. ASME Conf. Proc. **2011**(54839), 535–542 (2011). doi:10.1115/DETC2011-48519
43. Shahbazi, Z., Ilieş, H., Kazerounian, K.: A mechanical model of hydrogen bond. Tech. Rep, University of Connecticut (2012)
44. Shahbazi, Z., Pimentel, T.A., Ilies, H., Kazerounian, K., Burkhard, P.: A kinematic observation and conjecture for stable construct of a peptide nanoparticle. In: Advances in Robot Kinematics, Issue on Motion in Man and Machine. Springer, Berlin (2010)
45. Su, H., Parker, J., Kazerounian, K., Ilies, H.: A comparison of kinetostatic and multibody dynamics models for simulating protein structures. In: Mechanisms and Robotics Conference, ASME IDETC, Las Vegas, September 2007 (2007)
46. Subramanian, R., Kazerounian, K.: Improved molecular model of a peptide unit for proteins. In: ASME 2006 International Design Engineering Technical Conferences & Computers and Information in Engineering Conference, Philadelphia, Pennsylvania, USA, vol. DETC 2006-99315 (2006)
47. Subramanian, R., Kazerounian, K.: Kinematic mobility analysis of peptide based nanolinkages. Mech. Mach. Theory **42**(8), 903–918 (2007)
48. Subramanian, R., Kazerounian, K.: Residue level inverse kinematics of peptide chains in the presence of observation inaccuracies and bond length changes. J. Mech. Des. **129**(3), 312–319 (2007)

49. Tskhovrebova, L., Trinick, K., Sleep, J., Simmons, M.: Elasticity and unfolding of single molecules of the giant muscle protein titin. Nature **387**, 308 (1997)
50. Wirggers, W., Schulten, K.: Protein domain movements: detection of rigid domains and visualization of hinges in comparisons of atomic coordinates. Proteins **29**(1), 1–14 (1997)
51. Xu, D., Tsai, C.J., Nussinov, R.: Hydrogen bonds and salt bridges across protein-protein interfaces. Protein Eng. **10**(9), 999–1012 (1997)